ENHANCING LIGHT EXTRACTION EFFICIENCY OF InGaN/GaN MULTI QUANTUM WELL LIGHT EMITTING DIODES WITH EMBEDDED TWO DIMENSIONAL PHOTONIC CRYSTAL STRUCTURES

A THESIS

SUBMITTED TO THE GRADUATE PROGRAM OF MATERIALS SCIENCE AND NANOTECHNOLOGY

AND THE INSTITUTE OF ENGINEERING AND SCIENCES

OF BILKENT UNIVERSITY

IN PARTIAL FULLFILMENT OF THE REQUIREMENTS

FOR THE DEGREE OF

MASTER OF SCIENCE

By

Ali Güneş KAYA

August 2010

I certify that I have read this thesis and that in my opinion it is fully adequate, in scope and in quality, as a thesis for the degree of Master of Science.

_____

Prof. Dr. Salim Çıracı (Supervisor)

I certify that I have read this thesis and that in my opinion it is fully adequate, in scope and in quality, as a thesis for the degree of Master of Science.

_____

Res. Asst. Prof. Dr. Aykutlu Dâna (Co-supervisor)

I certify that I have read this thesis and that in my opinion it is fully adequate, in scope and in quality, as a thesis for the degree of Master of Science.

_____

Res. Asst. Prof. Dr. Bilge İmer (Co-supervisor)

I certify that I have read this thesis and that in my opinion it is fully adequate, in scope and in quality, as a thesis for the degree of Master of Science.

_____

Asst. Prof. Dr. Ali Kemal Okyay

Approved for the Institute of Engineering and Sciences:

_____

Prof. Dr. Levent Onural

Director of Institute of Engineering and Sciences

ABSTRACT

ENHANCING LIGHT EXTRACTION EFFICIENCY OF InGaN/GaN MULTI QUANTUM WELL LIGHT EMITTING DIODES WITH EMBEDDED TWO DIMENSIONAL PHOTONIC CRYSTAL STRUCTURES

Ali Güneş KAYA

M.S. in Graduate Program of Materials Science and Nanotechnology

Supervisor: Prof. Dr. Salim Çıracı

August 2010

Advance in the growth methods of III-Nitrides and researches in order to eliminate doping problems of gallium nitride (GaN) resulted in high band gap materials with increased crystal quality which have led to tremendous improvement in opto-electronic devices. Their durability under harsh environmental and operational conditions such as high pressure and high temperature, and large spectral coverage range including 200 nm deep ultra-violet (deep-UV) through 1500 nm infra-red (IR) make them excellent candidates for opto-electronic applications such as full color LCD panels, biomedical sensor devices, high resolution printers, high density storage devices, defense systems. Among III-Nitrides, GaN has attracted the most interest with its high electronic band gap of 3.4 eV at room temperature and ability to form compounds with other group III elements aluminum and indium which have band gaps of 6.2 eV and 0.7 eV respectively which results in a large optical spectrum.

However, potential performance of III-Nitride based devices is hindered mainly because of an optical phenomenon called total internal reflection (TIR). High dielectric constant of these materials prevents light to escape from the structure. Light is totally reflected back from the air-nitride interface for incident angles larger than critical angle. With a refractive index of 2.7, GaN material has 22°-24° critical angle which means less than 12% of light can just

escape the structure. While 66% of the light generated in quantum well region of a GaN based light emitting diode (LED) is trapped in the GaN layer, 22% of the light is guided in the sapphire substrate. Because of TIR, although internal quantum efficiency of GaN based LED with emission wavelength of around 400 nm is almost unity (higher than 90%), external quantum efficiency is very low. To enhance extraction, a lot of geometrical methods including surface roughening and facet shaping have been tried to reduce the effects of dielectric contrast between the device and medium.

In order to increase the extraction efficiency of GaN based LEDs, two dimensional photonic crystals were used in this thesis. LED wafers used were fabricated in collaboration with University of Santa Barbara, California (UCSB) which are InGaN/GaN multi quantum well (MQW) structures that emit light at 390 nm and 410 nm respectively. These LED wafers were processed in the scope of the thesis and photonic crystal (PC) structures were patterned on the p layer of the device.

This thesis work is concentrated on two parts; first part is characterization and fabrication, and second part is simulation. In characterization and fabrication part, firstly GaN material etching characterizations were completed using dry etching method by reactive ion etcher (RIE) since there had been no optimized recipe for GaN processing in the clean room know-how. In this characterization, main parameter was the etching anisotropy since vertical side-wall is crucial for LED processing and PC formation. After characterization step was completed, p doping activation was done in Middle East Technical University, Ankara (METU) and then LED wafers were processed in clean room class-100 environment at Bilkent University, Ankara by using the know-how and recipe obtained from characterization stage. As a final step, two dimensional square and triangular photonic crystal lattice structures were patterned by using electron beam writer and these structures were transferred on to p layer of GaN LED by using RIE. Measurements and imaging regarding material and optical properties, fabrication quality and extraction enhancement were done by using scanning electron microscope (SEM), atomic force microscopy (AFM), spectrophotometer (UV-Vis), ellipsometer and probe station. I-V characteristics, optical power measurements and intensity plots on black&white CCD camera images were taken. In simulations part, two and three dimensional simulations using plane wave expansion method, integral method and finite difference time domain method were completed. More than 40000 simulations were run in total during this thesis work.

As a result, PCs with 520 nm lattice period and 260 nm hole diameters in square and triangular geometries were modeled and fabricated. Final depth of lattices was around 100-

120 nm. Results of 2D integral simulations suggested around 15-20% of error between modeling and experiments because of imperfectness regarding fabrication of PC structures. Furthermore, damaging effects of RIE and focused electron beams were not considered. In measurements, extraction efficiency enhancement factors of about 2.2 and about 2.6 were found using square and triangular PC lattices with respect to LED devices without PC structure patterning. In simulations, while square PC lattice models showed 2.8 times enhancement in extraction efficiency, triangular lattice resulted in 3.1 times with respect to no PC models. In comparison of measurements and simulations, difference in the range of 15-25% was found which were expected as stated above with also considering the effect of processing damages on top p and p++ layer and quantum well region.

Keywords: Gallium nitride (GaN), Light emitting diode (LED), Photonic crystal, Finite difference time domain (FDTD) simulation

ÖZET

İKİ BOYUTLU FOTONİK KRİSTAL YAPILARI GÖMÜLÜ InGaN/GaN ÇOKLU KUANTUM KUYULU IŞIK SAÇAN DİYOTLARIN IŞIK ÇIKARIM VERİMLERİNİ ARTIRMA

Ali Güneş KAYA

Malzeme Bilimi ve Nanoteknoloji Lisansüstü Programı Yüksek Lisans

Tez Yöneticisi: Prof. Dr. Salim Çıracı

Ağustos 2010

Büyütme tekniklerindeki gelişmeler ve katkılama problemlerinin çözümü sonrasında büyütülen yüksek kristal kaliteli galyum nitrür başta olmak üzere III-Nitrürler, optronik teknolojisinin gelişmesinde önemli rol oynamışlardır. Uçdeğerlerdeki çevresel şartlar ve çalışma şartları altında dahi yüksek verimle çalışmaları ve 200 nm ila 1500 nm arasını kapsayan optik spektrumları sayesinde optronik uygulamalar konusunda vazgeçilmez hale gelmiş olup şu anda LCD panellerin arka aydınlatmaları, biyomedikal sensor uygulamaları, yüksek çözünürlükteki lazer yazıcılar, yüksek depolama alanlı optik diskler ve savunma sistemleri başta olmak üzere birçok alanda kullanılmaktadırlar. III-Nitrürler arasında en fazla ilgiyi 3.4 eV'luk yüksek elektronik bant genişliğiyle galyum nitrür çekmektedir. Bu bileşiğin diğer III-Nitrür elementleri olan alüminyum ve indiyum ile bağ yapabilme potansiyeli, III-Nitrür bazlı optronik cihazların kapsadığı optik spektrumu oldukça geniş bir hale getirmiştir.

Ancak, III-nitrürlerin potansiyel olarak sahip oldukları performans, yüksek kırılma indisleri nedeniyle oluşan tam yansımadan dolayı ketlenmektedir. Kırılma indisi 2.7 olan galyum nitrür içinde yol alan ışık, gelme açısı 22° ila 24° arasında olan kritik eşikten fazla olması durumunda hava-galyum nitrür sınırından geçememekte ve gerisingeriye malzeme içine yansımaktadır. Bu durumda, galyum nitrür tabanlı ışık saçan diyotların kuvantum kuyularında üretilen ışığın yalnızca %12'den daha az bir kısmı cihaz dışına çıkabilmektedir. Bu ışığın %66'lık büyük bir kısmı galyum nitrür içinde hapsolmakta, %22'lik bir kesimi ise taban

malzeme olan safir içinde yönlenmektedir. Her ne kadar 400 nm civarında ışık saçan galyum nitrür tabanlı diyotların öz kuvantum verimleri %90'dan fazla ise de, tam yansıma nedeniyle dışsal kuvantum verimleri oldukça düşmektedir. Bu durumu bertaraf edebilmek adına geometrik tabanlı birçok yaklaşım denenegelmiştir.

Bu tez çalışmasında, galyum nitrür tabanli ışık saçan diyotların ışık çıkarım verimlerini artırmak için iki boyutlu fotonik kristal yapıları kullanılmıştır. Bu bağlamda, Kaliforniya Santa Barbara Üniversitesi işbiliğiyle Amerika'da büyütülen ve 390 ve 410 nm'de ışıyan galyum nitrür tabanli malzemeler, Orta Doğu Teknik Üniversitesi ve Bilkent Üniversitesi'nde işlenmiş olup ardından fotonik kristal yapıları p katkı malzemeli katman üzerine basılmıştır.

Bu tez iki ana çalışmadan oluşmuştur. Bu çalışmalardan bir tanesi karakterizasyon ve üretim çalışmalarıyken diğer çalışma simülasyon ve modellemeleri kapsamaktadır. Karakterizasyon ve üretim aşamasında öncelikle galyum nitrür malzemesinin reaktif iyon delme (RIE) sistemiyle işlenmesi karakterize edilmiştir. Temel karakterizasyon parametresi olarak delinme işleminin eşyönsüzlüğü dikkate alınmıştır. Bu sayede, mümkün olan en dik duvar oluşturacak şekilde işlem karakterize edilmiştir. Karakterizasyon bölümünün tamamlanmasının ardında p tipi katkılama aktivasyonu Orta Doğu Teknik Üniversitesi'nde yapılmıştır. Ardından Amerika'da üretilmiş olan bu malzemelerin ışık saçan diyot üretimi sürecindeki işlemler Bilkent Üniversitesi bünyesindeki sınıf-100 mertebesinde bulunan temiz odada yürütülmüş ve karakterizasyon sırasında edinilen bilgiler ışığında diyot üretimi başarıyla tamamlanmıştır. Son bir basamak olarak fotonik kristal yapıları karesel ve üçgensel geometrilerde olmak üzere elektron ışını yazıcısında diyotlar üzerine basılmış ve reaktif iyon sisteminde son halini almıştır. Son ürünler üzerinde ölçümler prob istasyonu vasıtasıyla yapılmıştır. Bu ölçümler I-V karakteristiği, optik güç ölçümü, siyah beyaz CCD kamerada çekilen fotoğraflardan elde edilen ışık yoğunluğu olarak sıralanmıştır. Simülasyonlar ise iki boyutta ve üç boyutta yapılmış olup düzlem dalga açılımı metodu, integral metod ve sonlu zaman aralıklı etki alanı (FDTD) metodu kullanılarak tamamlanmıştır. Bu tez çalışması süresince, 40000'den fazla simülasyon sonucu değerlendirilmiştir.

Sonuç olarak 520 nm periyotlu, 260 nm çaplı fotonik kristal yapıları üçgensel ve karesel geometrilerde ışık saçan diyot üzerine basılmış ve aynı geometriler bilgisayar ortamında modellenerek simüle edilmiştir. Ortalama fotonik kristal derinligi 100 ila 120 nm'dir. İki boyutlu integral metodu kullanılan simülasyonların sonuç değerlendirmesinde, deneysel ölçümlerle üç boyuttaki simülasyon sonuçları arasında %15 ila %20'lik bir fark olacağı ögörülmüştür. Bu farkın temel kaynağının ise üretilen fotonik kristal şekillerinin dizayn

edilenden belirli tolerans dahilinde farklı olmasıdır . Bu toleransa RIE ve elektron ışın demetiyle yazım işlemi dahil edlmemiştir. Ölçümler sonucunda fotonik kristal yapılı diyotların ışık artırım miktarı kare ve üçgen geometriler için sırasıyla 2.2 ve 2.6 kat olarak bulunmuştur. Simülasyon sonuçlarında ise ışık miktarı kare ve üçgen geometrili kristal yapıları icin 2.8 ve 3.1 kat artış görülmüştür. Ölçümler ve deneyler karşılaştırıldığında ortaya çıkan %15 ila %25 arasındaki fark iki boyutlu integral metoduyla yapılan simülasyonda öngörülen farkla örtüşmekte, fazladan %5'lik kesim ise RIE ve electron ışın demetiyle yapılan işlemler sırasında kuvantum kuyularına ve p ve p++ katmanlarına verilen zararın sonucu olarak yorumlanmıştır.

Anahtar kelimeler: Galyum nitrür (GaN), Işık saçan diyot (LED), fotonik kristal, sonlu zaman aralıklı etki alanı (FDTD) simülasyonu

ACKNOWLEDGEMENTS

I would like to thank to my supervisor Prof. Dr. Salim Çıracı, co-advisors Asst. Prof. Dr. Aykutlu Dâna and Asst. Prof. Dr. Bilge İmer for their interest in this thesis.

I also thank to Mustafa Ürel for his help and contribution.

I thank to my group members Hasan Güner, Burak Türker, and Okan Ekiz.

Special appreciation goes to my dear, Ebru. Without her support and encourage, this thesis process would be much harder to complete, especially for the last 1.5 years. Thanks for staying with me in my hardest times, thanks for being in my life.

And finally, I appreciate all the efforts my family has done for me so far, from the very beginning since 1983. They have always been there, by my-side. They have always believed in me, even more than I do. It would not be possible to realize this thesis without their existence. Thanks for bearing me in my most stressful moments. Thanks for being much more than a family to me.

The financial support from TÜBİTAK is also gratefully acknowledged.

Aileme…

sevgili annem Süveyda'ya,

değerli babam Osman'a,

güzeller güzeli kız kardeşim Sıla'ya,

dostluğunuza ve varlığınıza…

Ebru,

Eb,

Ebbie,

Beb,

bi’ tane bizden bi’ tane yok ki…

Table of Contents

List of Figures

List of Tables

Chapter 1

1. Introduction

Nitride semiconductors have drawn a lot of attention for the last two decades. They can be used in high power, high frequency optoelectronics under harsh environmental conditions such as high temperature and high pressure. Their direct band gap properties and wide spectrum coverage which includes full visible range and most of ultraviolet (UV) down to 200 nm make them excellent candidates for optoelectronic devices. With the advancements in III-Nitrides growth techniques and solutions on the problems such as p type doping, III -Nitride based systems have been fabricated and commercialized including full color bright displays, illumination devices, visible-blind UV photo-detectors, high resolution laser printers, biomedical applications, high density storage devices, and defense systems.

Among III-Nitrides, gallium nitride (GaN) has gained the most attention since it has large direct band gap of 3.4 eV at room temperature while it can form compounds with other group III elements aluminum (Al) and indium (In) which have band gaps of 6.2 eV and 0.7 eV respectively. By varying the amount of elements in the compounds, AlGaN, InGaN and AlInGaN, one can reach spectrum range starting wavelength from 200 nm up to 1500 nm which covers deep UV - UV, full visible spectra and infrared (IR). Intense research on high power GaN based light emitting diodes (LEDs) has been continued for the last decade.

Light emitting diodes are based on radiative recombination of electron and hole pairs generated in the active layer of the material, which is called solid state lighting. LEDs are the ultimate sources of illumination because of their long life time, low energy consumption, high durability, resistance to mechanical effects, quick response time and high luminescence efficiency. One of the major goals of LED research is to use LEDs in general lighting.

Efficiency of traditional light bulbs is around 1% ~ 4% and efficiency of flourescents is around 15% ~ 20%. On the other hand, LEDs can have efficiencies up to 80%. Exchanging classic 100 W light bulbs that are used in houses by LEDs will save 70% of energy that is used for lighting purposes. In order to be able to use LEDs in general lighting, high intensity

white light with a natural color temperature should be realized by using solid state techniques. By tuning and mixing three main colors red, green and blue in proper ratios or using phosphor with highly efficient blue LEDs can enable to have white light with a natural color temperature. GaN based light emitting diodes make this dream possible by filling the gap of the blue color in the spectrum for solid state lighting technology.

In order to be able to use LEDs for general lighting, efficacy more than 200 lm/W should be achieved. Red, amber, orange and yellow LEDs that use AlGaInP chips have already better luminous efficiency than a 100 W incandescent lamp. Higher than 100 lm/W efficiency has been achieved by using these chips. On the other hand, extraction efficiencies of GaN based green and blue LEDs are not high enough. Considering that human eye responsivity is also very low for blue color, GaN based LEDs which illuminates in the wavelength of blue should have much higher extraction efficiencies.

Although internal quantum efficiency of these blue LEDs are around 90%, external quantum efficiency drops to about 10-12%. Main reason for low extraction efficiency for GaN based LEDs is total internal reflection. Most of the light emitted from active layer of these devices cannot be used. Light which cannot get out from the device is eventually absorbed by defects and quantum wells which also cause extra-heat that is detrimental for working life of LED.

Because of the high refractive index contrast between GaN (n=2.7) and outer space (n=1), light coming to the air-GaN interface reflects totally back for incident angles higher than critical angle. Critical angle for GaN is around 22°-24°. From top surface of the GaN based LED without any encapsulation, ratio of emitted light to the generated light in active layer of the device is around $1/4n^2 \approx 4\%$. Some of other issues about low extraction efficiency are reflection from metal contacts, substrate absorption, absorption of carriers by GaN defects, impurities and InGaN/GaN quantum well layer.

Main objective of this thesis is to increase low extraction efficiency of light from GaN based LEDs. In order to increase the light output from GaN based LED, either internal quantum efficiency or extraction efficiency should be increased. Internal quantum efficiency is related to quality of the crystal structure of the material and can only be altered during growth of the material. However, it is already close to unity.

On the other hand, extraction efficiency is mostly related to the geometry of the device. By designing proper surface geometry, most of the light trapped in the high refractive index medium because of total internal reflection can escape the structure.

Several methods have been tried out in order to enhance light output by enlarging the light escape cone geometrically such as surface texturing [1], modifying spontaneous emission by resonant micro-cavity [2], surface plasmons [3], incorporating 2D photonic crystals [4][5][6][7]. In this thesis, photonic crystals are studied in depth in order to increase the intensity of the light that comes out of the LED. In the literature, an average of intensity increase of 1.5~2.1 times by using 2D photonic crystal (PC) structures has been reported [8].

PC increases extraction efficiency by diffracting guided modes in the material to air. Light propagating in the material with an incident angle higher than critical angle is trapped in the dielectric material. By using PC structures, these in-plane wave-vectors are folded into leaky modes so that originally guided light in the GaN material couples out into air. In order diffraction condition to be satisfied and higher number of modes to be extracted from 2D PC structure, parameters such as wavelength, mode angle, PC depth, filling factor and lattice constant should be designed carefully. Higher extraction efficiencies on LEDs have been achieved by using rather larger lattice constants [9]. The a/λ interval where most extraction efficiency achieved is stated to be between from $a/\lambda = 1$ to $a/\lambda = 2$ [10]. This result shows that Bragg scattering has more influence on extraction efficiency than that of band-gap approach and/or Purcell effect. Therefore, design of the PC structure is based on Bragg condition in this thesis.

In the second chapter, information about background of GaN, growth techniques, material properties, and layer structure of LED wafer processed in this thesis work are given. Third chapter is about light emitting diodes and InGaN/GaN multi quantum well (MQW) structures. Development history of LEDs and progress in InGaN/GaN and GaN based LEDs, device principles and PC LEDs are discussed. In the fourth chapter, general information about photonic crystals is given. Theoretical background about Maxwell's equations, photonic band gap formation and fundamentals of Bragg scattering are argued. Fifth chapter comes with the details about characterization and fabrication of GaN material and PC structure. In this chapter, GaN material etching characterization, LED wafer processing steps and electron beam lithography (e-beam) based PC fabrication issues are explained comprehensively. In the sixth chapter, measurements about LED device and fabricated PC structures are shown. Technique and results of the simulations regarding extraction efficiency enhancement of GaN based LED with embedded PC structures are stated. Comparison of simulations and measurements are discussed. In seventh chapter, thesis work is concluded. At the end of the chapters, one can find references used in the thesis and appendix. In appendix, scripts and

codes are stated which are used and written for simulation pre-processing and post-processing.

Chapter 2

2. Gallium Nitride & Material Properties

2.1 Introduction

III-Nitrides are important semiconductors because of their direct band gap properties and wide spectrum coverage (full visible range and most of UV down to 200 nm). They can be used in high power, high frequency optoelectronics under harsh environmental conditions such as high temperature and high pressure. GaN is superior for having high breakdown field and high electron velocity. Since it is chemically inert, GaN is an excellent candidate for opto-electronic devices which works under harsh chemical environment.

III -Nitride based systems have been fabricated and commercialized so far including full color bright displays, illumination devices, visible-blind UV photodetectors, high resolution laser printers, biomedical applications, high density storage devices, defense systems.

Among III-Ns, GaN has gained the most attention since it has large direct bandgap of 3.4 eV at room temperature while it can form compounds with other group III elements aluminum and indium which have bandgaps of 6.2 eV and 0.7 eV respectively. By varying the amount of elements in the compounds, AlGaN, InGaN and AlInGaN, one can reach spectrum range starting wavelength from 200 nm upto 1500 nm which covers UV-deep UV, visible spectra and IR.

2.2 Direct & Indirect Band Gap Structures

Structure of band gaps of materials characterize the optical properties of the material. Momentum difference of bands are important especially for the materials to be used in opto-electronics. Accoring to wave-vectors of maxima and minima of bands, materials are classified in two groups as direct band gap materials and indirect band gap materials.

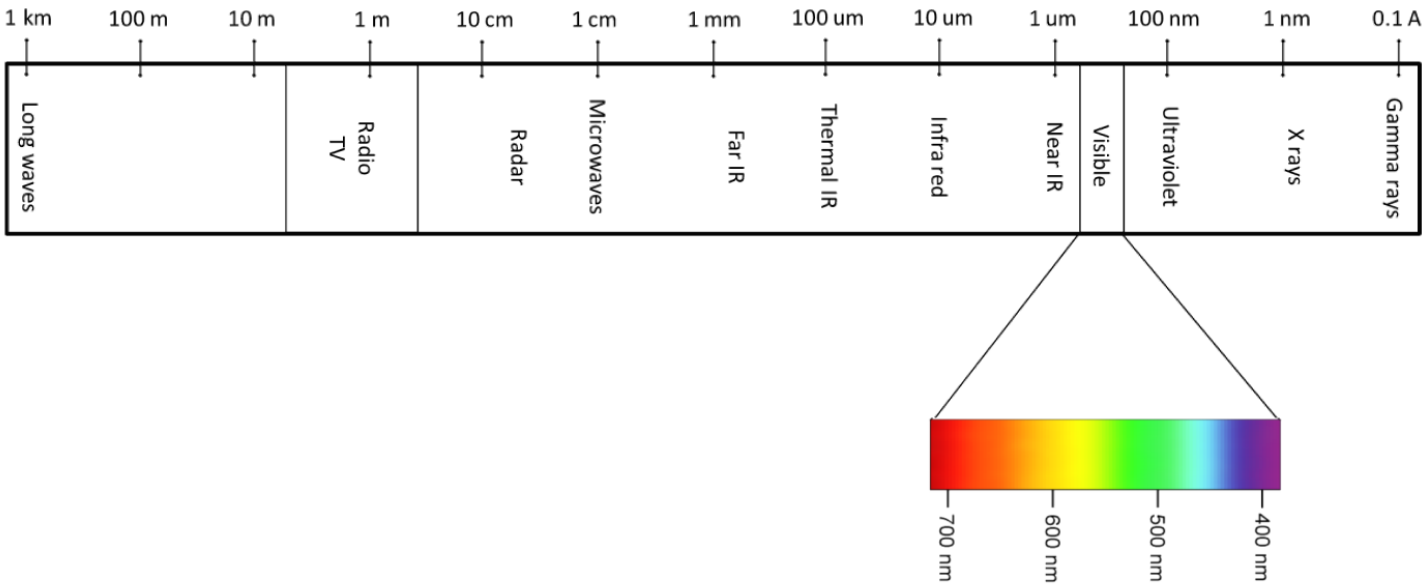

Figure 2.1 Electromagnetic spectrum and visible range

In a direct band gap material, minimum of conduction band and maximum of valence band of the material have the same wave-vector k=0 as seen in figure. On the other hand, in an indirect band

gap material, those minima and maxima have not same wave-vectors, but there is a considerable variance among them.

When an electron changes its energy state, both momentum and energy of electron must be conserved. For direct band gap recombinations, since wave vector does not change significantly, most of the energy goes out in form of photons. However, since there is large difference between wave-vectors of conduction and valence band states for indirect band gap materials, momentum transfer is also introduced to the system which is achieved by vibrations of atoms, which is called phonons. Indirect band gap materials usually cannot emit photons since most of the energy is given out by phonons.

2.3 III Nitrides Background

First AlN and InN was syntehsized in 1907 and 1910 by Fichter et al and Schröter et al respectively [11][12]. In 1928, first AlN is synthesised by Tiede et. al from metalic aluminum [13]. Johnson et. al synthesised first GaN by reaction of Ga with ammonia in 1932 [14] while Juza and Hahn synthesized InN from $InF_6(NH_4)$ in 1938 [15]. After a period of 30 years, we

come to 1969, when first single crystalline GaN was grown by chemical vapor deposition method (HVPE)

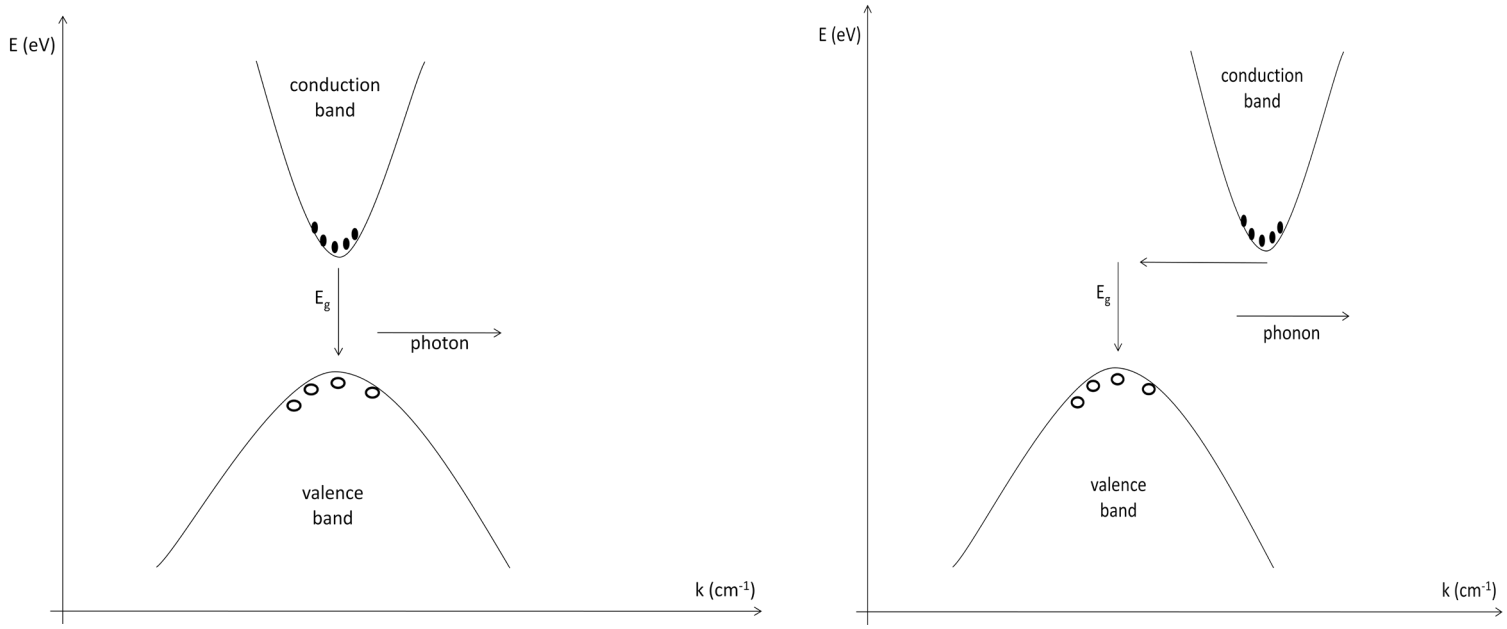

Figure 2.2 Direct and indirect band gap materials

with good electrical and optical properties by Maruska and Tiejen at RCA Laboratories [16]. Afterwards, Pankove et. al demonstrated first GaN LED which was fabricated with meta-insulator-semiconductor structure in 1971[17]. In the same year, Dingle et. al showed stimulated emission is possible from optically pumped GaN needles [18]. Early 1970s is also the time of a breakthrough in growth methods since MOCVD and MBE techniques were developed in 1971 and 1974 [19] [20].

However, research groups working in the field of GaN faced with some major problems like lack of p-type doping and proper substrate. These problems caused interest of most of the groups to change. Only a few groups remained which continued to work on GaN. One of them which had been headed by Yoshida used AlN buffer layer to improve the epitaxial quality of GaN film on sapphire substrate in 1983. Finally, in 1986, Akasaki's research group succeeded to grow high quality single crystal GaN films on sapphire which are free from surface cracks by using AlN buffer layer [21][22]. This was the first two step growth method. They grew GaN on sapphire heteroepitaxially first using a thin low temperature growth nucleation layer of AlN or GaN. Afterwards, high temperature epitaxial growth of GaN was carried out. High temperature growth on nucleation layer makes it possible GaN crystal to

grow not from the substrate but from the islands formed. Since this two-step procedure reduces impurity concentration and increases electron mobility, it has become a common method used for growing GaN.

In 1991, same group showed that it is possible to make p-type from Mg-doped GaN by using low-energy electron beam irradiation (LEEBI) [23]. S. Nakamura discovered just after Akasaki's p-type success that the same p-type GaN can be made by annealing Mg doped GaN under N_2 environment [24].

Until then, as the two main problems in the field of GaN were eliminated, high density researches have been ongoing since 1990s by several groups throughout the world.

2.4 Growth of GaN

GaN is grown epitaxially since epitaxy obtains high crystalline structure which is needed for opto-electronic devices to work. Since there is no common bulk GaN substrate, GaN is grown on most similar compound that can be found in which growth is called heteroepitaxial growth.

Bulk crystal growth techniques generally rely on solid-liquid phase equilibrium for the substrate material. Since melting point of GaN is very high, as the temperature is increased, compound starts to decompose and III-V elements start to melt. In order to prevent the decomposition, extra huge pressure of nitrogen is needed, which is not practical. Therefore, no bulk GaN crystal is commonly commercialized.

As choosing proper substrate for GaN, there are number of important criteria. First of all, substrate should be strong at temperatures higher than 1000 C° since growth temperature of GaN is around this temperature. Also thermal mismatch between substrate and GaN should be small in order to prevent crack generation while the film cools down to room temperature from high growth temperature. In addition, crystal structure of the substrate should be close to that of GaN to prevent cracking during growth. Therefore substrate should have three or six fold symmetry for wurtzite GaN and close lattice constant to lattice constant of GaN. As GaN LEDs are to be used in high power applications, substrate should have high coefficient of thermal conductivity so that heat generated in the LED can easily radiate away.

Alumina and SiC are the most proper substrates commonly used for GaN epitaxial growth. However, there still is high lattice and thermal mismatch between the substrate and GaN film, therefore high density of defects occur in the film. Although lattice mismatch between

substrate and film is much lower for SiC than that for sapphire (3.4 % vs. 13 %), quality of grown film is not as expected because of surface structure of SiC. High cost and low bandgap energies are also drawbacks of SiC as a substrate. Two-inch-sapphire substrate costs about $ 200 while same size SiC is around $ 3000. For comparison, widely used Si substrate is sold for $ 15. Therefore, alumina is more frequently used.

Some of the growth techniques which are used to grow GaN are MOCVD (Metal Oxide Chemical Vapor Deposition), HVPE (Hyride Vapor Phase Epitaxy), MBE (Molecular Beam Epitaxy), hot wall epitaxy etc. Among these, MOCVD is the most commonly used system. Most of the breakthroughs about GaN material was carried out by using MOCVD (or MOVPE-Metal Organic Vapor Phase Epitaxy) system.

MOCVD was pioneered by Manasevit et. al in late 1960s [19]. Metal organic vapor phase epitaxy (MOVPE) is the same technique in literature. Growth in MOCVD is based on chemical vapor deposition. Vapor phase of precursors of required compounds are sent to surface of the substrate. Solid starts to be deposited on the substrate by chemical reactions. In MOCVD, 30nm/min growth rate is usual. Thermal – lattice mismatch effect is low. There is high background carrier concentration up to 10^{19} /cm^3 in the grown film which is caused by incorporation of oxygen impurities [25].

In this system, metal organic (MO) compounds are used in order to grow the film on the substrate. In order to carry these MO sources, which are high vapor pressure liquids, high purity H_2 gas is commonly used. Wafer is heated by radio frequency (RF) heater in the quartz tube growth chamber. Substrate is placed on the SiC coated susceptor. As the substrate is heated, chemical reactions start to take place on the substrate since high temperature behaves as catalysor. As gaseous MO compounds are decomposed, GaN film is grown on the substrate. Growth rate can be judged by examining physical conditions such as substrate temperature, reactant partial pressure, gas flow etc. in the chamber during growth.

In order to grow GaN, MO compound precursor TMG (Trimethylgallium) and NH_3 (Ammonia) are used. Growth takes place under high temperature up to 1000-1100C°. Among sources, although TMG can be decomposed at temperature around 600C°, NH_3 requires much higher temperature values in order to decompose effectively. Since no bulk GaN substrate is feasibly present, GaN is heteroepitaxially grown on a different substrate. Because of the lattice constant mismatch and thermal coefficient mismatch, there occurs high thermal strain during period of cooling from temperature of 1000 C° down to room temperature. Although researchers have been working on a solution in order to decrease the growth temperature such

as changing sources or braking N_2 molecules into radicals, classical MOCVD precursors seem to give highest film quality.

In order to decrease the cracking and defects caused by thermal strain, a buffer layer between GaN and sapphire is used which is grown at lower temperature. Buffer layers of AlN and GaN are reported to have improvements on the epitaxial layer quality by Akasaki et al. and Nakamura et al. [21][26]. These buffer layers are generally grown around at 500~750 °C which give better quality than GaN grown on sapphire at 1000 °C. Akasaki et al. showed that low temperature grown AlN is amorphous [22][27]. This amorphous layer covers the substrate uniformly. On the other hand, GaN without buffer layer has columnar nucleation which ends up with defects after critical thickness and during cooling down. That amorphous layer crystallizes when temperature is increased during GaN layer growth, which forms a great growth surface for GaN. As a result, buffer layer decreases the amount of strain between GaN and sapphire which is caused by thermal and lattice constant contrast and gives a way to less defected GaN layer.

Below is the chemical reaction that occurs on the substrate while the GaN film is being grown.

$$Ga(CH_3)_3(v) + NH_3(v) \rightleftarrows GaN(s) + 3CH_4(v) \quad (2.1)$$

While growing AlGaN and InGaN layers, pre-cursors of trimethylaluminum (TMAl) and trimethylindium (TMIn) are used. In order to dope the film by p type and n type, cyclopentadienylmagnesium (Cp_2Mg) and disilane (Si_2H_6) or silane (SiH_4) are used respectively.

GaN has two faces to be grown on, Ga and N faces. Ga face is the usual grown face in MOCVD since it gives better surface characteristics. N face is also possible by highly doping with Mg; however, surface quality and stability of the film is not as good as that of Ga face grown film.

Other commonly used methods available for GaN growth are MBE and HVPE. In MBE, group V source Nitrogen is supplied as atomic nitrogen by using plasma. Since no ammonia is needed in this growth method, high temperature in order to break N-H bonds is not a must and therefore lower growth temperatures are possible. However, growth rate in MBE is low. In HVPE method, chlorine is used in order to transport group III materials and very high growth rates up to 100um/h can be achieved [28]. In this method, gaseous form of HCl is passed over

metallic Ga which is in liquid form. As a result of chemical reaction between two compounds, a new compound GaCl in gaseous state is formed. By uisng N_2 gas as carrier, GaCl is carried into the reaction chamber where it reacts with NH_3 to form GaN (solid). HCl (gas) and H_2 (gas) are by-products. This method is not suitable for fabricating optoelectronic devices though since film quality is not adequate.

2.5 Structure of InGaN/GaN QW LED wafer grown by collaboration with UCSB

LED wafers processed and patterned in this thesis were grown by collaboration with University of California Santa Barbara (UCSB). There are two different grown LED wafers. They have InGaN/GaN MQWs with 5% and 8% Indium concentration, which are called LED-1 and LED-2 respectively. Structures of LED wafers are drawn below in Figure 2.3 and Figure 2.4.

Electroluminescence and I-V curves of both wafers are stated in Chapter 6. Photonic crystal patterning is done on LED-1. Therefore, in this thesis, electrical and optical properties are mostly studied on LED-1 wafer.

As seen from structures, n type layer of LED-1 wafer is relatively thin and based on AlGaN compound. As will be stated later, metal contacts on n type AlGaN layer and thin n type doped layers show higher resistivity which end up with higher turn-on voltages. This kind of behaviour is also seen in measurements of processed LEDs in this thesis, which are shown in chapter 6.

Thin AlGaN layer with Mg doping on top of quantum wells is used in order to confine the carriers in quantum well regions. This layer is also called as electron blocking layer (EBL).

2.6 Chemical and Physical Properties of GaN

In this part, some of important properties of III nitride semiconductors are outlined. Although the properties stated mainly belongs to GaN, AlN and InN, properties for ternary compounds such as InGaN or AlGaN can be found by making interpolation between GaN and InN or GaN and AlN.

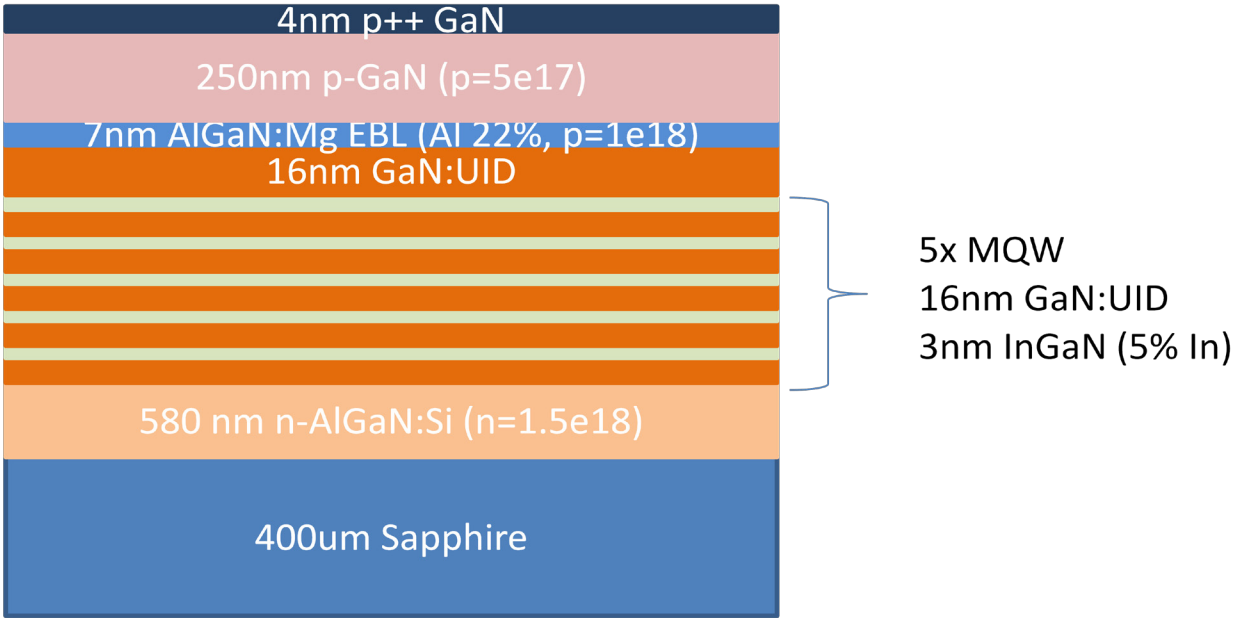

Figure 2.3 LED-1 InGaN/GaN MQW wafers grown by collaboration with UCSB, emission wavelength 390 nm

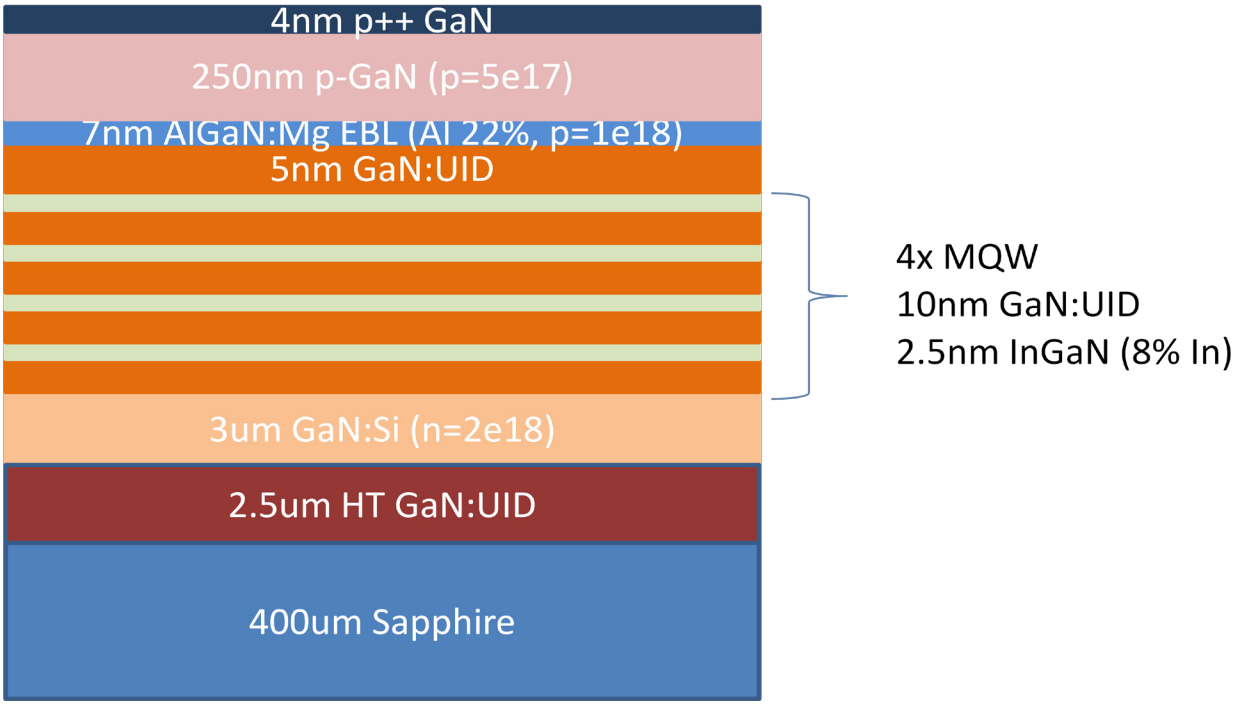

Figure 2.4 LED-2 InGaN/GaN MQW wafers grown by collaboration with UCSB,emission wavelength 410 nm

2.6.1 Band Gap of GaN and InN

Bandgap energy of GaN at room temperature is 3.39~3.43 eV. As the temperature is decreased to 1.6 K, band-gap increases to 3.503 eV [29]. Temperature dependence is formulized empirically below for T<295K as,

$$E_g(T) = \frac{3.503 - 5.08 \times 10^{-4} T(K)^2}{996 - T(K)} \tag{2.2}$$

where temperature T is in Kelvin. As seen from empirical formula, as temperature of the medium is decreased, band gap of GaN increases.

Since GaN is a direct band-gap material, absorption occurs by band to band excitation. Absorption coefficient can be expressed as below [30].

$$\alpha = A^* \sqrt{h\upsilon - E_g} \tag{2.3}$$

where $h\upsilon > E_g$ and A* is a function of electron and hole effective masses and inversely proportional to the refractive index. Dielectric constant of GaN at high frequency limit is ε_0 = 5.35 while low frequency limit is ε_∞ = 9.5 [31].

Electronic band gap of InN was believed to be 1.8-2 eV at room temperature. However, researchers have found that high quality InN grown on GaN by MBE or MOCVD has a true bandgap around 0.8-0.9 eV and can change between 0.7 and 1 eV due to the difference in crystallinity [32][33].

2.6.2 Bonding Structure

Bond strength between Ga and N atoms are very high. Bond length of GaN is 1.94 A° at 300K with 2.24 eV of cohesive energy [34]. Bond length of InN is 2.15 A° while cohesive energy is 1.93 eV [34]. Electronegativities among group III atoms are 3.0 for Nitrogen, 1.18 for Aluminum, 1.13 for Gallium, and 0.99 for Indium. This high difference between electronegativities and high bond strength makes chemical bonds of III Nitrides and GaN very strong and stable. Therefore, GaN has high thermal stability and high hardness.

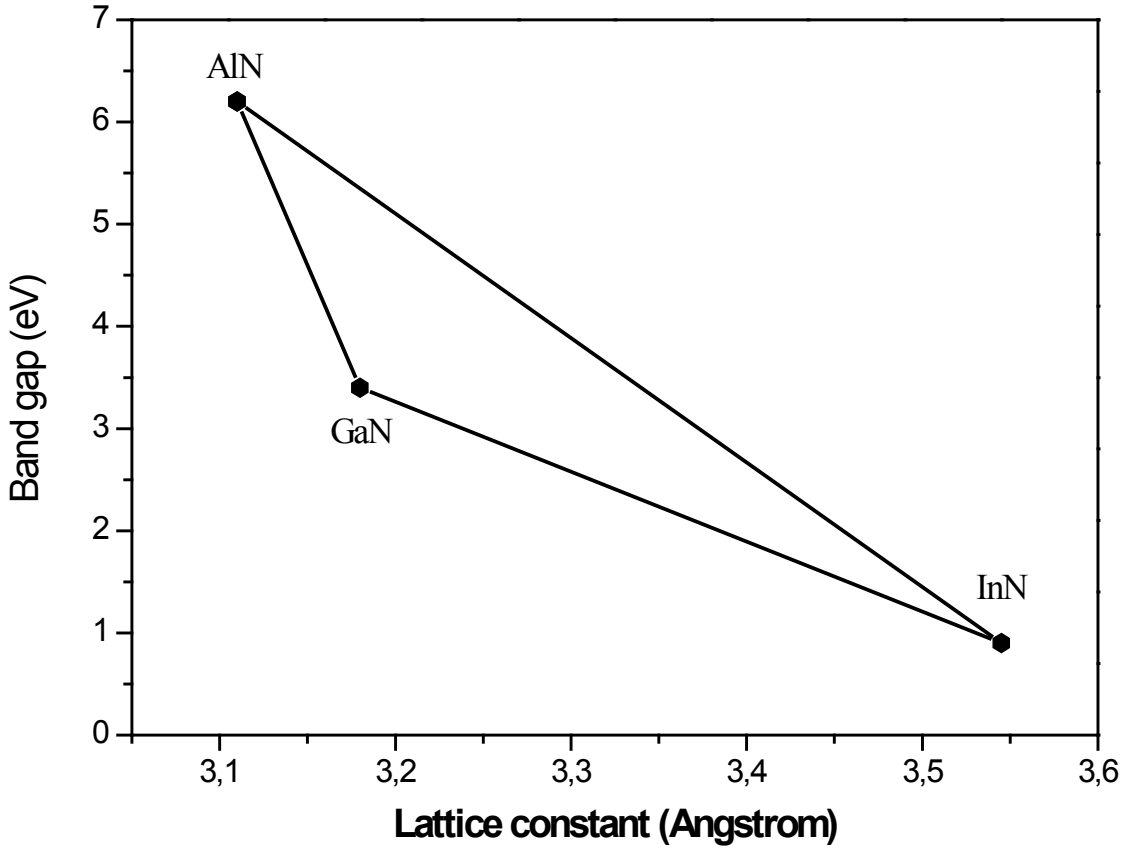

Figure 2.5 Lattice constant vs. Band gap of wurtzite III-Nitrides

Since bonds are strong, melting points of III nitrides are also high. Melting temperature of GaN is around 2500 C° while melting point of InN is around 1300 C°. However, decomposition temperature of GaN is much lower [35].

Thermal conductivity of GaN along c direction is 1.3 W/cmK at room temperature [36]. However, as the temperature is decrased, thermal conductivity decreases dramatically, down to 0.4 W/cmK.

2.6.3 Crystal Structure

III-Nitrides AlGaN, GaN and InGaN have covalent bondings. Because of high electronegativity of group V element Nitrogen with respect to group III elements Aluminum, Gallium and Indium, these compounds have also a strong ionic character which improves chemical stability of III-Ns.

Each atom in those compunds has four tetrahedral bonds. Since none of III-Nitrides have central symmetry for specific growth planes (no center of inversion), III-Nitrides induce strong polarization in the material.

III-Nitrides can be crystallized in three geometries, which are wurtzite, zinc blend and rock salt. Under room temperature and normal pressure, wurtzite structure is the thermodynamically stable one. For higher perssures, III-Ns crytallize in rock salt structure. Zinc blend structure has a metastable thermodynamics and can be achieved by epitaxial growth.

Wurtzite structure, which is the most common for III-Nitrides, is in $P6_3mc(C^4_{6v})$ space group and formed by two close packed hexagonal lattices that are shifted along c axis by an amount of 5/8c. Stacking order goes as AaBbAaBb [37]. While c-plane {0001} of GaN is polar because of none central symmetry, other two main planes a-plane $\{112\bar{}0\}$ and m-plane $\{11\bar{}00\}$ are nonpolar.

Lattice constants of wurtzite GaN are 3.188 A° for "a" side, 5.186 A° for "c" side at 294 K [38]. Lattice constants of wutzite InN are a=3.53-3.548 A°, c= 5.69-5.76 A° [39]. For wurtzite AlN lattice constants are "a" = 3.11 A°, "c" = 4.98 A°.

Lattice constants are dependent on temperature. In general, as the temperature increases, lattice constant also increases. Temperature dependence of lattice constants for "a" and "c" sides, and thermal coefficients of GaN grown on "a" and "c" planes is shown in the figures below [35].

Below in the Table 2.1, general properties of III Nitrides can be found.

2.7 Impurities in GaN

Impurities are foreign materials that are incorporated in GaN thin film. Parts of these impurities are unintentional which diffuses from the sources and the environment and should be decreased to minimum. Those which are intentional impurities are placed in the film on purpose, in order to control optical and electrical properties of the film.

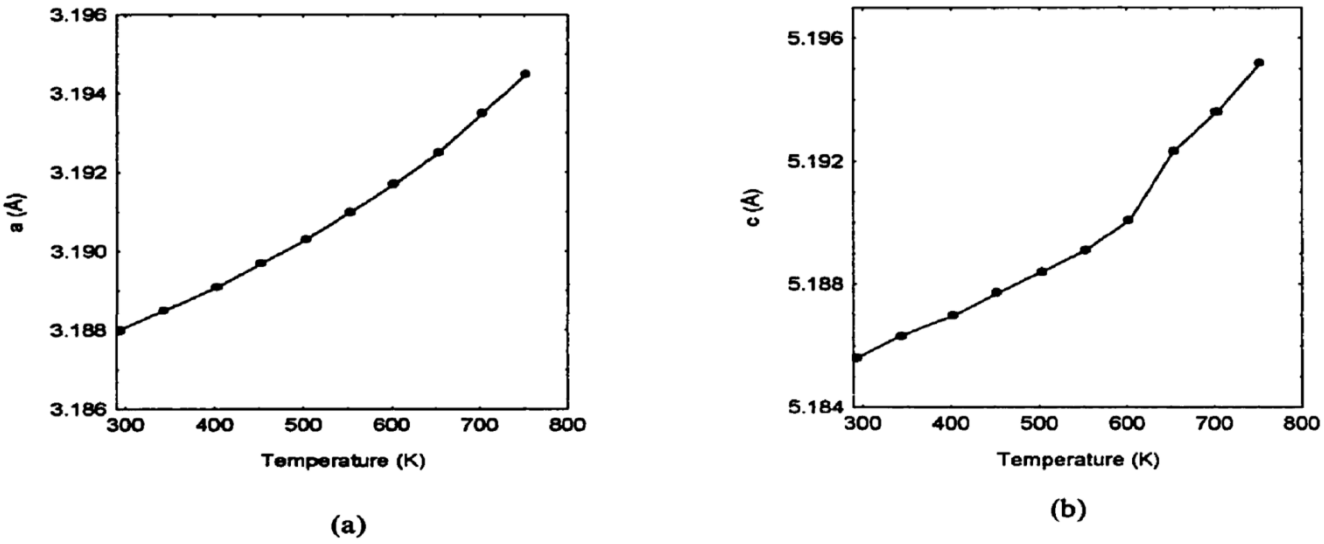

Figure 2.6 Temperature dependence on GaN lattice parameters. a) "a" side b) "c" side. (Adapted from ref. [40])

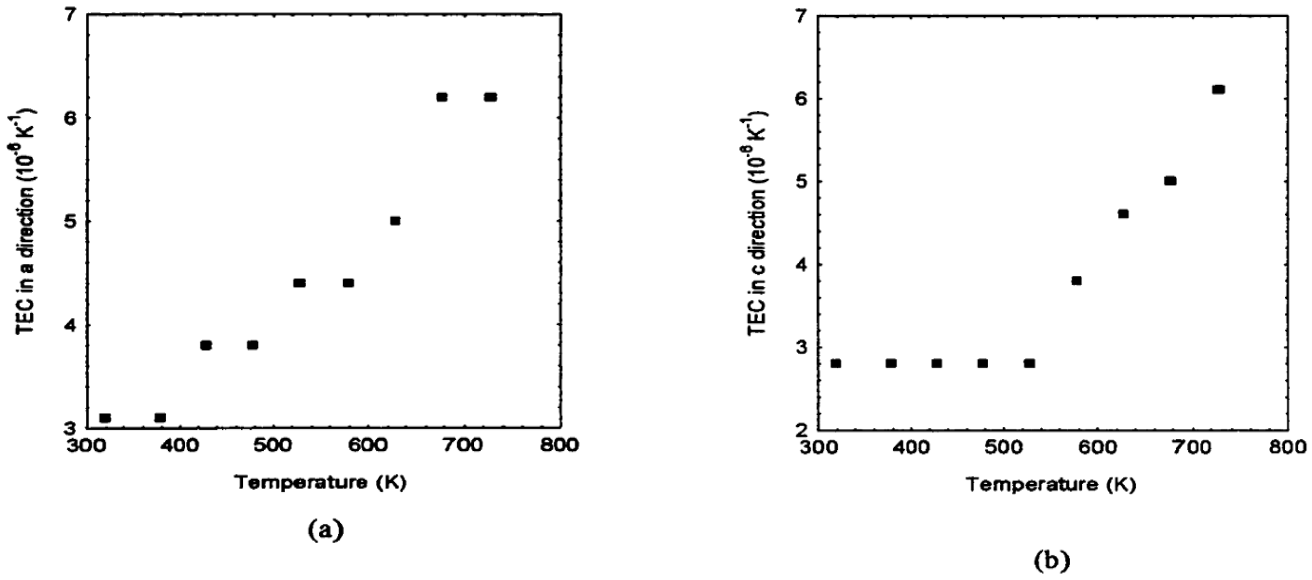

Figure 2.7 Temperature dependence on thermal expansion coefficients of GaN grown on a) "a" plane b) "c" plane. (Adapted from ref. [40])

Property	GaN wurtzite	AlN wurtzite	InN wurtzite	Sapphire rhombohedral	SiC 6H-wurtzite
Lattice constant a (A°)	3.188	3.11	3.54	4.75	3.08
Lattice constant c (A°)	5.186	4.98	5.7	12.99	15.12
Density (g/cm^3)	6.1	3.25	6.88		
Band gap energy 300 K (eV)	3.39~3.43	6.2	0.7~1	6.2	
Bond length (A°)	1.94	1.89	2.15		
Melting point (K)	1500	2500	1200		
Thermal expansion coefficient a direction ($10^{-6}\,K^{-1}$)	4.3	5.27	5.6	7.5	
Thermal expansion coefficient c direction ($10^{-6}\,K^{-1}$)	4	4.15	3.8	8.5	
Cohesive energy (eV)	2.24	2.88	1.93		
Dielectric constant	8.9	8.5	15.3		
Thermal conductivity	1.3	2		0.5	

Table 2.1 General properties of III Nitrides

Among unintentional dopants, carbon and oxygen are the most common ones that are encountered in grown GaN thin film. Carbon mainly comes from metal organic sources and also from the susceptor in the MOCVD chamber. Chemistry of the source material is distinctive for the level of carbon contamination since decomposition mechanisms of sources differ from each. High level of carbon incorporation causes n-type material to compensate.

Oxygen is another impurity that is diffused into film unintentionally. It occupies N site of GaN and acts as a donor. Oxygen impurity is based on contaminant in reactor or source gases. It is the main reason of high level electron concentration in unintentionally doped GaN.

Main intentional dopants are Mg and Si which are used in order to have p and n type GaN respectively.

2.7.1 Doping

Doping is crucial for optoelectronic semiconductor devices since optical and electrical properties of materials are greatly altered by different doping types and levels. Undoped GaN film generally shows n-type property which as described as unintentioanlly n-type. Reason for this unintentional n-type property is attributed to N vacancies [16] and/or residual impurities such as Si which replaces Ga, and O which replaces N [41].

There are two kinds of intentional doping types, n type doping and p type doping. In n type doping, related part of the semiconductor material is filled with excess free electrons that can move relatively free. As contrast, in p type doping, free positive charge carriers (holes) are introduced into the material. For GaN, n type doping is realized by SiH_4 or Si_2H_6, while p type doping is done by using Cp_2Mg precursors.

P type doping had been a major problem which decelerated and even stopped the progress of GaN research until the beginning of 1990s. Although studies on Mg doping had been ongoing since 1970s, no p type property was observed till 1989, which was achieved by using low electron energy beam irradiation (LEEBI) method on compensated Mg-doped GaN [23]. Afterwards, other post-process methods, such as annealing the Mg doped GaN under N_2-O_2 environment by Nakamura, were used [24]. Main reason of p type doping problem was the passivation of Mg dopants by hydrogen and forming Mg-H complexes during the growth of GaN. If the p doping of the GaN is not adequate, or there is a problem in activation of Mg,

parasitic resistance throughout the device occurs and high turn-on voltage values are seen in LEDs which is one probable cause of high working voltage of LEDs processed in this thesis.

Magnesium activation process is reversible. If the wafer is annealed under Hydrogen environment or processed under high temperature in an environment containing H_2, activated Mg dopants become passivated again by forming Mg-H complexes. Therefore, processes like plasma enhanced chemical vapor deposition (PECVD) and reactive ion etching (RIE) with using H_2 gases (SiH_4, CHF_3) may de-activate Mg and decrease the level of p type doping which will end up with high internal resistance and low current spreading.

Silicon is used to make n type GaN material during growth by using SiH_4 or Si_2H_6 precursors. High levels of electron concentration as much as $6x10^{19}$ cm^{-3} can be achieved [42]. However, as the concentration of Si doping is increased, so the stress induced on the film, which results degradation of the film quality by formation of V shaped cracks [42].

Hole concentration is lower than electron concentration in GaN because Mg acceptor level for GaN is 170 meV higher above valance band which is much larger than thermal energy at room temperature. This causes resistivity of p layer is much higher than that of n layer GaN. In order to decrease n layer resistivity more, rapid thermal annealing method is used for Ti/Al metallization at around 700~900 °C [43].

2.7.2 Defects in GaN

GaN based materials can be used in a wide range of spectra from near infrared to deep UV under high power, high temperature conditions. However, high density of defects in GaN material prevents GaN and GaN based compounds to be used in full performance for opto-electronic applications.

Mostly faced structural defects in GaN are stacking faults and dislocations.

Stacking faults are 2D defects and caused by crystal structure change from wurtzite to zinc blend. Free energy between these crystal structures is very small [44]. These defects are parallel to c growth direction which extends to surface.

There are also 1D point defects in GaN which plays crucial role in terms of optical and electrical properties. 1D defects can be intrinsic, Ga and/or N vacancy, or extrinsic caused by impurities such as C, H, O, Mg, Si etc. 1D defects are centers for electron traps, electron-hole recombinations, scatterings and also act as donors and acceptors.

Threading dislocations form at growth interface because of the strain caused by lattice mismatch between substrate material and film. Since no large enough GaN substrate with single crystal exists for homo-epitaxy, GaN based semiconductor materials are grown on foreign substrates which have thermal constant and lattice constant not the same but close to that of GaN. Sapphire is the most commonly used substrate for growing GaN based films.

Lattice mismatch between the sapphire substrate and GaN and AlN nucleation layer is higher than 13 %. High mismatch causes film to be stressed and lead to island growth of GaN and AlN on sapphire. GaN crystals continue to grow not from the substrate but from these islands formed at high temperature. Dislocations are formed by coalescing of these initial islands [45]. The result is a high amount of grains and grain boundaries.

GaN materials grown on sapphire substrate have dislocation density of about 10^8-10^{10} /cm^2. There two main type of dislocations seen in GaN thin films. These are edge and screw dislocations. Edge dislocations are formed by an extra plane that is inserted in the crystal lattice structure while screw dislocations have additional lattice which is seen as a lattice step on the outer surface of the crystal. Dislocations are formed mainly during epitaxial growth.

Pure edge dislocation is the most dominant dislocation type seen in GaN material and has an increasing percentage from 40% to 70% for the film thickness from 1um to 5um [45]. Pure screw dislocation has 10 % percentage for MOCVD grown GaN materials [46]. Others are just mixed dislocations that of edge and screw.

Screw dislocations stay in the growth direction and extend to the surface such as stacking faults.

During GaN growth, up to first 2 um, both edge and screw dislocation density is high. However, since edge dislocations terminate around this level of growth, film grown on this 2um GaN will have lower density of edge dislocation but still large amount of screw dislocations. Therefore, first 2um layer of GaN is also said to be template layer and GaN films are grown thick [47], generally more than 5 microns in order to have good surface quality.

Dislocations have negative effects on the performance of the devices [48], such as serving as scattering centers for carriers, non-radiative recombination centers, charge scatter centers, deep level traps for minority carriers and current leakage paths [48] [49]. For LED case, since refractive index difference is high between GaN and air, most of the light generated in the active layer reflects back into the material. Majority of this reflected light is absorbed by defects and active layer.

With the efforts to decrease the dislocation density, new growth methods such as lateral epitaxial overgrowth (LEO), facet controlled LEO, high temperature annealing with over-pressurized N_2 [50][51] are applied resulting in threading dislocation density range of 10^5 – 10^6 /cm^2.

Main aim is to develop a 2" bulk GaN substrate so that stress formed between the substrate and film can be decreased tremendously which results in less threading dislocations.

2.7.3 Defect related Illumination Peaks seen on GaN

Beside main illumination at bandgap energy of 3.4 eV, there are also seen peaks at energy levels of 1.8 eV, 2.2-2.3 eV and 2.8-2.9 eV, which are called as red, yellow and blue illumination peaks. Main reason of these secondary peaks is because film quality is not very well for GaN [52]. There have been different thoughts on the cause of these illuminations whether they are caused by impurities and residuals (carbon, silicon, magnesium) and impurity based trap centers [53][17][52], grain boundaries-dislocations [54], intrinsic point defects such as Ga or N vacancies [55]. Most of the researchers now lean to side of point defects (Ga vacancy) especially for yellow illumination case.

The yellow luminescence has been observed in both bulk crystal and also epitaxially growth thin films, which are undoped and doped, by several methods such as MOCVD, MBE, HVPE. While intenisty of yellow luminescence can vary, good quality crytals show almost no yellow illumination [55].

Mechanism for yellow illumination is explained to be a transition from a shallow donor to a deep acceptor [56].

2.8 Polarization Issues and Quantum Confined Stark Effect (QCSE)

Wurtzite structured III-Nitrides posses different optical and electrical properties from other semi-conductors because of symmetry issues. Wurtzite structures show central symmetry with respect to m- and a- planes but not for c- plane. This lack of central symmetry causes strong spontaneous polarization fields in the material.

There also occur piezoelectric fields in the material because of lattice mismatch. During the film growth, layers of the film are stressed in case there is difference between lattice constants of the subsequent films (e.g. InGaN on GaN). Strain formed along the layers of the film induces piezoelectric polarization field. Spontaneous and peizoelectric fields in the material add up to large internal electric fields.

As a result of these polarization effects, structures of InGaN-GaN quantum wells are distorted and electron and hole wave functions get separated. Reduced overlap between electron and hole functions reduces recombination rates. Amount of tunneling of carriers through quantum well regions increases which decrease carrier life time and causes absorption spectra to broaden [57].

In-field polarization results with a valence band splitting, red-shifting of emission wavelength, polarized emission from active layer, decrease in intensity of light output and different refractive indices between direction parallel and vertical to the growth axis [58].

In order to decrease QCSE, thin quantum well regions are required. Details about QCSE can be found in chapter 3.

Chapter 3

3. Light Emitting Diodes and InGaN/GaN Multi Quantum Wells

3.1 Introduction

Light emitting diodes are based on radiative recombination of electron and hole pairs generated in the active layer of the material, which is called solid state lighting. LEDs are the ultimate sources of illumination because of their long life time, low energy consumption, high durability, resistance to mechanical effects, quick response time and high luminescence efficiency. One of the major goals of LED research is to use LEDs in general lighting. Efficiency of traditional light bulbs are around 1% ~ 4% and efficiency of flourescents are around 15% ~ 20%. On the other hand, LEDs can have efficiencies up to 80%. Exchanging classic 100 W light bulbs that are used in houses by LEDs will save 70% ~ 85% energy. By tuning and mixing three main colors properly or using phosphor with highly efficient blue LED can enable to have white light with a natural color temperature. GaN based light emitting diodes make this dream possible by filling the gap of blue color in the spectrum for solid state lighting technology. III-nitride LEDs can be used for numerous applications in illumination systems such as traffic lights, color displays, device backlighting, decorative and white light emitting diodes.

To be able to use LEDs for general lighting, efficacy more than 200 lm/W should be achieved. Main reason for low extraction efficiency for GaN based LEDs is total internal reflection. Therefore, most effort has been given to increase extraction efficiency by changing the geometry of the shape of device so that larger amount of light could escape from high refractive index material GaN.

In this chapter, mainly history of general LED development and particularly GaN based LED development, p-n junctions, effect of multi quantum well hetero-junctions and emission from

these junctions, InGaN-GaN multi quantum well LEDs and their properties, polarization in InGaN-GaN quantum wells and its effect on optical properties of the LED will be described.

3.2 Background of LEDs and III Nitride LEDs

Research on LEDs has started before 1907; however, first practical p-n junction LED was fabricated by Nathan in 1962 [59]. By now, with improved material quality, material growth systems and metal contacts, LED technology has shown great advancement systems for the last 50 years. Red, amber, orange and yellow LEDs that use AlGaInP chips have better luminous efficiency than a 100 W incandescent lamp. Higher than 100 lm/W efficiency has been achieved by using these chips. However, for green and blue LEDs, emission efficiency should be increased.

First III-Nitride light emitting diode is fabricated by Pankove et. al in 1971 by using metal, Zn-doped GaN and unintentionally doped n-type GaN [60]. LEDs which illuminate in blue-green region were fabricated by using InGaN/AlGaN double hetero-structure active layers at first in 1993. Although light output of these devices were larger than 1 cd, their full width half maximum (FWHM) values were around 70 nm. Therefore light goes out from LED included the spectral range from violet to yellow-orange which made the color white-blue to human eye. Moreover, these LEDs became saturated at high current because of low density of states.

By using single quantum well as active layer, great improvements have been achieved on the quality of the light. LED color became more distinct since FWHM values came down to 20-30 nm and luminous intensity from 2 cd up to 12 cd has been realized [61][62].

One of the main purposes of LED research is to be able to fabricate white LED. First white LED was reported in 1994 by Nichia Corporation [63]. They used blue GaN LED with yttrium aluminum garnet (YAG) phosphor to get white light. Afterwards, some countries including USA and Japan started out national projects in order to exchange conventional lighting systems with GaN based LEDs which accelerated development of LEDs. In 2005, 74 lm/W, in 2006 130 lm/W, in 2007 150 lm/W efficacy white LEDs were reported.

In the year of 1995, efficiencies of 9.2%, 8.7% and 6.3% were gathered for the LEDs illuminate at 405, 450 and 520 nm respectively in violet, blue and yellow colors. These LEDs were fabricated by using $In_xGa_{1-x}N$ single quantum well by using 9%, 20%, 45% indium respectively.

In 1997, first UV LED was manufactured. High power UV LEDs have considerable importance since air, food and water purification, high density storage etc. becomes possible by using those LEDs. As an example, instead of 650 nm red laser diode, laser diode that operates at 351 nm which is commercialized as "blue-ray" made it possible to increase storage area by 5 to 6 times [64]. Advances in AlGaN based ultra-violet solid state lighting continue since 2000 with reported increasing power [65].

Although the growth technology has led to big advance in short wavelength LEDs, high refractive index difference between the semiconductor and environment remains to be a problem.

3.3 p-n junction and emission of light

In a simple LED, there exists a p-n junction where holes and electrons are injected from p side and n side respectively. In a p-n junction, p type is where holes are in excess; n type is where electrons are the majority carrier. When forward bias is applied, potential difference between p and n side of material is increased by amount of bias beside built-in potential. Applied voltage forces carriers to pass the junction to the other side of the material (from p to n or vice versa) at where these carriers are called excess minority carriers. In order to increase efficiency of LEDs, carrier life time must be as small as possible since carriers may be trapped by impurities or dislocations in longer time. Therefore, diffusion length should be minimum.

Inside a p-n junction, light is emitted when electron, which is excited to conduction band, recombines with hole in valance band in a direct band gap semiconductor since energy outgoes as photon in such semiconductors. III nitrides are direct band gap materials. However, if the electronic band gap structure is indirect, emitted energy is in form of vibration of atoms, which is called phonon. In an indirect band gap structure, no light or light with very low efficiency is emitted but mostly heat is generated.

Different methods can be used in order to generate electron-hole pairs. If those pairs are created by using photon absorption, this is called photo-luminescence. When electron-beam irradiation is used, that is called cathode-luminescence. If these pairs are formed by injection of electrons and holes (minority carriers) under forward bias, which is the usual case for

LEDs, this method is called electro-luminescence. Electro-luminescence is the method used in this thesis.

For a structure with p-n homo-junction, when p and n materials are attached to each so that they are in contact, electrons start to recombine with holes until diffusion of carriers are in equilibrium. At this time, Fermi levels are aligned with bending of bands and finally a depletion layer where there are no carriers is formed.

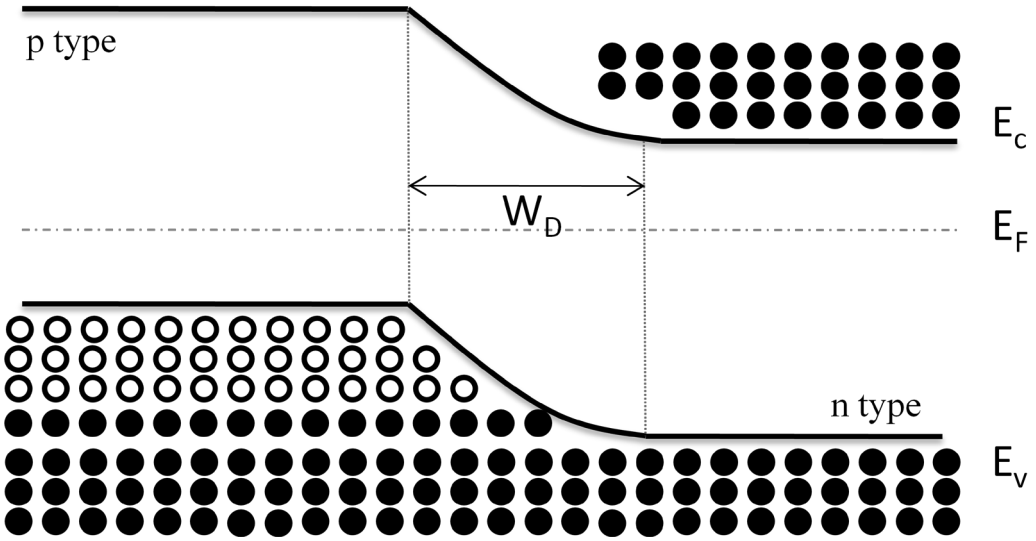

Figure 3.1 p-n homojunction with no bias

When bias is applied, majority carriers have energy to pass through the depletion layer and become minority carriers in the opposite type material. Probability of electrons in conduction band to recombine with holes in valence band increases which result in increased radiative recombination and enhanced light emission.

For a hetero-junction, a lower band gap material is introduced to the structure in order to confine electrons and holes and therefore to decrease diffusion lengths especially for structures with high defects such as III-nitrides. When bias is applied, carriers are trapped in well layers. Confinement of the carriers gives a way to increased efficiency of radiative recombination.

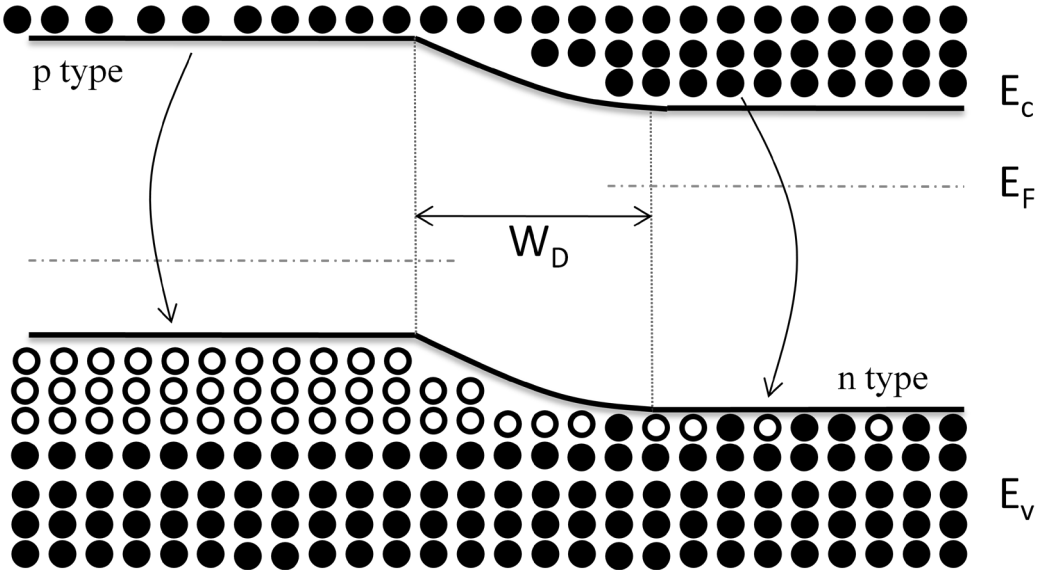

Figure 3.2 p-n homojunction with forward bias

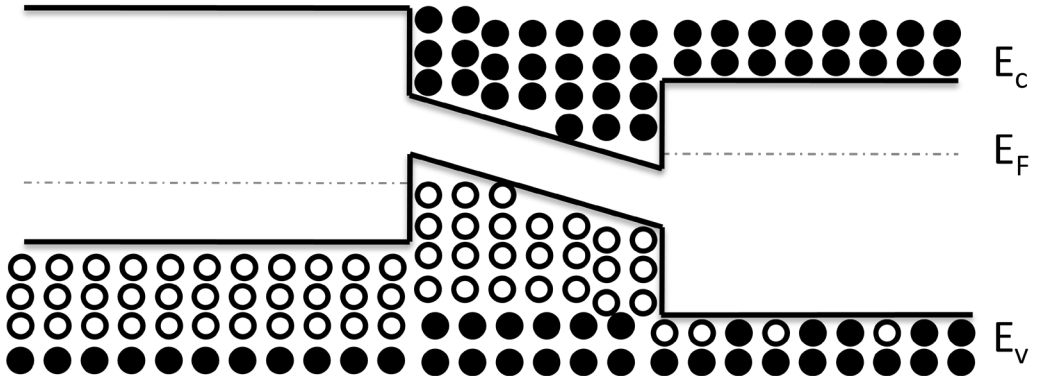

Figure 3.3 p-n junction with hetero-structure under forward bias

There are some concepts, namely internal quantum efficiency, external quantum efficiency and extraction efficiency, that help us to evaluate the performance of the device and quality of the material and structure.

Internal quantum efficiency which is defined as the ratio of photon generation rate in device to the flow rate of electrons through the pn junction.

$$\eta_{iqe} = \frac{P_{\text{int}} / h\upsilon}{I / e} \tag{3.1}$$

where P_{int} is the number of photons emitted into structure. η_{int} depends on radiative recombination efficiency (η_r) and injection efficiency (η_e) of minority carriers. η_r is the ratio

of non-radiative electron life time to the total electron life time and η_e is defined as the ratio of electron diffusion current to the total diffusion current.

In order η_{int} to be high, non-radiative electron life time should be very high so that almost no recombination happens non-radiatively. This implies that material should have very low defect density so that non-radiative trapping probability is lowered. Also, diffusion length of carriers in p side of material should be small and resistivity of the n side of the device again should be as small as possible, which depends on the amount of n-type doping. As the doping level is increased, resisitivity will be decreased. However, since highly doping of n type will cause V defects in GaN film, which will behave as non-radiative trap centers and therefore will decrease η_{int}, it should be paid attention to the value of n doping level. For InGaN/GaN LEDs with low indium concentration, η_{int} is about 90% [66].

Another efficiency term which has been defined for light emitting diodes is external quantum efficiency η_{eqe}, which is multiplication of η_{int} with a light extraction efficiency η_{ext}. η_{eqe} is defined as amount of photons coming out from the device with respect to the amount of electrons passing through the junction of the device. η_{ext} is ratio of number of photons emitted from the device to the number of photons emitted from quantum well layers.

$$\eta_{iqe} = \frac{P_{\text{int}} / h\upsilon}{I / e}$$

$$\eta_{ext} = \frac{P}{P_{\text{int}}} \tag{3.2}$$

$$\eta_{eqe} = \eta_{iqe}\eta_{ext}$$

Therefore, instead of η_{int}, η_{eqe} is more commonly used by experimental researchers in order to evaluate the performance of LEDs. If it was possible to take out all the light generated in the active layer of the device, then η_{ext} would be equal to η_{int} since η_{ext} would be 1.

Both extraction efficiency and internal quantum efficiency can be effected by PCs [67]. Internal quantum efficiency can be increased by using photonic crystals, with the principle called Purcell effect. However as the temperature is increased to room temperature, Purcell effect becomes negligible.

3.4 InGaN/GaN Multi Quantum Well (MQW) LEDs

Heterojunctions are used instead of homojunctions for GaN based LEDs in order to have more power output. In p-n homo-junction, device is composed of one material but with n type dopant and p type dopant regions. Although light can be generated with this kind of design, total output will be very low in GaN based devices since diffusion length is very long and minority carriers spread over a very large area. Concentration of minority carriers and radiative recombination rate are decreased since GaN has high density of defects.

In order to decrease long diffusion lengths, hetero-structures are used. In these structures, a well region with a lower band-gap is introduced between p and n type material. Owing to this lower band gap well structure which has dimension much lower than diffusion length, minority carriers are trapped in the well region in both p and n sides. As a result, radiative recombination efficiency is increased.

However, there are some drawbacks of this kind of well design. Since the well region is small, active region tends to be saturated easily so that additional carriers do not increase the light intensity. To overcome this issue, increasing the number of quantum well regions is introduced. Now, volume for additional carriers is increased and saturation is decreased.

In InGaN/GaN multi quantum well LEDs, GaN is the barrier and InGaN is the quantum well layer. Using multi quantum well instead of single quantum well increases the quantum efficiency by reducing threshold current density. However, since InGaN thermal stability is low, as the number of quantum wells increase, uniformity between top and bottom quantum wells decreases in the InGaN/GaN multi quantum well. This decrease causes broadening of gain spectrum [68]. So there is an optimum number of quantum wells. Thickness of the wells is also critical. Since polarization effect in the GaN LED separate the hole and electron functions apart, reduction in radiative recombination and consequently internal quantum efficiency occurs if QW layers are not adequately designed. Therefore, in order to reduce the amount of separation, InGaN/GaN multi quantum well layers are kept thin.

By using InGaN/GaN multi quantum well structures, high luminescence LEDs have been fabricated. For example, violet LED which has 405 nm peak produced 5.6mW power at 20 mA direct current with an external quantum efficiency of 9.2 % by Nichia Corporation [61]. In these LEDs, GaN is used as barrier for minority carriers in order to confine them into InGaN wells. InGaN in this structure behaves as the active layer where radiative recombinations occur. Therefore, wavelength of the LED depends on the energy band gap of

InGaN layer which can be altered by changing In concentration of the InGaN quantum well layer. As the indium concentration is increased, wavelength of light emitted from the InGaN/GaN well increases.

In quantum well region, there is no continuum of energy states as it is the case in bulk materials. As the thickness of the material is decreased, so the number of atoms in a unit volume decreases and energy states start to get apart from each. Finally, there occur discrete energy levels. In such structures, electrons can only have definite energy values.

Emission from the InGaN-GaN quantum well depends on the difference of discrete energy levels between lowest conduction band and highest valance band. Since carriers are willing to stay at lowest energy level, emission wavelength is mainly determined by lower energy levels.

Wavelength of light emitted from quantum well is given below;

$$\lambda = \frac{(h)(c)}{E_{c_1} - E_{v_1}} \tag{3.3}$$

where c is the velocity of light in vacuum, h is Planck's constant, E_{c_1} and E_{v_1} are lowest energy state in conduction band and highest energy state in valence band.

Relative positions of the energy levels to the band edge in InGaN-GaN QW structure are dependent on indium mole fraction of the well, well thickness and barrier thickness. As the mole fraction of indium or thickness of the well is increased, so as the emission wavelength.

The band gap of InGaN is given by:

$$\text{Eg } (In_xGa_{1-x}N) \text{ [eV]} = (x)\ [E_g\ (InN)] + (1\text{-}x)\ [E_g\ (GaN)] - (x)\ (1\text{-}x)\ (b) \tag{3.4}$$

Here b is bowing parameter that can be obtained from the Figure 3.5 below [69].

LED wafers processed in this thesis work contain 5% and 8% indium in InGaN quantum well region respectively. For In concentration of 5%, b is 2.15; for In concentration of 8% b is 2.0.

So, taking band gaps of InN and GaN as 0.95 and 3.4 respectively, calculated band gaps for different In concentration GaN LEDs are below.

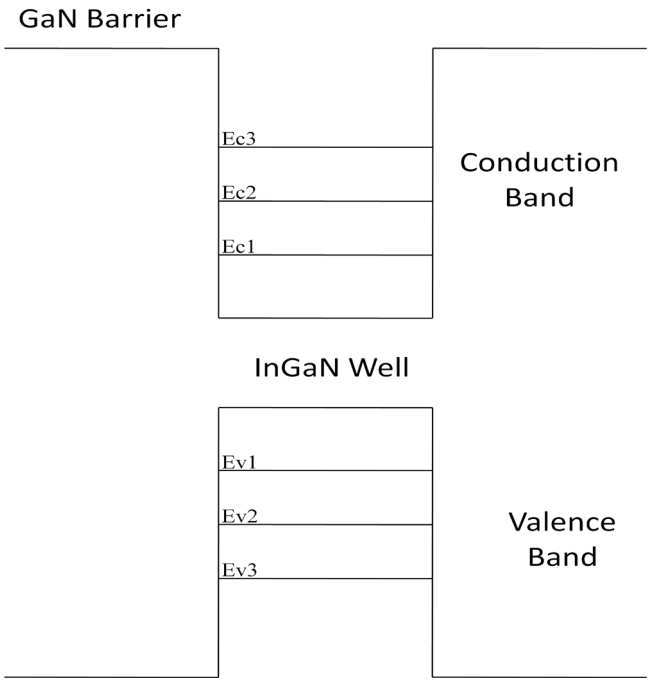

Figure 3.4 Discrete energy levels in quantum well region

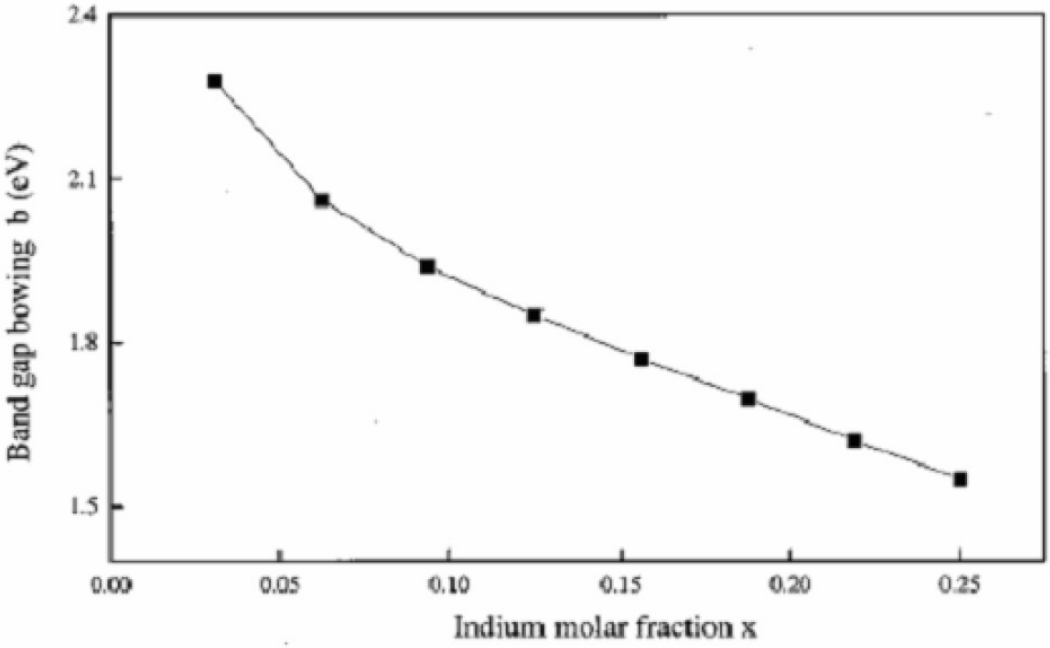

Figure 3.5 Bowing parameter with respect to Indium molar fraction (ref. [69])

0.05 In fraction

$$E_g(In_{0.05}Ga_{0.95}N) = (0.05)(0.95) + (0.95)(3.4) - (0.05)(0.95)(2)$$

$$= 3.18$$

$$\lambda = \frac{1240}{3.18}$$

$$\lambda = 390 \text{ nm}$$

0.08 In fraction

$$E_g(In_{0.08}Ga_{0.92}N) = (0.08)(0.95) + (0.92)(3.4) - (0.08)(0.92)(2)$$

$$= 3.06$$

$$\lambda = \frac{1240}{3.06}$$

$$\lambda = 405 \text{ nm}$$

Calculated wavelength values are very close to results of wavelength measurement regarding processed LED samples. Electroluminescence measurement results can be seen in Figure 3.6 and Figure 3.7 below.

3.4.1 Indium fluctuation in QW layer

Internal quantum efficiencies and properties of light radiated from the active layer depend on the variation difference of Indium along well layer and quantum confined Stark effect caused by the strain between layers of InGaN and GaN. In concentration variation in active layer creates some places with higher radiative recombination where is called intense luminous centers [70]. Fluctuation of Indium in the active layer gives a way for high quantum

efficiency by acting as a quantum dot [71]. Internal quantum efficiency of InGaN/GaN LEDs with low fraction of Indium is around 90% [66]. This property also affects the polarization stage of the emitted light from the quantum well. Indium cluster sizes are around 10~15 nm [72].

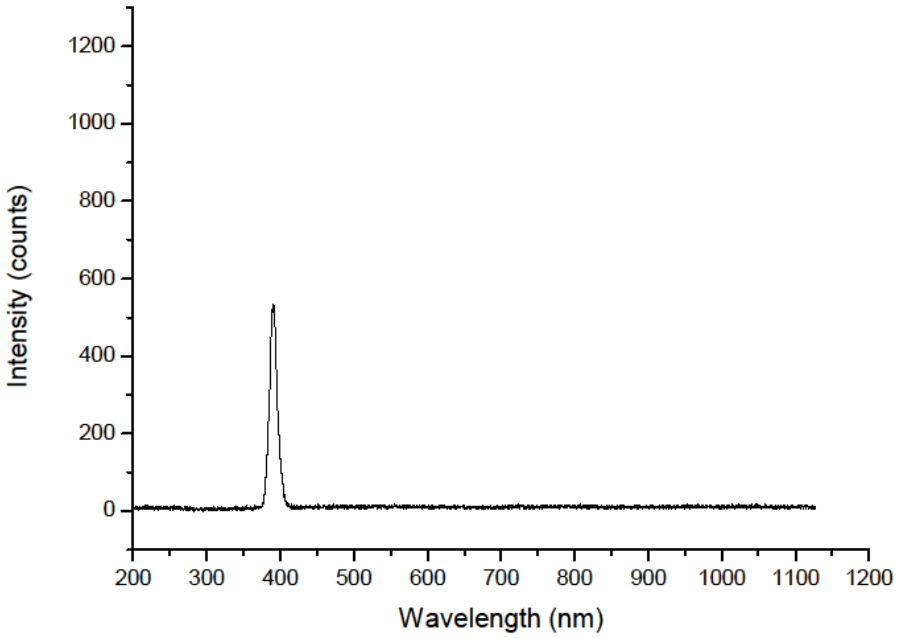

Figure 3.6 Electro-luminescence spectra LED which emits at wavelength of 390 nm

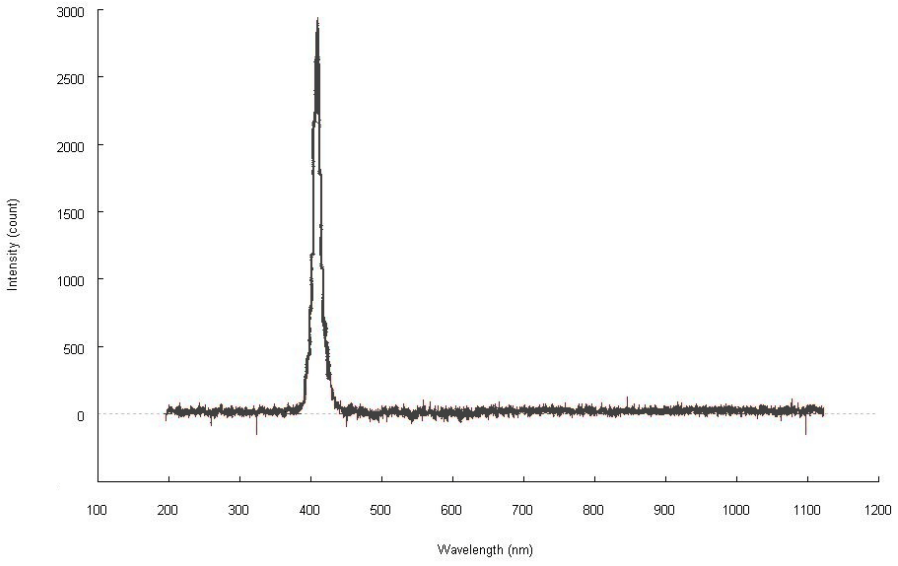

Figure 3.7 Electro-luminescence spectra LED which emits at wavelength of 410 nm

As the indium concentration is increased, homogeneity of In along the layer decreases which results in lower emission polarization. On the other hand, as the In percentage is decreased, well layer becomes more homogeneous and the compressive strain starts to dominate on the emission property which causes an increase in TE polarization. While quantum dot behavior of In fluctuations do increase TM polarization component, compression between GaN and InGaN layers favor TE polarization component. Therefore, as the wavelength goes to more UV range up to a limit of Indium concentration, degree of optical polarization increases [71].

This is why InGaN/GaN LEDs illuminate with high power although they have high density of defects. However, those defects still reduces the strength of the device. These LEDs can fail under static charge, high forward or reverse bias easily. Temperature is also problem for In fluctuation because of thermal instability of InGaN. Metal migration through these defects may short the diode which has also been an issue during processing of LEDs and measurements in this thesis.

Indium fluctuation in InGaN quantum well region increases IQE. However, because of the high lattice mismatch between InN and GaN, higher indium percentage in QW layer causes decomposition of the structure which decreases the quantum efficiency of LED for higher wavelengths. IQE of 450, 520 and 540 nm LEDs are 60%, 35%, and 10% respectively [73].

Moreover, extra decrease in Indium concentration or no Indium in quantum well will also result in lower quantum efficiency and dramatic decrease in optical power output. Without indium in the well, no In fluctuation which forms localized energy state can take place. As a result, carriers will not be captured by these localized states but they will be trapped into high number of non-radiative recombination centers. Moreover, since quantum dot structure caused by Indium droplets are not present anymore, QCSE will increase which results in separated electron and hole wave-functions. Therefore, as the Indium concentration goes to zero, internal quantum efficiency decreases dramatically.

3.4.2 Quantum confined Stark Effect and Polarized Light Emission from InGaN/GaN QW

Spontaneous polarization is seen in nitrides because of unsymmetrical crystal structure having high electro-negativity difference. On the other hand, piezoelectric polarization is caused by

compressive stress which originates from the difference in lattice constants between GaN barrier and InGaN well layer in quantum well active layer.

When there is an electric field applied to quantum well, electron and hole functions are separated from each other to the opposite sides of the energy states as seen in the Figure 3.8. In some materials such as wurtzite and zinc-blende III-nitrides, external electric field is not necessary for this separation to occur since the internal electric field caused by both spontaneous and piezoelectric polarization of the material itself is enough for a sizeable Stark shift.

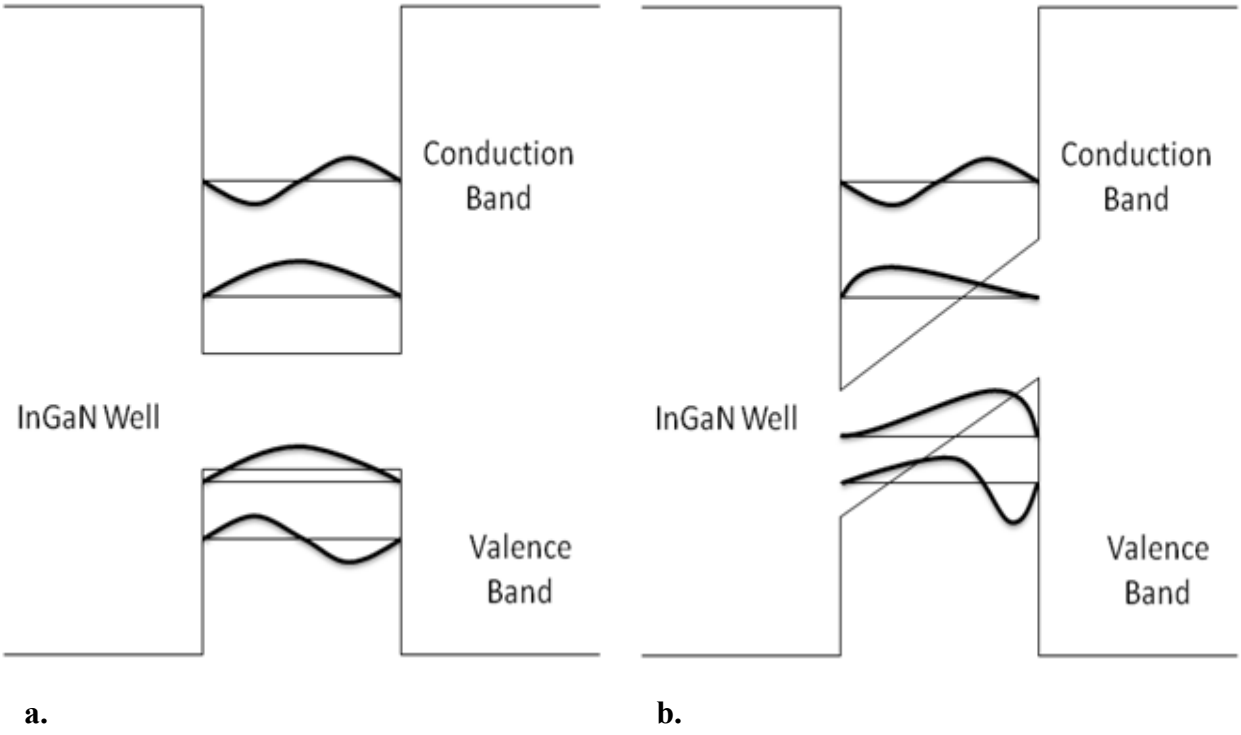

Figure 3.8 Separation of electron-hole functions under forward bias. a. No bias. b. Forward bias

(0001) growth direction for wurtzite and (111) direction for zinc-blende structures show this kind of polarization effect because of their non-centrosymmetric nature. GaN, InN and AlN are examples of such materials.

For InGaN wells on GaN barriers, InGaN is under compressive stress since lattice constant of InGaN is higher than that of GaN. This in-plane compressive strain causes piezoelectric polarization field directed towards (0001) direction. Electric field induced by this polarization is pointed from surface to substrate.

Although spontaneous polarization has a contribution to total polarization rate, piezoelectric polarization is dominant for InGaN quantum well region since spontaneous polarization difference between InN and GaN is small ($P_{sp,GaN}$=-0.029, $P_{sp,InN}$=-0.032), however lattice mismatch is high [74].

These polarization fields cause wavelegth to shift in longer wavelengths and weakens the radiative recombination, which is called quantum confined Stark effect. However, as the current is increased, this QCSE is screened by increased free carriers with the increased current density. These free carriers produce new field which decrease QCSE, results with decrease in carrier seperation and electron-hole wave functions start to match. Tilt of energy band by QCSE is decreased and as a result, effective radiative recombination is increased. Therefore, emission from quantum well is blue-shifted. Although thermal effect causes light to red shift, in III nitride LEDs, as the current density is increased, emitted light is blue shifted because of screening effect of QCSE, up to a limit. Generally, thermal effect is negligible for lower current densities. However, if the current is increased beyond the limit, than thermal effect is not negligible any more and may be dominant which makes the light more red shifted [74].

Light emitted from InGaN/GaN MQW with low Indium fraction is polarized in plane of quantum wells, which is called transverse electric (TE) polarization. In TE polarization, electric field is aligned along the quantum well plane. This TE optical polarization field covers 80 % of all emitted light from QW. Main reason of TE polarization in InGaN/GaN MQW is spontaneous and strain induced piezoelectric polarization.

In order to decrease QCSE, thin quantum well regions are required.

3.5 Electrical Properties of GaN based LEDs used in this Thesis

In general, resistivity of p type GaN is very high compared to n layer, which can also be seen from n-n and p-p I-V graphs in chapter 6. This requires using larger contacts all along top p layer in order to have uniform current spreading. Although the LED design in this thesis has this kind of contact metal as seen in figure below, since no transparent contact layer such as ITO that covers the whole p layer is used, there is problem about homogenous current spreading in LEDs which results with non-uniform emission. Because of RIE etching process, thin n layer LED structure and n metallization on AlGaN layer also decreases the uniformity.

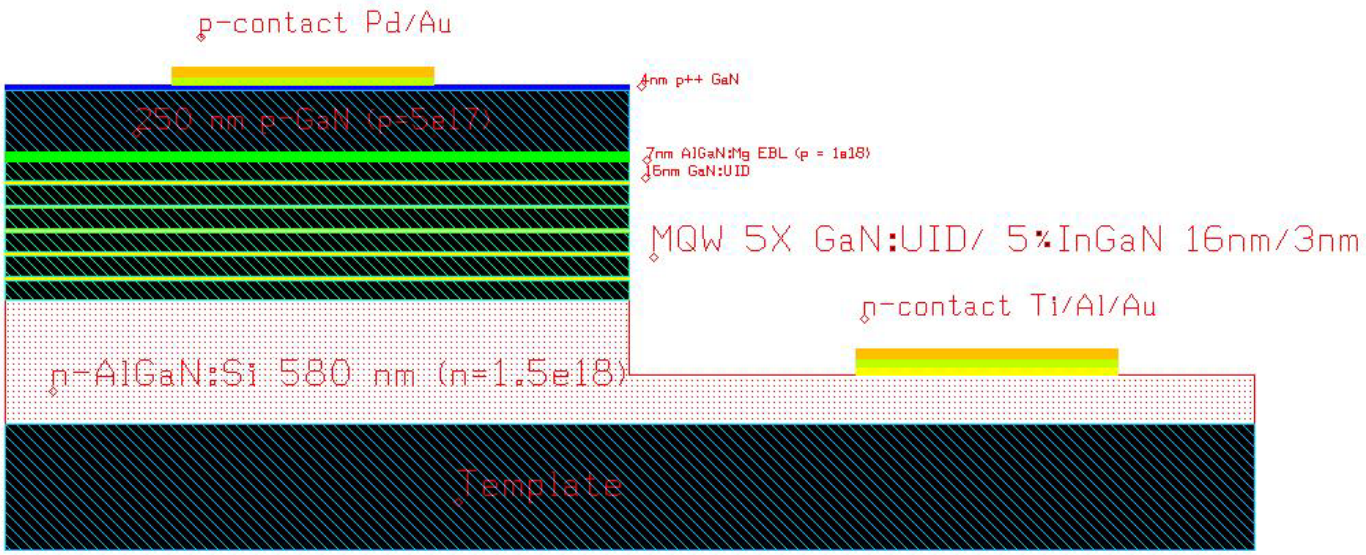

a.

b.

Figure 3.9 Layer structure of LED wafers grown in UCSB a. 390 nm LED b. 410 nm LED

General turn-on voltage of InGaN/GaN QW LEDs is around 3~3.2 V in the literature. However, it is stated that thin n layers may cause higher forward voltage than usual [75]. Furthermore, if n contact is placed on AlGaN layer, turn on voltage is said to be increased dramatically [76].

LED structures fabricated regarding this thesis are given below. These structures radiates at 390 nm and 410 nm. As clearly seen from I-V graphs in Chapter 6, turn on voltages of LED samples are very high. Damaged p++ top layer by RIE etching process and bad metal contacts are possible causes for this high turn on voltage. As stated above, reasons also include relatively thin n layer of the LED wafer (~580 nm) and metal contacts on Silicon doped n type AlGaN layer.

It is also possible that Mg dopants have been de-activated again during processing. All LED chips were treated with RIE cleaning process under O_2 (g), PECVD growth of SiO_2 by SiH_4 (g) and RIE etching with CHF_3 (g). H_2 gas with high temperature might have caused Mg dopants to form complexes with H which cause high resistivity and consequently high turn on voltage.

3.6 Optical Properties of GaN based LEDs and Photonic Crystals to Increase Extraction Efficiency

InGaN based LEDs have already been used in traffic lights, automobile lamps, LCD back lights, illumination systems [77]. However, extraction efficiencies of these LEDs are very low and therefore most of the light emitted from active layer of these devices cannot be used. Light which cannot get out from the device is absorbed by defects and quantum wells which also causes extra-heat which is detrimental for working life of LED. Efficiency of LED decreases with temperature and emission wavelength is red-shifted which causes low intensity and colour rendering problems. Furthermore, human factor and physical abilities come to the situation. Although human eye responsivity is very high for color of green, it drops rapidly when the wavelength of light goes down to blue region. Therefore, InGaN based blue LEDs also have to overcome human eye responsivity issue.

Because of the high refractive index difference between the GaN (n=2.7) and outer space (n=1), light coming to the air-GaN interface reflects totally back for incident angles higher than critical angle, which is calculated as;

$\theta_{critical} = \arcsin(1/n_{GaN})$ (3.5)

Critical angle for GaN, $\theta_{critical,\ GaN}$, in this study is therefore around 22°. From top surface of the GaN based LED without any encapsulation, ratio of emitted light to the generated light in active layer of the device is around $1/4n^2 \approx 4\%$ [78].

Moreover, even if light comes to the interface at 0° incident angle, not 100 % of light can escape out according to the Fresnel reflection. Transmission ratio for a vertical incident light is,

$$T = \frac{4(n_{air})(n_{GaN})}{(n_{air} + n_{GaN})^2} \tag{3.6}$$

For $n_{GaN} = 2.7$, around 79 % of light is transmitted to the air side and 21 % is reflected back in case it is assumed that no absorption is in question.

Some of other issues about low extraction efficiency are reflection from metal contacts, substrate absorption, absorption of carriers by GaN defects, impurities and InGaN/GaN quantum well layer.

Main objective of this thesis is to increase low extraction efficiency of light from GaN based LEDs. In order to increase the light output from GaN based LED, either internal quantum efficiency or extraction efficiency should be increased. Internal quantum efficiency is related to quality of the crystal structure of the material and possible defects which reduce radiative recombination rate and can only be altered during growth of the material. Internal quantum efficiency of InGaN/GaN LEDs in concern is already around 90 % [66]. On the other hand, extraction efficiency is mostly related to the geometry of the device. By designing proper geometry, most of the light trapped in the high refractive index medium because of total internal reflection can escape the structure.

Encapsulation is a required mechanism for LEDs which protects the chip from mechanical effects and also increases critical angle by acting as a transition medium from high index material (semiconductor) to low index medium (air). However, there are some drawbacks about using organic encapsulants. First of all, under high intensity, they turn opaque and do not allow light to pass anymore after a cutoff power. Secondly, since encapsulants increase source optical size, they tend to decrease the surface brightness of the device. Therefore, encapsulation may be a problem for high power and high intensity applications.

In order to increase extraction of light and protect the LED chip, hemi-sphere epoxy dome with refractive index of 1.5 is used on top of the chip. However this dome can only give a few percent of extraction enhancement for the case of GaN. Below is an integral method simulation which compares transmission ratios with and without epoxy. Simulation is done by using plane waves with incident angles from 0 to 90 by 2 degrees interval. Waves are sent from GaN layer and total transmission in air region is calculated by the formula given in chapter 6.

When there is no epoxy coating over the LED chip, extraction efficiency is about 3.2%. In case there is epoxy, extraction efficiency increases 0.4%.

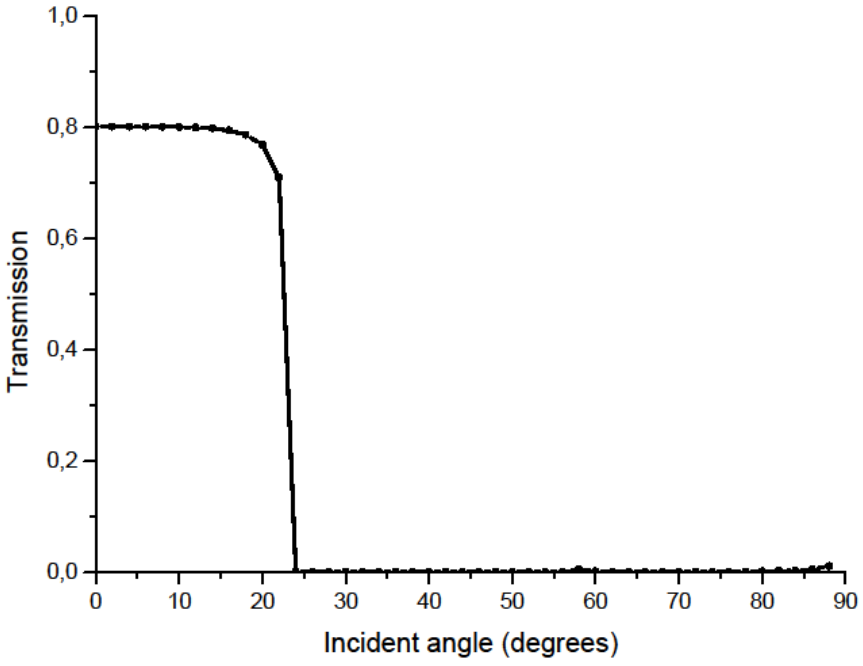

Figure 3.10 Extracted light from InGaN/GaN LED without epoxy, extraction efficieny is 3.2%

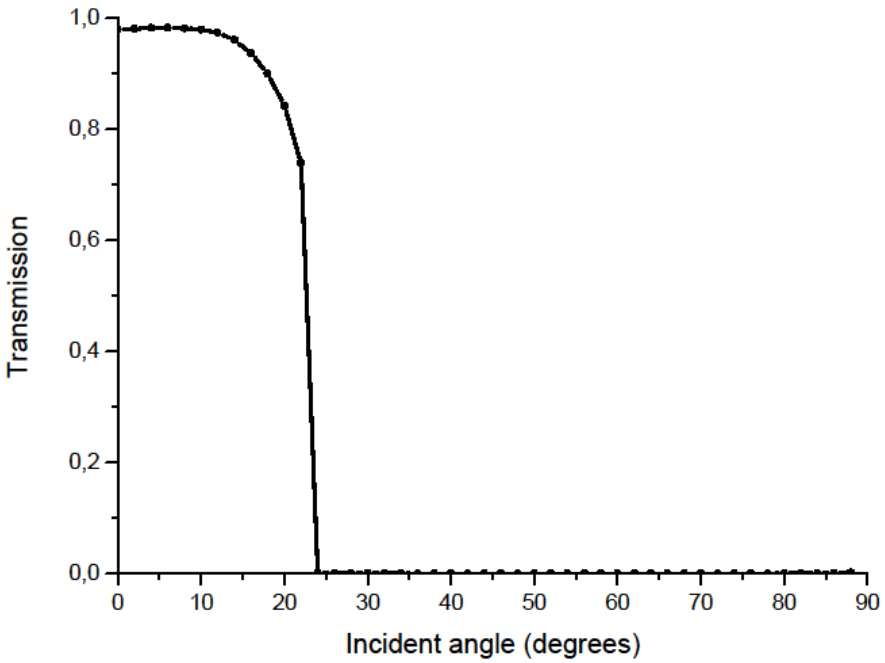

Figure 3.11 Extracted light from InGaN/GaN LED with epoxy, extraction efficiency is 3.6%

Other geometrical approaches in order to increase extraction efficiency include geometrical chip shaping and surface roughening [79][80]. Using five sides of the cubic LED chip to extract light instead of one top layer is one of the methods tried. In this geometry, up to 20% efficiency is achievable. However, guided light because of the total internal reflection cannot be out-coupled since the facets are vertical. In order to extract these modes, facets are etched such that they are inclined with respect to each other. Therefore, reflected rays from one facet can be extracted from the other inclined facet since the incident angle is changed. With this geometry, 50 % extraction efficiency is achieved in GaN based LEDs. Because of the limited area of the chip and increase in propagation time of light in the absorptive medium, this approach is also limited. One more draw-back of these geometrical approaches is out-coupling of light in every direction. Additional systems should be used in order to redirect the light into useful directions. Roughening the surface is another solution to increase light extraction efficiency which changes incident angle of incoming light. By placing a mirror on the other side, chance of out-coupling is increased. With this kind of geometry, 75% extraction efficiency is achieved in encapsulated GaN based LEDs. Again absorption in the medium by active layer and carrier traps are limiting problem for this roughening approach.

Moreover, profile of light gets out from device cannot be tailored and scattering is random [47].

These geometry based methods do not help for controlling the extracted light. Direction of the extracted light and amount of light extracted from the device cannot be predicted. Nevertheless, it is possible to design the profile of the emission pattern by using photonic crystal (PC) structure. Photonic crystals are layers of dielectrics with high refractive index contrast which fold the in-plane propagating light mainly by Bragg diffraction.

Using embedded photonic crystal structure on p type GaN increases external efficiency of LED with respect to that of non-photonic crystal LED. In the literature, it is stated that usual extraction enhancement gained is around 1.5~2.1. [8]. Light with incident angle higher than critical angle totally reflects back because of high dielectric contrast between outer medium and GaN. PC structures which are etched through p layer fold this guided light above the light line. As a result, previously confined light in the GaN material couples out into leaky modes.

By using PCs, encapsulation may not be needed anymore since PC itself increase the intensity of the light coming out of LED and LEDs with PC structure show higher optical power than LEDs with encapsulants [75].

Chapter 4

4. Photonic crystals (PCs) and light extraction efficiency enhancement of PC LEDs

4.1 Introduction

With the advances in semiconductor physics, 20th century became the era of electronics. Tailoring the conducting properties of some specific materials gave a way to initiate the transistor revolution. Development of fabrication techniques based on lithography has made it possible to fabricate smaller devices so that more transistors can be put in a single chip. However much further miniaturization does not seem to be possible since the electronics technology is about to come to the limit put by quantum mechanical effects.

In the last decade, a new frontier has emerged, controlling the interaction between light and matter. Light propagation inside the material can be controlled and be used instead of electrons to transfer information by a much faster way in a smaller volume. Materials can be engineered in such a way that light can only propagate in certain directions with certain frequencies. Prohibiting light propagation at all directions or localizing light in a specified volume is also possible by altering the property and geometry of the material, namely photonic crystals (PC).

Intense research has been done in the field of micro-nano photonics to enhance the optical properties of light emitters, detectors and waveguides. One of the instruments which has been intensely researched to improve the optical properties of the devices is photonic crystals. Advances in photonic crystals will allow denser, cheaper, faster and more efficient optical devices.

Light emitting diodes (LEDs), especially III-Nitride LEDs, suffers from low extraction efficiencies while their internal quantum efficiencies are about 90%. Most of the light is trapped inside the III-Nitride material because of total internal reflection (TIR) which is caused by high refractive index contrast between air and GaN material (n_{air}=1, $n_{nitrides}$=2.5~3.5). Photonic crystal integrated LED chips show higher extraction efficiencies

since the trapped light in the medium is extracted by the PC structure so that higher proportion of light can escape from the high index material.

4.2 Definition and History of Photonic Crystal

The history of the study of electromagnetic propagation in a periodic media started extensively by Brillouin [81]. Then, Othaka worked on the dielectric spheres in a periodically ordered 3D lattice and published the band diagram of the lattice in 1979 [82]. However, the photonic crystal concept was first proposed by Yablonovitch [83] and John [84] in two separate Physical Review Letter articles with 2 months apart in 1987. What Yablonovitch argue was the possibility of inhibiting spontaneous emission of photons within the photonic band gap while John dealt with the localization of light, which were both formed by photonic crystal structures. These two research works had resulted in the same conclusion that in a media with spatially varying and lossless dielectric function, matter can interact with the electromagnetic field in a way that a stop band may occur.

The unique optical properties of photonic crystals offer practically unlimited control on the propagation of light in a microscopic scale. Because of this, area of PC attracted many researchers around the world from diverse fields in the last 2 decades. Shortly, photonic crystal is an optical material which has a periodically changing spatial refractive index so that it creates a photonic band gap in the lateral PC plane. Photonic band gap (PBG) is defined as the energy range where propagation of light is inhibited in certain directions. In this thesis, PCs are designed to couple the light propagation to vertical direction by placing PC periodicity in lateral directions so the light extraction efficiency will be enhanced. The periodicity and dimensions of PC should be on the order of the wavelength of incident light in order to control the photons via band formation just like the periodicity in the solid state crystals which determines the energy band structure [75] [85].

In 1991, Yablonovitch group demonstrated a photonic crystal which exhibits a full 3D photonic band gap in microwave regime experimentally [86]. And first 2D PC was tested experimentally in 1995 in a thick slab of porous silicon [87] while first GaAs based 2D PC was fabricated in 1996 [88]. Afterwards, each year came with new advances and progress has been continuing so far.

Photonic crystal concept can actually be said to be just a good example of bio-mimetic approach. Natural photonic crystals such as butterfly wings, opals and peacock feathers have drawn special attention throughout time. The structures of these natural creatures have also been researched in order to understand the physics and optics behind their own special structures. There are some examples of natural photonic crystals in Figure 4.1 below.

The real power of PCs arises with their integration into functional devices. However, fabrication of periodic structures can be challenging especially for the length scales of micrometers and nanometers. Gallium Nitride (GaN), which is the main semiconductor material studied in this thesis, is one of the most robust material. Processing and integrating these wavelength scale PC structures into GaN LED wafer is more challenging. For these structures, sophisticated fabrication techniques are required.

Once integrated successfully, PCs show promising applications on opto-electronic devices such as light emitters, resonators, filters, polarizers, antennas, waveguides, fibers, non-linear optical devices [5][6] [89]. They can be used to tailor the shape of extracted light. Therefore, PCs are important for imaging and non-imaging applications where etendue is crucial such as headlamps and projectors [44]. Recently, photonic crystals are used to extract unpolarized light from conventional LEDs as polarized light which is essential for back-lighting for devices such as LCD panels [90].

Defects introduced in the periodicity of PCs allow photon states to be able to appear in the PBG, which is created by PC structure. Defects can be used to localize light in the optical material. Since the scope of this thesis is mainly photonic crystals without any defects, particularly 2D photonic crystals integrated in III-Nitrides LEDs, the subject of defects in PCs is only outlined here. Further information could be gained elsewhere [91][92][93][94]. Three types of defects can be created in PC structure. One dimensional defects are used to localize light in a single cavity so that single mode cavities can be realized. Two dimensional defects are planar defects. With two dimensional defects, light with the wavelength in PBG can be guided in the plane without any loss, so called lossless waveguides. Three dimensional defects are useful to confine the light in a cage.

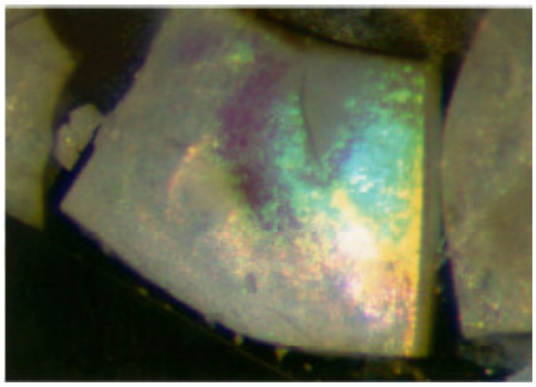

a. Green opal

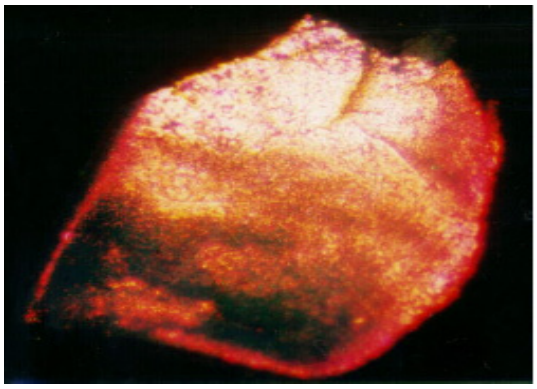

b. Red opal[8]

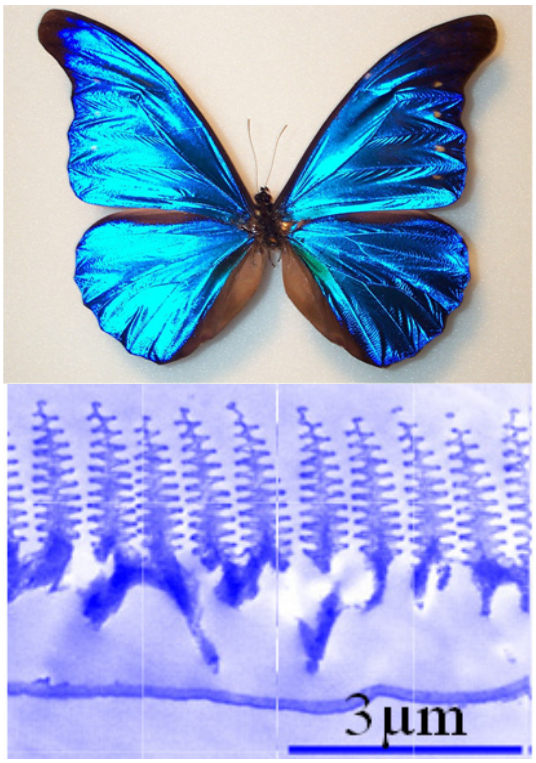

c. Morpho rhetenor butterfly

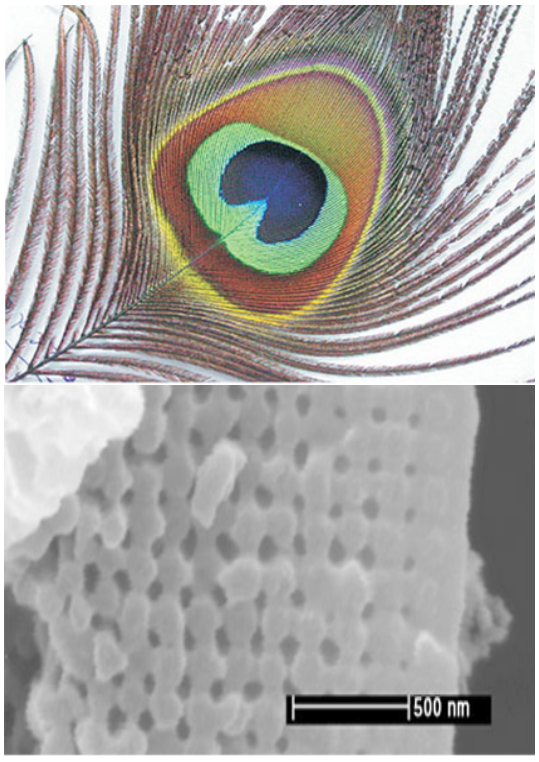

d. Peacock feather [10]

Figure 4.1 Natural Photonic Crystals. a) Green opal which reflects light at λ=560nm, with periodic lattice constant d=420nm (ref. [95]). b) Red opal which reflect light at λ=680nm, with periodic lattice constant d=490nm (ref. [95]). c) Morpho rhetenor butterfly and the periodic structure inside its wings which creates the unique color (ref. [96]). d) Peacock feather and its nano-structure with different lattice constants which gives feather diversified colors [97].

There are three different classifications of photonic crystals, one dimensional (1D), two dimensional (2D) and three dimensional (3D) PCs, which are based on their lattice periodicity directions and their capacity to posses PBG along those specified directions.

Figure 4.2 illustrates these types of phonic crystals. 1D structure is just a series of thin films with alternating refractive index values and has periodicity in only one direction, while 2D

and 3D photonic crystals are structures which have spatial refractive index variation periodicity in two and three directions, respectively. A practical 2D PC consists of periodic lattice of dielectric columns in air or periodic air holes in a dielectric material. 3D PCs can posses a full three dimensional PBG so that light propagation can be controlled at all possible directions. However, to fabricate those structures successfully has been proven to be really difficult even with the technology at the time this thesis is being written.

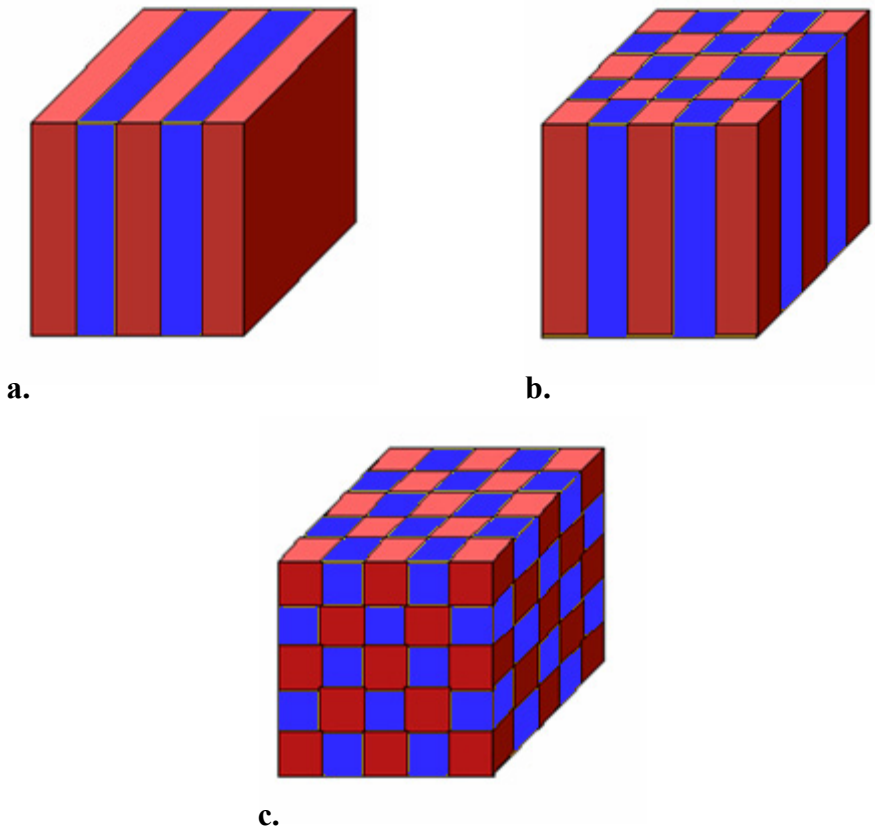

Figure 4.2 Types of Photonic Crystals

a. One dimensional **b. Two dimensional** **c. Three dimensional**

Since realizing 3D PCs is a big challenge, much attention has been given to 2D PCs. When designed carefully, 2D PCs can give approximate successful results like that of 3D PCs. For extraction of light in LEDs, planar 2D PCs will be sufficient to enhance the light output.

Not much work was reported related to PC structures for III-Nitrides for blue-UV wavelengths until beginning of 2000s since processing III-Nitrides, particularly GaN, and fabricating PC structures is very hard due to robust mechanical properties of the material. In

this thesis, 2D PC which is formed by drilling periodic air holes in GaN substrate is studied in order to enhance the light output from the GaN LED wafer. Although generally circular holes are used in order to fabricate PCs for guiding light, it is stated that elliptical holes can also be used to control the polarization of light [98]. In Figure 4.3 a 2D PC which is formed by creating periodic air holes in a dielectric substrate with triangular lattices can be seen.

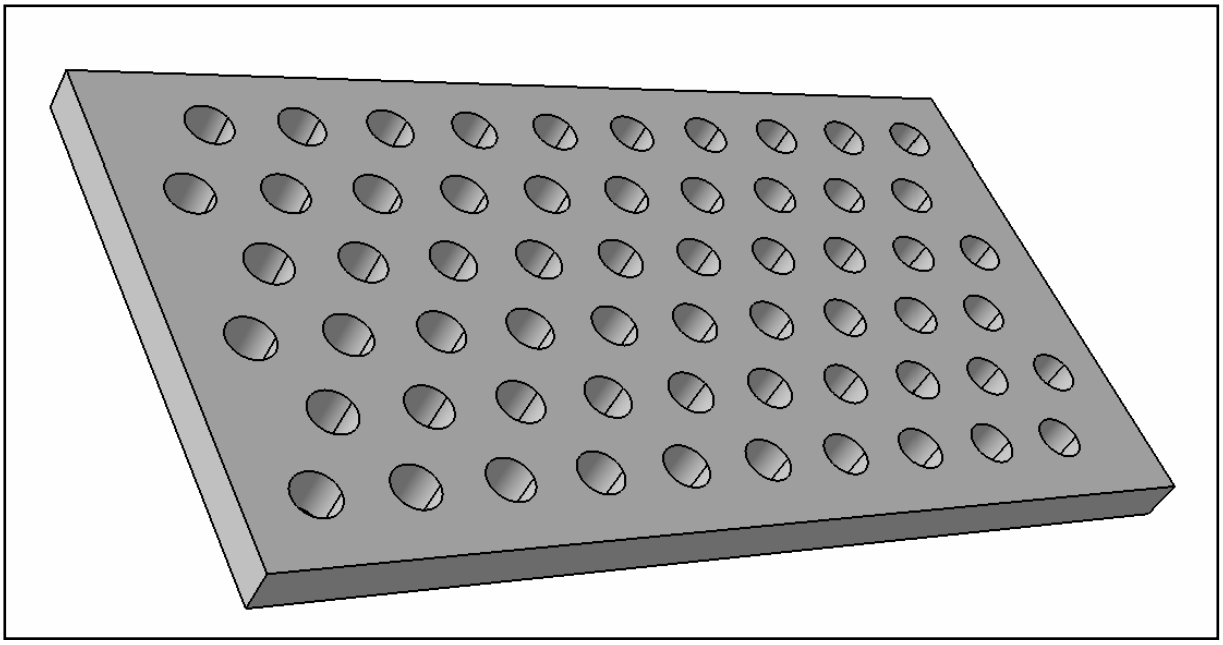

Figure 4.3 2D PC formed by triangular air lattices in a dielectric material

4.3 Maxwell Equations In Dielectric Mediums

Maxwell equations govern propagation of electromagnetic fields in free space and in dielectrics. In order to study photonic crystals and light propagation properties in PCs, Maxwell equations should be defined first.

Electro-magnetic field is composed of electric field and magnetic field. Electric field E(r,t) and magnetic field H(r,t) are related to each other by partial differential equations that are called Maxwell's equations.

Four main Maxwell equations in free space are stated below.

$$\nabla \times E = -\mu_0 \frac{\delta H}{\delta t}$$

$$\nabla \times H = \varepsilon_0 \frac{\delta E}{\delta t}$$

$$\nabla \bullet E = 0 \qquad (4.1)$$

$$\nabla \bullet H = 0$$

Here, ε_0 and μ_0 are electric permittivity and magnetic permeability of free space with $\varepsilon_0 \approx (1/36\pi)(10^{-9})$ and $\mu_0 = (4\pi)(10^{-7})$. E is macroscopic electric field, H is macroscopic magnetic field, $\nabla \times$ is curl operation, $\nabla \bullet$ is divergence operation where,

$$\nabla \times = (\frac{\delta_z}{\delta y} - \frac{\delta_y}{\delta z})i + (\frac{\delta_x}{\delta z} - \frac{\delta_z}{\delta x})j + (\frac{\delta_y}{\delta x} - \frac{\delta_x}{\delta y})k$$
$$\nabla \bullet = \frac{\delta_x}{\delta x} + \frac{\delta_y}{\delta y} + \frac{\delta_z}{\delta z} \qquad (4.2)$$

Maxwell equations become as below when fields propagate not in free space but in a medium.

$$\nabla \times E = -\frac{\delta B}{\delta t}$$

$$\nabla \times H = \frac{\delta D}{\delta t} + J$$

$$\nabla \bullet D = \rho \qquad (4.3)$$

$$\nabla \bullet B = 0$$

where D is electric flux density or electric displacement field, B is magnetic flux density.

Since we are looking for a solution in a medium with photonic crystal structures, we can limit the medium properties such that structure is invariant with time, composed of mixed dielectrics with no current and free charge. So, ρ and J can be set to 0.

In order to make equations easier to solve, some assumptions should be made without moving out of the line so that physical meaning of the problem does not change.

These assumptions are;

1) Field strengths are assumed to be small enough such that problem is in linear regime.

2) There is no material dispersion. Value of dielectric constant is chosen for the frequency range to be considered.
3) There is no absorption. Dielectric constant $\varepsilon(r)$ is positive and real.
4) Material is isotropic and macroscopic. $E(r,\omega)$ and $D(r, \omega)$ are related to each other by $\varepsilon_0\varepsilon(r, \omega)$, where $\varepsilon(r, \omega)$ is called relative permittivity. $H(r,\omega)$ and $B(r, \omega)$ are related to each other by $\mu_0\mu(r, \omega)$, where $\mu(r, \omega)$ is called relative permeability.

Taking into account these assumptions and remembering $\mu(r)$ is close to 1 for most of dielectric materials, D(r) and B(r) can be described as,

$$\begin{aligned} D(r) &= \varepsilon_0 \varepsilon(r) E(r) \\ B(r) &= \mu_0 H(r) \end{aligned} \tag{4.4}$$

Finally, Maxwell equations become as the following.

$$\begin{aligned} &\nabla \times E(r,t) + \mu_0 \frac{\delta H(r,t)}{\delta t} = 0 \\ &\nabla \times H(r,t) - \varepsilon_0 \varepsilon(r) \frac{\delta E(r,t)}{\delta t} = 0 \\ &\nabla \bullet \left[\varepsilon(r) E(r,t) \right] = 0 \\ &\nabla \bullet H(r,t) = 0 \end{aligned} \tag{4.5}$$

Both electric and magnetic fields are functions of space and time. However, they can be separated into functions of time alone and space alone since Maxwell equations are linear and separable in 2D. Therefore, we can treat these fields separately by taking set of harmonic modes that change with time.

$$\begin{aligned} E(r,t) &= E(r) e^{-i\omega t} \\ H(r,t) &= H(r) e^{-i\omega t} \end{aligned} \tag{4.6}$$

In these harmonic modes, H(r) and E(r) are mode profiles or spatial patterns. In order to obtain physical fields, real parts of the harmonics are taken into account.

Putting these harmonic modes into Maxwell equations, we can get the time independent Maxwell equations.

$$\nabla \times E(r) - i\omega\mu_0 H(r) = 0$$

$$\nabla \times H(r) + i\omega\varepsilon_0\varepsilon(r)E(r) = 0$$

$$\nabla \bullet \left[\varepsilon(r)E(r)\right] = 0 \tag{4.7}$$

$$\nabla \bullet H(r) = 0$$

Divergence equations above confirm that no point sinks or point sources of magnetic fields and electric fields present in the medium and these fields are composed of transverse electromagnetic waves.

Re-arranging curl time independent Maxwell equations and remembering vacuum light speed $c = 1/\sqrt{\varepsilon_0\mu_0}$, one can get the master equation which describes the states or modes of the system.

In order to obtain the master equation, first divide the magnetic field curl equation by ε(r).

$$\frac{1}{\varepsilon(r)}\nabla \times H(r) + i\omega\varepsilon_0 E(r) = 0 \tag{4.8}$$

Then take the curl of this equation.

$$\nabla \times \left[\frac{1}{\varepsilon(r)}\nabla \times H(r)\right] + \nabla \times \left[i\omega\varepsilon_0 E(r)\right] = 0 \tag{4.9}$$

Use the curl equation of electric field in time independent Maxwell equation to eliminate E(r) in the equation above.

$$\begin{aligned}
&\nabla \times \left[\frac{1}{\varepsilon(r)}\nabla \times H(r)\right] + i\omega\varepsilon_0 \nabla \times E(r) = 0 \\
&\nabla \times \left[\frac{1}{\varepsilon(r)}\nabla \times H(r)\right] + i\omega\varepsilon_0 \left[i\omega\mu_0 H(r)\right] = 0 \\
&\nabla \times \left[\frac{1}{\varepsilon(r)}\nabla \times H(r)\right] - \omega^2\varepsilon_0\mu_0 H(r) = 0 \\
&\nabla \times \left[\frac{1}{\varepsilon(r)}\nabla \times H(r)\right] - \omega^2\left(\frac{1}{c}\right)^2 H(r) = 0
\end{aligned} \tag{4.10}$$

Using speed of light in vacuum equation, master equation of the system is obtained.

$$\nabla \times \left[\frac{1}{\varepsilon(r)} \nabla \times H(r) \right] = (\frac{\omega}{c})^2 H(r) \tag{4.11}$$

This master equation is an eigen-value equation since for every allowed spatial mode H(r), an eigenvector, has a solution with a constant eigen-value, $(\frac{\omega}{c})^2$. Here, eigen-value solutions describe the squared frequencies of allowed modes in the material or system.

Master equation is used for spatially known dielectric mediums. So, we have ε(r) that we will put into the master equation to find the allowed modes H(r) and consequent allowed frequencies ω. Then, by using curl equation of magnetic field time independent Maxwell equation, we can get the allowed electric field states E(r).

$$E(r) = \frac{i}{\omega \varepsilon_0 \varepsilon(r)} \left[\nabla \times H(r) \right] \tag{4.12}$$

Operator of the eigen-function, $\nabla \times \left[\frac{1}{\varepsilon(r)} \nabla \times \right]$, is Hermitian and a linear operator such that these eigen-value solutions must be real numbers and any linear combination of solutions is also a solution.

In order to minimize the energy functional, fields with lower frequencies are concentrated in materials with higher dielectric constant according to Variational Theorem [99]. Therefore, in dispersion band diagrams, first band is called dielectric band, and second band is called air band.

4.3.1 Optical Power and Optical Intensity

Energy is swapped between magnetic field and electric field periodically. Therefore, amount of energy of electric field at time T=π is equal to that of magnetic field at T=2π for TEM (transverse electromagnetic) modes. Physical energy of the mode is related to amplitude of the field. Power of the system can be found by calculating the time average of Poynting vector S and taking the real part which gives the rate of electromagnetic energy flow.

$$\begin{aligned} S &= \frac{1}{2} E \times H^* \\ P &= \mathrm{Re}\{S\} \end{aligned} \tag{4.13}$$

4.4 Structure Of Photonic Crystals

4.4.1 One Dimensional Photonic Crystals And Band Gap Formation

In order to understand the effect of periodic change of dielectric mediums in two dimensional space, we can use the basic principles such as band-gap formation that we can obtain more easily from one dimensional case.

1D photonic crystal structure can be considered as multi-layers of films with high difference of refractive indices among each other. Thus, dielectric function will vary in only one direction and it will be invariant along other two directions. If it is designed properly, this kind of photonic crystal structure may reflect all the incident light along a specific direction (may also act as omni-directional reflector) which is also called Bragg mirror or distributed Bragg reflector (DBR). We will firstly analyze this type of photonic crystal structure in terms of band models and then will generalize to two dimensional case.

Below in figure, multi-layer films are shown on top of each along z direction; thus, dielectric constant of the system is a function of z direction, ε(z) and it does not change in x or y directions.

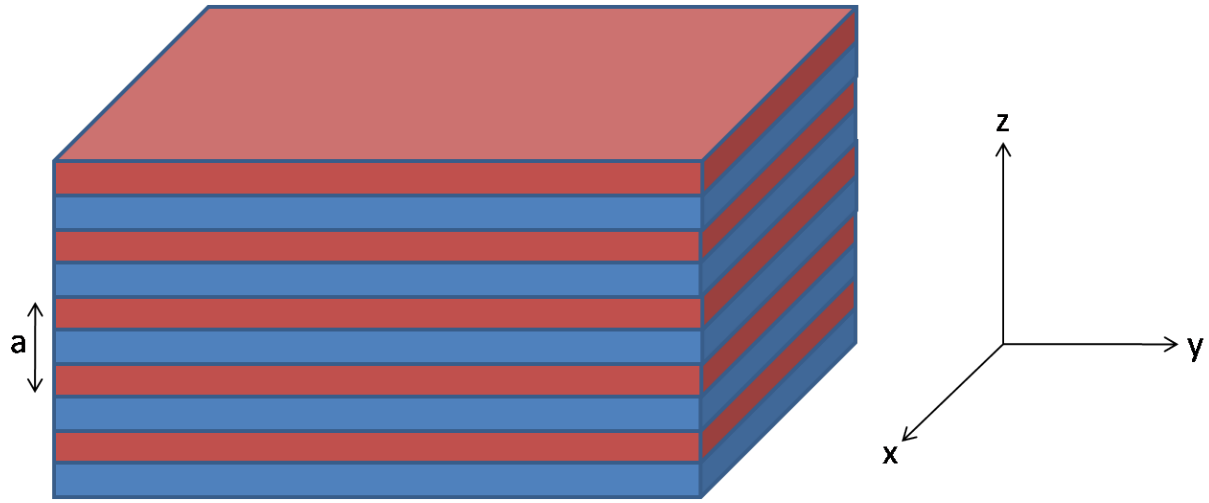

Figure 4.4 1D Photonic Crystal Structure with lattice constant "a"

4.4.1.1 Band Structure of 1D PC Structure

Periodic structure of the system helps us to define the modes of the system by using wave-vector parallel to the homogenous x-y plane ($k_{||}$), wave-vector in the direction of periodicity (k_z), and band number n. In Bloch form, modes can be written as,

$$H_{k_z,k_{||},n}(r) = e^{ik_z z} e^{ik_{||}\rho} u_{k_z,k_{||},n}(z) \tag{4.14}$$

where ρ is any vector in homogenous plane, u(z) is a periodic function with $u(z) = u(z + ba)$, b is any integer and a is the lattice constant. In-plane wave-vector $k_{||}$ can take any vector without restriction since the system is homogenous in x-y plane. However, k_z is bounded by the first Brillouin zone ($-\pi/a < k_z \leq \pi/a$) because of the translational symmetry in z direction. Any mode with a larger in-plane wave-vector folds back into first Brilloin zone.

In such a periodic 1D system, as the difference between dielectric constants is increased, a photonic band gap region occurs where no mode is allowed to exist in. In other words, density of states (DOS) in a photonic band gap is zero. There may occur two types of band gaps. These are called complete band gap and stop-band. In a complete photonic band gap, regardless of wave-vector, there is no allowed mode which has frequency settles in the gap. On the other hand, if there is a band gap just along certain directions so that modes are not able to survive just in those directions, these gaps are called stop bands. Light with a frequency which stays in stop band cannot propagate in that specific direction where stop band exists.

Photonic band gaps that are created by photonic crystals can be very beneficial in various applications. They can be used in order to make narrow-band filter (i.e. rejecting all frequencies but allowing just the one that is desired), directing light in specific directions and even in succeeding of optical integrated circuits if the band-gap frequencies can be altered by continuously changing of dielectric constant.

As stated above, dielectric contrast gives a way for photonic band gaps. Main principle can be understood by using variational theorem [99].Considering a 1D PC case with wave-vectors along translational symmetry direction, nodes of the modes should stay in the structure without violating the symmetry. Therefore, nodes will be placed in low or high dielectric (ε) areas. Here comes the variational theorem, which says that while high frequency modes settle down in low ε regions, low frequency modes are found in high ε areas in order to lower

their energies as seen in Figure 4.5. As a result, there occurs a gap between the modes; higher the ε contrast, larger the frequency shift and larger the gap. Since low ε region is generally air especially in two and three dimensional photonic crystals, those modes above the gap is called air band and below the gap is called dielectric band.

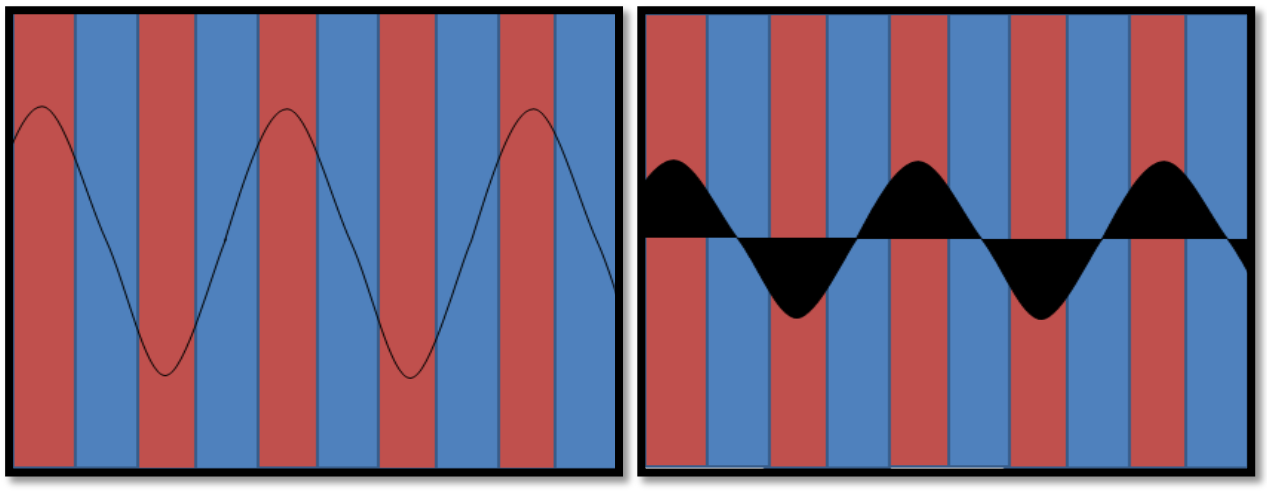

a. b.

Figure 4.5 Electric field and energy density of dielectric band

4.4.1.2 Bragg Reflection in Real Space

Frequency of band gap formation basically relies on Bragg condition to be maintained. Bragg scattering concept is generally used for determining crystallographic structure. A beam of X-Rays is directed on a solid-state crystal in order to get the information about geometry of lattice planes of the crystal structure. This incident X-Ray beam is weakly reflected by the atoms from various planes. However, for certain angles of incidence, each of these scattered beams adds up in phase resulting in a large reflection for particular direction, which is called constructive interference. When these constructively interfered scattered beams are projected on a screen, result is the shiny spots with high intensity light, which are the lattice planes in reciprocal space. Bragg scattering makes it possible to measure the distances between the planes formed by the atoms of the crystal. This phenomenon was first formulated by Sir Lawrance Bragg in 1913 [100].

Consider electromagnetic (EM) rays reflecting from the planes of atoms as shown in figure 3.5 below. In order constructive interference to happen after reflection, path difference between the reflecting rays must be a multiple of the wavelength in the medium.

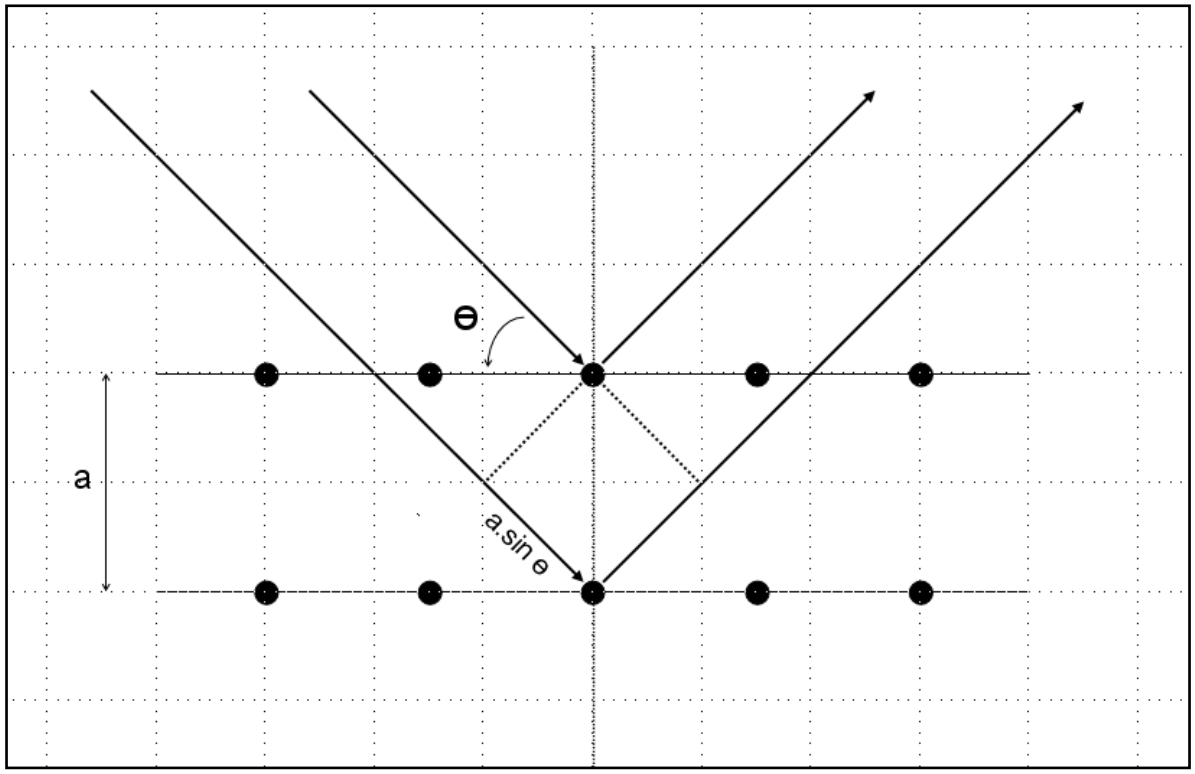

Figure 4.6 Bragg Condition in order to have constructive interference

For a Bragg period 'a' and an incident angle θ, which is measured from the plane of atoms to the incident ray, Bragg condition is given as;

$$2na\sin\theta = m\lambda_0 \tag{4.15}$$

where n is the refractive index of the material, m is a positive integer that determines the number of Bragg Reflection (i.e. when m=2, it is said to be the condition for second order Bragg Reflection), and λ_0 is the wavelength of the incoming ray in air.

When equation 3.5 satisfies, for that specific angle and lattice period, a band-gap will form since the incident light is fully reflected without transmission and no EM radiation with the specified wavelength will propagate through the material in that direction. If the light comes with 90^0, perpendicular to the plane of atoms, then Bragg condition simplifies to;

$$2a = m\lambda_f \tag{4.16}$$

where λ_f is the wavelength of EM radiation in the material.

Let us now use the procedure described here in order to find band gap frequencies (wavelengths) of a 1D PC structure. Again, we constrain the wave-vector to be in direction of lattice periodicity, $k = k_z$. Then, Bragg condition with $\sin\theta=0$ comes to be;

$$2na = m\lambda_0 \tag{4.17}$$

where n is refractive index, m is integer, a is lattice constant, λ_0 is free space wavelength. Here the product na is optical path length of the single period. Let us say refractive indices of periodic dielectrics in 1D PC structure are n_1 and n_2 , with layer thicknesses of d_1 and d_2. Therefore, optical path length will be $n_1d_1 + n_2d_2$. Now, Bragg condition can be written as,

$$2(n_1d_1 + n_2d_2) = m\lambda_0 \tag{4.18}$$

If we leave λ_0 alone, we can find the wavelengths where band-gap occurs, i.e. light is diffracted constructively so that all the incoming light is reflected backwards.

$$\frac{2(n_1d_1 + n_2d_2)}{m} = \lambda_{gap} \tag{4.19}$$

2D PC structure that is fabricated in the scope of this thesis has the lattice constant $a = 520$ nm with r/a ratio of 0.25 where r is the radius of the PC lattice hole. Along x and y directions pointing from the center of PC lattices, structure can simply be thought as one dimensional. If we apply the Bragg constructive diffraction rule for this lattice with n_1=2.7 (refractive index of GaN) and n_2=1 (refractive index of air), we see that there occurs no gap for the wavelength of 390 nm which is the main emission wavelength of InGaN/GaN light emitting diodes fabricated regarding this thesis. However there occurs a band gap around a/λ = 0.27 (a = 105 nm) as seen from calculations below, which is also consistent with the results of two dimensional simulation based on plane wave expansion method (see related chapter for details).

$$\begin{aligned} \lambda_{gap} &= \frac{2\left[(2.7)(260)+1(260)\right]}{m} \\ \lambda_{gap} &= \frac{1924}{m} \end{aligned} \tag{4.20}$$

As the order of Bragg scattering is increased, ratio of the band gap decreases. Therefore, possible wavelengths for photonic band gaps are around 1900 nm, 920 nm, 640 nm and 480 nm. It is clear that we do not expect a gap around 390 nm from 1D calculation. On the other hand, for a = 105 nm where a gap shows up from 2D simulation, 1D calculations predict a gap around second order Bragg reflection for wavelength of 390 nm.

$$\lambda_{gap} = \frac{2\left[(2.7)(105)+1(105)\right]}{2}$$
$$\lambda_{gap} \cong 390 \text{ nm} \tag{4.21}$$

Second order Bragg condition is the most desired design criteria since it gives the highest efficiency of photonic band gap [101][6][85]. As stated above, no mode is supported in the frequency region of photonic band gap. When light with a frequency in band gap region is sent into the structure, that mode is not extended in the structure but it is evanescent which decays exponentially with a complex valued wave vector. In Bloch form with a complex wave-vector $k + i\kappa$, it can be written as,

$$\mathrm{H_k}(r) = e^{ikz} e^{-\kappa z} u_k(z) \tag{4.22}$$

where u(z) is periodic function. Mode decays with a ratio of $1/\kappa$. Decay constant κ increases when mode frequency shifts around mid-gap. Therefore, if the band gap is enlarged (e.g. increasing the dielectric contrast), larger κ will cause less light to penetrate into the gap area.

4.4.1.3 Bragg Reflection in Reciprocal Lattice

Reciprocal lattices are important since it gives diffraction properties regarding the lattice planes directly. In order to visualize folding of wave-vectors by PC structures in reciprocal lattice, Bragg reflection is explained using Ewald's construction this time below.

In reciprocal space (k-space), as Laue Condition states [100], constructive interference occurs if the reflected wave-vector k* differs from incoming wave-vector k by reciprocal lattice vector G as shown in figure 3.6.

In this figure, black dots are the reciprocal lattice points of a PC structure of real square lattices. This circle is drawn in this way: First, a point is chosen from which incident beam is reflected. This is point O in the figure 3.6. Here |AO| is the wave-vector of the incident beam, k, with length of $2\pi/\lambda_f$ where λ_f is wavelength of the light propagating in the dielectric. Then a circle is drawn, named Ewald's Construction Circle, with origin being the A point, radius $2\pi/\lambda_f$. Afterwards, it is checked if there is any intersection between the reciprocal lattice points and the circle. If there is, that means that some plane of the real lattice reflects the incoming light with wave-vector $2\pi/\lambda_f$. In the figure, there is an intersection at point B. The drawn vector |AB| is the wave-vector of the reflected beam, k*. Since it is assumed that no absorption happens, scattering can be said to be totally elastic. So, the magnitudes of the

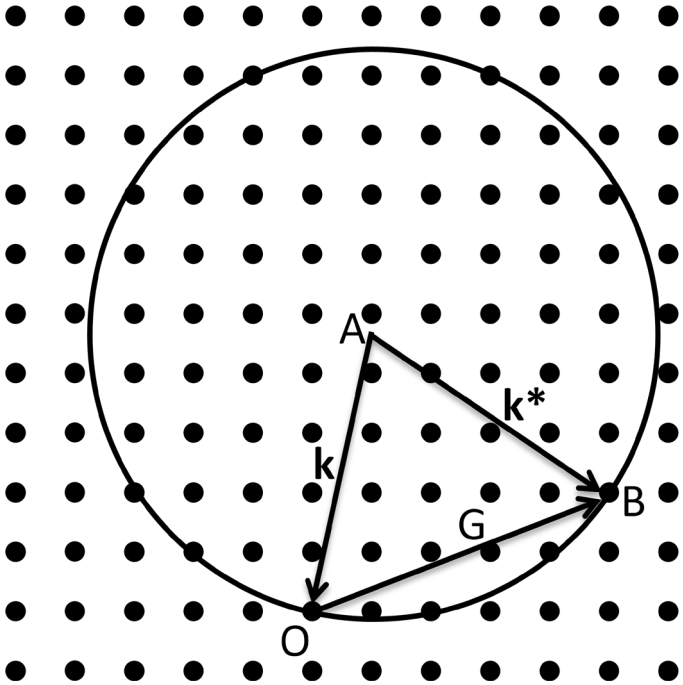

Figure 4.7 Bragg Reflection in k-space showing in Ewald Construction Circle

wave-vectors of incident and reflected beams are the same, but just the directions are different. And this direction difference comes from the reciprocal lattice vector G, which is drawn in the figure as |OB|. Because G is reciprocal lattice vector (i.e. |OB| starts and ends on a reciprocal lattice point, it is normal to some real lattice plane. So length of G is $2\pi/a$, where 'a' is the distance between two adjacent real lattice planes, i.e. periodic lattice constant.

4.4.2 Two Dimensional Photonic Crystals

In a 2D PC structure, dielectric constant has a periodicity in two directions rather than one. Most generally used lattice types for 2D structures are square and triangular lattices. In square lattice, PC structures, which are air holes in this thesis, are placed in a square order on the plane. Below is a figure of 2D PC structure with square hole lattice where ε changes periodically along x and y directions but invariant in z. In triangular PCs, lattice holes are placed on the surface in triangular form.

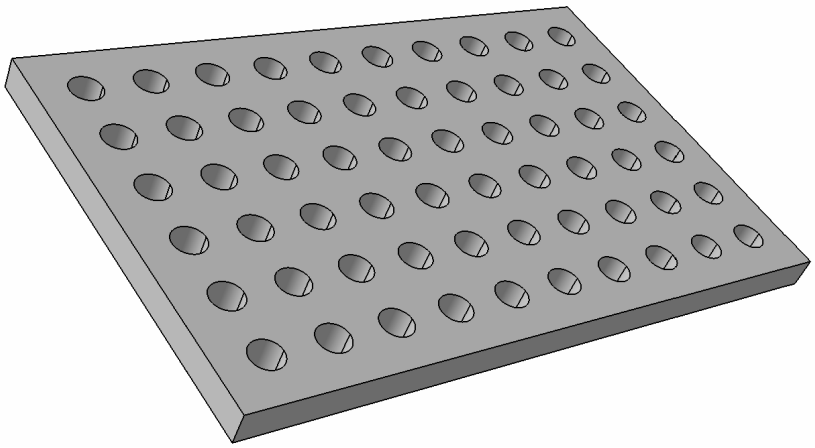

Figure 4.8 Two dimensional PC structure with square lattice

For such a photonic crystal lattice, lattice constant "a" and lattice radius "r" are important design parameters. Lattice constant "a" is the distance between centers of two adjacent holes and lattice radius "r" is the radius of the PC hole. The parameter r/a which is used to calculate filling ratio is an important one which defines the characteristics of the band map.

Square PC Structure

Reciprocal lattice of a square lattice is again square, however with a 90° turn. Reciprocal lattice vectors are calculated with formula below in (4.23).

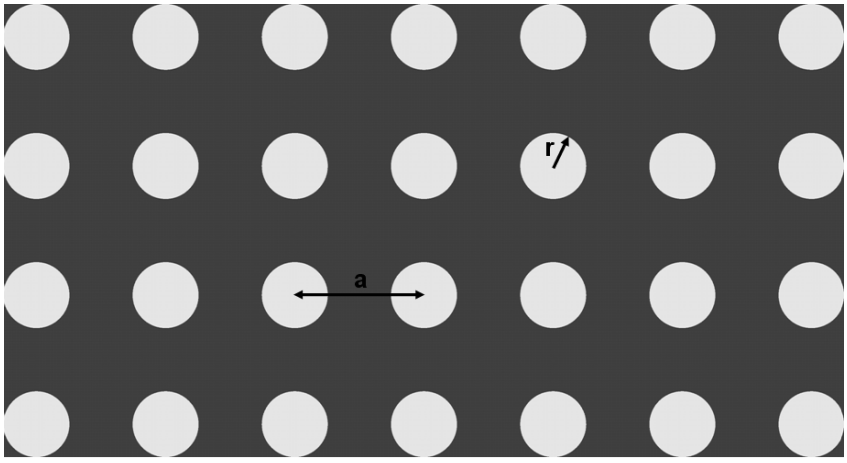

Figure 4.9 Square PC lattice, with lattice constant "a" and lattice radius "r"

$$\vec{b_1} = 2\pi \frac{\vec{a_2} \times \vec{a_3}}{\vec{a_1} \bullet (\vec{a_2} \times \vec{a_3})}$$
$$\vec{b_2} = 2\pi \frac{\vec{a_3} \times \vec{a_1}}{\vec{a_1} \bullet (\vec{a_2} \times \vec{a_3})} \qquad (4.23)$$
$$\vec{b_3} = 2\pi \frac{\vec{a_1} \times \vec{a_2}}{\vec{a_1} \bullet (\vec{a_2} \times \vec{a_3})}$$

where $\vec{b_1}, \vec{b_2}, \vec{b_3}$ are reciprocal lattice vectors and $\vec{a_1}, \vec{a_2}, \vec{a_3}$ are real lattice vectors. As real lattice is periodic, regarding reciprocal lattice is periodic too. For two dimensions, vectors along z direction is regarded as unit vector.

For square real PC lattice, real lattice vectors are $a\hat{\mathrm{x}}$ and $a\hat{\mathrm{y}}$, and corresponding reciprocal lattice vectors are $2\pi / a\hat{\mathrm{x}}$ and $2\pi / a\hat{\mathrm{y}}$.

Unit cell of periodic reciprocal lattice is called first Brillouin zone. Since modes are folded back from the edges of this zone, only first Brillouin zone is used while studying band maps. This zone is further divided into parts using symmetry and just 1/8 of the zone comes to be sufficient in order to define and understand the photonic band structure. This divided zone is called Irreducible Brillouin zone as seen in Figure 4.10.

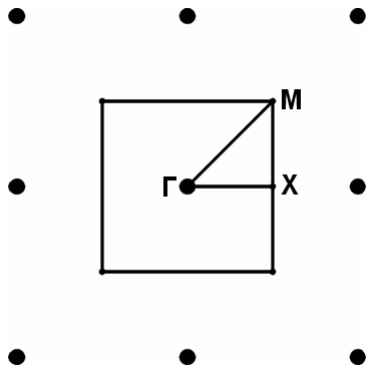

Figure 4.10 First Brillouin zone and Irreducible Brillouin zone for square lattice

Here, Γ, X and M are symmetry points which represent wave-vectors $k = 0$, $k = \pi / a\hat{\mathrm{x}}$ and $k = \pi / a\left(\hat{\mathrm{x}} + \hat{y}\right)$ respectively.

In order to study photonic band structures, edges of irreducible Brillouin zone is used since band gaps most generally occur at the zone edges.

Triangular PC Structure

Another PC lattice type commonly used is triangular lattice which can be seen from the figure below.

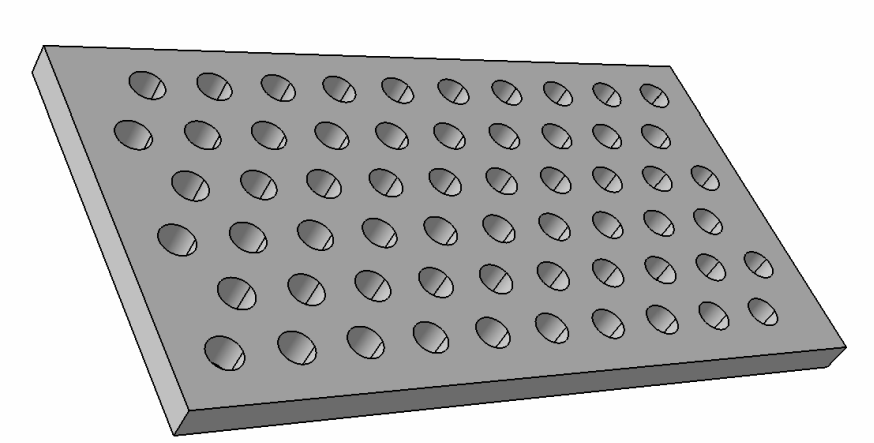

Figure 4.11 2D triangular PC lattice

In this type of PC structure, holes are placed at the corners of triangles on a plane. Since there are more symmetry directions than that of square lattice, triangular lattice supports larger photonic band gaps.

This type of PC lattice has lattice vector lengths of a and corresponding reciprocal lattice vector lengths are $4\pi / a\sqrt{3}$.

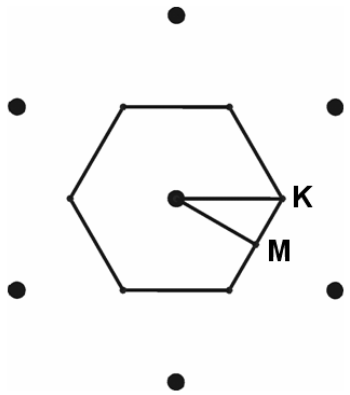

Figure 4.12 First Brillouin zone and edges of irreducible Brillouin zone for triangular lattice

4.4.2.1 Band structure of 2D PC structure

Let us assume that we have a square PC lattice made up of air holes. We can use the same derivation method that we used in 1D case in order to get the modes of the system. However, there are some differences. Our system is periodic in x-y plane but homogenous in z direction this time. We can again apply Bloch's theorem such that

$$\mathrm{H}_{\mathrm{k}_z,\mathrm{k}_{||},n}(r) = e^{ik_z z} e^{ik_{||}\rho} u_{k_z,k_{||},n}(\rho) \tag{4.24}$$

where ρ is any linear combination of real primitive lattice vectors of 2D square PC lattice, u is a periodic function in x-y plane, $k_{||}$ is bounded by the periodicity of the system, k_z is free to take any value.

There is a mirror symmetry along x-y plane since structure is invariant along x and y directions. This mirror symmetry makes it possible to separate modes into two, TE and TM modes. TE mode has E_x, E_y and H_z components while TM mode has H_x, H_y, and H_z components.

TE polarized mode basically has electric field component along the x-y plane while magnetic field component is normal to the plane. TM polarized mode has magnetic field along x-y plane and electric field is normal to the plane. Structures may support only TE, only TM or both TE and TM photonic band gaps. If TE and TM gaps overlap, that photonic gap is called complete photonic band gap.

Generally rod PC lattices in air have TM gaps while air PC lattices in dielectric support TE photonic gaps. Here is why: As we remember from the discussion in 1D PC band structure, electric field of the mode settles down on higher dielectric constant material in order to lower its frequency, and thus lower its energy. Such band is called dielectric band. Since upper bands must be orthogonal to first band regarding variational theorem, they stay mostly in lower index areas with higher frequency modes, namely air bands. For TM modes with PC rod lattice structure, electric field is normal to the plane and parallel to the PC rods. This field would desire to rest in higher dielectric regions, i.e. PC rods. Since field line is parallel to the rods, most of the energy of TM mode is concentrated in high dielectric regions. Furthermore, because upper bands will mostly stay in air region, frequency shift between the first dielectric band and the second air band will be high. This shift in frequency results with a large TM gap. However for the case of TE mode, there is generally no gap in this kind of lattice structure

since in-plane electric field of the mode must penetrate into air region because of vertical angle between the rods and the field. As a result, mode cannot concentrate its energy fully in dielectric region but just partially in air and dielectric material, which is not sufficient to create a photonic band gap.

For air hole PC structures, mostly supported photonic band gaps are TE polarized. In-plane electric field of TE mode can concentrate its energy in dielectric material along the x-y plane since field lines can find places to rest in higher refractive index material without penetrating into air region.

In general, while TE gaps prefer connected lattices with high dielectric constant, TM gaps are supported by isolated high refractive index areas.

In this thesis, PC hole lattices are preferred since InGaN/GaN multi quantum well light emitting diodes emit light primarily in TE polarization (around 75%~85%) [6][102][103][104][105] [106][107].

4.5 Photonic Crystals to increase extraction efficiency of LEDs

With the progress in light emitting diodes based on wide band gap III-Nitride semiconductors especially in the last decade, the gap for the wavelength of blue color has been filled in order to realize the white light. As a result, LEDs have become a strong candidate for solid state lighting technology. Since LEDs have low power consumption, long life time and smaller sizes, they can replace the conventional incandescent and florescent lamps used for general lighting purposes. Beside just lighting, light emitting diodes with high extraction efficiency are used in a variety of applications such as flat panel displays, printers, optical interconnects in computers. High brightness UV LEDs are sought for medical applications and chemical-biological agents detection. However while internal quantum efficiency (IQE) of InGaN/GaN quantum well (QW) is close to 100%, most of the light is lost due to high refractive index contrast between GaN (n=2.7) and air(n=1). Light is guided in the semiconductor and QW, finally absorbed by parasitically by defects and QW. As a result, only $1/4n^2$ (where “n” is the refractive index of the material) of light generated in QW can escape from the top of the device [78]. Several methods have been tried in order to enhance light output by enlarging the light escape cone such as surface texturing [1], modifying spontaneous emission by resonant micro-cavity [2], surface plasmons [3] and incorporating 2D photonic crystals [4][5][6][7]. These methods except PC structures are reported to enhance extraction efficiency by 1.5~2 times [9].

In this thesis, photonic crystals are studied in depth in order to increase the intensity of the light that comes out of the LED. In the literature, an average of intensity increase of 1.5~2.1 times by using 2D photonic crystal structures has been reported [8].

4.5.1 Total Internal Reflection and InGaN/GaN LED

By Snell's Law, light is refracted by banding away from the normal line while passing through high index material to low index material. There is a critical angle for incident light such that just smaller angles than critical angle can be transmitted to the other side but those with higher angles are totally reflected back from the high/low index interface. This phenomenon is called Total Internal Reflection (TIR) and is the major cause of low extraction efficiency of InGaN/GaN LED.

The shape of LED is planar as shown in Figure 4.13 below. Light is produced in the quantum well region. However, all the light generated in the QW cannot get out of the device because of TIR. Generally QW region has higher refractive index so that some of the light is guided in the well region, but majority of the light is guided in the plane of GaN LED since n_{GaN}=2.7 and n_{air}=1.

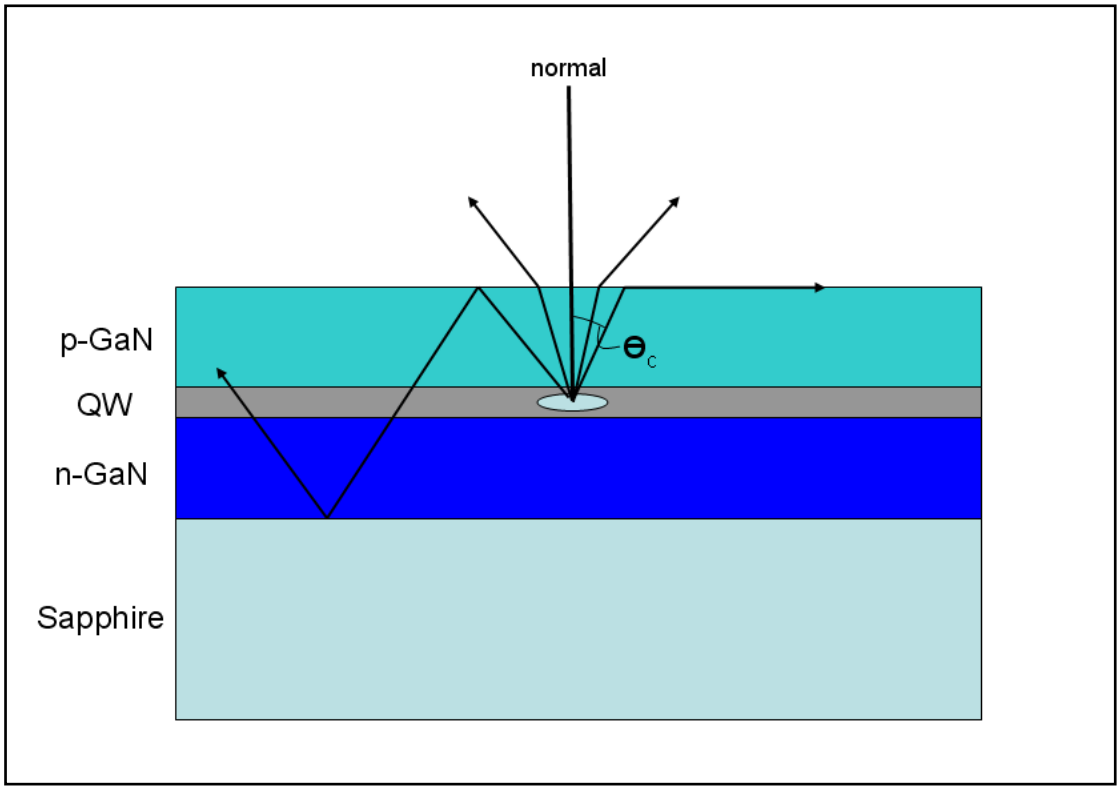

Figure 4.13 Light is totally reflected from the GaN-air interface for angles higher than critical angle

Let k_i and k_r be the wave-vector of incident and reflected light, respectively.

Then;

$$k_i \sin\theta_i = k_r \sin\theta_r \tag{4.25}$$

Let k_0 be the wave-vector of light in free-space. Substituting $k_i = n_i k_0$ and $k_r = n_r k_0$ into (4.25) gives the equation called Snell's Law;

$$n_i \sin\theta_i = n_r \sin\theta_r \tag{4.26}$$

To find the critical angle between interface of GaN and air, reflected angle is taken as 90^o;

$$n_{GaN} \sin\theta_c = n_{air} \sin 90^\circ$$

$$\sin\theta_c = (1)(1) / n_{GaN} \tag{4.27}$$

$$\theta_c = \sin^{-1}(1 / n_{GaN})$$

If n_{GaN} is 2.7, then θ_c is ~22^o. Wave vectors which have incident angles smaller than critical angle value of 22^o can get out of the device (also called light cone) and remaining will be totally reflected back into the LED layer, which is encapsulated and eventually absorbed in the GaN material. In total, just $1/4n^2$ of the light generated in the LED active region (QW) can escape from the top layer of GaN. This means that InGaN/GaN LED can only give 4% of generated light out if no alteration is done on the structure of the device.

Refractive index of an optical mode in dielectrics is defined as, $n=k_{||}/k_0$. In order a mode to be propagative in air, it should support the inequality $k_{||} < n_{air}\, k_0$. If the wave vector of the mode is in between $n_{air}\, k_0$ and $n_{GaN}\, k_0$, $n_{air}\, k_0 < k_{||} < n_{GaN}\, k_0$, mode is guided in GaN. If the mode has a wave-vector larger than $n_{GaN}\, k_0$, $n_{GaN}\, k_0 < k_{||} < n_{Sapp}\, k_0$, mode propagates in sapphire substrate [47].

In total 66% of light is guided in GaN, 22% of light is guided in sapphire and rest is extracted [66].

Several methods have been applied so far to increase the extracted light from higher index material to lower one, which are outlined previosly. These methods are mainly concerned on the geometrical shape of the device and light extraction enhancement relies on randomness and thus uncontrollable.

This thesis covers PCs as main light extraction tool for many reasons. First of all, beside the geometry of the structure, it is also important to take the light out of GaN as soon as possible since increase in propagation time of the light in the material ends up with an increase in parasitic absorption. Compared to other solutions, PCs help to decrease length of extraction of light so that less light is absorbed by the material. Secondly, emission profile of extracted light can be designed by designing the dimensions of PC structures. Therefore, PC approach provides ability to control the extracted light.

4.5.2 Designing Photonic Crystal Structure

Photonic crystals should be designed carefully in order to gain the maximum benefit in terms of light propagation control. Considered design elements are lattice type, lattice pitch, photonic crystal depth and filling ratio. By altering the structure of the PC lattice carefully, light propagation can be controlled.

Photonic crystals that are on the scale of the wavelength can be designed to increase extraction efficiency either by folding the guided light into leaky modes by principles of Bragg diffraction, band gap formation [108][109] and/or increasing internal quantum efficiency by so called "Purcell Effect" [110]. In band gap formation approach, guided mode emission is prevented and all light is radiated outwards [108]. In Bragg diffraction, PCs are used as diffraction grating, which couple guided modes into radiation modes [111][112].

4.5.2.1 Purcell Effect and Band Gap Formation

When lattice constant and depth of PCs are carefully designed, spontaneous emission rate and extraction efficiency can be enhanced due to band structure and nano-cavity formation. If light is encapsulated in a cavity with dimensions proportional to its wavelength, emission rate of the structure increases, which is called Purcell effect. Purcell enhancement factor is defined as [113][4];

$$f = \frac{3Q(\lambda / 2n)^3}{2\pi V_{cav}} \tag{4.28}$$

where Q is the quality factor, g is mode degeneracy, λ is wavelength, n is refractive index and V_{cav} is cavity volume. Here Q is around 10 to 30 at room temperature [114], n refractive

index is 2.7, λ wavelength is 400nm, V_{cav} cavity volume is 0.0024μm^3. So, for a single degeneracy, Purcell effect on extraction enhancement at room temperature condition is limited. Purcell effect gives better results at low temperatures but as the temperature is increased, non-radiative recombination effect hinders the performance [101].

In photonic band-gap approach, the structure is designed to be periodic in lateral directions with a band-gap specific to emission wavelength by adjusting lattice constant and filling ratio. As a result, emitted light from the active region cannot propagate in the plane of PCs and the only way that light can travel remains vertical direction. So light goes directly upward or downward with an increased extraction rate in the device.

In order both Purcell effect and band gap formation to work properly and efficiently, PC structures should be etched through the active layer. However, when the PC holes are penetrated into QW active layer area, effect of surface recombination comes to the scenery which decreases extraction efficiency by acting as trap centers for carriers, resulting in increase of non-radiative recombination rate [115]. Moreover, if PCs are etched through active layer, portion of quantum well area is decreased. As a result, light generation is degraded. When the ambient temperature is increased, Purcell effect is much less effective in extraction efficiency since quality factor decreases with increase in temperature because of parasitic recombination effects.

Moreover, these approaches necessitate very small structures to be fabricated which requires extensive time, high technology and small tolerance values. Structures with dimensions around 100 nm must be fabricated with a tolerance of less than 10 nm in order to control the propagation of light of 400 nm wavelength in a medium with n = 2.7 refractive index.

To conclude, since Purcell effect on the extraction efficiency can be neglected for a device working at room temperature and since band gap formation is very hard to realize especially for high refractive index and high energy band gap semiconductors in terms of fabrication procedure, these approaches are generally not used for researches regarding enhancement of light extraction efficiency. Band gaps are demonstrated on mostly membrane structures [75].

4.5.2.2 Bragg Diffraction

Since design and fabrication procedure is prone to making faults for band gap approach, as a more effective way to increase the light output intensity, Bragg diffraction approach is used.

With this approach, guided light in the material is out-coupled by PC structures that fold the light into leaky modes. Dimensions of diffraction PC lattices are larger than those of band gap method. Generally PC lattice pitches are at high Bragg orders [116].

In Bragg diffraction method, PCs are more likely to be used as gratings [75] [10]. Although guided modes are allowed in the structure, these modes are eventually outcoupled by the effect of diffractive properties of PC structure. Generally, PC lattice constants are designed such that diffraction regime is higher than first order.

PC increases extraction efficiency by diffracting guided modes in the material to air. Below in the Figure 4.14, schematic explanation can be viewed.

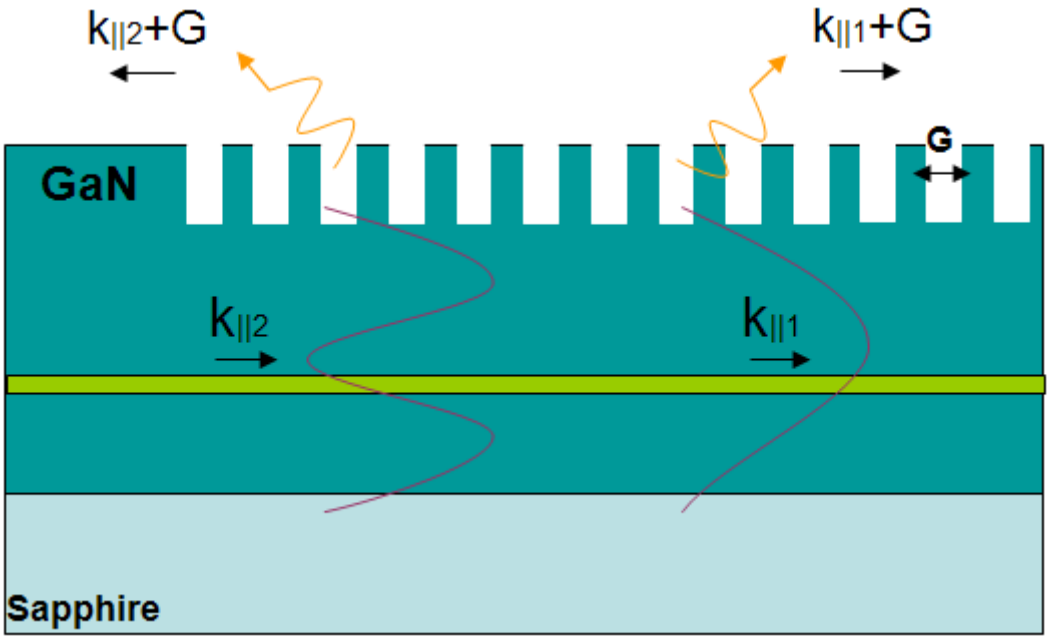

Figure 4.14 Schematic of the PC Bragg diffraction of guided modes in GaN

In order waves to radiate into air, in-plane wave-vector length β should be smaller than $n_{air}k_0$. Here, total **k** vector is square root of $\beta^2+\gamma^2$ where β is parallel component, γ is perpendicular component of **k.**

In the equations below, condition to be satisfied in order modes to out-couple from the dielectric material is outlined.

$$n = \frac{k_{\|}}{k_0} \qquad k_{\|} = nk_0$$

$$k_0 = \frac{2\pi}{\lambda_0} = \frac{\omega}{c} \qquad k_{\|} = n\frac{2\pi}{\lambda_0} = n\frac{\omega}{c} \tag{4.29}$$

$$\beta < k_0 n_{GaN} \sin\theta_c \qquad k_0 n_{GaN} \sin\theta_c = n_{air} k_0$$

$$\beta < n_{air} k_0 \qquad \beta < k_0$$

It is clear from these equations that parallel component of wave-vector in the dielectric should be smaller than wave-vector in free space. Since light propagating in the material with an incident angle higher than critical angle has larger in-plane vectors length than that of free space wave-vector, light is trapped in the dielectric material. By using PC structures, these in-plane wave-vectors are folded such that length of resultant in-plane wave-vector decreases so that $\beta_x - iG_0 < k_0$ condition is satisfied. Light folding by PC structures are explained in detail below.

As seen in the figure above, photonic crystals diffract light so that light originally guided in the GaN material couples to leaky modes and eventually radiates into air. Those guided modes can be described by their in-plane wave vectors $k_{\|}$ such that,

$$\beta_x = \frac{2\pi}{\lambda_0} n_{GaN} \sin\theta_x \approx \sqrt{\left(\frac{2\pi}{\lambda_0} n_{GaN}\right)^2 - \left(\frac{x\pi}{L}\right)^2} \tag{4.30}$$ [75]

where λ_0 is wavelength in free-space, L is total thickness of n and p GaN layers, n_{GaN} is refractive index of GaN, θ_x is propagation angle of x^{th} guided mode in GaN and **x** is the mode number.

Guided modes with in-plane wave vector $k_{\|}$ become Bloch modes with harmonics $k_{\|} - G$ in photonic crystals structure with periodic reciprocal lattice vector **G.**

In order PCs to fold the light wave-vector such that light is radiated into air, lattice constant a should satisfy the diffraction condition below,

$$\left|\beta_x - iG_0\right| < \frac{2\pi}{\lambda_0} \tag{4.31}$$

where i is integer which represents harmonic number of diffraction. $\beta_x - iG_0$ is length of wave-vector modified by PC reciprocal lattice vector **G**. As long as diffraction condition above is satisfied, Bloch modes are called leaky modes since modified in-plane wave-vector falls in escape cone. As a result, light radiates into air with an angle which can be altered by varying lattice constant as it propagates in the PC structure. In order diffraction condition to be satisfied and higher number of modes to be extracted from 2D PC structure, parameters such as wavelength, mode angle, PC depth, filling factor and lattice constant should be designed carefully. As the thickness of the GaN film is increased, number of guided modes increase [75]. In general, GaN based LEDs support up to tens of modes. Higher order modes are likely to be extracted more efficiently than those of lower order since higher order modes overlap more with PC structure. Increasing PC depth helps to increase overlapping and thus extraction efficiency.

4.5.2.3 Design considerations for PC structures fabricated in the scope of this thesis

Optical Bragg Scattering plays a dominant role in the description of PCs. In the literature it is reported that higher extraction efficiencies on LEDs have been achieved by using rather larger lattice constants [9]. The a/λ interval where most extraction efficiency achieved is stated to be between from a/λ =1 to a/λ =2 [10]. This result shows that Bragg scattering has more influence on extraction efficiency than that of band-gap approach and/or Purcell effect. Possible explanation for this is because tolerance in PC dimensions and anisotropy is extremely low in band-gap approaches. Requirement of PC structures to be etched through the active layer which results in non-radiative recombination and damaging of MQW active layer by plasma ions during dry etching process may be an additional cause. Because of the large surface to volume ratio, surface of PCs act as trap centers where non-radiative recombination occurs when they are etched through quantum well layer. In order to prevent this effect, PCs are separated from the active layer [72]. Furthermore, when PCs are etched through active layer, they reduce the area of the quantum well region which also results in reduction of radiative recombination.

Because of the surface recombination problem and dry etching induced damages in quantum well active regions, PCs in this thesis were not etched through active layer but shallowly etched for about 100 nm, which is 170 nm above from the InGaN/GaN multi quantum well.

Therefore, spontaneous emission control becomes much less effective and 2D PCs in this thesis act mostly like gratings.

Since diffractive properties of PC structures are of great consequence, lattice constants of photonic crystal structures have been kept larger than first order. According to two dimensional integral simulation results which are shown in the simulation section in chapter 6 in this thesis, most enhanced extraction efficiency was obtained by PC structure with lattice constant of 520 nm, which is higher than first order, and with r/a (ratio of radius of pc to the lattice constant of the PC) ratio of 0.25. Depth of the PC obtained from the simulation which gives highest extraction efficiency was 180 nm. However, because of ease of fabrication, PCs were fabricated to be at around 100 nm depth.

PCs fabricated in this thesis work have filling factor of 0.2~0.23 for square and triangular PC lattice types. Filling ratio was tried to be kept low since etched PC area causes extraction efficiency to decrease because of less dielectric resulting with lower current distribution and increased resistivity [67]. Furthermore, low filling ratio and higher lattice constants help to reduce the etch effects caused by RIE process and electron beam diffusion which occurs during e-beam lithography which both have detrimental results for p layer and quantum well region of the device.

High filling ratio of PC hole formation also increases the resistivity and it reduces the current injection level. This results in decreased light emission homogeneity. Furthermore, working temperature of the device goes up with an increase in high filling ratio since rate of heat transfer is lowered as a result of lower surface to volume ratio. Consequently, total surface area where convective and total dielectric material in which conductive heat transfer occurs are reduced.

Therefore, area of etching was decreased by designing PCs with a large period and low filling ratio.

In extracting light, propagation distance (extraction time) of light is another crucial parameter. As the propagation time increases in the material, extraction efficiency decreases due to absorption of some part of the modes because of trap centers such as defects and also the absorptive property of GaN. Re-absorption of the emitted light by active layer may also be a problem. However, probability of re-absorption is declared to be less than 20% [117]. Absorption coeeficient of GaN is stated to be around $\boldsymbol{\alpha} = 3\text{x}10^{4}$ cm^{-1} at room temperature [118]. This means when light propagates a distance of $1/\boldsymbol{\alpha} = 0.33$ um, energy of the light is

decreased by 1/e. If there were no absorption in the medium, all light can be out-coupled by Bragg scattering PCs [114]. So, it is important to diffract light as fast as possible.

PCs are good at extracting light in short propagating lengths. Therefore, absorption issues are less pronounced for PC method with respect to other geometrical approaches which are based on mostly random scattering [8]. Extraction length for all modes in GaN is expected to be in between 60~200 microns [66] [76][6]. In the Figure 4.15 below, extraction length of one of the higher order TE modes which is common in thick GaN structures versus PC fill factor and PC depth is given.

From the figure above, extraction length is about 170~200 nm for a PC structure with depth of 100 nm and filling factor of around 0.2. Therefore, neglecting absorption effect, 200 nm PC structure is sufficient to extract all the guided modes above light line.

Light line has in-plane wave-vector of k_0 and frequency of ck_0. In reduced frequency versus reduced wave-vector band diagram, modes above the light line are called leaky modes and they eventually leaks out from the dielectric [117]. Their energy is not confined into the high index material. However, below the light line, modes are confined in the dielectric and bandgaps can occur here. Pc periodicity folds the guided mode in the material (which stays under the light line) to leaky modes over the light line. This PC folded mode leaks as Bragg scattered light. In a GaN dielectric, all modes above reduced frequency of 0.66 ($a/\lambda > 0.66$) are out-coupled as Bragg scattered light [9][119]. In PC design of this thesis, a/λ raito is held at 1.3, where modes are above light line so that they are leaky and scattered out by PC structure. Furthermore, at this reduced frequency, bloch mode wave-vector versus frequency dependency is almost flat which means that frequency of the mode does not change with in-plane direction among dielectric and speed of light is mostly decreased.

These circumstances results in enhanced coupling and increased interaction of the mode with the PC structures which ensure enhanced extraction efficiency.

Below in the Figure 4.16, there is band diagram of two dimensional triangular PC lattice holes structures on GaN dielectric. Light line and mode at $a/\lambda = 1.3$ are also shown.

In the literature, extraction enhancement range is stated to be between 1.5~2.1 [120][8][121] for electrically pumped photonic crystal devices. However, regarding the case of optical pumping, extraction efficiency increases by 10 to 20 times [10][9].

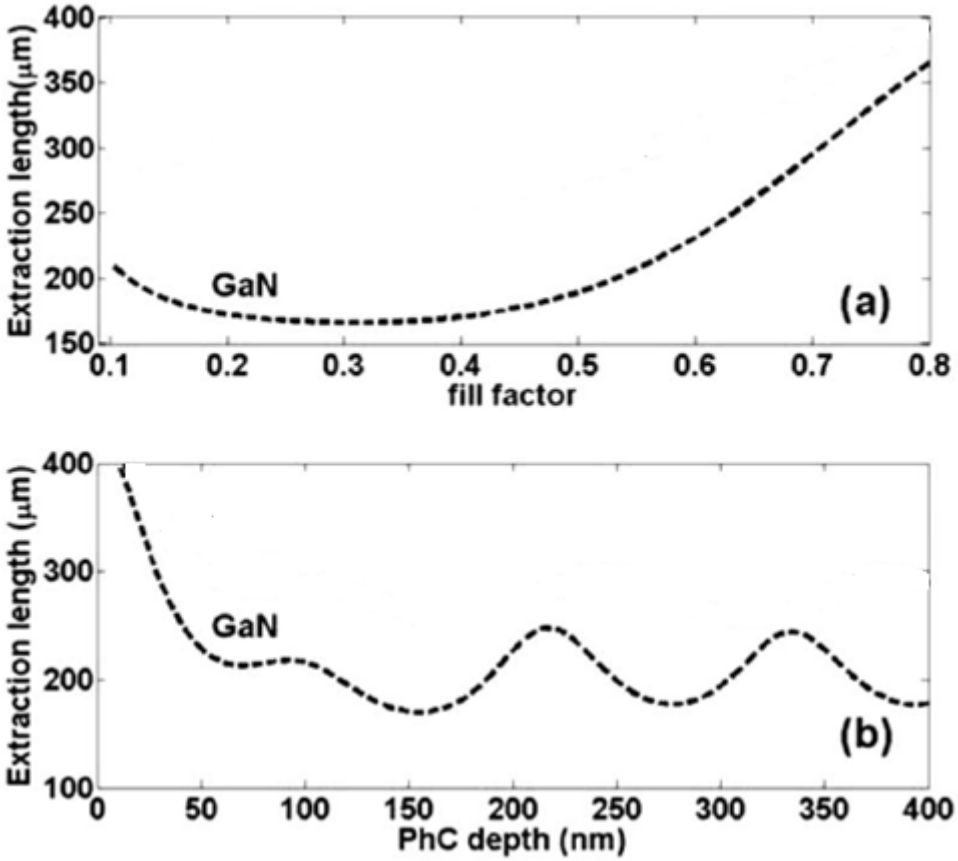

Figure 4.15 PC extraction length with respect to fill factor and PC depth for TE9 mode (79)

In this thesis work, InGaN/GaN MQW LEDs were patterned by Bragg PC structures, which were pumped with electrical injection. Power measurements are in agreement with finite difference time domain (FDTD) and integral method simulations, which gave about 2.2~2.6 times extraction enhancement.

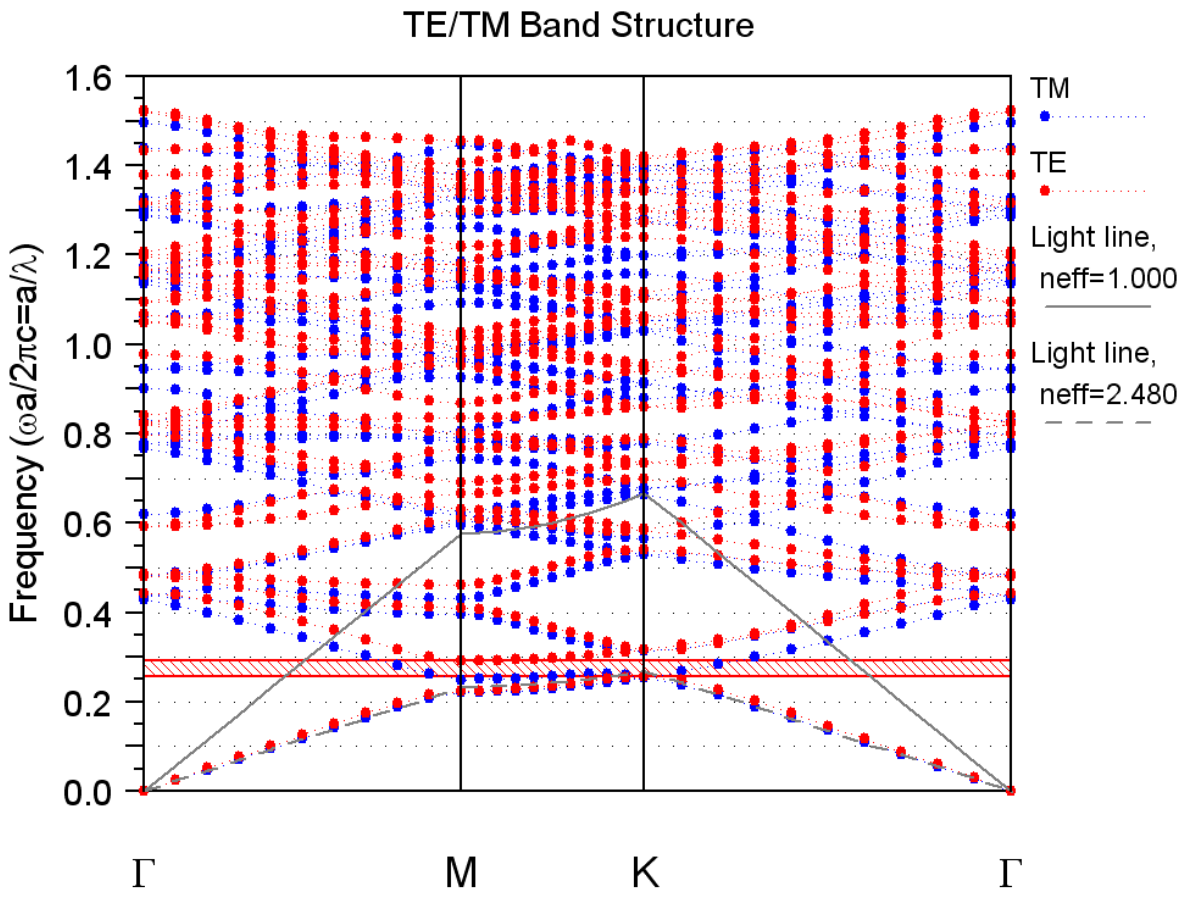

Figure 4.16 Photonic Band Gap Diagram for TE and TM modes for triangular lattice hole PC structure in GaN with r/a = 0.5

Chapter 5

5. Characterization, Processing, Fabrication

5.1 Etching of GaN

Proper etching of GaN is crucial for LED and PC processing. Regarding LED processing, in order to make metal contacts and pads onto n layer and p layer of GaN without causing shortage between the contacts, mesa structure should be etched as vertical as possible. Besides, in PC processing, formation of photonic band-gaps and Bragg diffraction planes are quite dependent on dimensions of the PC. Since tolerance is low, PC side-wall structures must be etched as much vertically as possible.

Dry etching is a preferred processing method for III-Nitrides and especially for GaN over wet etching since it has advantages such as high selectivity, precise etch depth control, smooth surfaces and high anisotropy. Furthermore, since GaN is one of the most robust materials known and therefore highly resistant to chemical solutions, wet etching is not a common method. It is not possible to have exact control on etch depth in wet etching and undercut is an important issue.

Dry etching is a combination of physical and chemical etching. Therefore, advantages of both methods can be used together. In this type of etch, no wet solutions are used but gases to etch the target material. After gases form plasma in the chamber, chemical reactions start to occur on the surface of the target material where ions continue to etch the material physically by momentum transfer at the same time.

Plasma etching is purely a chemical etching. In chemical etching, etch rates are controlled by free radicals generated in the plasma. Those free radicals diffuse into and are adsorbed by the target material to be etched. After chemical reaction comes to an end on the surface, volatile and non-volatile byproducts are formed. Non-volatile byproducts which forms a thin film on the target are etched physically by ions (sputter effect) while volatile ones are thrown out by

vacuum pumps. One draw-back of chemical etching, which is undercutting and/or isotropic etching, can be reduced by directional physical etching of ions in dry etching process.

Dry etching is not crystallographic etching as it is the case in wet etching. Therefore, etch rates does not change dreadfully with respect to different atomic plane directions. However, one should be careful while choosing proper mask material for selectivity purposes. There should be high selectivity between the target material and the mask. So that, although active ions and plasma attacks on target and mask, target will be etched more effectively with negligible undercut. As a result, by using dry etching method, vertical side-walls can be achieved; given that using proper chemicals and mask under optimized physical conditions such as power, flow rate and pressure.

One adverse effect of dry etching is contamination and alteration of stoichiometry for GaN target material. After an RIE etching process, hydrogen concentration has been found to be 10^{20} cm^{-3} in InGaN layer. This hydrogen contamination causes Mg to be passivated and therefore increase the resistance of the device. Annealing GaN may help to reduce this passivation effect.

Dry etching systems available for III-Nitrides are reactive ion etching (RIE), electron cyclotron resonance etching (ECR), magnetron reactive ion etching (MIE) and inductively coupled plasma (ICP). Among these, RIE system which was also used for the processing of GaN material in this thesis work has the lowest anisotropy degree and lowest etch rates. This is mainly because of the lower plasma densities and higher chamber pressures. General etch rate values with RIE using chlorine based gases is around 30-40 nm/min while this value can be up to 700 nm/min for ICP [122][123].

In ICP system, plasma density can be increased with lower DC bias on the wafer. Therefore higher etch rates and improved surface characteristics can be achieved by this system [124].

In this thesis work, RIE was used as the dry etching method. Below in Figure 5.1 there is the schematic of an RIE system.

5.1.1 Gases that are used in plasma for etching GAN

Basically chlorine based gases have been being used for etching GaN with RIE and ICP systems. By mixing chlorine with other gases, etching rate of GaN can be controlled and vertical sidewalls and high etch rates can be achieved.

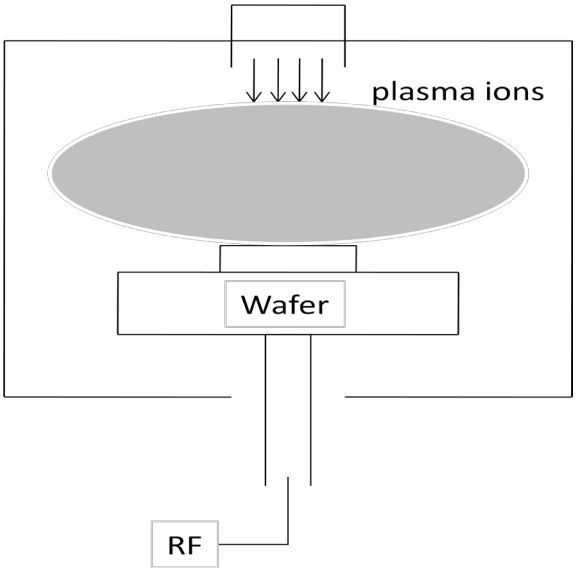

Figure 5.1 Schematic of RIE system

Fluorides are also used for etching GaN since chlorine based gases are very hazardous and corrosive. However, non-volatile byproduct GaF_3 is formed on the surface during etching process which decreases the etch rate.

Cl_2 /SF_6, Cl_2/Ar, Cl_2/N_2, BCl_3/Cl_2, H_2/Cl_2, SF_6, CHF_3 and CF_4 are some of the gases that are used for dry etching GaN.

In this thesis work CCl_2F_2 gas, which is also known as Freon, was used.

5.1.2 Effect of etching on device performance

Dry etching of GaN layer has some draw-backs such as damaging active layer, increasing p layer resistance and decreasing current injection.

RIE etch may damage the quantum well layer and also the top p++ GaN layer which decreases extraction efficiency and causes carrier traps [66]. High turn on voltage encountered in this thesis work and difference between the result of simulations and measurements may also caused by damaging of p++ and quantum well region during RIE etch.

5.2 GaN Etching Characterization

In order to etch GaN, dry etching technique reactive ion etching (RIE) system was used. CCl_2F_2 was used as etchant gas. Etching was optimized to have vertically etched side-walls. On the other hand, etching rate optimization was not the priority. Number of etch processes were tried by changing one variable at a time while holding other variables constant. Samples were etched for 20 minutes. Etched samples were examined under SEM after cleaving. RIE parameters and the range where characterization was done are outlined in Table 5.1 below.

Pressure (ubar)	1 - 8 – 64
Power (W)	100 – 200 – 400
Flow Rate (sccm)	10 – 20 – 40

Table 5.1 RIE GaN etch characterization parameters

Nickel, Chromium and 5214E photoresist were used as masks for RIE etch process. Nickel was hard to remove and disperses on the edges GaN surface under RIE plasma as seen from in Figure 5.2 below.

Chromium did not disperse on the edges as Nickel and showed better masking performance. On the other hand, it induced zigzag structures on the etched side walls which were mainly caused by RIE bias and metal lift-off process as seen in Figure 5.3.

5214E photo-resist was another alternative mask layer for etching of GaN. However, stepped patterns may occur if photo-resist is used without post-bake. Generally resist thickness near the edges are less than that of middle surface. If the resist is not post-baked after developing, it cannot show enough resistance in Freon plasma and etched. This is the case in Figure 5.4.

Therefore, in characterization process Chromium and photo-resist are continued to be used as masking layers.

Starting point was set to be pressure of 8 ubars, power of 200 W and flow rate of 20 sccm. These values had been used for a long time by researchers in clean-room, however they were not the optimum values for vertical side-wall etching.

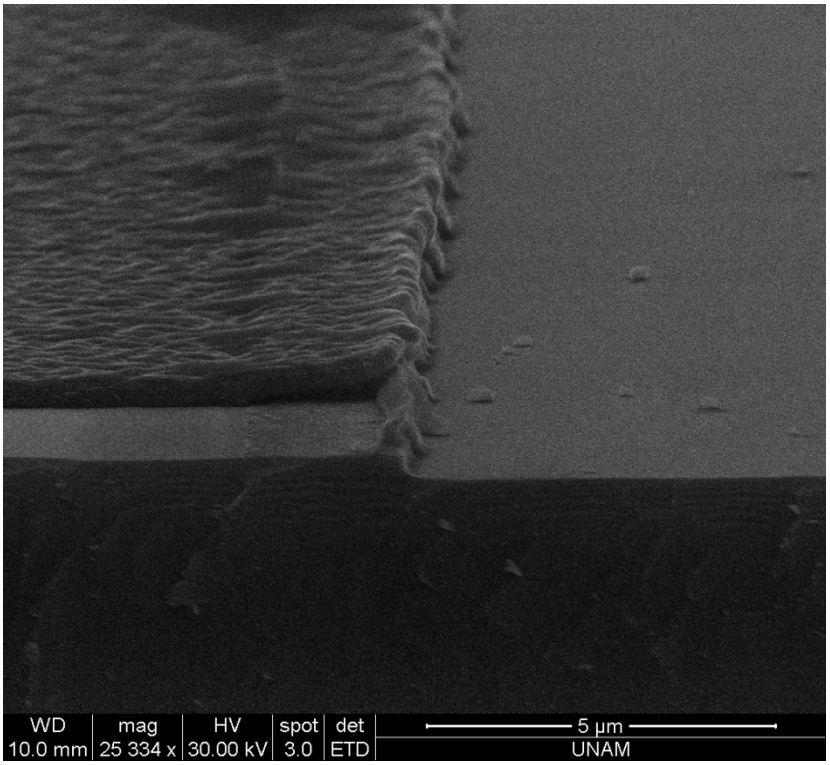

Figure 5.2 Nickel as etching mask

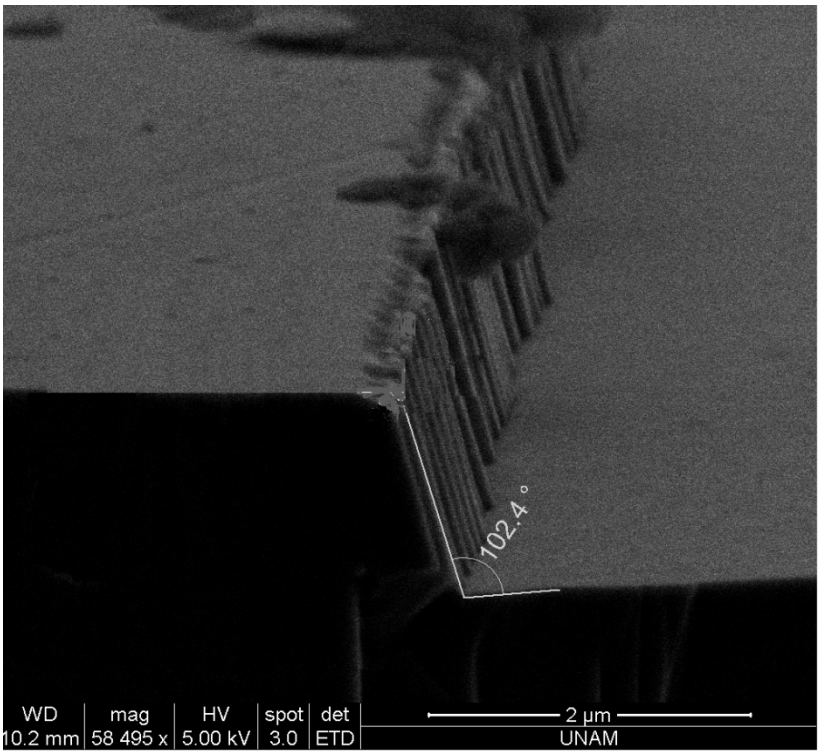

Figure 5.3 Chromium as etch mask

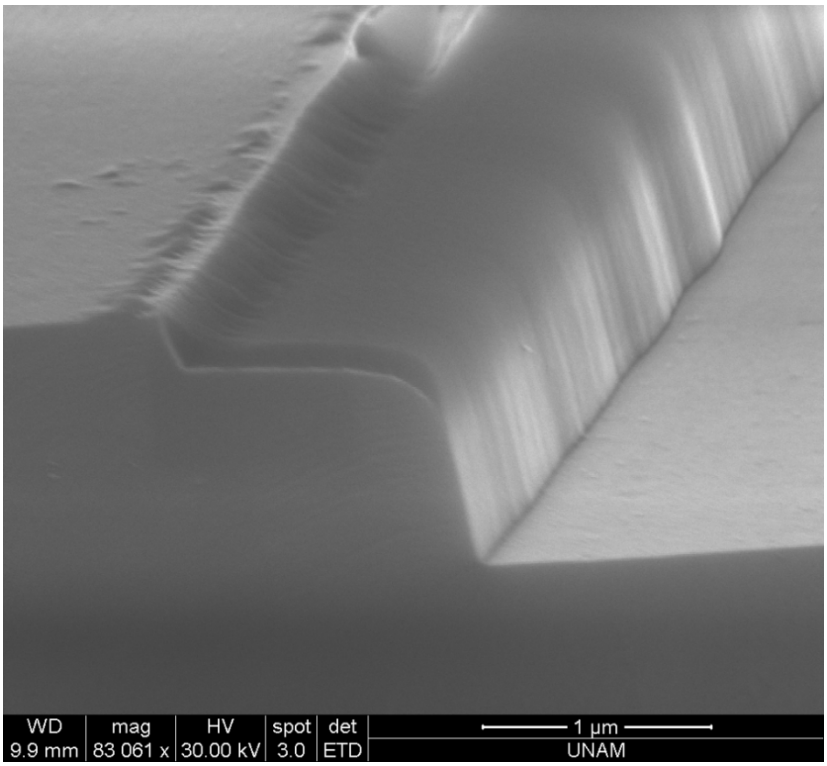

Figure 5.4 5214E photo-resist as etchant mask

This starting condition gives side-wall angle about 105° with an etch rate of 40 nm/min. Final etched GaN can be seen in Figure 5.5.

First, power was varied to see the effect on the etched side-wall angles. As a starting point, power was set to be at 400 W. However, RIE system in clean room did not support that high power rate. Maximum power that can be used was 240 W. Therefore, power was adjusted to be at 240 W. All other variables were kept constant. Chromium was used as mask. However, even this much power caused GaN to be deteriorated as seen from SEM picture below in Figure 5.6.

Afterwards, power was decreased to 100 W and the result was examined under SEM. Again Chromium was used as a mask. Side-wall angles were decreased by 3° to 9° with respect to the starting point. GaN etching rate was calculated to be 35 nm/min. Zig-zag patterned structures occurred from lift-off process of Chromium in Figure 5.7.

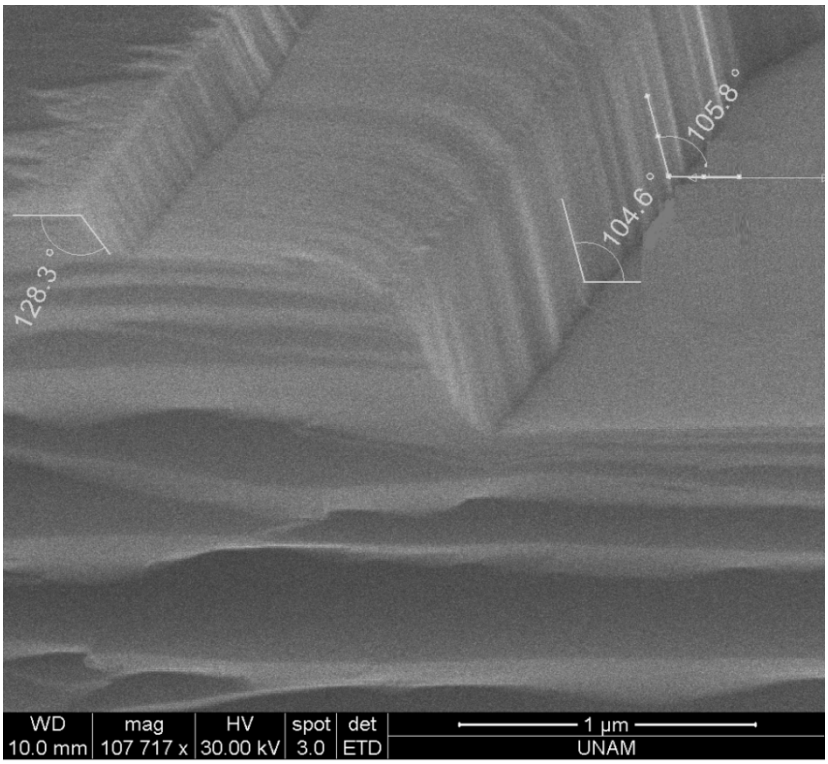

Figure 5.5 Etching starting point: 8 ubar, 200 W, 20 sccm

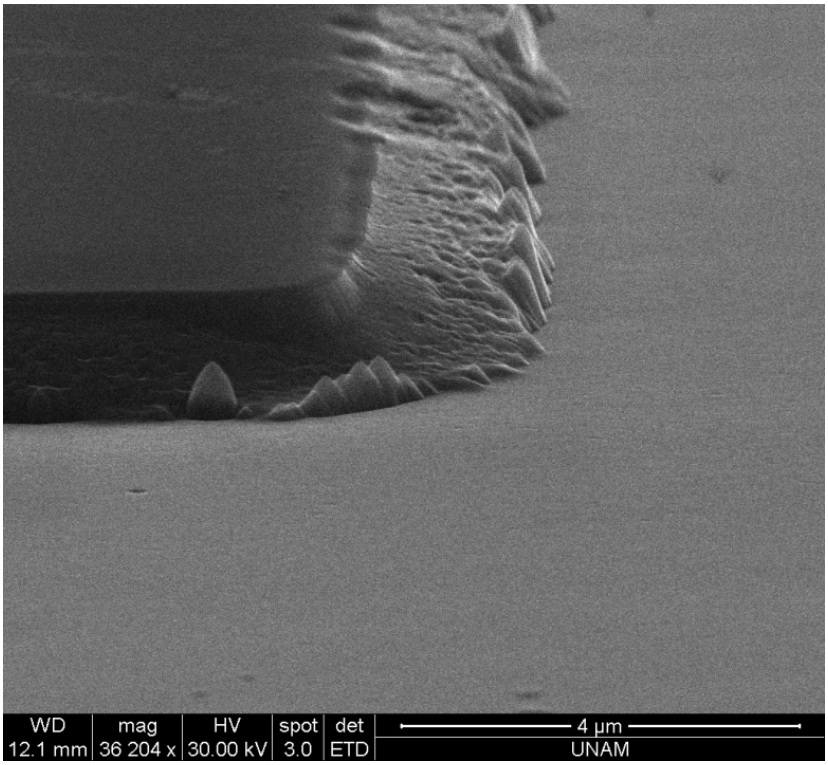

Figure 5.6 At max power of 240 W

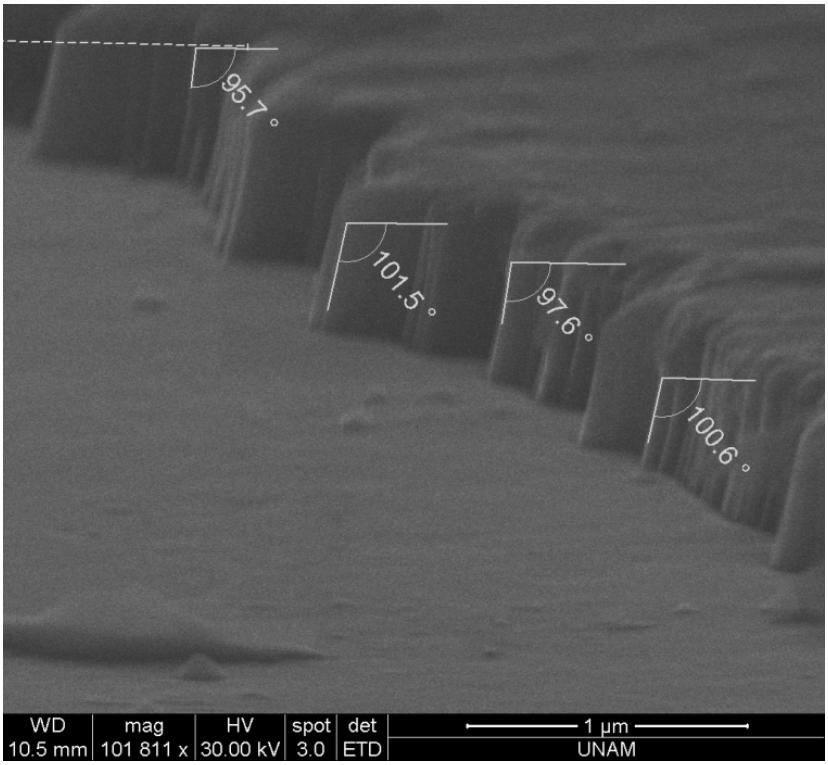

Figure 5.7 100 W power

Because of capacity of the RIE system, lowest power value attained was 100 W. As a result of the first stage of characterization process, lower power values were found to give better results.

As a second process variable, amount flow rate was chosen. First, it was tried to increase flow rate to 40 sccm but RIE system did not allow any flow rate higher than 30 sccm for Freon gas. So, upper limit was set as 30 sccm. Increasing flow rate decreased the side-wall angle too, about 3° though. Side-wall angles were found to be around 102°. Under 8 ubar, 200 W and 30 sccm, etch rate of GaN was calculated to be 57 nm/min. This was the highest etch rate obtained from the RIE system during characterization process.

Then, flow rate was decreased to 10 sccm. However RIE system did not stay stable at this flow rate. Although power was set to be at 8 ubars, it went down to 4.6 ubars at first seconds after the plasma was formed. At third minute, pressure was around 4.3 ubars and stayed stable at this value. This time side-wall angle was worse than starting point. Average side-wall angle was around 108° ~ 110°. Etch rate of GaN was calculated to be 40 nm/min.

As a final variable, pressure values were altered. It was planned firstly to increase pressure to 64 ubars. However, system again did not stay stable and pressure rapidly fell down to 56 ubars when the plasma was formed. It then started to increase slowly, first to 56.6 ubars at the second minute, to 59.1 at fifth minute and to 61.3 ubars at eleventh minute and stayed constant at this value.

Surface was found to be deteriorated again, as it was the case for high power. Etch rate was calculated to be 40 nm/min. Final structure is seen in Figure 5.8

Afterwards, pressure was adjusted to 1 ubar. System stayed stable after first minute at 1 ubar, 200 W and 20 sccm. At the end of 20 minutes etch process, SEM results were found to be around 103°. GaN etch rate was calculated to be 33 nm/min.

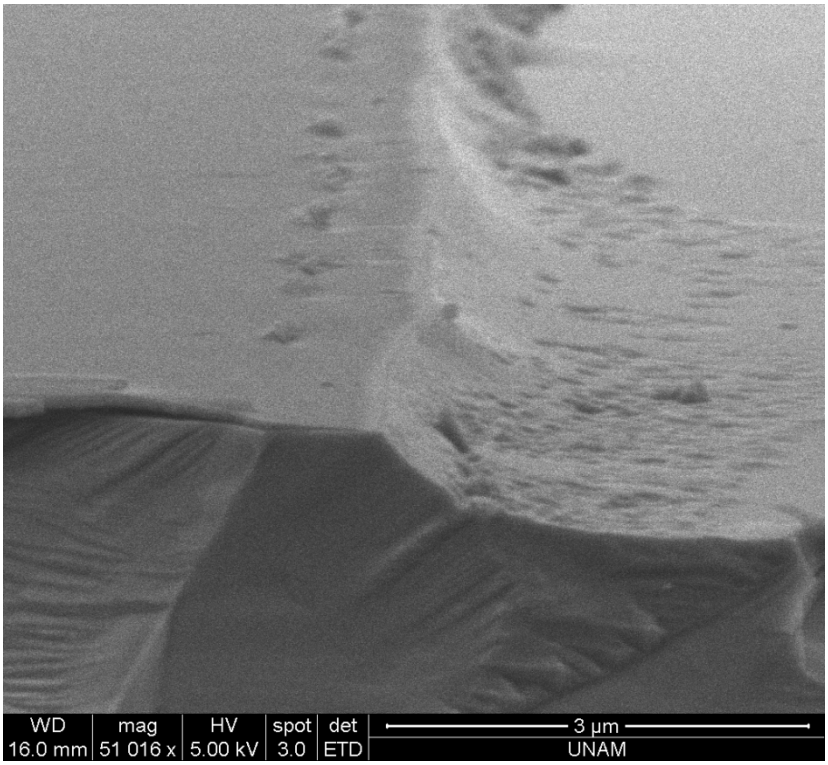

Figure 5.8 Max pressure

At the end of the characterization process, it was concluded that decreasing power and pressure, and increasing flow rate gave better side-wall etching results. Therefore, as a final step, RIE system was tested with pressure, power and flow rate set at 1 ubar, 100 W and 30 sccm respectively. As a mask, 5214E photo-resist was used.

Results were as expected. Side-wall characteristics were improved by more than 6°, to be around 98° ~ 100° as seen in Figure 5.9. However, GaN etch rate was reduced considerably, down to 20 nm/min which can adversely affect the etching selectivity during photonic crystal fabrication.

Therefore, it was decided to use the RIE parameters of 8 ubars, 100 W, 20 sccm, which also gives approximate etching characteristics with parameters of 1 ubar, 100 W and 30 sccm.

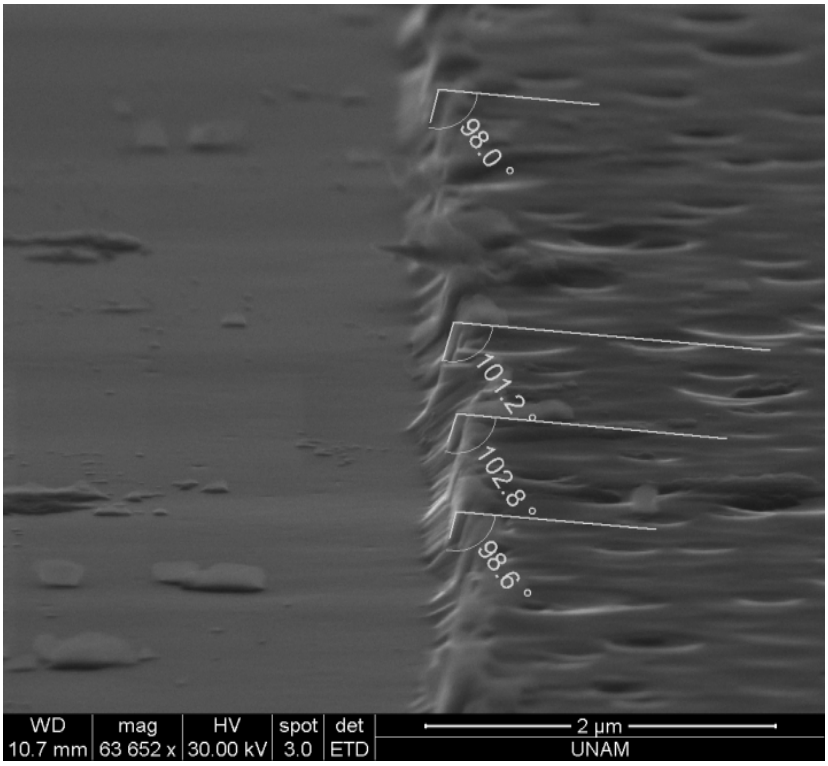

Figure 5.9 Optimum etching parameters, 1 ubar, 100 W, 30 sccm

Below in the Table 5.2 are stated which summarizes all the etching characterization process.

Pressure (ubars)	Power (Watts)	FlowRate (sccm)	EtchRate (nm/min)	Side-wall Degree (degrees)
8	200	20	40	103-105
8	240	20	50	110-115
8	**100**	**20**	**35**	**98-102**
8	200	30	60	100-105
4.3	200	10	40	105-110
60	200	20	40	115-120
1	200	20	30	100-110
1	**100**	**30**	**20**	**98-103**

Table 5.2 Etch rates and side-wall angles

5.2.1 RIE etching recipes

During thesis work, RIE etching processes regarding photoresist 5214E, SiO_2 and GaN were characterized. Recipes are outlined below in Table 5.3.

Used gas	Ethed material	Flow rate (sccm)	Power (W)	Pressure (ubar)	Etch rate (nm/min)
CHF_3	SiO_2	20	100	26	**23-25**
CCl_2F_2	GaN	20	100	8	**32-35**
CCl_2F_2	SiO_2	30	100	1	**11**
CCl_2F_2	SiO_2	20	100	8	**20**
CCl_2F_2	AZ5214E	20	100	8	**30**
CHF_3	GaN	20	100	26	**5**

Table 5.3 RIE etch recipes

5.3 LED Processing

InGaN/GaN LED wafers were grown in collaboration with University of California Santa Barbara (UCSB). There are two wafers with different grown structures. Layer structures and growth conditions of LED wafers can be found in Chapter 2 and Chapter 3.

Regarding this thesis work, these as grown LED wafers were processed and PC structures were incorporated in LEDs.

Before starting processing the wafers, p layer activation was done. During high temperature growth of GaN layer, p type doing material magnesium (Mg) and hydrogen (H) establishes bonding and this causes Mg to be passivated. For p layer activation, this bond should be broken. After the p-layer activation, processing of LEDs started by mesa etch, and continued with p-metal deposition, annealing of p-metal, n-metal deposition and pad metal depositions. In the subsection below, LED processing is explained in detail.

5.3.1 p-dopant activation

Mg atoms which give GaN p type property are passivated by H atoms during growth of GaN at high temperature. In order to active the p layer of the GaN, wafer should be annealed under

Nitrogen (N_2) and Oxygen (O_2) environment in a controlled manner. Reason for using O_2 is to lower annealing temperature. Because indium compounds in quantum well region are decomposed at high temperatures, temperature level is a critical point. Since Bilkent clean room facilities had not the capability at that time, annealing process was done with collaboration of METU laboratories.

In p activation, wafer should be annealed by rapid thermal annealing (RTA) system at 700 °C under N_2/O_2 environment for 15 minutes. Since RTA system in Bilkent Univeristy was not capable of making the process for 15 minutes under O_2 environment, annealing was made in a resistive furnace that can be heated up to 1100 °C in Middle Eastern Technical University (METU) laboratories. However, since it was not possible to increase temperature in the resistive furnace rapidly, wafers were put into furnace after desired temperature was obtained. Furthermore, since it was not possible to cool down the sample rapidly but in a controlled manner by resistive furnace, sample was hold in the outside of the chamber at 70 °C for a while and taken out to room temperature. Details about the flow rates are given in the Table 5.4 below.

Time needed to warm up furnace up to 700°C	75 mins
Flow rate ratio of N_2:O_2	7:1
Anneal time at 700 °C	15 mins
Cool down time at 70 °C	30 mins
Cleaning of samples under O_2 RIE plasma	5 mins

Table 5.4 Details about annealing of p layer GaN

5.3.2 Mask Layout of LED and photolithography recipe

During processing LEDs, photolithography mask below in Figure 5.10 Photolithography LED mask was used. This mask was designed by my colleague Mustafa Urel.

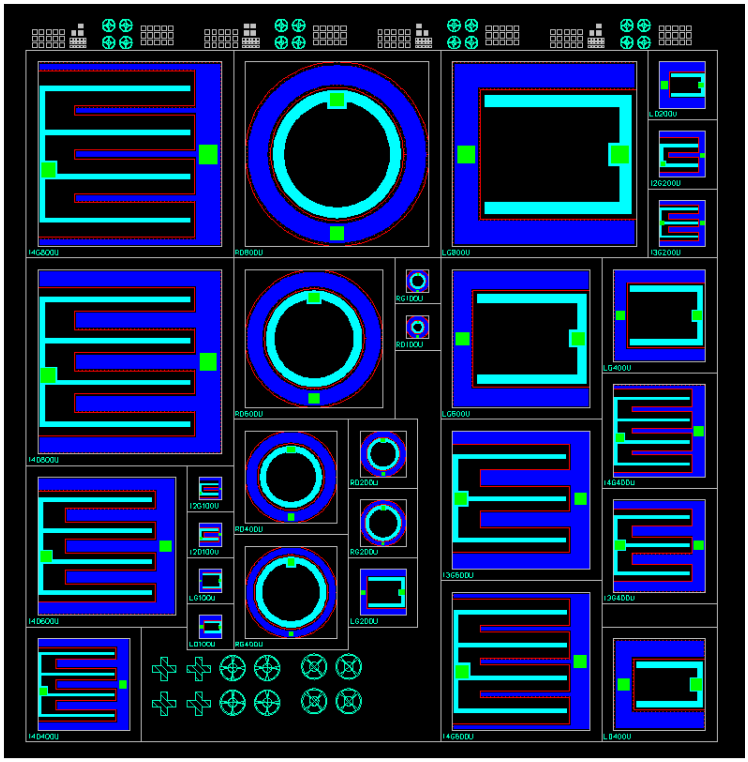

Figure 5.10 Photolithography LED mask

There are three different geometries of LED chips with four different dimensions. Ring shaped, U shaped and inter-digitated geometries with dimensions of 200 um x 200 um, 400 um x 400 um, 600 um x 600 um, and 800 um x 800 um LEDs are spreaded on the mask layer. Mask consists of four different areas which are used during mesa etch, p-metal deposition, n-metal deposition and deposition of pad metals. Colored regions in the mask were coated with chromium in order to prevent the resist under those areas to be exposed by ultra-violet (UV) light during optical lithography process.

AZ 5214E photo-resist was used during lithography of LED processing. This resist can be used as both positive and negative resist by changing exposure dose and development procedure. In positive resist, exposed area under UV source is dissolved in developer. On the other hand, in negative resist, exposed area gets hardened and unexposed area is dissolved during development process. Exposure energy used in this thesis work was 4 W/cm^2.

In order to use AZ 5214E as positive resist, resist is exposed for one time after it is pre-baked. Then it is developed and rinsed in distilled water (DI). Developer used was AZ400K with ratio of 1 : 4 (400K : DI). In order to harden the resist for subsequent dry etching process, it is post-baked. At 5000 rpm, resist thickness was around 1.2 microns. Below in the Table 5.5 is

the positive resist development recipe that was used during processing of LEDs in this thesis work.

	Time (sec)	Temperature (°C)	Speed (rpm)
HMDS	30		5000
Spinner	40		5000
Pre-bake	50	110	
Exposure	50		
Development	40		
Post-bake	120	110	

Table 5.5 Positive resist recipe

For using 5214E as negative resist, resist is exposed for two times. First exposure lasts relatively less than second one. After the first exposure, resist is baked. Second exposure is flood exposure such that all the resist area is exposed without using a mask. Below is the recipe for negative resist process in Table 5.6. Negative resist process was only used for p-metal lithography during LED processing stages.

5.3.3 LED Processing Flow of LED wafer

During processing of LED wafers, AZ5214E photoresist was used as a resist for photolithography steps, and as a masking layer for RIE dry etching steps. When the resist was to be used as masking layer, it was post-baked prior etching in order to harden the resist to prevent excessive eroding. Etch rates of various materials under CCl_2F_2 and CHF_3 are given in Table 5.3 in this chapter.

During LED processing throughout this thesis work, first mesa of LED device was formed using positive resist lithography and RIE GaN etch step.

	Time (sec)	Temperature (°C)	Speed (rpm)
HMDS	30		5000
Spinner	40		5000
Pre-bake	50	110	
1st Exposure	35		
Bake	120	110	
2nd Exposure	57		
Development	40		

Table 5.6 Negative resist recipe

Then, p metal layer was formed using negative resist recipe, evaporation of p-metals (Palladium-Pd and Gold-Au) and subsequent lift-off process. However, it should not be forgotten to dip the wafer into HCl:DI with a ratio of 1:3 prior p metal deposition in order to wet etch the thin oxide layer formed on p layer GaN at room temperature. This step reduces contact resistance. Details about evaporation process are given below in Table 5.7.

	Deposition rate (A°/sec)	Thickness (nm)
Palladium	1	5
Gold	1	5

Table 5.7 P-metal evaporation

5 nm Pd and 5 nm gold metal layers were deposited on p layer of GaN on top of InGaN/GaN MQW LED device. P-metallization ended up with lift-off process.

After p metal deposition, wafer was annealed in RTA system at 500 °C for 3 minutes in order to make contact layer between p-metal and p-type GaN Ohmic. This is a crucial step for reducing the contact resistance of the device.

Next step was to deposit n-metal on the n-layer which had been etched during mesa formation. Used n-metals were titanium, aluminum and gold with thicknesses of 20 nm, 200 nm, and 300 nm respectively. Again, one should remember to use HCl:DI to etch the oxide layer that might have been formed during RTA process and subsequent etching and lithography processes. Details about n-metal evaporation is given below in Table 5.8.

	Deposition rate (A°/sec)	Thickness (nm)
Titanium	2	20
Aluminum	5	200
Gold	5	300

Table 5.8 N-metal deposition

After the evaporation process, metals on the resist area were lifted-off by agitating the wafer in acetone.

As a final step, pad metals were evaporated on to p and n metal contact layers that were deposited before. Pad layers were thicker than metal contacts since electrical potential would be applied by touching probes on to pad metals. Pad metals evaporated were titanium and gold with 20 nm and 200 nm thicknesses respectively. After evaporation, lift-off process was required. Below in the Table 5.9, details of evaporation of pad metals can be obtained.

	Deposition rate (A°/sec)	Thickness (nm)
Titanium	2	20
Gold	5	300

Table 5.9 Pad metal deposition

Complete flow of the LED processing and picture of fully processed LED can be found below in Table 5.10 and Figure 5.11

P dopant Mg activation
Resistive furnace, 700 °C
O2 : N2 1:7
Mesa Formation & Mesa Etch
Aceton 2 mins agitation
Isopropan 2 mins agitation
Drying with N2 low pressure flow
Positive resist recipe, Table 5.5
GaN etch recipe, 23mins, Table 5.3
Aceton resist removal, 2 mins agitation
Isopropan 2 mins agitation
Drying with N2 low pressure flow
P metal deposition
HCl:DI 1:3 dip
DI rinse for 40 secs
Drying with N2 low pressure flow
Negative resist recipe, Table 5.6
Evaporation of Pd-Au, 5 nm-5 nm, Table 5.7
Aceton, Lift-off
Iso-propan rinse
Drying with N2 low pressure flow

P metal annealing
RTA at 500 °C, 3 mins
N2 environment
N metal deposition
HCl:DI 1:3 dip
DI rinse for 40 secs
Drying with N2 low pressure flow
Positive resist recipe, Table 5.5
Evaporation of Ti-Al-Au, 20 nm-200 nm-300 nm, Table 5.8
Aceton, Lift-off
Isopropan rinse
Drying with N2 low pressure flow
Pad metal deposition
Positive resist recipe, Table 5.5
Evaporation of Ti-Au, 20 nm-300 nm, Table 5.9
Aceton, Lift-off
Isopropan rinse
Drying with N2 low pressure flow

Table 5.10 LED processing overview

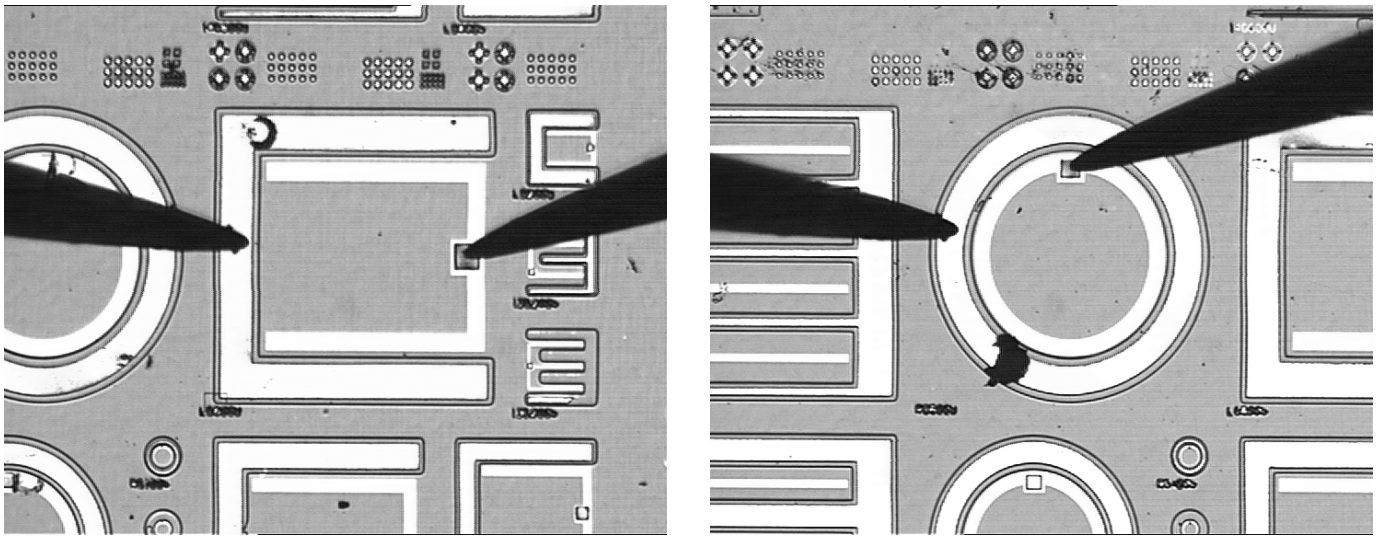

Figure 5.11 Snapshots from fully processed LEDs

5.4 Photonic Crystal Characterization and Fabrication

Photonic crystals are periodic structures that consist of lattice arrays with different dielectric constants. Since these structures are designed to guide the light, their deimensions should be in wavelength scale.

The PC structures designed in this thesis have 260 nm diameter holes with 520 nm lattice periods. Resolution of optical contact photo-lithography is around one micron and it is not possible to make these sub-micron features by photo-lithography. Rather, high end nano-patterning and nano-writing techniques such as focused in beam patterning (FIB), electron beam induced deposition (EBID), and electron beam lithography (e-beam) systems are used to fabricate nanometer sized structures.

In order to fabricate PC structures and to characterize the PC fabrication parameters, I tried FIB, EBID and e-beam lithography systems respectively.

5.4.1 FIB Trials

FIB system is generally used in material science for patterning, sputtering, milling and deposition for feature sizes down to nano-meter scale. Its working principle is almost the same with that of scanning electron microscope (SEM). However, FIB system uses focused beam of Gallium (Ga) ions instead of electrons onto the substrate. Ga ions formed in the

system are accelerated under potential and focused on to the material with the help of electrostatic lenses. Since Ga ions are much larger than electrons, they have enough momentum to break the bonds of the target sample. As a result, specific site where Ga ions are hit can be sputtered or milled.

Since it is a maskless process and relatively easy to pattern PC structures in one step, FIB was firstly tried for PC fabrication.

Ga ions were accelerated by 30 kV potential and exposed on to InGaN/GaN LED p layer surface. Beam current was around 100-300 pA. Patterned area of PC was 30 um x 30 um. As dwell time of Ga ions hitting on p layer was increased, depth of PC was also increased. Below is the graph of etched PC depth versus dwell time of focused beam of Ga ions which hit on the LED surface in Figure 5.12.

After the process was completed, the LED wafer was checked on probe station in order to see the effect of the patterned PC structure by FIB. However, there were no light coming out from the area around where PC was etched which can be seen in Figure 5.13.

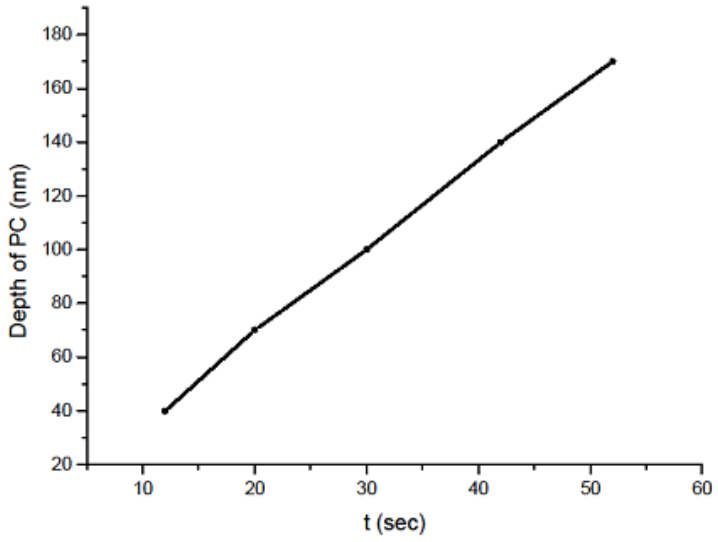

Figure 5.12 Dwell time vs. PC depth during FIB PC patterning

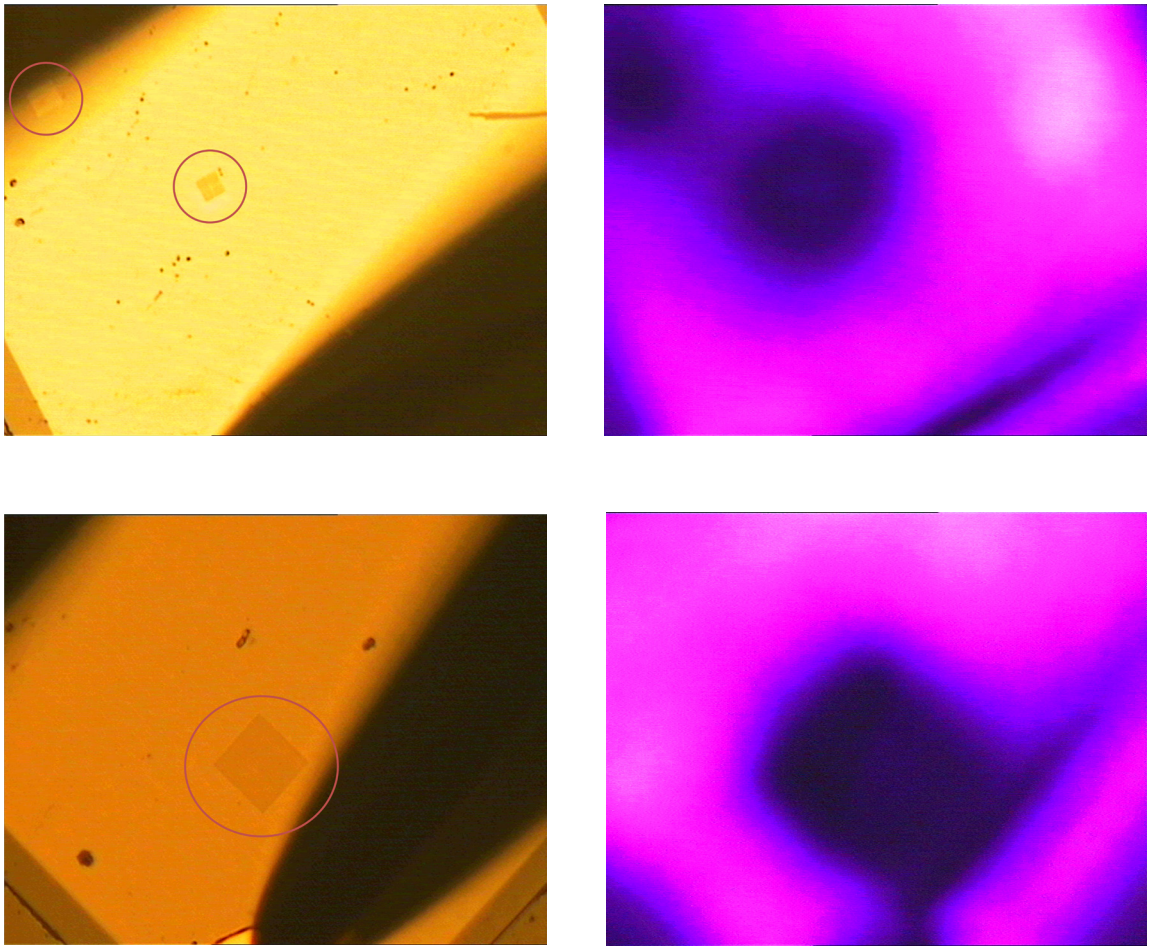

Figure 5.13 PC patterned areas by FIB system using 30 kV gallium ions

FIB was tried on couple of other LED chips even with lower depth of PC, but all chips were damaged by Ga ions. Main reason considered was damaging of thin p layer and p-doping and quantum well active region by high energy Ga metal ions. One possible solution was to use reduced acceleration by decreasing potential from 30 kV, but that time energy of Ga ions were not sufficient to be able to etch the GaN surface.

5.4.2 E-beam Induced Deposition of Platinum (EBID)

As a second approach, it was tried to pattern PC structures by using nano-meter scaled Pt spheres as a mask which are to be deposited on the LED p-layer GaN surface. In order to deposit the metal spheres on GaN, I used focused electron beams of e–beam writer.

In this method, gaseous Pt precursors are sent into the electron microscope chamber (E-beam chamber) which is under high vacuum. These gaseous precursors are hit subsequently by high

energy focused beam of electrons which results with deposition of non-volatile Pt fragments on to the substrate. As scanning the electron beam and adjusting the spot size of the beam, Pt spheres can be deposited on the intended are with user defined shape and dimensions [125].

Below is the picture of GaN LED p layer surface with an area of Pt spheres deposited in Figure 5.14.

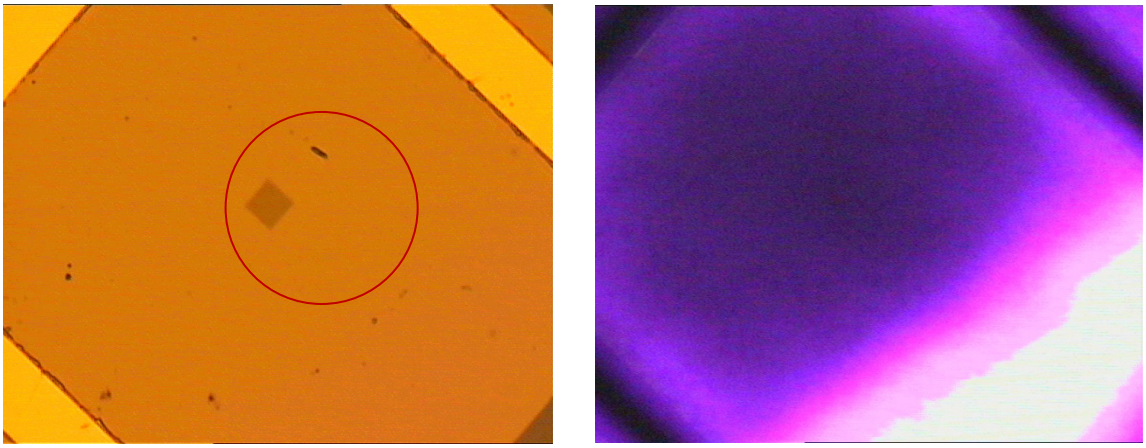

Figure 5.14 Area of platinum deposition by electron beams on p layer of GaN

After deposition, the structures and condition of LEDs were examined on probe station. Surprisingly again, scanned area where Pt spheres were deposited and beam of electrons hit was totally damaged and did not emit light. Trials on other LEDs gave the same result. It was concluded that even electron beams have enough energy to damage active layer and thin p layer of LED.

5.4.3 PC fabrication characterization by E-beam lithography

Since FIB and Pt deposition did not work, last choice was to use electron beam writer to fabricate PC structure.

However, quantum wells and p-layer of the GaN are very sensitive, therefore firstly it was characterized the maximum allowable electron beam energy that can be used to write the PC structure on PMMA without giving harm to the LEDs. Different area of LED chips was scanned by electron beam under SEM system for three minutes with 2 keV, 3 keV, 5keV, 10 keV and 20 keV. While areas where electron beam hit with up to 5 keV energy was not damaged considerably, places hit by electrons with 10 keV and 20 keV did not emit light. However, at a later time, when it was tried LED chips that were fabricated with same

processing layout with 70 nm PMMA coated and 120 nm SiO_2 grown on the surface of p-layer, 10 keV and 2 keV electron beam did not give any considerable harm to devices. Therefore, I had to use e-beam writer with lower energy of 5 keV first, which complicated the process extensively. However, final structures were fabricated using e-beams with 10 keV acceleration.

In e-beam lithography, there is no mask needed but rather focused electron beams scan the substrate and expose user-defined positions with user-defined energy. (PMMA, polymethyl methacrylate) is used as radiation sensitive e-beam resist, which is coated on the substrate to be patterned.

E-beam fabrication is a slow technique because of serial writing nature of this method, especially for circular shapes to be patterned on large area [120]. Therefore, it is used just for research prototyping purposes. Larger structures more than a few hundreds of micrometers cannot be written by e-beam at once because of beam deflection. Therefore, they should be stitched to each other by movement of the sample stage with respect to beam. Stitching accuracy is also very important for design of PCs.

5.4.3.1 E-beam System Adjustment

Before starting to e-beam patterning, system components such as stage, write-field, aperture, astigmatism should be aligned and adjusted if necessary. Without proper alignment and adjustment of variables end up with a totally useless patterned structures since e-beam writer is quite sensitive in terms of dimensions and spatial resolution.

5.4.3.1.1 Write-field Alignment

Larger structures more than a few micrometers cannot be written by e-beam at once because of beam deflection issues. Therefore, they should be stitched to each other by movement of the sample stage with respect to beam. Stitching accuracy is very important for fabrication of PCs [120]. In the picture below in Figure 5.15, stitching error can be seen clearly in PC structures on LED surface. This kind of error has detrimental effects on the extraction performance of PC LEDs.

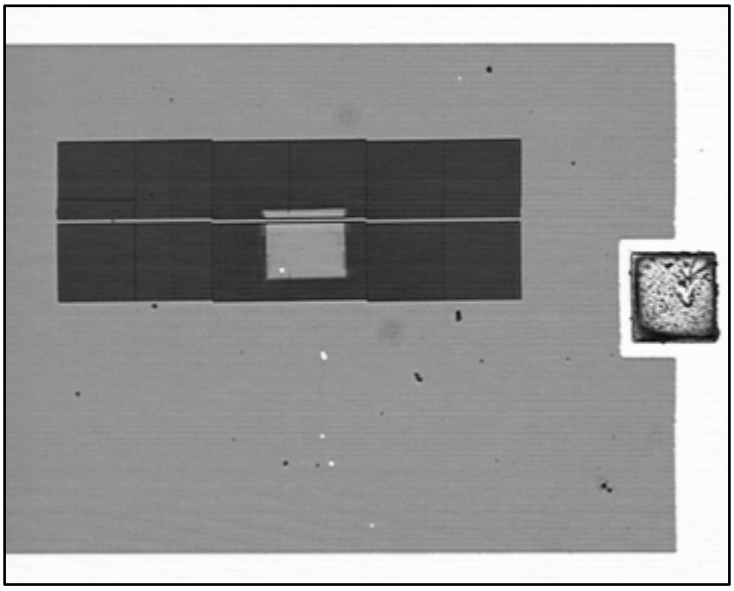

Figure 5.15 Final PC structure patterned by e-beam lithography system, stitching error

Write-field alignment should be performed in order to correct the stitching error that is shown above. In write-field alignment, beam is aligned with respect to sample coordinates. This alignment should be done whenever new working distance or new write-field size is used. After the alignment procedure, stitching errors should be reduced.

5.4.3.1.2 Stage adjustment

There are two main coordinate systems related to stage in e-beam, which are stage corrdinate system XY and sample coordinate system UV. In order to localize the area to be patterned or has already been patterned without re-exposing the sample, these two coordinate systems should be adjusted and aligned with respect to each other. Since write-field alignment is also based on these two coordinate systems, alignment of coordinate systems is crucial in order to have better patterning results.

Angle correction and origin correction are two basic steps of stage adjustment. In angle correction, angle between the edges of sample and stage is reduced to make stage and sample coordinate system parallel. In origin correction, origin of the sample is defined as also the origin of the stage. This is a needed procedure since sample can be placed at any place on the stage.

After completing adjustment of stages, it is possible to locate any definite area on the sample without viewing the sample through focused electron beams, thus number of re-exposures are

reduced. Since PMMA and our substrate material GaN is highly sensitive to electron beams, exposing times should be reduced as much as possible.

5.5 Characterization Parameters

In order to fabricate PC structures, very first thing to do is to pattern the structure on PMMA e-beam resist. Correct patterning is very crucial since subsequent steps will follow up the first patterning scheme on PMMA.

Patterning on PMMA by e-beam writer requires a good characterization procedure. PMMA thickness which is defined by coating revolution speed, PMMA developer MIBK (4-methyl-2 pentanon) to the IPA (2-propanol) mixing ratio, develop and rinse time of PMMA after e-beam writing are characterization steps for PMMA itself.

Regarding e-beam writer, exposure parameters such as step size, beam dose, dwell time, beam current, settling time should be adjusted and calibrated in order to get the desired dimensions and shape.

5.5.1 PMMA thickness and development

PMMA used throughout this thesis is PMMA 950K A2. As stated above, I had to work first at low accelerating potential 5 keV in order to prevent possible electron beam damages to the quantum well and p-layer of the InGaN/GaN LED device. However, this low potential increases the complexity of the PC patterning. 5keV is very low in order to pattern high resolution structures. Therefore, thinner PMMA thickness should be used to reduce under-cutting caused by highly scattering of electrons due to low acceleration and to get desired dimensions with adequate resolution. Thin PMMA is another issue during transfer of patterned structures on to substrate by dry etching techniques since PMMA erodes very easily in dry etching process. Therefore, an additional masking layer should be used, which reduces resolution of the structure more. I used SiO_2 as sacrificial layer which also increases isolation which has already caused by 430 micron thick sapphire structure. Using oxide sacrificial layer is a must in order to transfer PC patterns on to GaN but it also necessitates higher accelerating potential for adequate resolution. Since potential cannot be increased due to sensitivity of quantum well layers of the device, e-beam process should be optimized as much as possible under these conditions.

In order to obtain acceptable resolution at 5 keV, I coated PMMA layer with a thickness of 65~70 nm. Below in the Table 5.11, one can find details about coating speed and bake conditions. To harden the PMMA resist, post-bake process is applied prior dry etch after development to improve resist stability during etching process.

After PMMA is exposed regarding user defined patterns, it is developed where the area hit by electrons is decomposed and patterns are formed. Developer used is MIBK as stated above. However, it should be diluted with isopropanol (IPA) for controlled developing. MIBK:IPA ratio is kept at 3:1. After development is complete, sample is rinsed in IPA in order to completely stop developing process. Starting point of characterization was 30 seconds MIBK, 30 seconds IPA.

	Quantity	Speed	Time	Temperature
PMMA A2	0.25 ml			
Spin Coating		3000 rpm	45 sec	
Pre-bake			75 sec	180 °C
Post-bake			90 sec	100 °C
Film Thickness	70 nm			

Table 5.11 PMMA resist recipe

Regarding desired dimensions, final developing procedure was 50 seconds MIBK, 20 seconds IPA. After rinsing in IPA, sample was dried under low pressure Nitrogen flow.

5.5.2 Exposure Parameters

In order to obtain desired shapes and dimensions, it is crucial to understand and adjust exposure parameters properly. Although soft-mask which is drawn in the system has user defined dimensions, using not optimized or adjusted exposure parameters end up with undesired shapes and/or dimensions.

5.5.2.1 Step size

Step size is the distance between two adjacent settling positions of the focused electron beam and should be adjusted carefully to have desired geometry. In order to have good resolution, step size should be at least 1/5 of the minimum feature size in the structure. In general, as the step size is decreased, smoothness of the edges of the structure and resolution increases.

It is also crucial to use step size value to fit the periodicity of the features in structure in order to have desired shapes at desired coordinates.

In fabrication of PC structures with diameter of 260 nm and periodicity of 520 nm, optimum step size was found to be at 20 nm.

5.5.2.2 Clearing dose

Clearing dose is defined as the number of electrons hit on a unit area. In case of dot doses, since no area is in consideration, dot clearing dose is just the number of electrons hit to that specific position. Unit of the clearing dose is $\mu As/cm^2$ for area dose, μAs for dot dose. Clearing dose is directly proportional to the beam current and dwell time of the beam. Dwell time is amount of period that focused electron beams hit a position at every step size. Using lower clearing dose than optimum value results with smaller feature sized patterns with lower resolution. Higher clearing dose causes features to have larger sizes than user-defined values. Using high clearing dose values may also harm quantum well regions. So, an optimum value should be found. Number of trials have been done in order to find the optimum value of dot clearing, circle clearing and area clearing dose which are shown in details later in this chapter.

5.5.3 Beam current

Beam current can be defined as number of electrons hit a position at unit time. It is directly related to the clearing dose. While lower beam current provides larger depth of focus but higher exposure time, higher beam current decreases exposure time for a given clearing dose. However, decreasing exposure time ends up with increased beam speed which causes reduce in placement accuracy and broadening in shapes of feature geometry. Therefore, optimum value should be found for desired shapes and resolution.

5.5.4 Beam energy

Energy of the beam is kinetic energy of electrons in the beam which is gained by acceleration potential. In general, in order to have better resolution features for patterns with lower dimensions, beam energy should be above 20 keV. However, higher beam energy requires higher clearing dose since interaction time between electrons and resist is decreased considerably. As a result, both high beam energy and high clearing dose may damage InGaN/GaN multi quantum well structure of the LED devices which results in no emission. Therefore, lower beam energy values were used for PC fabrication process throughout this thesis. Since beam with lower energy has lower velocity electrons, scattering effects become visible in the resist which causes undercut. Because the pattern of PMMA is transferred on to layers below in etching process, this undercutting causes PC dimensions to enlarge and ends up with different diameter cylinders throughout the depth of the PCs. In order to reduce the level of undercutting, resist thickness should be decreased. PMMA thickness used in this thesis was optimized to be 70 nm. As stated above, reduced resist is more easily eroded under dry etching process. Therefore, sacrificial mask layer is needed for pattern transferring from PMMA down to GaN, which was selected to be SiO_2 for ease of growth and processing. This layer, on the other hand, reduces resolution and distorts the shape of PC structures and also increases electrical isolation between the sample surface and the e-beam writer table. This decreased conduction may cause charging effect on the surface of the GaN. As a result of charging, beam is deflected on the surface and focusing ability is decreased. Written patterns under these conditions have distorted shapes with very low resolution. To reduce charging effect and to increase resolution of the transferred patterns while maintaining sufficient thickness regarding the etch selectivity between PMMA, SiO_2 and GaN, oxide thickness was optimized to be around 100 nm.

5.6 Characterization and fabrication of photonic crystals

5.6.1 PMMA Thickness

PMMA was used as resist for e-beam exposure. Since accelerating potential was 5 keV, resist thickness should not be high to prevent large scattering effects of electrons. After exposing and developing PMMA resist, thickness and the resultant geometry was examined with atomic force microscopy. As can be seen from Figure 5.16 below, thickness of the PMMA is around 65 nm.

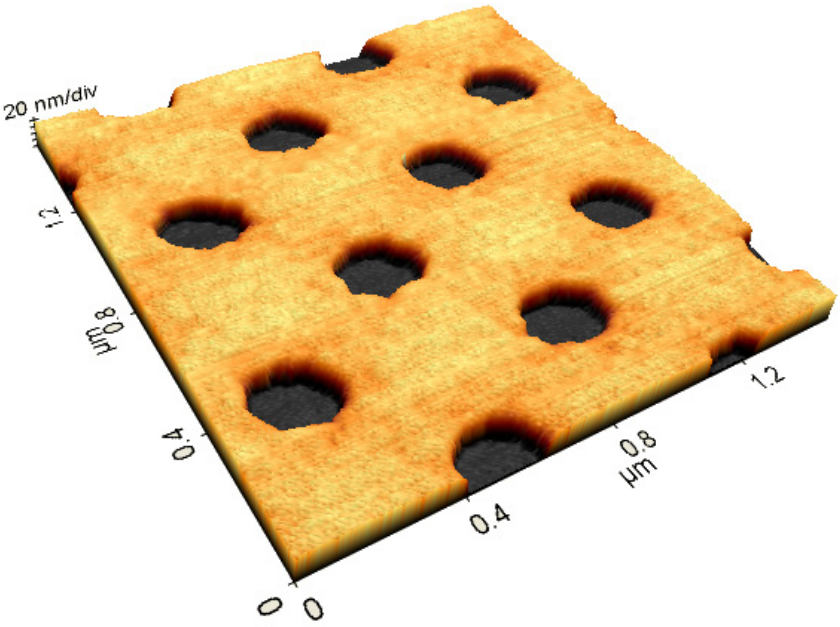

a.

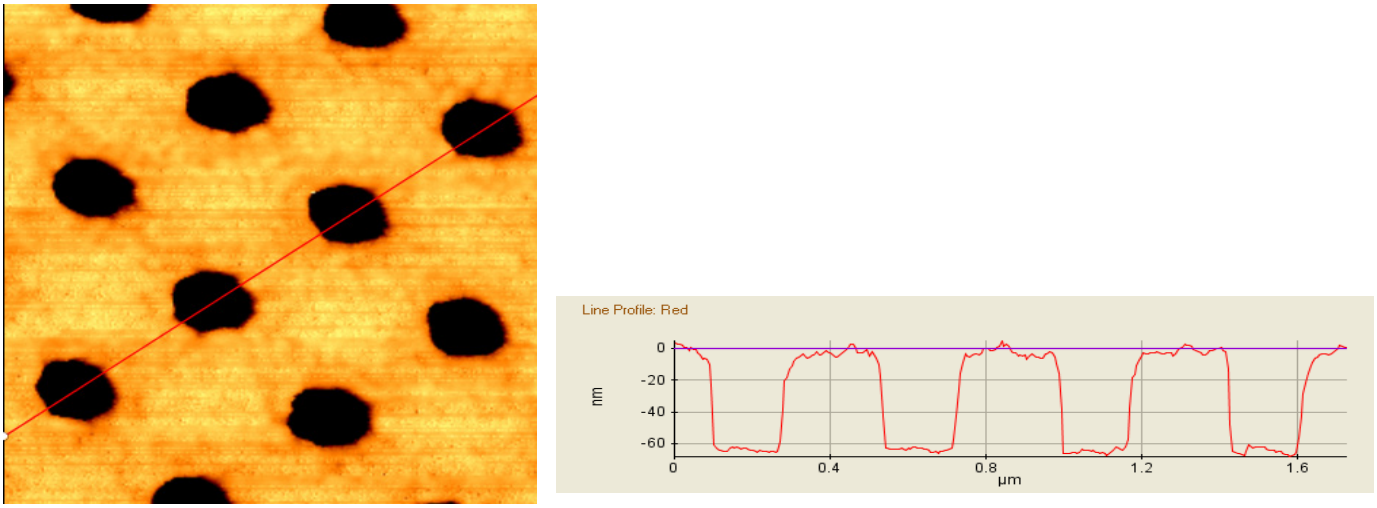

b.

Figure 5.16 AFM pictures of PMMA resist on GaN a. 3D image of PMMA resist b. Line profile of the PMMA resist

5.6.2 Eroding of PMMA under RIE Etching

Since PMMA is very thin and not resistant to sputter effects and Chlorine based gases, it is eroded very easily in the first few minutes of GaN dry etch with using Freon gas. Re-exposing the PMMA after development may help PMMA to get hardened. In the figures below, one can see the difference between re-exposed region and non re-exposed regions of PMMA which is used as a mask for GaN PC patterning. Even though PC structures under PMMA masking regions that are exposed just once are damaged by subsequent plasma ions after eroding of PMMA, those structures under re-exposed

PMMA masking regions are formed well and stays undamaged. Although re-exposing PMMA solution works well, it is not a feasible way since it is hard to expose large PC regions homogenously.

Thin PMMA resist is eroded easily in reactive ion etching process. Using PMMA as a mask for RIE etching for patterning PC structures on to GaN layer results in damaged PC structures as can be seen from Figure 5.17.

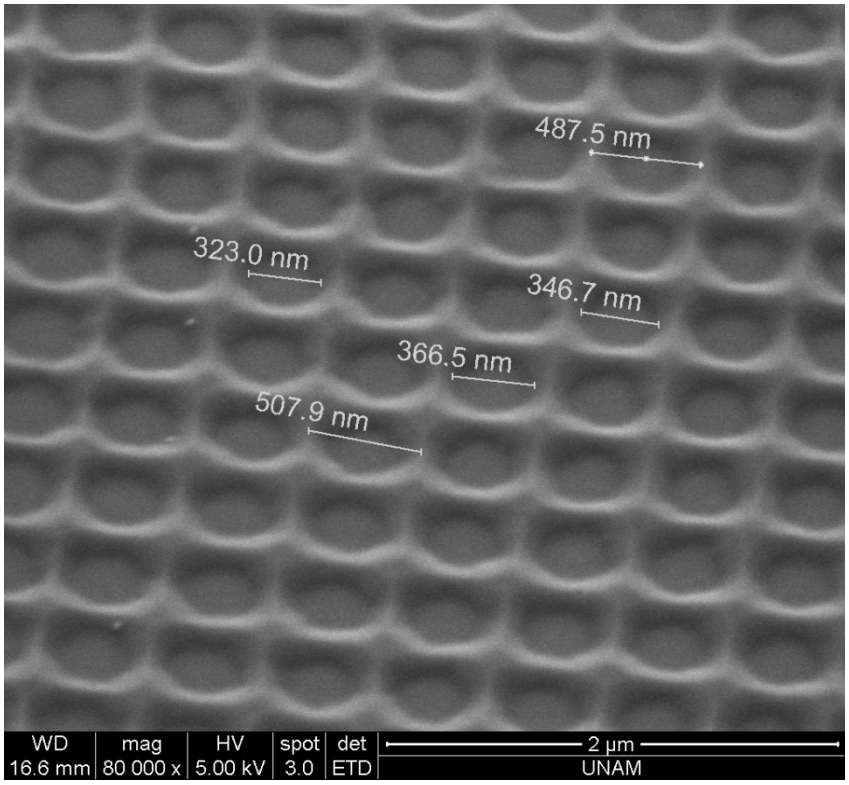

Figure 5.17 Damaged PC structures because of eroded PMMA

In the process above, 70 nm PMMA was used as mask layer and it was post-baked at 90 °C for 90 seconds. Afterwards, 5 minutes RIE GaN etch recipe was applied. However, PMMA was fully eroded in first few moments of etching. Therefore PC structures were damaged. In order to reduce eroding rate of PMMA under RIE, PMMA resist was re-exposed by e-beam after development. Then, again 5 minutes RIE etching was applied.

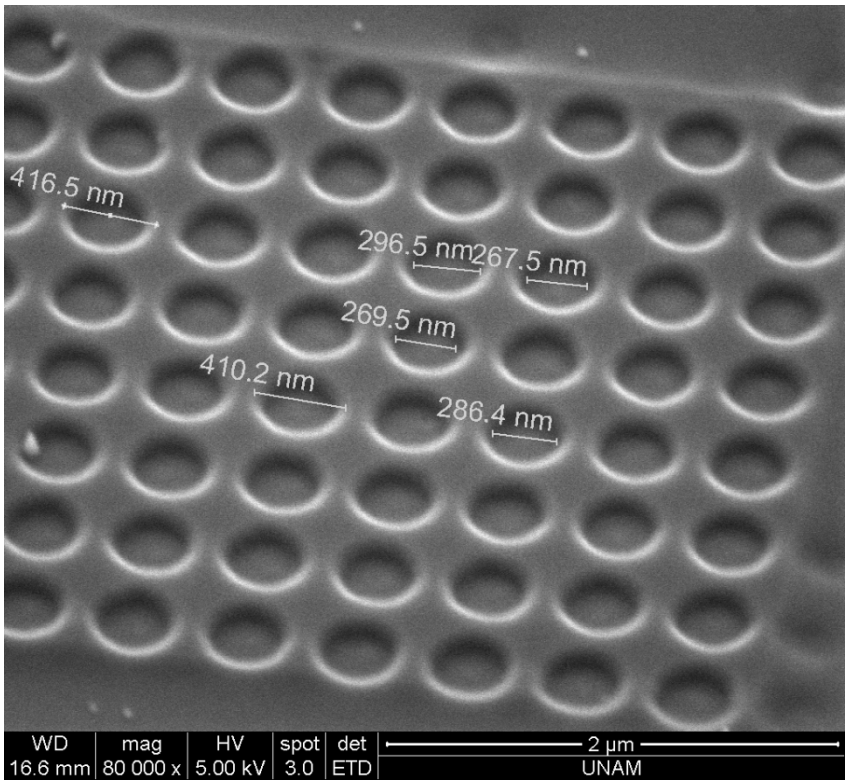

Figure 5.18 Re-exposed PMMA under RIE etch

Result in Figure 5.18 was acceptable, PC structures under re-exposed resist was not damaged much. However, it is hard to characterize the re-exposure dose and to re-expose large area of PC structures homogenously.

In case over re-exposure is used, no pattern is transferred to GaN layer as seen in Figure 5.19.

5.6.3 Choosing Sacrificial Layer

Since PMMA is eroded very fast in chlorine based dry etching which is used to etch GaN to transfer PC patterns, a sacrificial layer should be used. First Chromium was tried since its plasma etch resistance is high. Chromium metal was deposited on the GaN as a sacrificial layer. Over Chromium, PMMA was coated to be patterned by e-beam exposure. After developing PMMA, patterns were transferred down to Chromium by wet etching and PMMA was removed. In the Figure 5.20, PMMA was removed from the surface. Dimensions are larger than expected because of isotropic etch property of wet etching technique. Also it is clear that chromium could not be etched fully from the surface, which caused awkward surface structure after 3 minutes reactive ion etching (RIE) process by using GaN etch recipe in Figure 5.21.

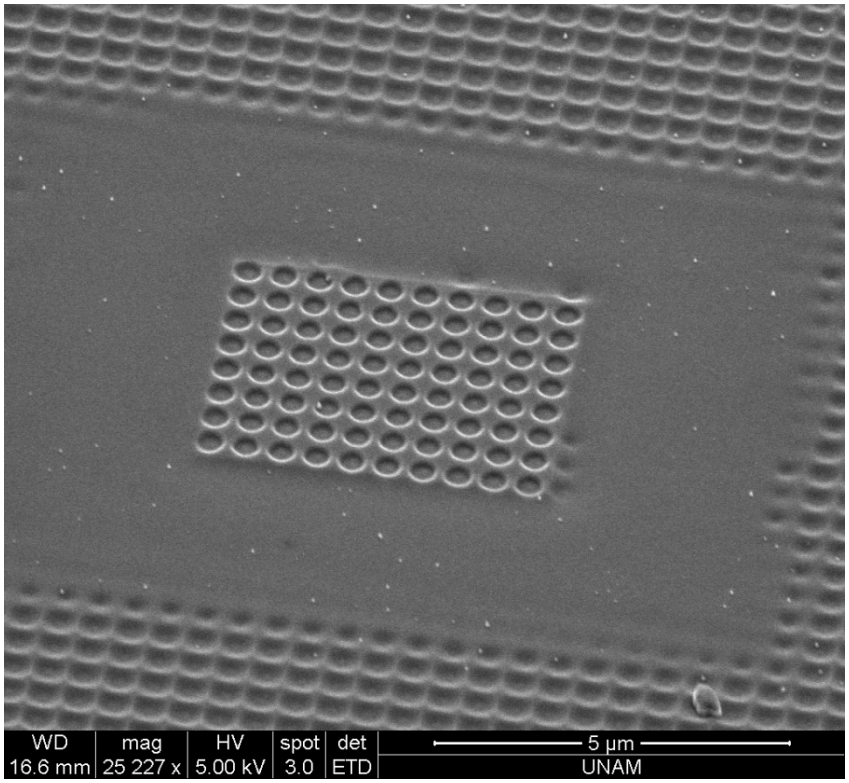

Figure 5.19 Over re-exposure causes all PC patterns to be washed off

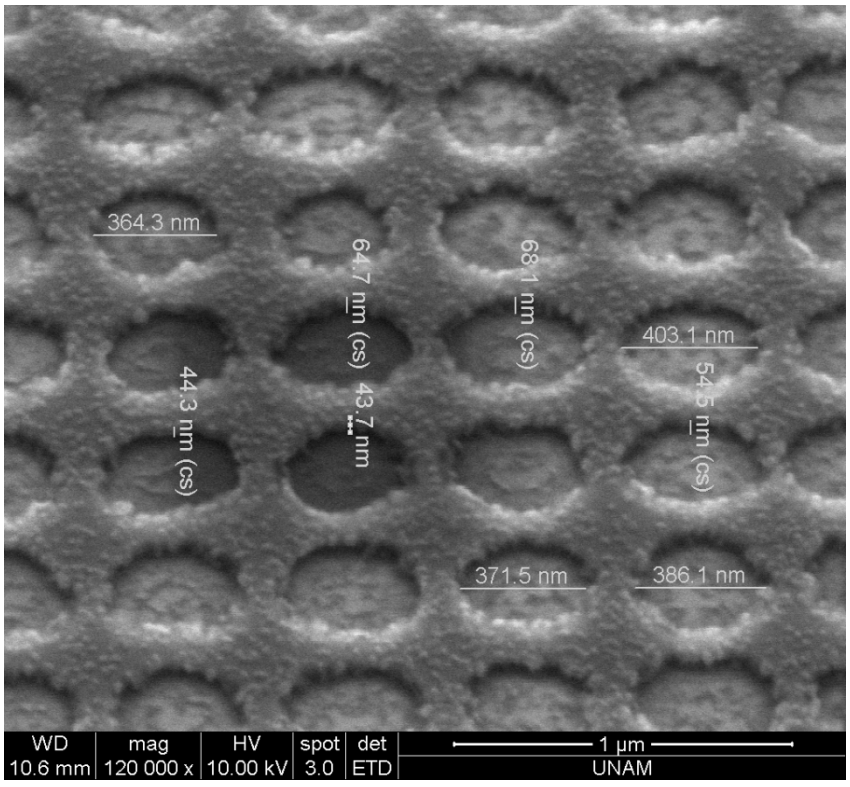

Figure 5.20 Chromium sacrificial etching mask after PMMA removal

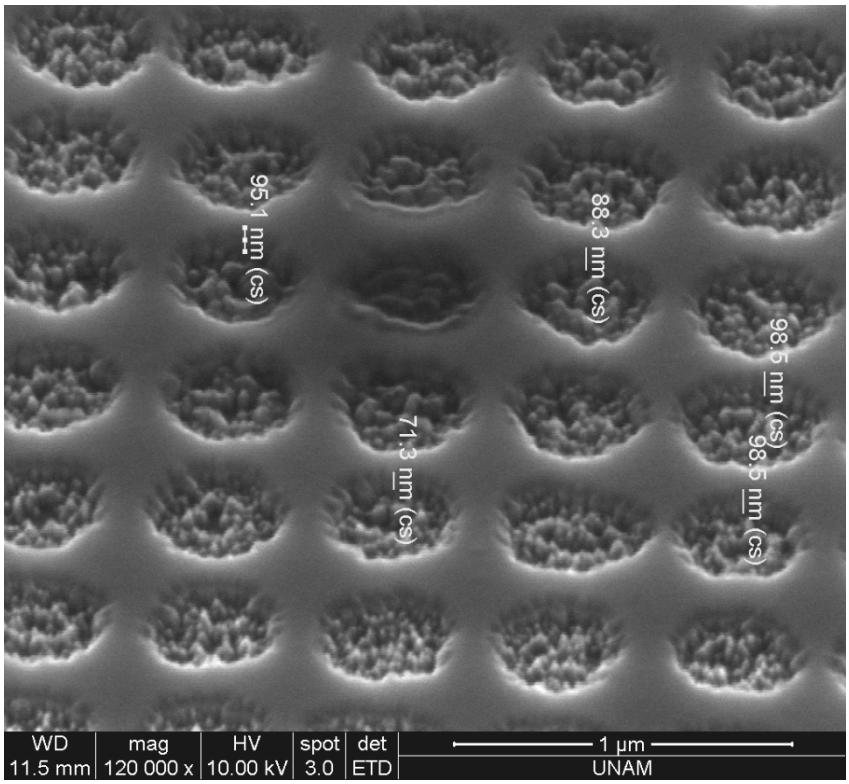

Figure 5.21 Chromium mask layer after RIE etching

Therefore, SiO_2 was used as sacrificial mask layer. It was grown by using plasma enhanced chemical vapor deposition with recipe given in Table 5.12 below.

Used gas	Flow rate (sccm)	Power (W)	Temperature (C)	Growth Rate (nm/min)
SiH4	180			
N2O	710			
		7	100	12

Table 5.12 SiO_2 growth recipe by PECVD

In order to balance isolation amount because of thick oxide layer and pattern transferring performance, oxide thickness was kept around 100 nm.

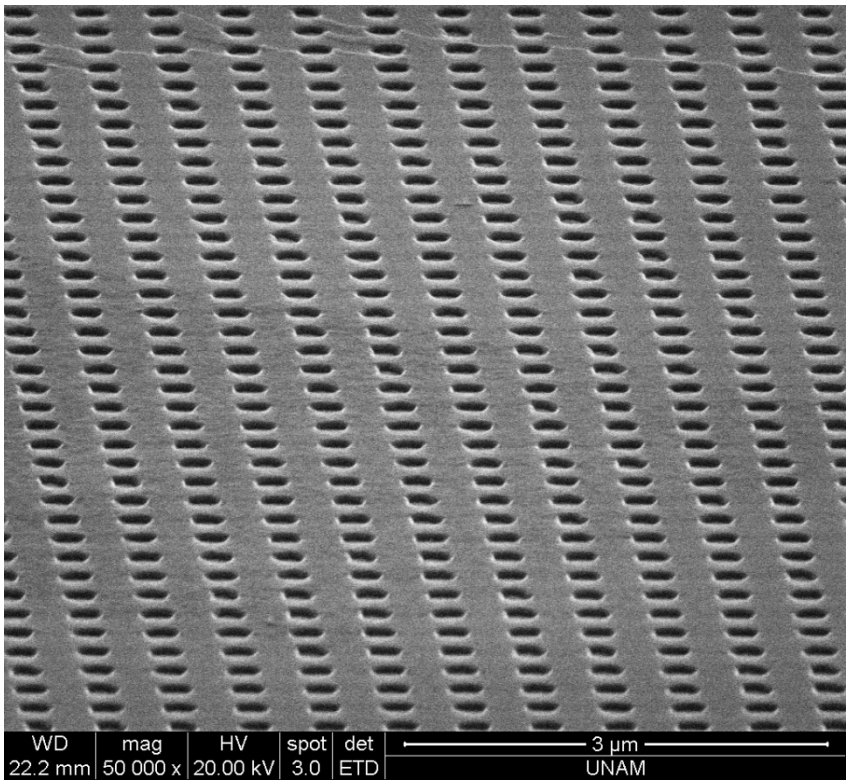

Figure 5.22 SiO_2 used as sacrificial mask layer

5.6.4 Dose Characterization

Although PC patterns have user-defined dimensions, clearing dose amount should be adjusted accordingly in order to get the same dimensions on the resist. By decreasing or increasing the dose, dimensions can be changed because of amount of time for electrons to scatter in the resist.

Three different clearing dose types were used. These are dot dose, circle dose, and area dose. In dot dose, all beam energy is focused to a point. By varying amount of clearing dose, diameter of the hole can be adjusted. In circle dose, electron beams scan the circumference of the circle discretely by user-defined step sizes. In area dose, all area is discretized by step size where electron beam scans. Circle dose and area dose uses the same principle, former is in circular mode though.

As a sacrificial mask layer, SiO_2 were used. This oxide layer were grown on GaN during characterization stages by PECVD in two ways, which were called oxide-1 and oxide-2 growth processes. Conditions about growth are outlined below in Table 5.13 and Table 5.14. Samples were prepared for e-beam writer by coating 70 nm PMMA. PMMA recipe was given before in this chapter. After writing process was completed, PMMA was developed, dried and

post-baked for hardening purposes regarding subsequent RIE etching. First, silicon dioxide was etched by using PMMA as the mask layer. Afterwards, patterns transferred to oxide layer were re-transferred to GaN layer by GaN RIE etch. RIE etching recipes regarding SiO_2 and GaN are given in the next subsection below. After etching processes, final sample was examined under scanning electron microscope (SEM).

Used gas	Flow rate (sccm)	Power (W)	Temperature (C)	Growth rate (nm/min)
SiH4	180			
N2O	710			
		7	100	12

Table 5.13 Oxide-1 PMMA growth conditions

Used gas	Flow rate (sccm)	Power (W)	Temperature (C)	Growth rate (nm/min)
SiH4	200			
N2O	180			
		12	250	33

Table 5.14 Oxide-2 PMMA growth conditions

5.6.4.1 Dot dose characterization

Since writing is fast with respect to other dose types, dot dose was first choice for characterization. Clearing dose in dot choice is defined as number of electrons hit on a point which is calculated by multiplying beam current by dwell time of the beam. As the amount of dose is increased, so the hole diameter increases. However, positive resist PMMA behaves as

negative in case dose is increased beyond a limit. Therefore, residual PMMA was a problem during characterization process.

In the process in Table 5.15 below, sample was prepared with oxide-2 growth recipe. Final thickness of the oxide was 65 nm. 3 minutes RIE oxide etch and 5 minutes RIE GaN etch was subsequently used. In e-beam writing process, exposure parameters that were used are outlined.

Beam current (nA)	0.11
Accelerating voltage (keV)	5
Step size (nm)	-
Clearing dose type	dot
Clearing dose amount (uAs), (uAs/cm2)	0.1 x (1.0-2.0)

Table 5.15 Dot dose characterization

As dose was increased, diameter of the holes also increased. Intended PC structure had 520 nm period and 260 nm diameter. Therefore, clearing dose of 0.1x1.6, 0.16 uAs would be sufficient. However, if SEM pictures are examined carefully, all PC holes have black dots around center. This is residual PMMA left after development since PMMA acted as negative resist because of high amount of clearing dose. This residual PMMA affected the RIE etch process and this pattern transferred to other layers as seen below in Figure 5.24.

Center of holes were not etched because of the residual PMMA left. In order to reduce the amount of residual resist, electron beam was de-focused during writing process. For the sample below, de-focusing was provided by turning the fine adjustment knob by 1.5 turns at the magnification of 100k as seen in Figure 5.25.

Resultant holes were awkward. While some of circles were large, others were small. Shapes were distorted. De-focusing worked for residual resist but this time reproducibility was low. Depths of holes were not adequate either. AFM results are stated in Figure 5.26.

De-focusing with 1 turn, ¾ turn, ½ turn were also tried. Beam currents of 80 pA and 0.22 nA did not give better results either.

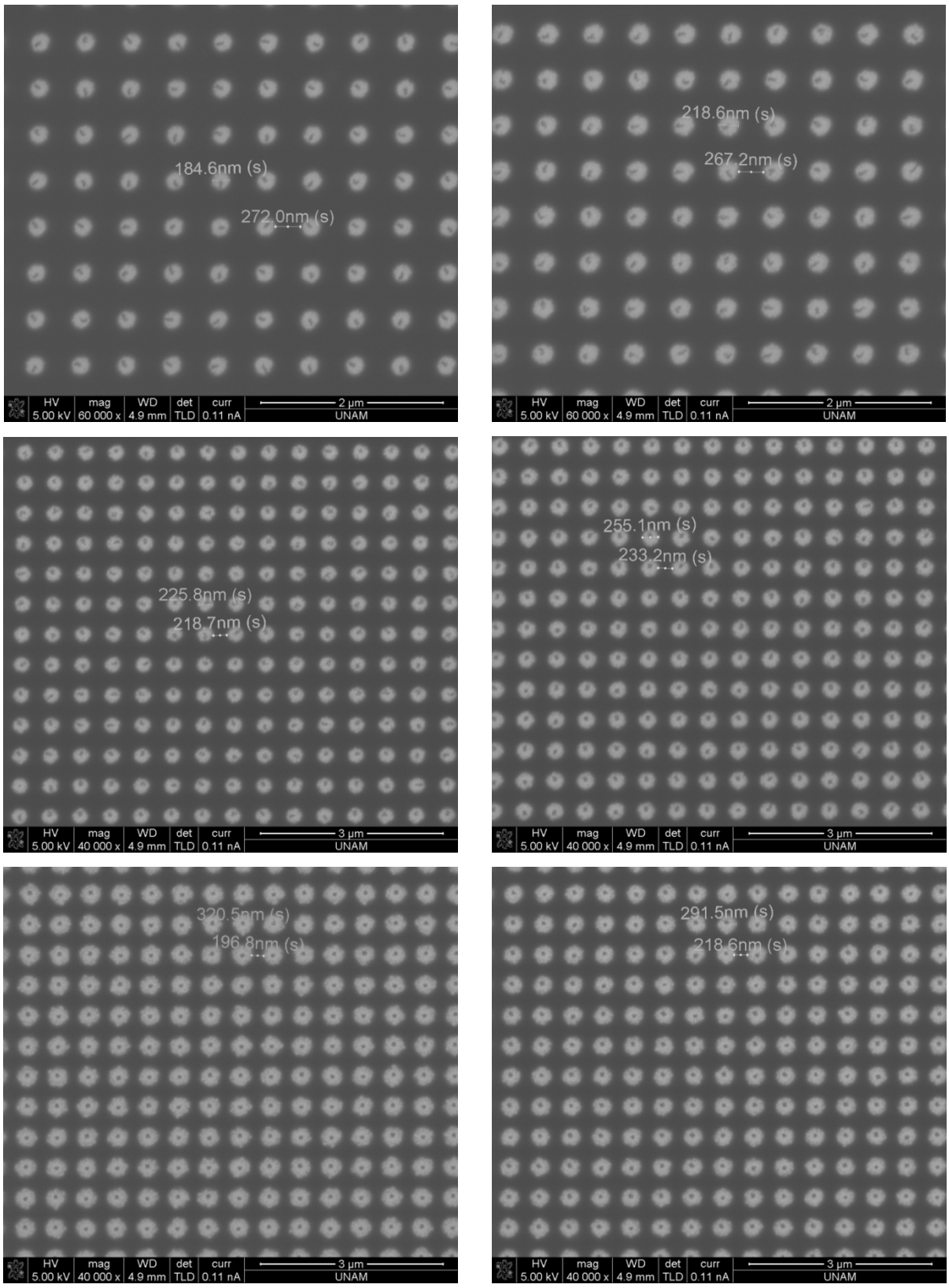

Figure 5.23GaN-SiO_2- PMMA sample after PMMA develop.

Dose amounts varies from 0.1 to 0.2 by 0.02 intervals from top right to down left respectively

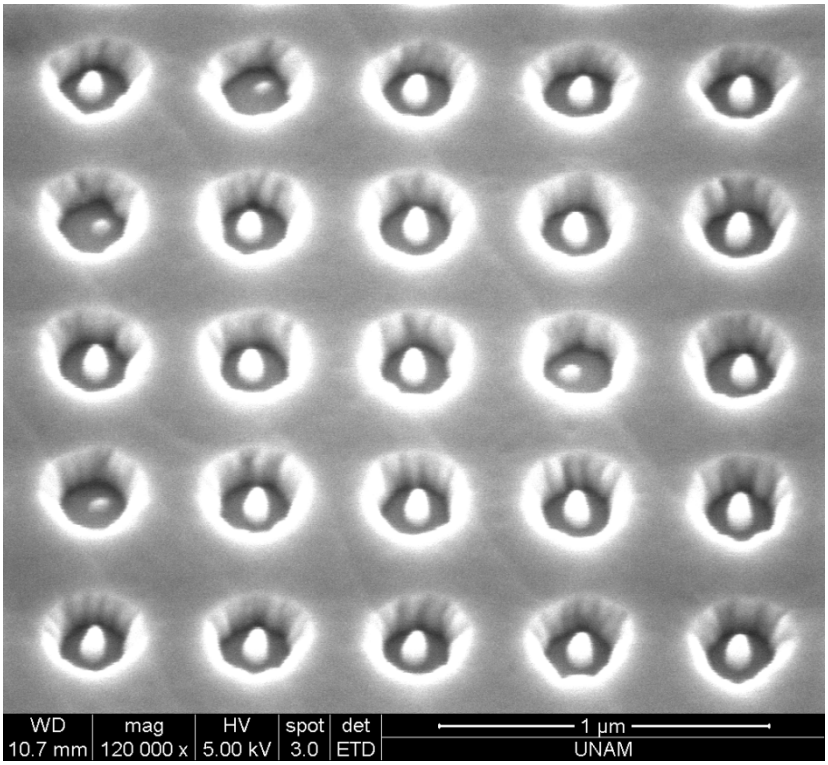

Figure 5.24 RIE etch after e-beam dot dose

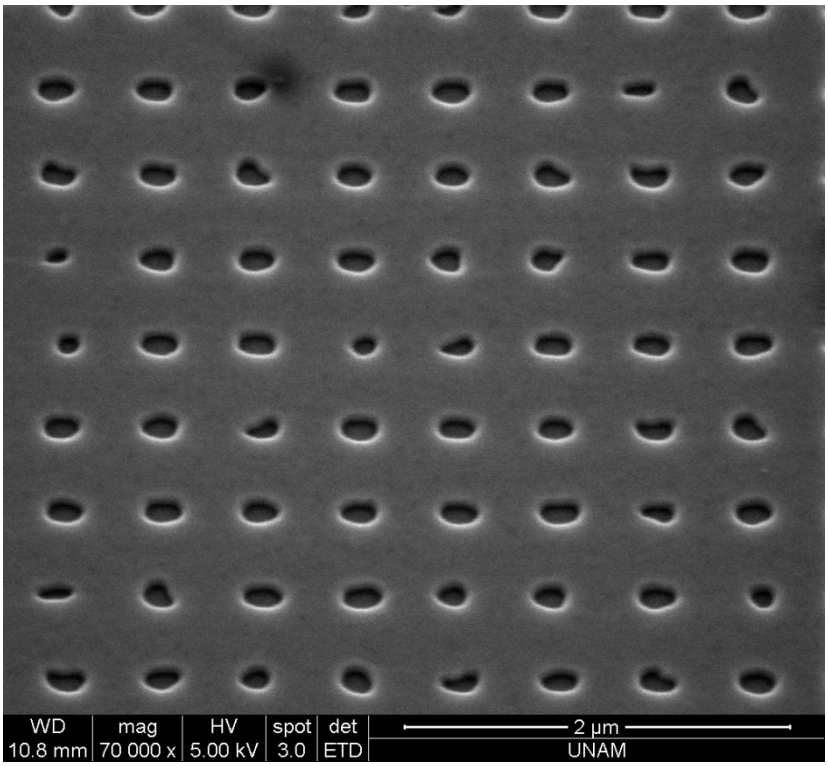

Figure 5.25 RIE etched sample after dot-dose exposure with de-focusing

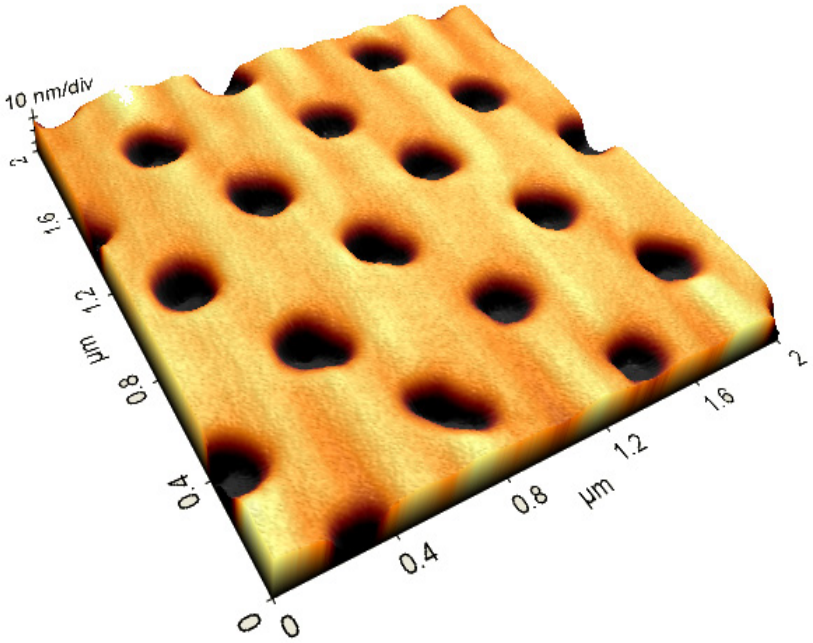

a.

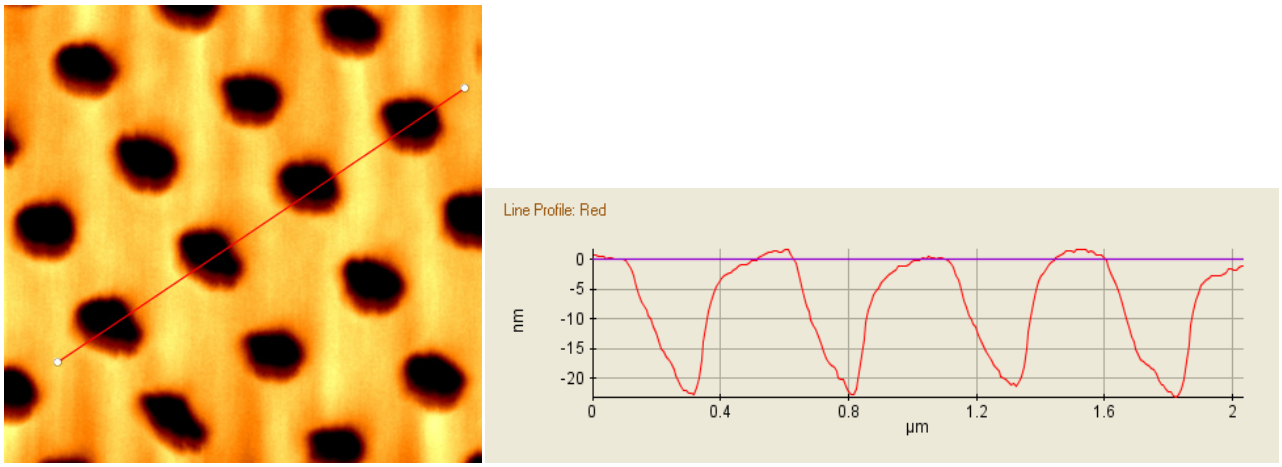

b.

Figure 5.26 AFM image of de-focused dot dose sample a. 3D image b. Line profile

5.6.4.2 Circular Dose Characterization

Since dot dose did not give sufficient structure geometry, circular dose was tried. In this clearing dose type, full circle is discretized by small dots which are arranged around circumferences of nested circles with intervals of circular step size. This process is figured below in Figure 5.27.

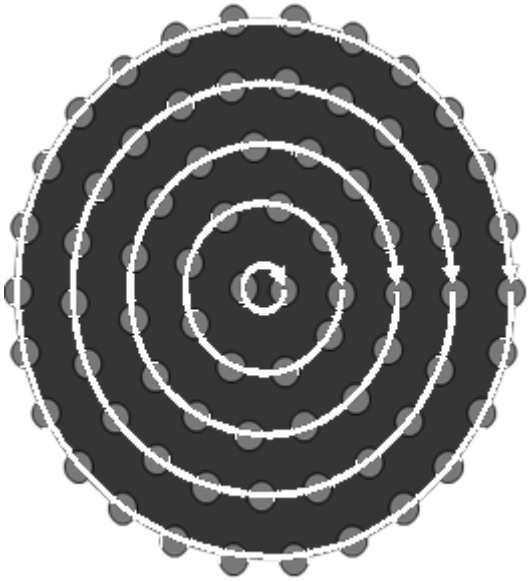

Figure 5.27 E-beam circular dose writing scheme

All trials were made using 5keV beam energy and 0.11 nA beam current. Details about exposure parameters are stated in Table 5.16.

Beam current (nA)	0.11
Accelerating voltage (keV)	5
Step size (nm)	44
Clearing dose type	circular
Clearing dose amount (uAs), (uAs/cm2)	20 – 70

Table 5.16 Circle dose characterization parameters

Clearing dose from 20 uAs/cm^2 up to 70 uAs/cm^2 was used. Resultant structures were not holes but ring-shapes in all trials. However, as the dose was increased, diameter of the inner undeveloped region decreased. But diameter of the whole structure increased at the same time, therefore dimensions of the user-defined PCs had to be also decreased. This procedure requires many characterization trials. Since it takes too much time for patterning PC holes in

circular mode by e-beam lithography, I did not continue characterization in circular dose mode. Below in figures, RIE etched PC patterns written by e-beam in circular mode can be viewed in Figure 5.28.

E-beam dose matrix used for these structures were between 30 and 60 uAs/cm^2 by intervals of 6 uAs/cm^2. Structures are not fully etched but they have ring shapes. As clearing dose is increased, although area of central non-etched section decreases, diameter of full PC structure increases. Therefore, user-defined dimensions for PC structures must be lowered.

Below one can find the AFM measurement results of a sample which was patterned with circle dose of 28 uAs/cm^2 with cicular step size of 44 nm in Figure 5.29.

5.6.4.3 Area Dose Characterization

Because circular dose mode takes much time for patterning PC structures of 520 nm period with 260 nm diameter in an area of 100 um x 100 um, area dose method, which is less time consuming, was used. In this method, area of the polygon is discretized into smaller areas where electron beam is focused subsequently. Distance between each of these discretized areas is called step size. In this thesis work, optimum step size for area dose was charactirezed to be 20 nm.

Speed of the patterning is directly related to the number of edges of the polygon. As the number of edges are increased, exposure time to pattern all structure also increases. However, in order to have a circular PC structure using polygons, number of edges must be increased. In trials, rectangular and octagonal shapes were used. Although octagon gave acceptable results, rectangular shape polygon was unable to produce circular holes. During characterization, clearing dose amounts between 20 and 72 uAs/cm^2 were used. Beam current was also varied in order to see the effect of beam current on the resultant shape. Used beam currents were 0.11, 0.22 nad 0.45 nA.

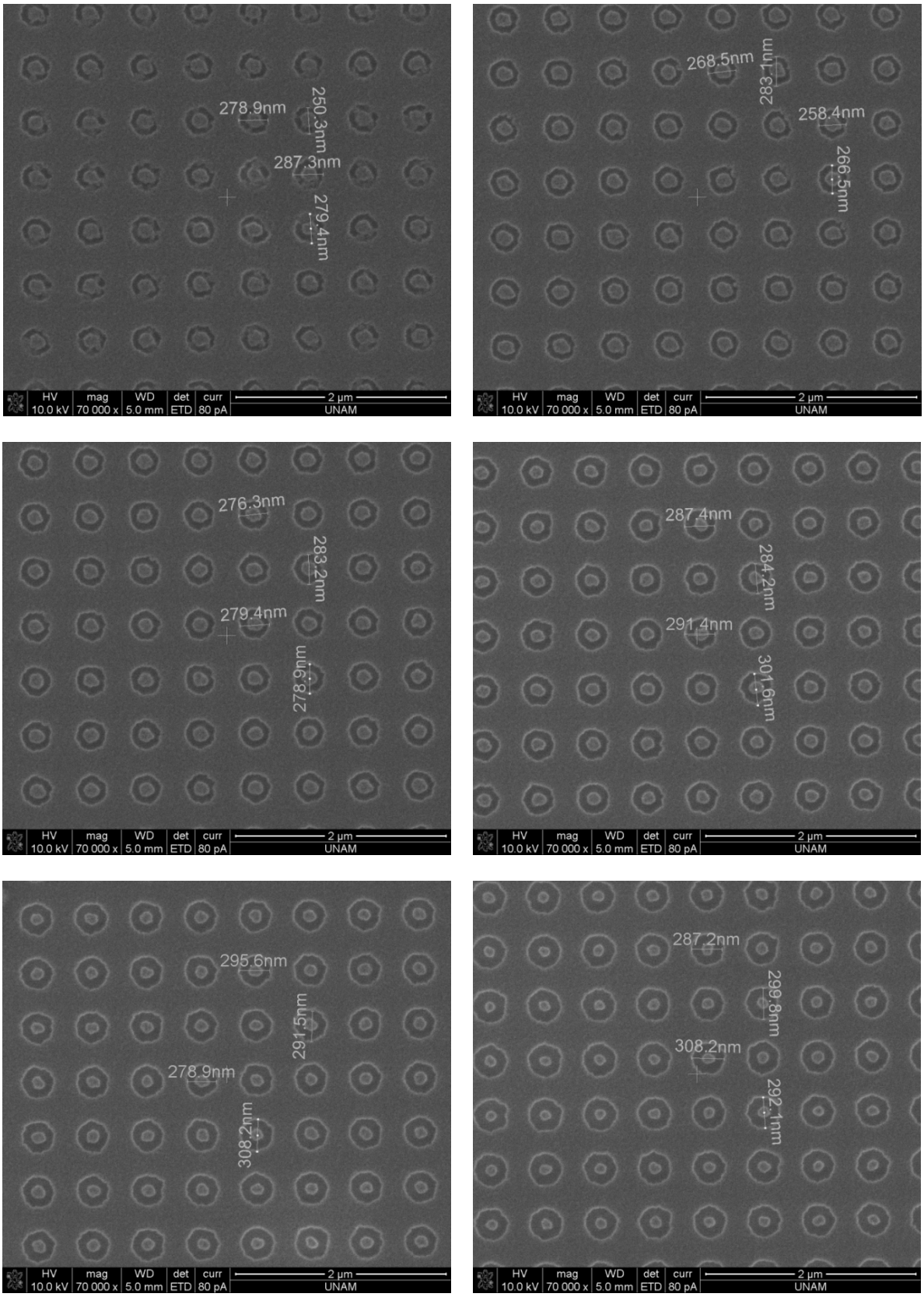

Figure 5.28 RIE etched patterns after circular dose e-beam exposure using dose matrix

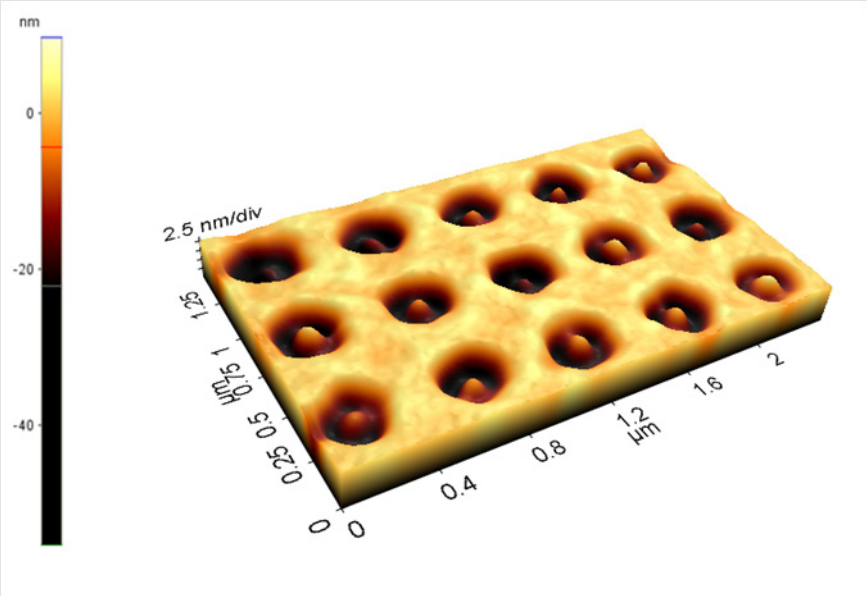

a.

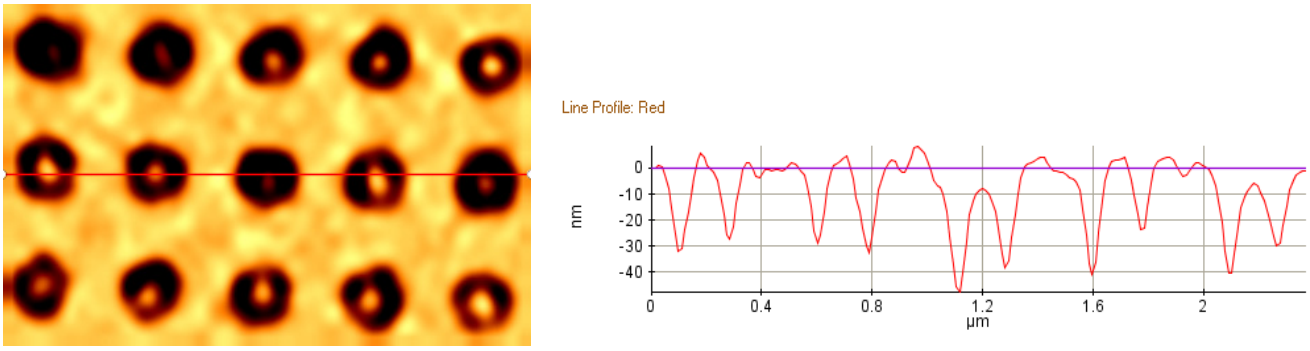

b.

Figure 5.29 AFM of sample patterned with circular dose e-beam lithography

a. 3D image b. Line profile

Eventhough it requires less time to pattern structures than that of circular mode, octogonal shape area dose consumes considerable amount of time. However, resultant structure was better. Below in the SEM pictures, samples were patterned by area dose method using octagonal shape and etched by RIE. Used beam currents were 0.45 nA and 0.22 nA. As clearly seen in Figure 5.30, patterns with 0.22 nA gave better results for the same area clearing dose since electron beam had more time to expose the resist than that of 0.45 nA.

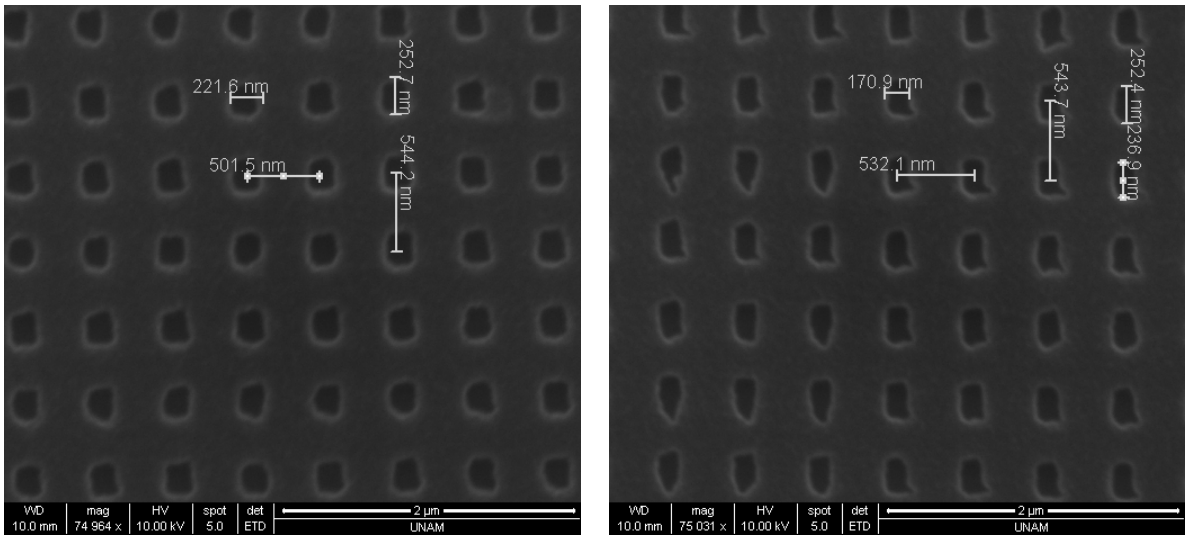

a. **b.**

Figure 5.30 Resultant patterns after RIE etched area dose mode samples by using octagonal shape with beam current used of a. 0.22 nA b. 0.45 nA

Clearing dose is directly related to beam current and dwell time. Holding step size and area dose constant, other two variables beam current and dwell time are related inversely to each other. Therefore, lower beam current gives better results. However, if the beam current is decreased too much, final pattern is again distorted.

Regarding samples figured above, beam current 0.22 nA produced more circular shape as expected. Both samples were patterned using 30 uAs/cm^2 area dose with step size of 20 nm at 5 keV. However, patterns written at 0.45 nA had distorted shape because of reduced dwell time. Furthermore, although total dose is equal for the two samples, beam current of 0.45 nA had dimensions smaller than that of 0.22 nA because of insufficient dwell time.

Best geometry using octagonal shape in area mode was obtained by using the parameters below in Table 5.17.

RIE etched sample which were patterned using parameters above with octagonal shape soft mask is below in Figure 5.31.

Beam current (nA)	0.22
Accelerating voltage (keV)	5
Step size (nm)	20
Clearing dose type	area
Clearing dose amount (uAs), (uAs/cm2)	48

Table 5.17 Exposure parameters for octagonal shape

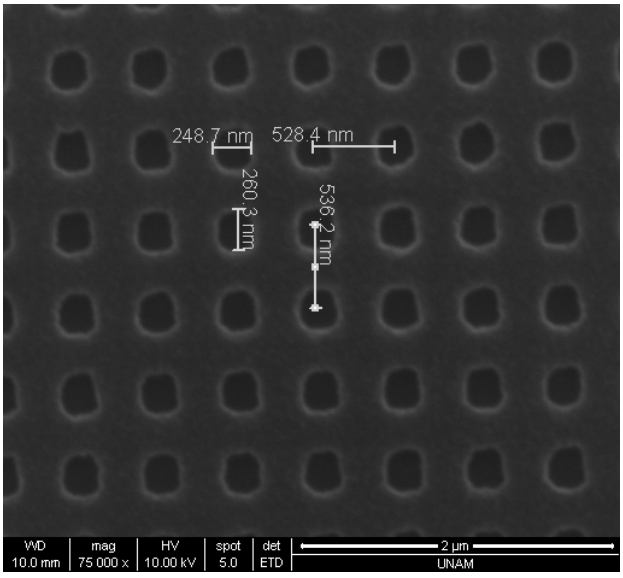

Figure 5.31 PC structure produced by octagonal shaped soft mask, optimum exposure parameters

In order to decrease exposure time, number of edges of the polygon should be decreased. So, rectangular shaped soft mask was used to reduce consumed time. But, this time structures became rectangular. To make structures round, de-focusing technique was used. Below in the figures, structures patterned with different beam currents and varying de-focusing amounts are shown.

For the sample shown in Figure 5.32, 0.22 nA beam current and 20 nm step size was used. De-focusing was done by turning fine tuning knob by 1.5 rounds. Total clearing dose was 60 uAs/cm^2.

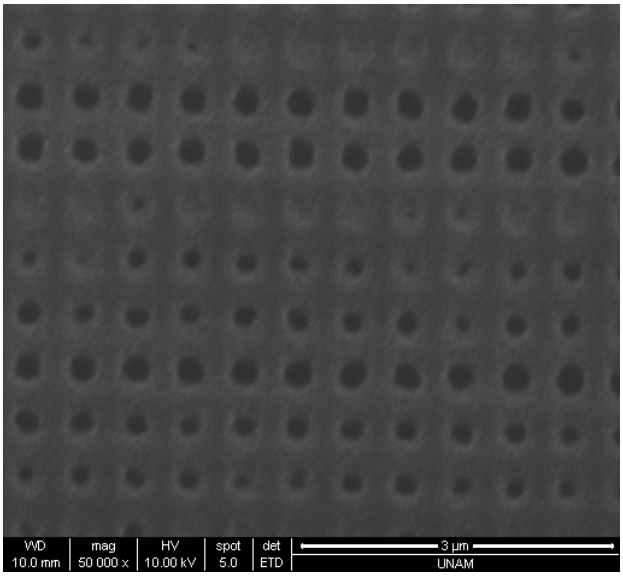

Figure 5.32 Sample patterned with rectangular mode, 1.5 turn de-focusing, 0.22 nA

It is obvious that de-focusing had worked and shapes became round. However, because of the de-focusing, diameters of holes were not constant and reproducibility decreased. This result was also seen in dot dose de-focusing process. Furthermore, beam current of 0.22 nA was not sufficient this time since electron beams were not focused on the surface.

In the Figure 5.33 below, beam current was increased to 0.45 nA. De-focussing ratio is lowered to ¾ turns. Area clearing dose and step size were held constant.

This time all holes were open and 0.45 nA beam current was enough. Structures were again circular; however, de-focusing effects were still in considerable amount.

To reduce distortion, de-focusing ratio was further decreased to ½. Step size, beam current and clearing dose were held constant. Resultant shape is in Figure 5.34.

Because of low de-focus, round shape started to turn into rectangular. Furthermore, side length shapes were longer in one direction, which was direction of beam scan. This kind of pattern was caused possibly by high settling time, which adjusts waiting period before exposing at each step and by charging effects because of high insulation of oxide and sapphire layer under the GaN surface.

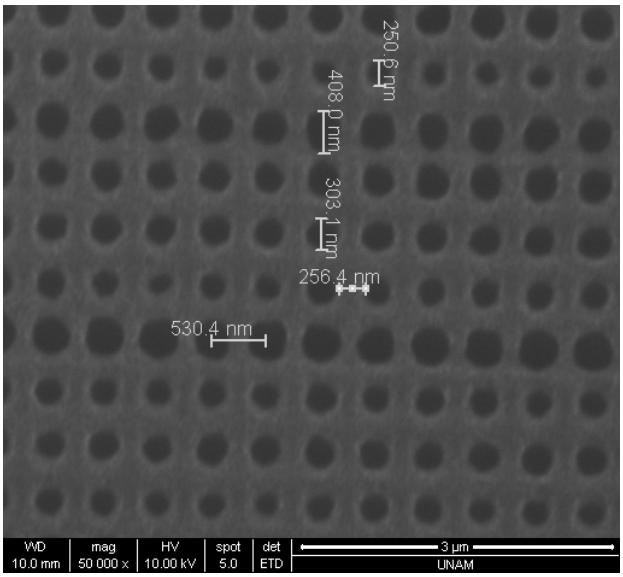

Figure 5.33 Sample patterned with rectangular mode, ¾ turn de-focusing, 0.45 nA

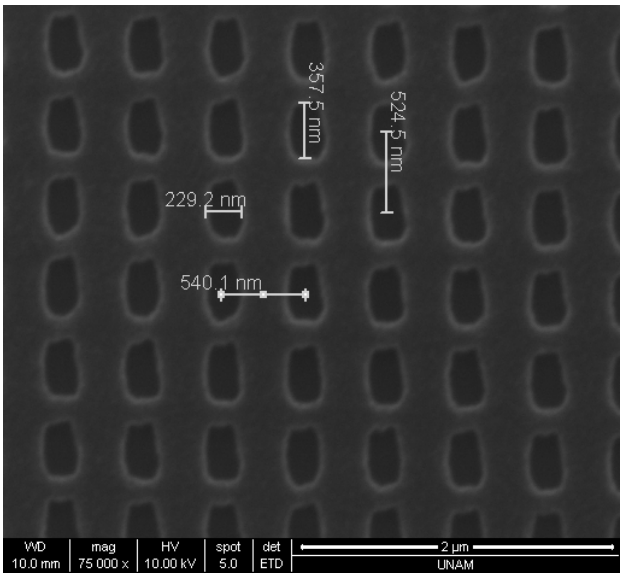

Figure 5.34 Sample patterned with rectangular mode, ½ turn de-focusing, 0.45 nA

Because de-focusing did not work, I stopped using it to produce round shapes. Instead, I continued with the rectangular PC structures since enhancing light extraction by PCs in this thesis work is based on folding Bloch modes over light line by higher order Bragg diffraction and there is no significant difference between circular shape and rectangular shape in terms of diffraction condition. Certainly, there would be a decrease in extraction enhancement, but that would not be as drastic as the case of band gap approach. In band gap generation, symmetry and precision of dimensions are very crucial. However, since it is not expected to see any

band gap formation and band gap effects regarding PC structures with diameter of 260 nm and period of 520 nm embedded in 400 nm InGaN/GaN MQW LED, it is acceptable to use rectangular shapes.

To find optimum exposure parameters that produces finest PC structures, a lot of trials had been done. Below in the Table 5.18, all tried exposure parameters are listed. Since higher than 5 keV was not used at this stage of characterization, all exposure trials were done under beam energy of 5 keV. From the resultant samples, it turned out that effect of step size was minimum. However, it should have proper length regarding PC lattice length and period as it was stated in parameters section in this chapter.

Beam current (nA)	0.11-0.45
Accelerating voltage (keV)	5
Step size (nm)	10-30
Clearing dose type	area
Clearing dose amount (uAs), (uAs/cm2)	20-84

Table 5.18 Exposure parameters variation range for optimization

Best PC structures were obtained using 20 nm step size with around 50 uAs/cm^2 area clearing dose. However, beside geometry, anisotropy is also important. Side walls of PC structures should be as vertical as possible. Therefore, in the next figured samples, one of the considerations were side-wall angle of PC lattices.

For the sample below in Figure 5.35, 0.22 nA beam current, 20 nm step size and 52 uAs/cm^2 beam clearing dose was used under 5 keV beam energy. After exposure and development, sample was etched by RIE oxide etch recipe and GaN etch recipe respectively.

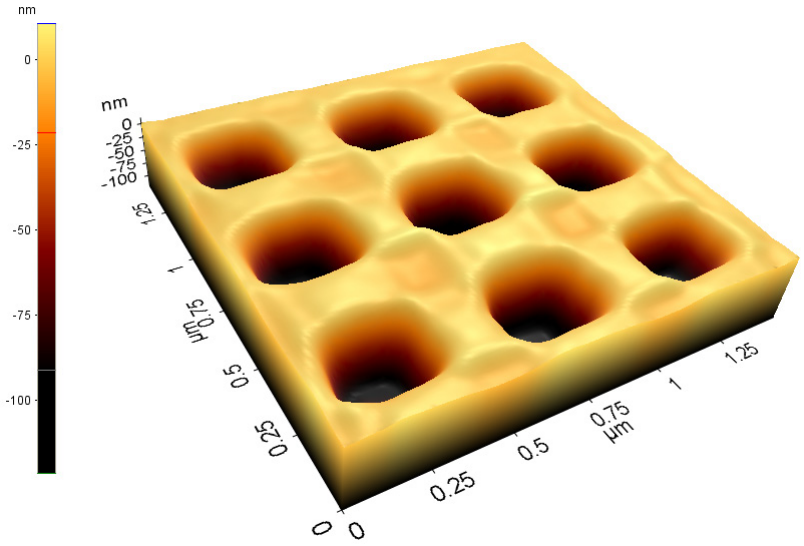

a.

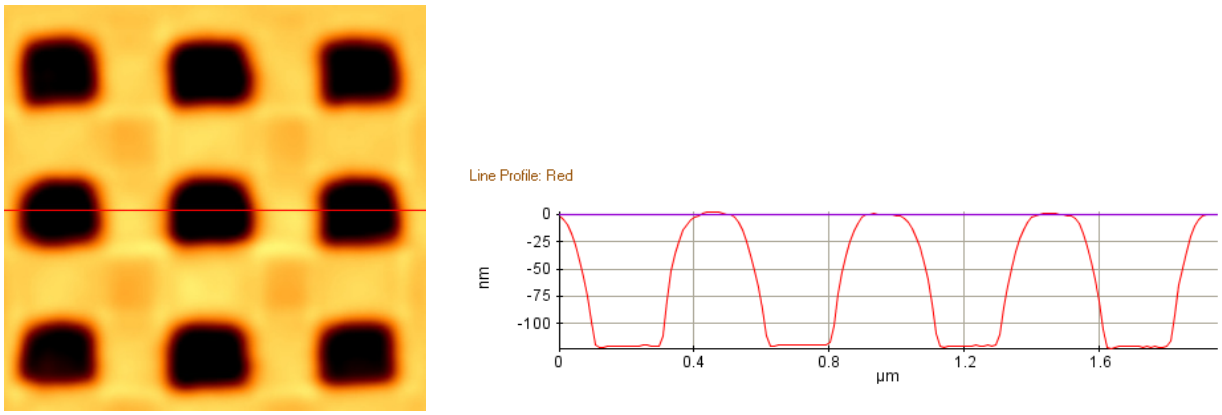

b.

Figure 5.35 AFM picture of rectangular PC structure, 52 uAs/cm^2 beam clearing dose

a. 3D image b. Line profile

PC lattices were not round as expected, but rectangular. Furthermore, lattice length was a little large, but acceptable. Depth of PC was around 100-120 nm which were as intended. Side-wall angle was around 60°. Considering tip effect, angle was expected to be about 70° which was acceptable.

In GaN etching characterization section, etch rate of GaN under 8 ubar pressure, 100 W power and 20 sccm flow rate of CCl_2F_2 freon gas was found to be around 35 nm/min and side-wall angle was around 100°. However, because of RIE lag (129) caused by small feature

sized structures, etch rate was reduced by amount of 10 nm/min and side-wall angle was increased to more than 120°. To see the effect of RIE lag better, one can see the SEM pictures below in Figure 5.36. Both pictures are taken from the same sample, but different areas.

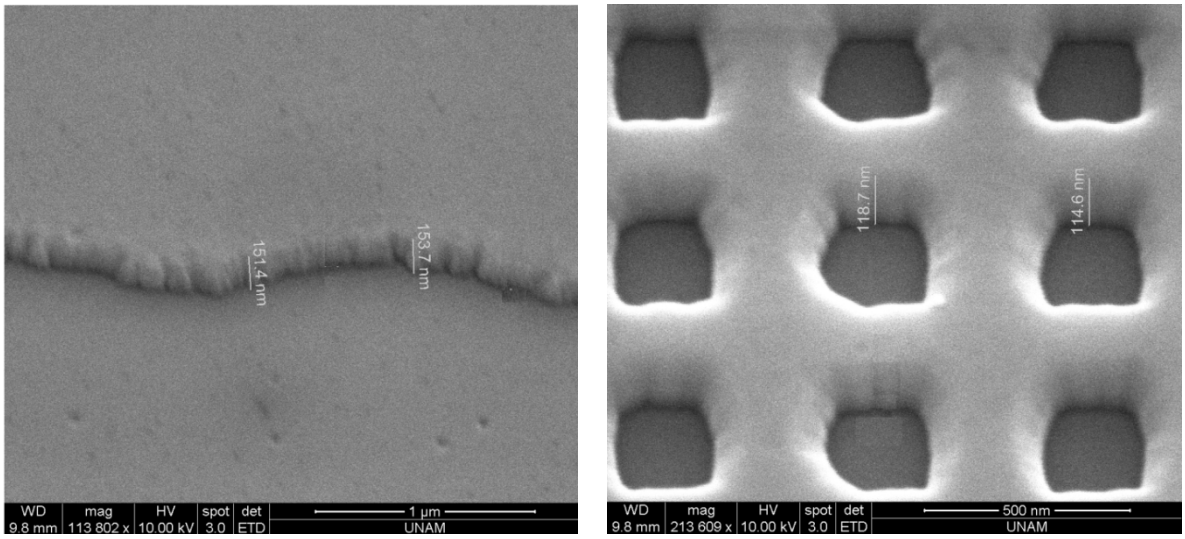

a. **b.**

Figure 5.36 RIE lag effect. a. Etching in larger structures b. Etching in smaller structures

This sample was processed with RIE CCl_2F_2 freon gas with 8 ubar pressure, 100 W power and 20 sccm flow rate for 5 minutes. During GaN etch characterization, etch rate was found to be 32-35 nm/min. In the figure left, dimension of structure was in microns order and total etched depth was around 154 nm which gave 31 nm/min etch rate. However, in case dimensions of features reduced to nanometer scale, as in the figure right, total etch depth reduced to around 114 nm, which gave 23 nm/min etch rate.

To reduce the PC length, lower values of area clearing dose were used. Sample figured below had 65 nm SiO_2 sacrificial mask layer which were grown by oxide-1 growth recipe and 70 mm PMMA resist. Exposure parameters were 48 uAs/cm^2 area clearing dose, 20 nm step size, 0.22 nA beam current, 5 keV beam energy. Pattern was triangular PC lattice type with side length of 260 nm and period of 520 nm. After exposing, PMMA was developed by using MIBK:IPA (1:3) developer for 30 seconds and rinsed in IPA for 30 seconds respectively.

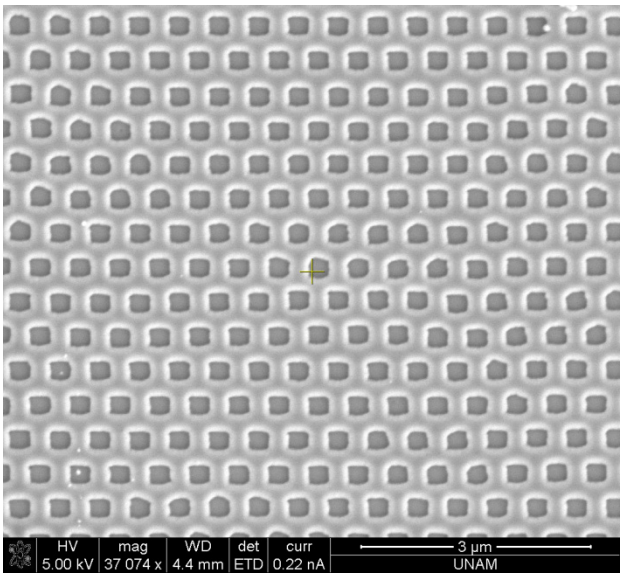

Figure 5.37 Rectangular shape, triangular PC lattice, after PMMA development

Period and length of PC lattice sides were acceptable. After development, sample was processed by RIE in order to transfer patterns on PMMA to first oxide and then GaN layer. Therefore, RIE oxide etch recipe and GaN etch recipe were used for 3 and 5 minutes respectively. Finally, oxide layer was removed by dipping in HF solution. Resultant SEM and AFM measurements were given in Figure 5.38 and Figure 5.39.

Even though lattice length, lattice period and PC depth were acceptable, side-wall anisotropy had to be increased. In order to decrease dwell time, beam current had to be increased so that scattering of electrons in the resist would be lowered which would result in reduced undercut and enhanced resolution with anisotropy.

Samples were exposed with 60 uAs/cm^2 area clearing dose beam. However, PC lattice sizes increased that time. Therefore, optimum clearing dose at 5 keV was found to be 52 uAs/cm^2.

Optimized e-beam exposure parameters at beam energy of 5 keV were stated in Table 5.19 below. Resultant structure had 120 nm depth PC square lattice holes with side-wall angle of 115° $\pm$ 5°. At the middle depth of PC holes, edge length was around 260 nm and period was 520 nm. All dimensions were acceptable, therefore final exposure parameters were held at beam current of 0.22 nA, step size of 20 nm, area clearing dose of 52 uAs/cm^2 for 5 keV beam energy.

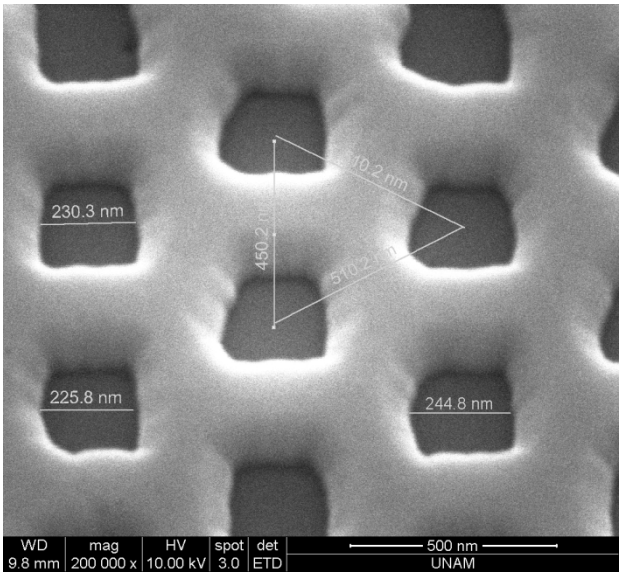

Figure 5.38 AFM picture of triangular PC lattice

Beam current (nA)	0.22
Accelerating voltage (keV)	5
Step size (nm)	20
Clearing dose type	area
Clearing dose amount (uAs), (uAs/cm2)	52

Table 5.19 Optimized e-beam exposure parameters at 5 keV

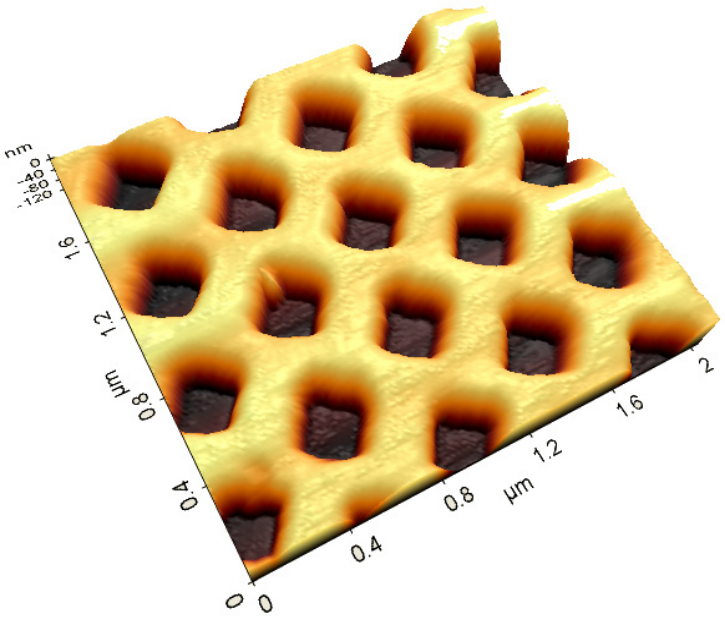

a.

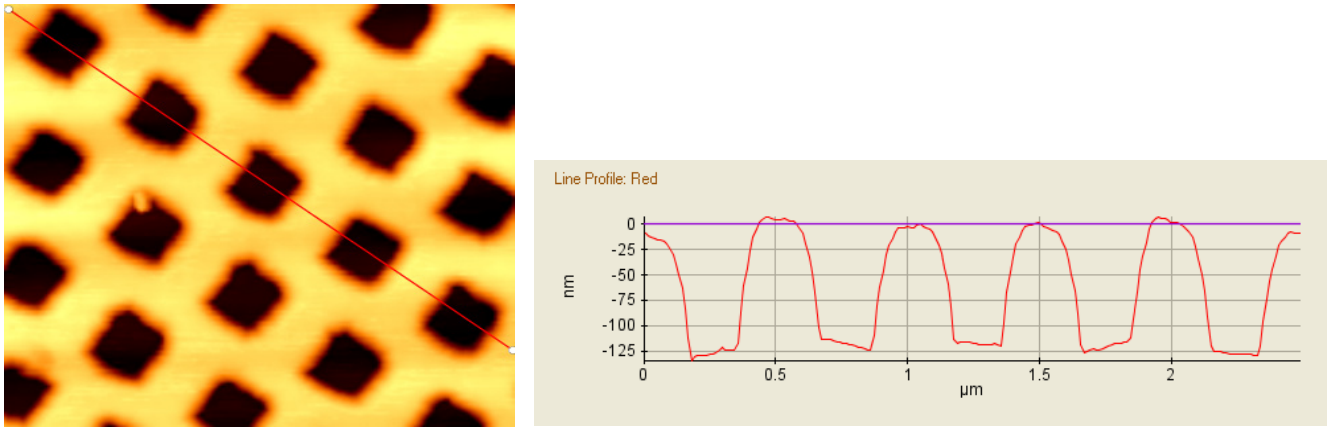

b.

Figure 5.39 AFM pictures of triangular PC lattice type a. 3D image b. Line profile

5.7 Photonic Crystal Fabrication embedded in InGaN/GaN MQW LED

Photonic crystal lattice parameters were optimized regarding simulation results. Diameter and period of the PC structures were designed to be 260 nm and 520 nm respectively. In order to reduce the etch effects caused by RIE process and electron diffusion occurs during e-beam lithography, area of etching was decreased by designing PCs with a large period and low filling ratio. Two types of PC lattice types were fabricated, triangular and square lattices. Both structures had filling ratio of around 0.2. Although maximum enhancement was expected for depth of 180 nm PC structures which had been obtained from simulations, because of RIE lag, PCs were patterned with depth of around 100-120 nm. In order to minimize non-radiative recombination effect, holes are not etched into active layer [102].

It was found out that beam energy levels of 10 keV and 20 keV did not harm the quantum well region considerably after trials with SiO_2 sacrificial mask layer with PMMA were done. Therefore, final PC structures were patterned by using 10 keV acceleration voltage which would help for reduced scattering, decreased under-cutting, increased resolution and therefore enhanced side-wall anisotropy. Since beam energy was doubled, beam current would also be around two times of that of 5 keV. Thus, final characterization steps were done around 90-100 uAs/cm^2 for beam energy of 10 keV. In order patterning to finish fast, rectangular shape without using de-focus was used. Final optimized exposure parameters were given below in the Table 5.20

.

Beam current (nA)	0.16
Accelerating voltage (keV)	10
Step size (nm)	20
Clearing dose type	area
Clearing dose amount (uAs), (uAs/cm2)	94

Table 5.20 Optimized exposure parameter for PC fabrication at 10kV

In order to fabricate PCs on InGaN/GaN MQW LED device, 90 nm of SiO_2 was grown on top p layer of the device as a sacrificial layer for transferring PC patterns from PMMA layer above to GaN layer below. This oxide layer was grown by plasma enhanced chemical vapor deposition (PECVD) system by using oxide-1 growth recipe which is given in the Table 5.13. Afterwards, 70 nm PMMA A2 resist of e-beam lithography was coated by spinner at 3000 rpm on the oxide layer. Details about PMMA resist coating was given in Table 5.11. After pre-baking the resist, PC structures were patterned by e-beam lithography using optimized exposure parameters above in Table 5.20. After exposure, exposed PMMA was developed using MIBK:IPA developer solution in 1:3 volume ratio for 30 seconds and subsequently rinsed in IPA for 30 seconds, following a fast low pressure nitrogen flow drying. In order to harden top PMMA patterned layer, sample was post-baked at 100 °C for 90 seconds. Next, sample was etched in RIE system using oxide etch recipe for 4 minutes given in Table 5.3. In this step patterned PC structures on PMMA layer were transferred to oxide layer. Since oxide layer is more durable than PMMA under CCl_2F_2 RIE etch, it was used as sacrificial layer. As a final step, GaN etch recipe given in Table 5.3 was used to transfer PC patterns on to LED device.

Final structure had full width half maximum (FWHM) PC lattice side length of 260 nm and period of 520 nm. PC depth was around 100 – 120 nm. Side-wall angle of PC structures were about 60° – 65° which were obtained from AFM. Considering the conic angle of the tip, side-wall angle of PCs was expected to be about 70° – 75°. Side-wall angles about 75 degrees are acceptable [7]. Representative AFM pictures of both square PC lattice and triangular PC lattice can be seen in Figure 5.40 and Figure 5.41 respectively.

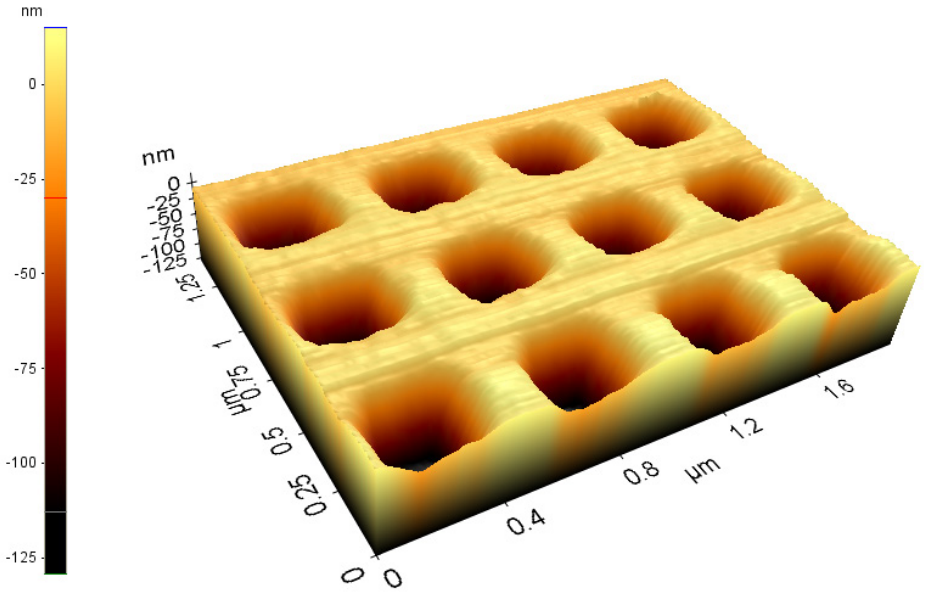

a.

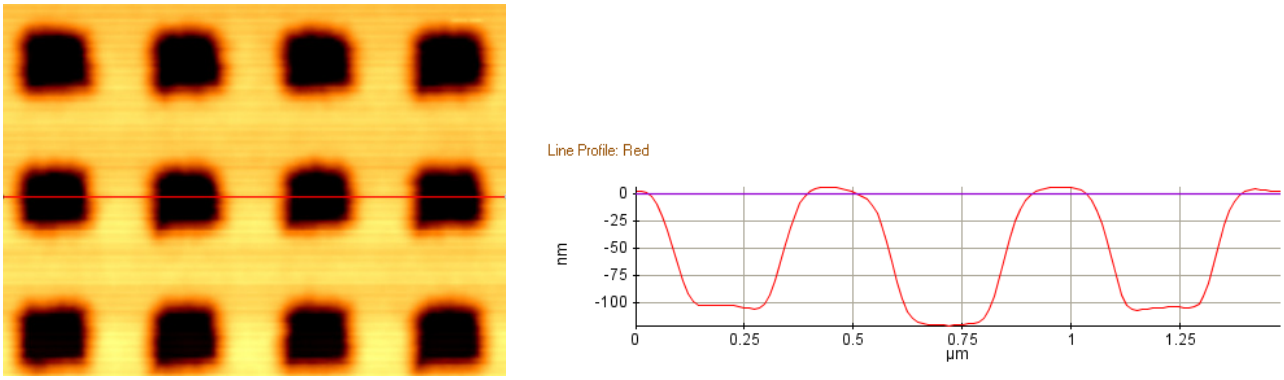

b.

Figure 5.40 Representative AFM images of fabricated PC structures a. 3D image b. Line profile

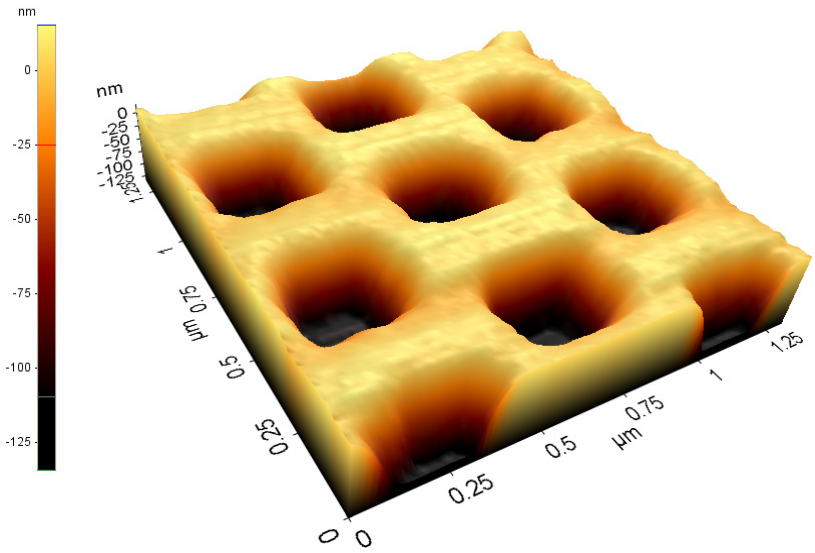

a.

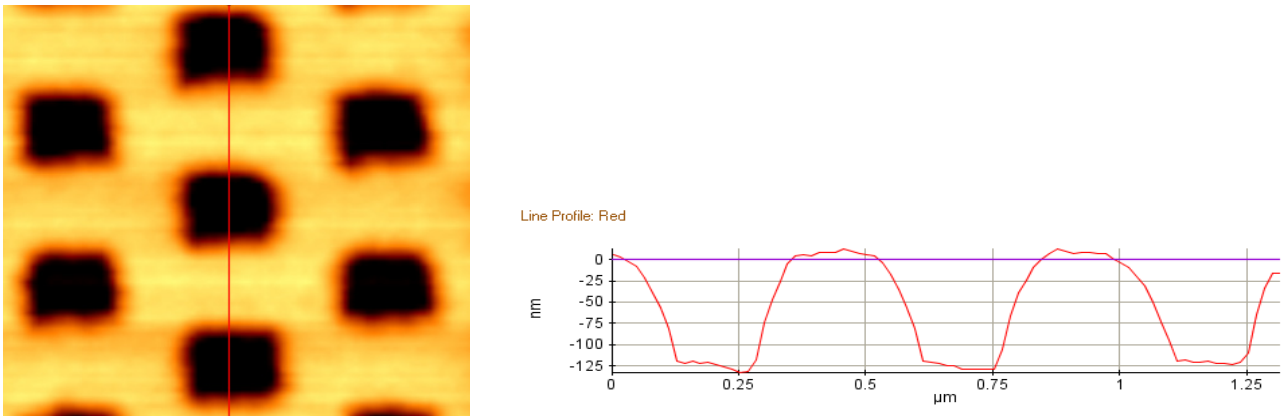

b.

Figure 5.41 Representative AFM images of fabricated PC structures a. 3D image b. Line profile

Chapter 6

6. Measurement and Simulations

6.1 Introduction and measurements

In this chapter, processed LEDs and embedded PC structures are studied regarding electro-luminescence, I-V measurements and photo-diode optical power measurements, CCD camera images and two dimensional and three dimensional simulation results. Material characteristics such as absorption and transmission curves and refractive index measurements are also stated which had been produced by using spectrophotometer and ellipsometer.

Power obtained from photo-diode measurements and three dimensional Finite Difference Time Domain (FDTD) simulations were compared and concluded that they were in agreement considering the damaging of p layer and quantum well region by e-beam and etching processes, high contact resistivity and assumptions made for the ease of calculations in simulations.

Because of RIE etching steps, unoptimized p type dopant activation and metallization processes, resistance of the chips increased in considerable amount. Furthermore, as it was stated in chapter 3, thin n layer of the device structure and n-metallization on AlGaN layer might also have caused the resistance to increase. Therefore, turn on voltage of devices was high and current passed through the MQW chips was very low. This resulted in inhomogeneous current spreading and light extraction especially for low current values as seen in Figure 6.1 below.

As the current was increased, spreading and light extraction became more homogenous. However, because of high turn on voltage, device cannot withstand current rates higher than a few milliamperes. Therefore, I-V measurements, CCD camera shots and photo-diode optical power measurements were done under current of 1 mA.

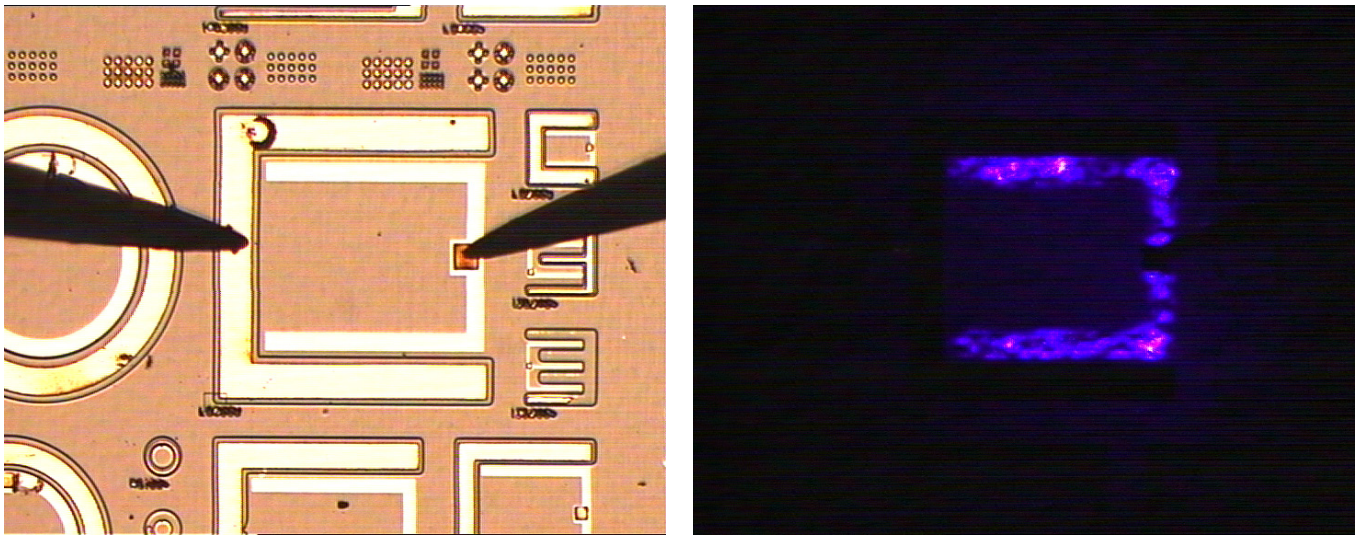

Figure 6.1 Inhomogenous current spreading because of high contact resistivity

6.1.1 Refractive Index Measurement

Refractive index of InGaN/GaN LED wafer was found by ellipsometer in the range of 350 nm - 450 nm. Regarding process was stated in Figure 6.2 below.

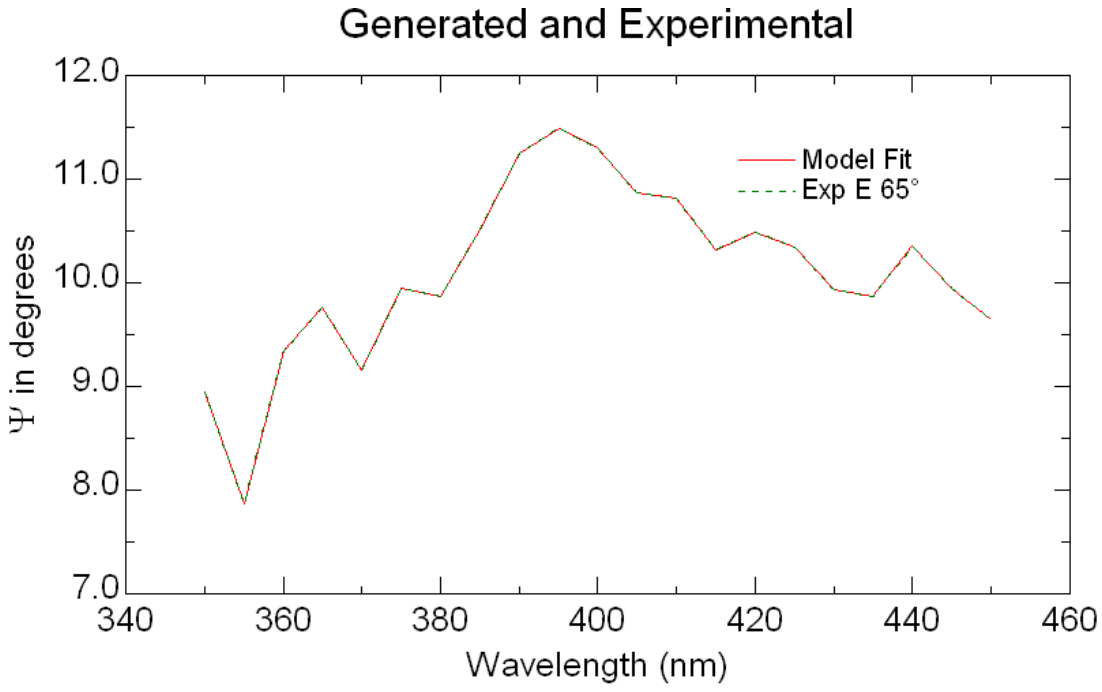

Figure 6.2 Refractive index calculation by ellipsometer

Refractive index of the wafer was found to be 2.7 at around wavelength of 400 nm.

6.1.2 Absorption and Transmission Curves

Absorption and transmission characteristics of the LED-1 wafer was calculated and plotted by using spectrophotometer in the range of 200 nm – 900 nm. Regarding curves are stated in Figure 6.3 and Figure 6.4 below.

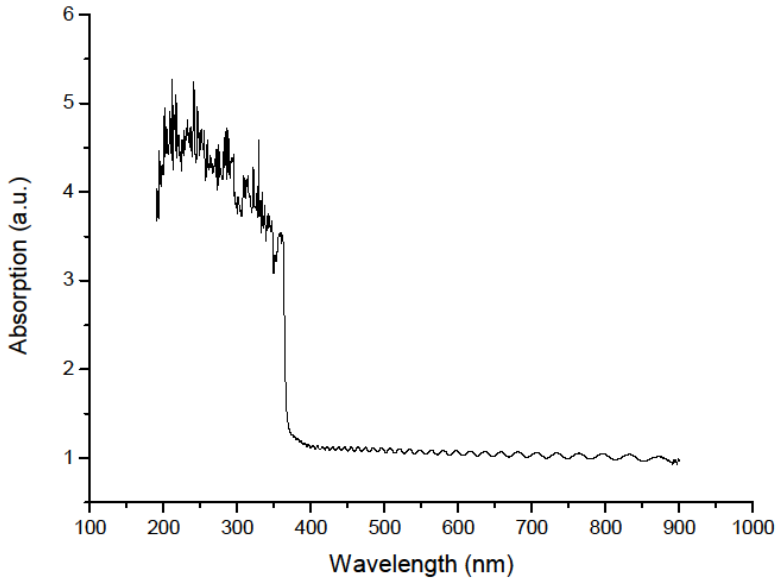

Figure 6.3 Absorption curve of LED-1 wafer

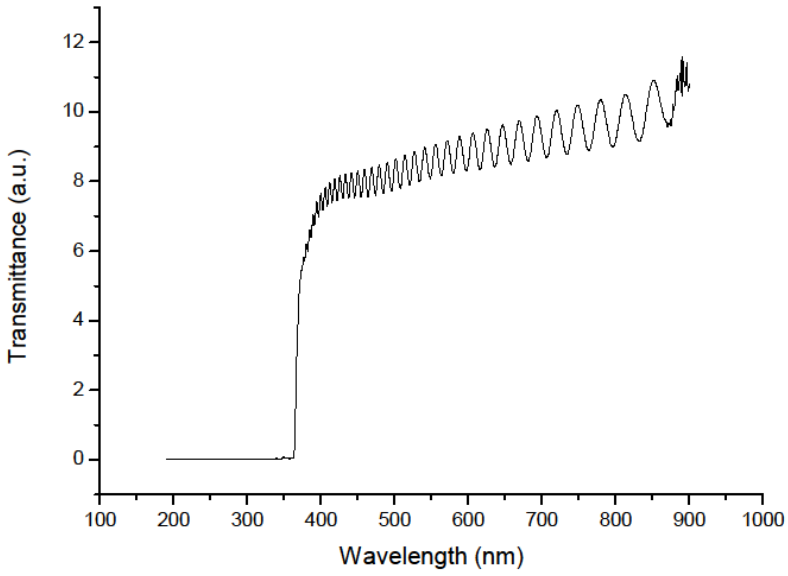

Figure 6.4 Transmission curve of LED-1 wafer

6.1.3 I-V Measurements

I-V measurements of LEDs were done using probe-station. Because of high resistivity, very high turn on voltages were examined. One can find p-p, n-n I-V characteristics for determining resistivity below.

As doping level is increased, resistivity is decreased. In GaN based devices, because of lower concentration of p type dopants, p layer resistivity is higher than n layer resistivity. Regarding the wafers processed in this thesis work, while n doping is around $2x10^{18}$, p doping is around $5x10^{17}$. Furthermore, unoptimized p type dopant activation increased resistivity more. Below in Figure 6.5 and Figure 6.6, I-V contact resistance characteristics of n-n and p-p layers are given respectively.

From the I-V characteristics of n-n and p-p layers, resistivity difference can be examined clearly. While current can pass through n to n layers with almost no threshold, threshold value is around 5 V for p-p region. Slope of I-V plot regarding p-p characteristics is much lower than that of n-n.

As it is clear from the Figure 6.7, turn on voltage of the LED was higher than 7 V and it passed current of 1 mA at 11.3 V. High voltage values reduced the life time and endurance of the chips that were processed. Therefore, current was not increased more than 1.5-1.6 mA in order to prevent break-down of the device because of excessive heat or shorting caused by metal diffusion. As stated in chapter 3, InGaN/GaN MQW LEDs are prone to be shorting.

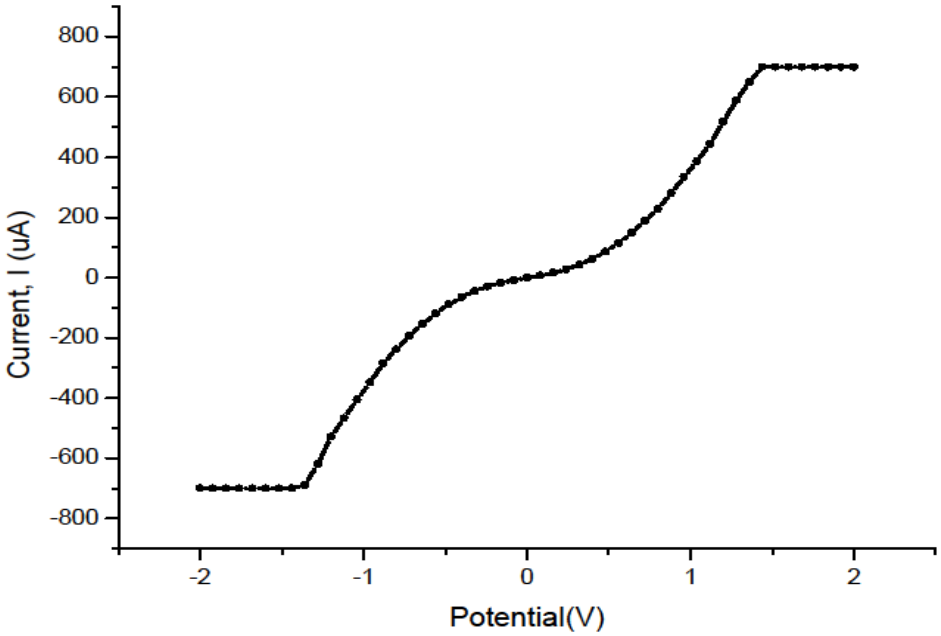

Figure 6.5 I-V characteristics of n to n layer

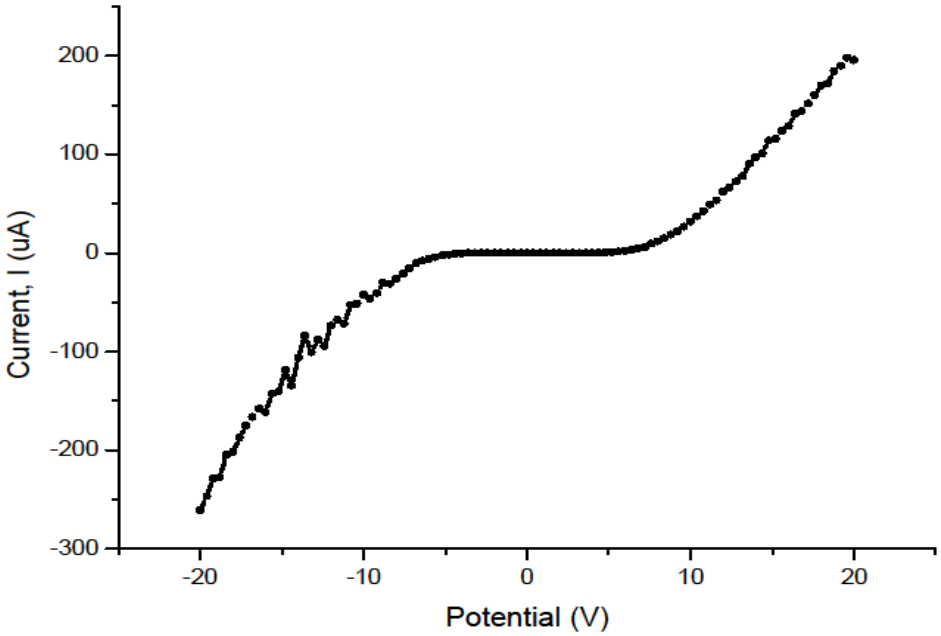

Figure 6.6 I-V characteristics of p to p layer

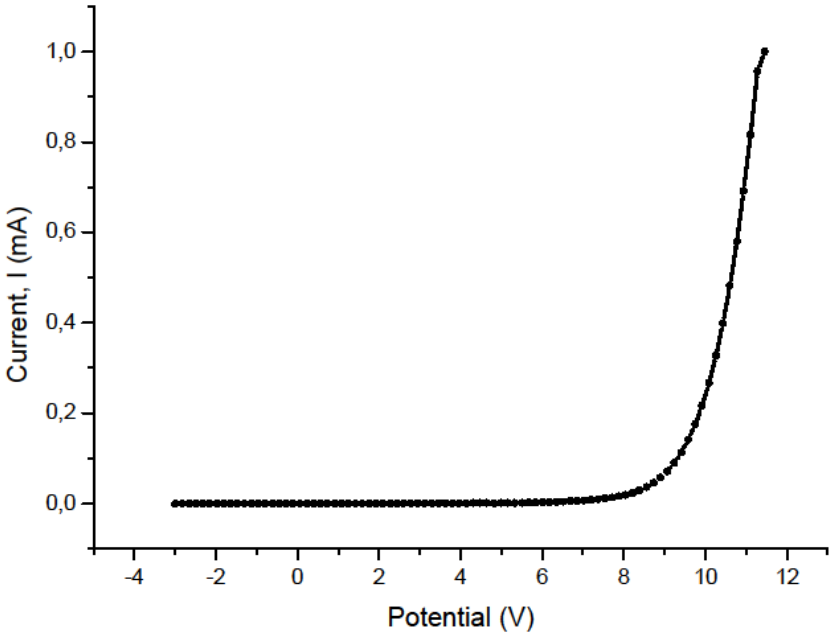

Figure 6.7 I-V characteristics of an LED chip processed in this thesis work

Since scope of this thesis work is not based on electrical properties of LEDs but optical properties, high turn on voltage and low values of current passed through the device is tolerable and acceptable. Below in the Figure 6.8, I-V characteristic of LED with and without PC structures are shown in the same graph. As stated previously, PC structures etched into p layer have some draw-back like increasing working temperature by decreasing effecting heat transfer area, decreasing current injection and increasing resistivity of the device because of reduced p layer material. From the Figure 6.8, turn-on voltage had not changed considerably. However, slope of the I-V curve was slightly decreased for the chip with LED structure which confirms the statements regarding draw-backs of PC structures.

6.1.4 Electro-luminescence spectra

In this thesis work, electrons in the MQW region were excited by applying electrical potential, which is called electro-luminescence. Two different led wafers which had various layer structures were processed. These LED structures were outlined in chapter 2 and Chapter 3. Wafers had 5% and 8% Indium concentration respectively which illuminates at 390 and

410 nm. Electro-luminescence spectra of both LED wafers are stated below in Figure 6.9 and Figure 6.10.

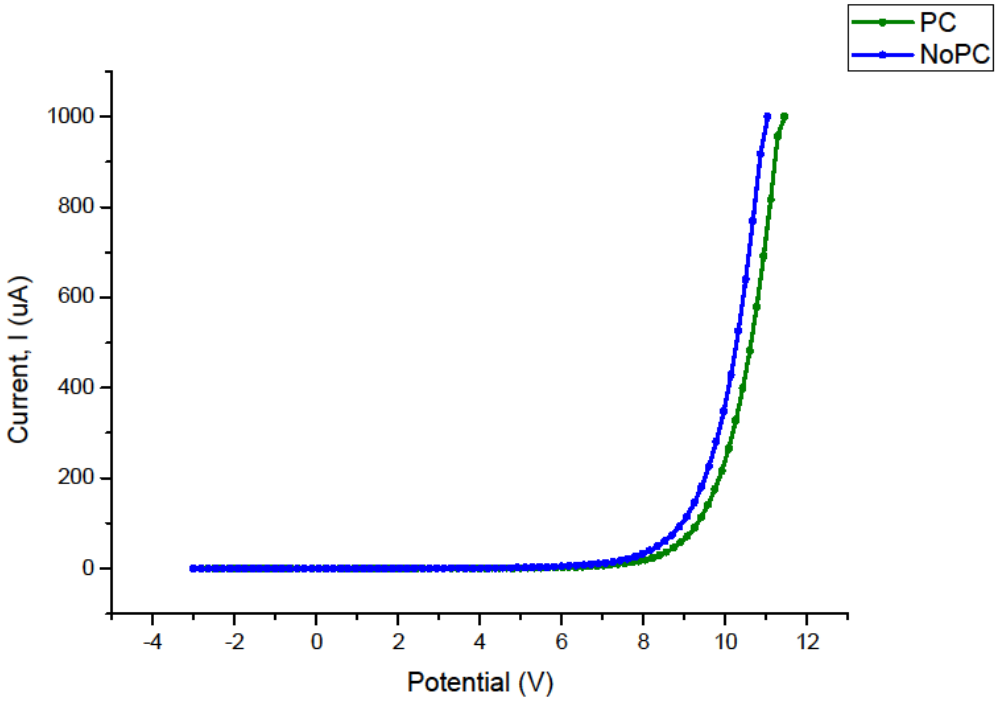

Figure 6.8 I-V Characteristics of PC/NoPC LED chips

Luminescence peaks of the LEDs were at 390 nm and 410 nm. Photonic crystal structure was patterned to the LED chip which had peak at 390 nm. Corresponding electro-luminescence spectra of this PC LED is figured below in Figure 6.11. This LED with PC had a peak at 387 nm, with a 3 nm blue-shift with respect to that of LED without PC structure.

6.1.5 Optical Power Measurements

Photonic crystals enhance extraction efficiency of LEDs. PC structure in this thesis work was designed to have lattice diameter of 260 nm, lattice period of 520 nm and filling ratio of 0.2 and 0.23 respectively for square lattice and triangular lattice PC types. In order to evaluate extraction efficiency enhancement of PC device with respect to non-PC LED, optical power measurements were done by using a silicon photodiode which had response for electromagnetic spectrum wavelength range between 190 nm and 1100 nm. Responsivity of the photodiode at about 400 nm was 0.18 A/W. Photodiode was placed on top of the LED with a distance such that light collected by diode would be in numerical aperture of 0.25.

Below is the optical power characteristics of LEDs with and without PC structures in Figure 6.12

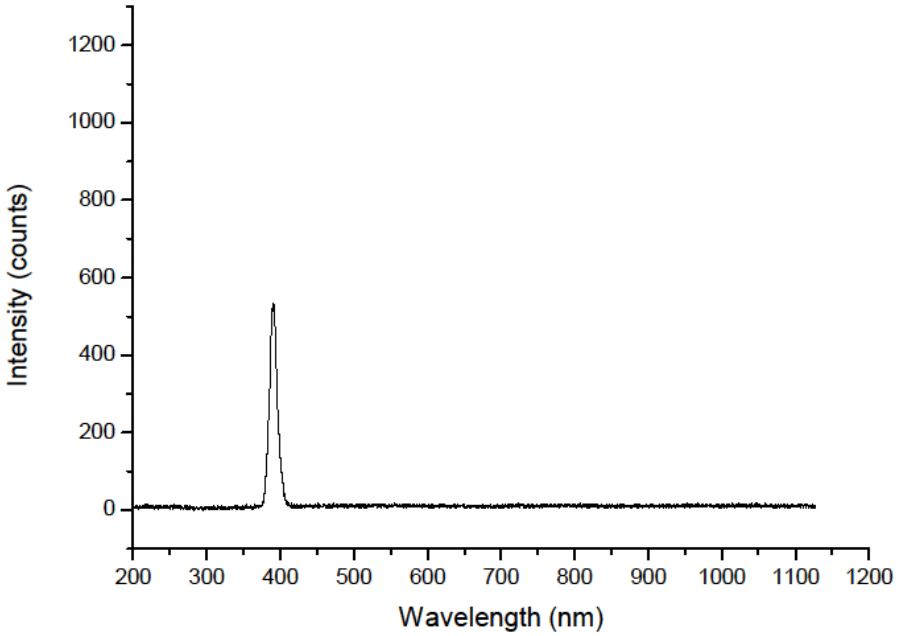

Figure 6.9 Electro-luminescence characteristic of 390 nm LED without PC structure

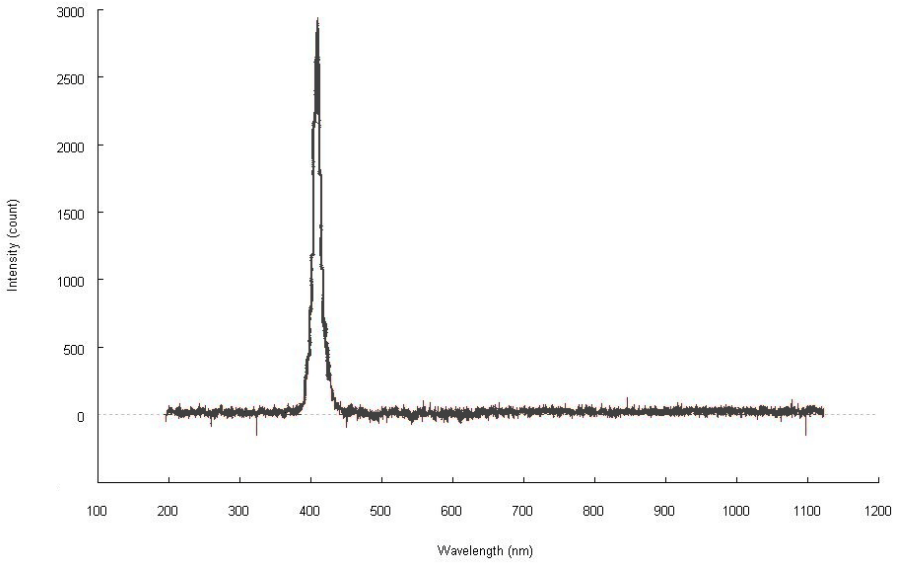

Figure 6.10 Electro-luminescence characteristic of 410 nm LED without PC structure

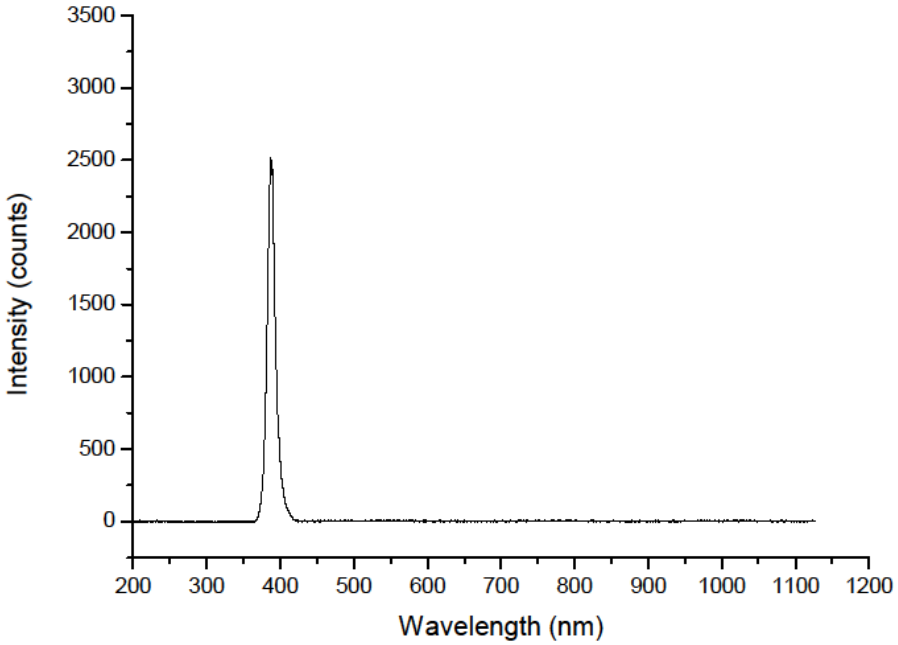

Figure 6.11 Electro-luminescence characteristic LED with PC structure, peak is at 387 nm

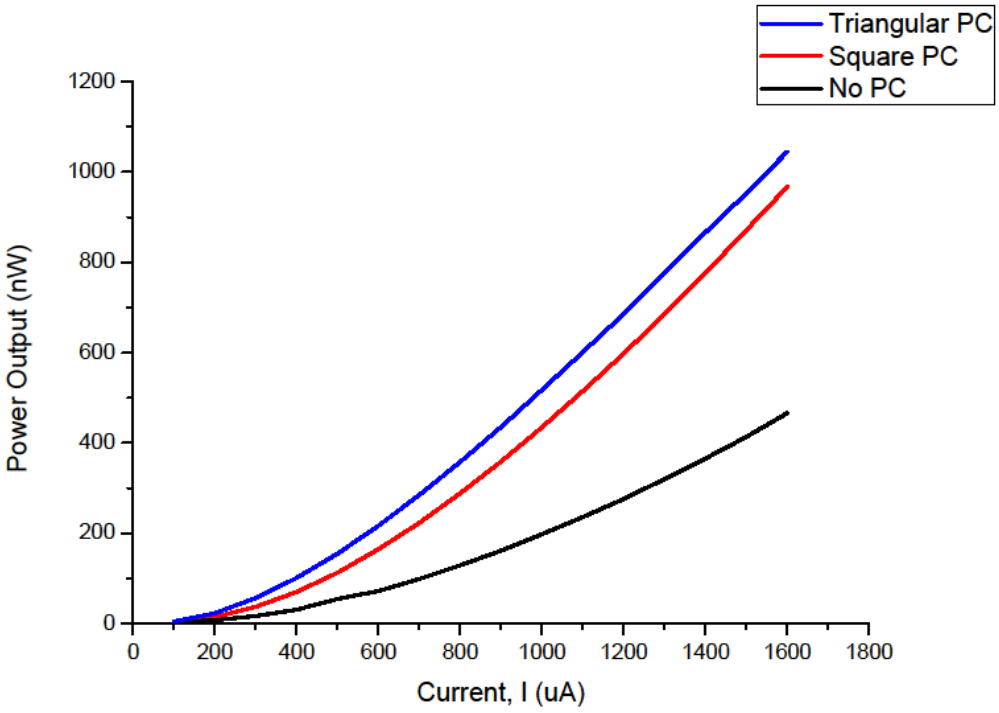

Figure 6.12 Optical power characteristics of LEDs with and without PC structures

LED devices with patterned PC structures showed more light output. Since LED wafer quality and growth layer structures were not optimized and electrical properties were not good, current passed through LEDs were not increased beyond 1.6 mA in order not to damage devices. At around 1 mA, light output homogeneity was acceptable. Therefore, extraction efficiencies of all LEDs in this thesis work were evaluated at 1 mA. At this current value, extraction efficiency enhancements of triangular PC lattice and square PC lattice were about 2.5-2.6 and 2.1-2.2 respectively with respect to LED device without PC patterning.

6.1.6 CCD Camera Snapshots

For visualization concern, photonic crystals were captured under CCD camera using probe-station. As clearly seen from the Figure 6.13 and Figure 6.14, PC structures fold light into leaky modes so that otherwise trapped light in the GaN layer couples out from the device. Pictures were captured by an optical lens with numerical aperture of 0.25.

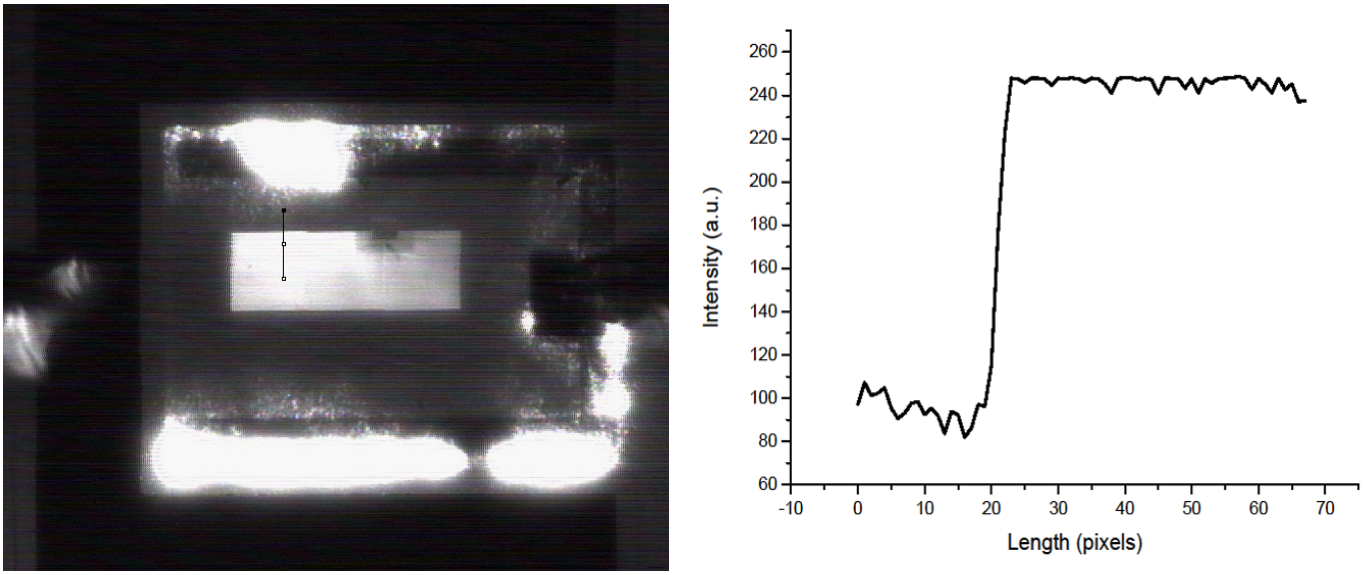

a. **b.**

Figure 6.13 a. CCD image of triangular PC lattice captured in black&white mode b. Intensity plot along the black line

For triangular PC lattice type, intensity contrast was about 2.5-2.6 as seen in Figure 6.13. It is also apparent that light homogeneity and current spreading was not good because of the reasons stated before.

Below in Figure 6.14 are some other PC patterned LED devices. Light intensity was quite increased along PC patterned areas.

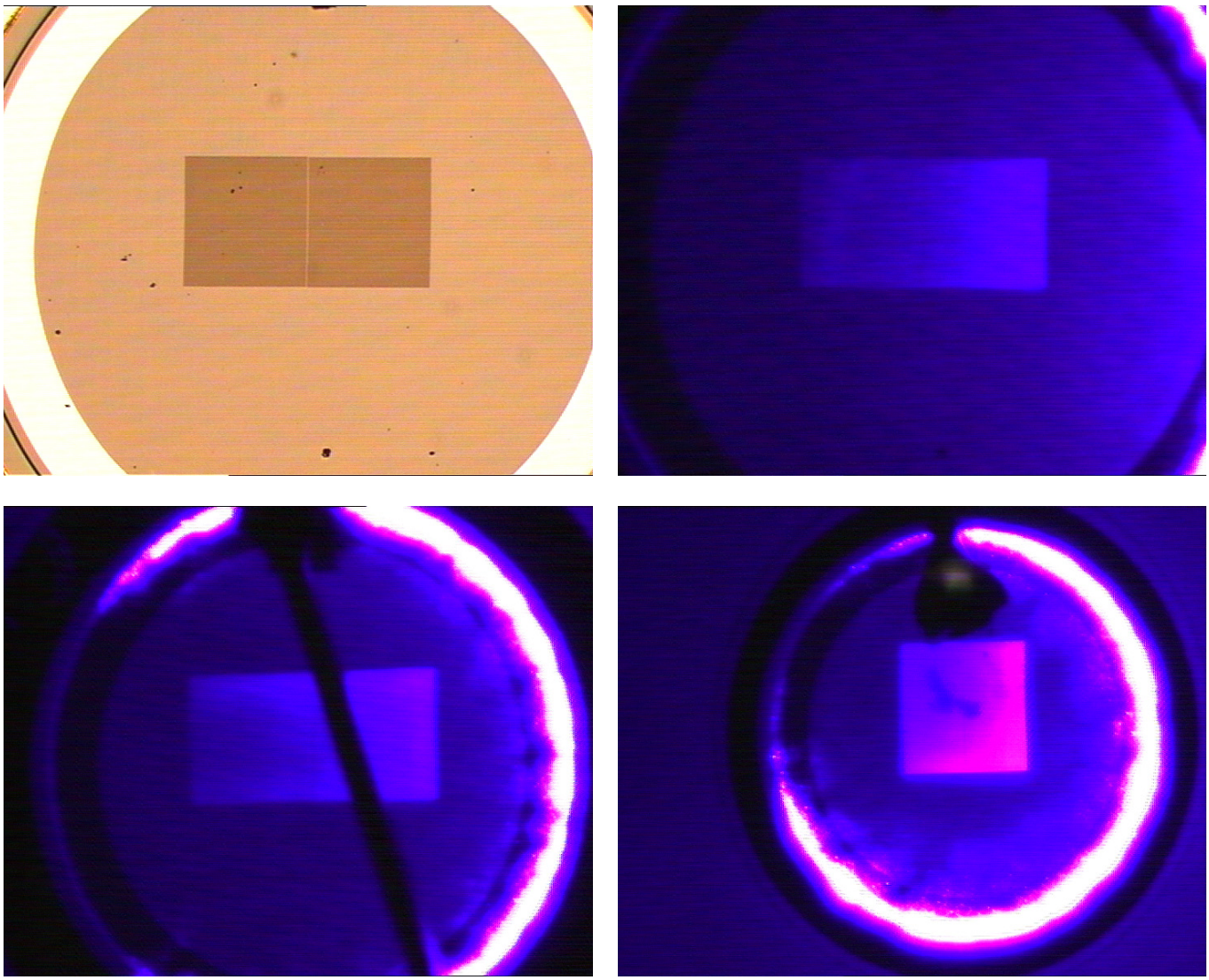

Figure 6.14 Some other PC patterned LED devices under forward bias

6.2 Simulations

Several simulations were completed during this thesis work regarding photonic crystal structures embedded in InGaN/GaN light emitting diodes. Methods which were used in simulations included finite difference time domain (FDTD), plane wave expansion (PWE), and integral method.

FDTD method was used to understand the light propagation in the system of interest and to find out the possible maximum extraction efficiency of the system; PWE method was used in

order to calculate band dispersion diagrams of different structures; and integral method was to calculate transmission ratios of different photonic crystal structures in a faster way to get an idea for the starting point of designing. Since integral method was fast, simulating photonic crystal structures by sweeping all the design parameters such as filling ratio, depth, and lattice type by integral method was done and PC structures were fabricated regarding results of this simulation sweeping results.

6.2.1 Band Structures and Band Gaps

In order to find the band structures of different PC structures, plane wave expansion model was used in two dimensions since it is fast and reliable. PWE method is time independent and takes Fourier expansion of dielectric function ε(r) with electro-magnetic field and calculates eigen-value equation reduced from Maxwell equations numerically. PWE method uses periodic boundary condition for the boundaries of the simulation area. Results of the simulation are basically eigen-values which are frequency of the modes; and eigen-vectors that are mode profiles. Then, photonic band structure is drawn by using eigen-values as a function of edge wave-vector regarding irreducible Brillouin zone.

One drawback of the PWE method is convergence problem if the system has large dielectric contrast. Furthermore, PWE method is applicable for only non-dispersive materials where material properties do not change with frequency of the field. Since basic assumption for the system in the scope of this thesis is being non-dispersive, PWE method can be used.

In order to find maximum band-gap ratio possible that the system could possess, filling ratio which is one of the most important design parameters, was swept. Filling ratio defined as the ratio of total areas of PC lattice holes and unetched dielectric region. Reason for using gap ratio rather than maximum band-gap width is because Maxwell equations are scalable. Although gap width changes with up-scaling or down-scaling, band gap ratio stays constant. Therefore, studying band gap ratio is a better way of designing since it does not vary with system dimensions.

Filling ratio was swept in a large interval, from 0.05 up to 0.95, for both square and triangular PC hole lattice types embedded in dielectric with refractive index of 2.7. There occurred no TE gap for any interval of filling ratio for square lattice. This is because the number of translational symmetry directions in square PC lattice is just two and it is not enough to open

a gap with a refractive index difference of 1.7. However, after filling ratio of 0.7, there are four TM gaps with gap/mid-gap ratios of 0.02, 0.03, 0.05 and 0.06~0.2 as seen in the Figure 6.15 below.

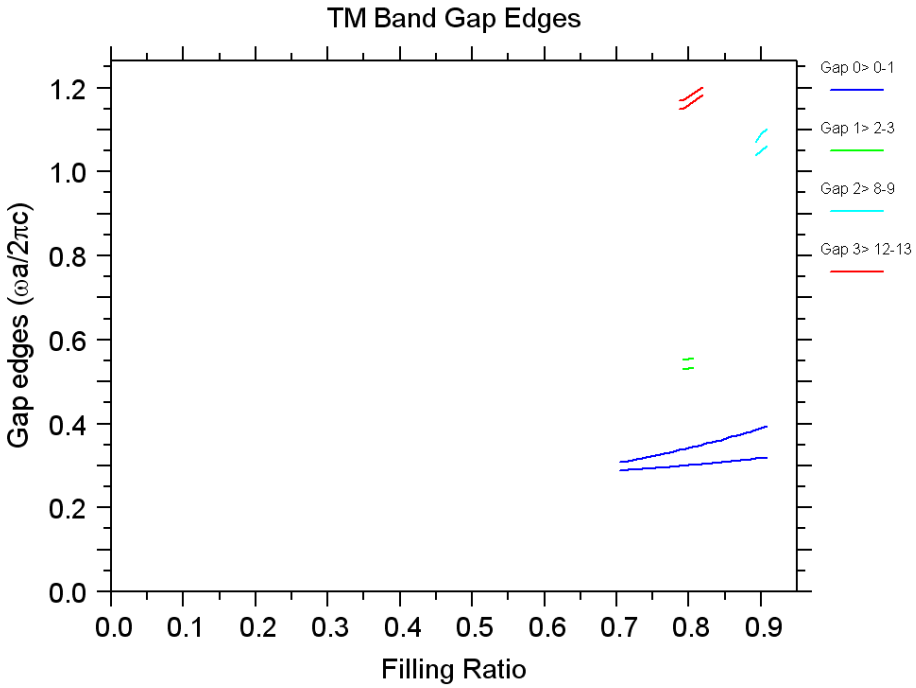

Figure 6.15 TM Band Gap Edges for different filling ratios in square PC lattice

For the case of triangular lattice, since number of symmetry directions are increased, enhanced band gap properties are expected. In the Figure 6.16, filling ratio was varied between 0.05 and 0.95. PC lattice holes were embedded in dielectric with refractive index of 2.7 in triangular formation geometry.

As expected, large TE band gap was opened for triangular lattice holes. To evaluate the strength of the gap, band gap ratio versus filling ratio diagram is figured below inFigure 6.17. Gap ratio is calculated for every filling ratio point by taking the frequency of the gap center divided to the photonic band gap width. Since it is dimensionless, gap ratio stays constant with respect to variation of system scale. As the gap ratio is increased, so the strength of the band gap of the photonic system since the amplitude of evanescent waves decreases as they propagate in the gap region and they are attenuated more as the gap width is increased.

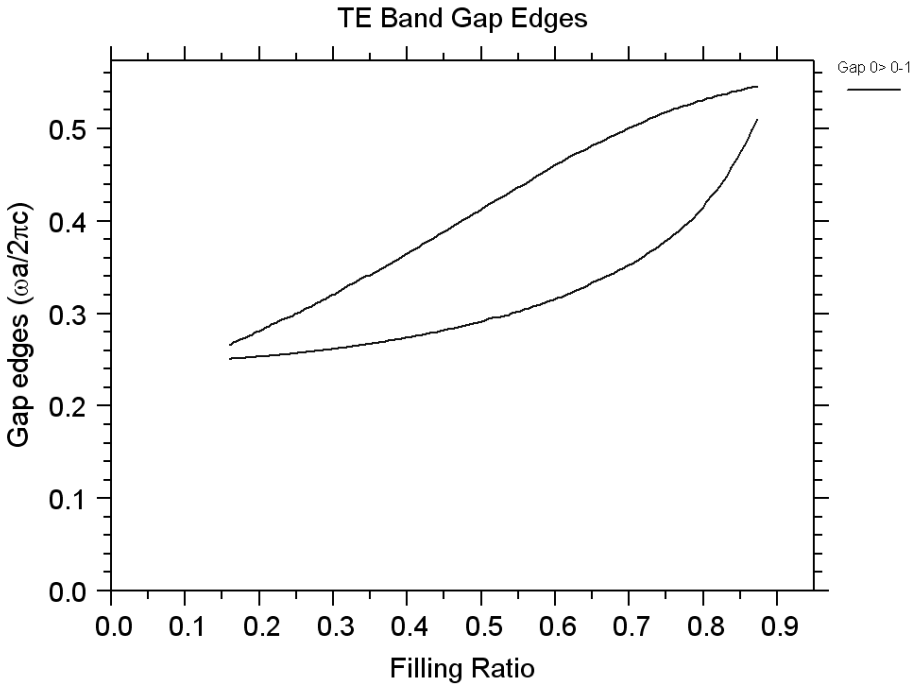

Figure 6.16 TE Band Gap Edges for different filling ratios in triangular PC lattice

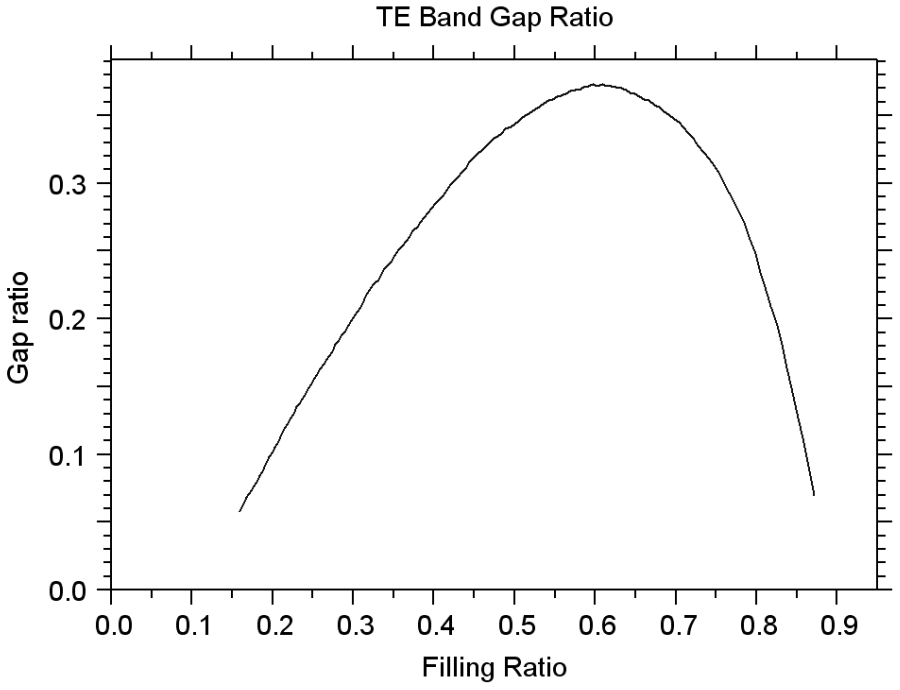

Figure 6.17 TE band gap ratio with respect to filling factor for triangular hole lattice

In chapter 4, it was stated on photonic band gap strength is studied. From the gap width figure below, maximum gap width obtained was around filling ratio of 0.6 which gave ~38% of gap width.

As stated in chapter 4, holes in dielectric mainly supports TE band gap, however, for high filling ratios, TM mode may also be supported because of isolated dielectric material among holes. In the Figure 6.18, TM band gap also occurred for filling ratios higher than 0.5 for the same triangular lattice structure, with a smaller gap width though.

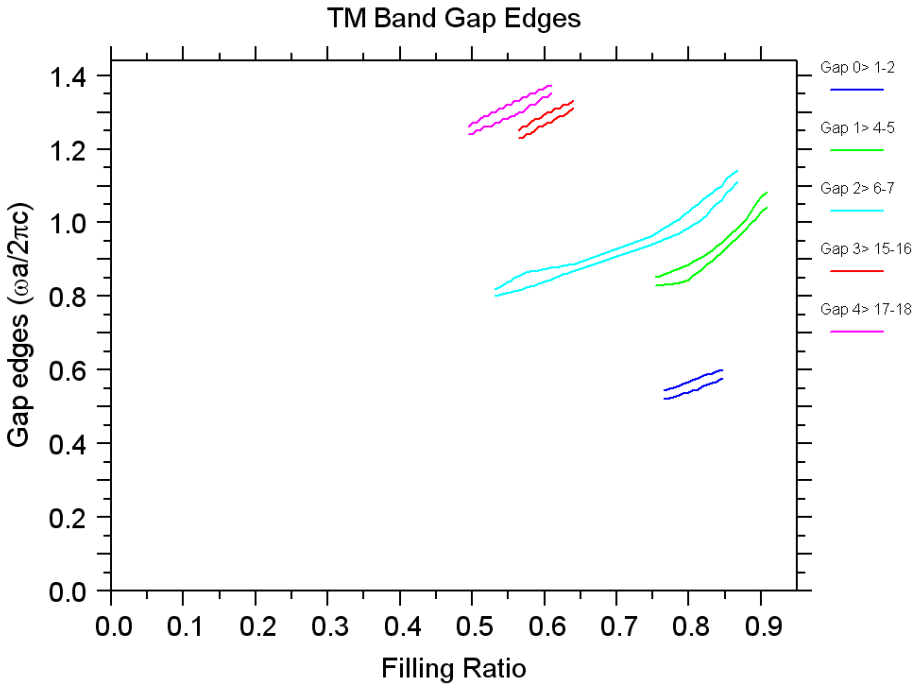

Figure 6.18TM Band Gap Edges for different filling ratios in triangular PC lattice

Since hole lattice system is designed basically for TE band gap formation, strength of TM gaps formed was low with a very low gap ratio values.

Band diagrams give dispersion properties of modes which is related to the energy ω(k) of the photons with respect to propagation direction **k**. In free space, dispersion relation is given as $\omega=k_0c$ where ω is the frequency of the light, k_0 is the wave-vector and c is the speed of light in free space. This free space relation is also known as light line which is shown in the band diagrams as black lines below. The second black line in the figures which is below the light line is called dielectric light line and dispersion relation is given as $\omega=k_0c/n$ where n is the refractive index of the semiconductor. Modes between those light lines are trapped

in the structure and they are called guided modes. This region is where photonic band gaps most usually occur.

Fabricated PC structure of 520 nm period with d/a ratio of 0.5 was simulated by PWE method to figure out whether the system supports any photonic band gap. 1D analytical calculations in chapter 4 did not predict band gap for wavelength of 390 nm which is main emission wavelength of InGaN/GaN PC LED device processed in this thesis.

Below in Figure 6.19 and Figure 6.20, there is the band diagram of square and triangular air hole PC structures with filling ratio of 0.2 and 0.23 which were calculated by PWE. Axes of the diagram are dimensionless and normalized by a/2π by using scalability property of Maxwell equations.

As seen from the dispersion diagrams drawn for refractive index contrast of 2.7:1 with filling ratios of 0.2 and 0.23, there only seems TE band gap for triangular PC lattice hole around reduced frequency a/λ = 0.28. However, there is no photonic band gap for the frequency region regarding designed PC structures in this thesis work. This is an expected result since design considerations did not include photonic band gap formation. In order to increase the extraction efficiency in this thesis, Bragg diffraction conditions were taken into consideration.

Beside to form photonic band gaps, PCs are designed to fold the originally guided modes into leaky Bloch modes and to couple out from the device. Bloch modes which stay above light line in the dispersion diagram are called leaky modes and all leaky modes eventually radiate out from the device [75]. Strength of the coupling out depends on the interaction between PC structure and the related mode. As the number of modes above the light line increases, extraction efficiency is also increased [117]. Moreover, group velocity of the modes is also important for the level of interaction. Lower velocities end up with higher interaction with PC lattices.

520 nm pitch length of PC lattice structure in this thesis work corresponds to a/ λ of 1.3. At this reduced frequency, modes are above the light lines and density of states is high.

Furthermore, in band diagram, group velocity of modes that propagate in the structure can be obtained by taking partial differential of reduced frequency with respect to reduced wave-vector, $v_g = \partial\omega / \partial k$ which gives the slope of bands. When the slope goes to zero, that means that group velocity of the mode also goes to zero, as a result velocity of light propagates in the system is lowered. Lower mode velocity is desired regarding better coupling of light with the photonic crystal structure since light will have more time to interact with the material. For the

reduced frequency of 1.3, both square and triangular PC lattice dispersion diagrams show lower mode slopes which result in lower group velocity and increased extraction efficiency.

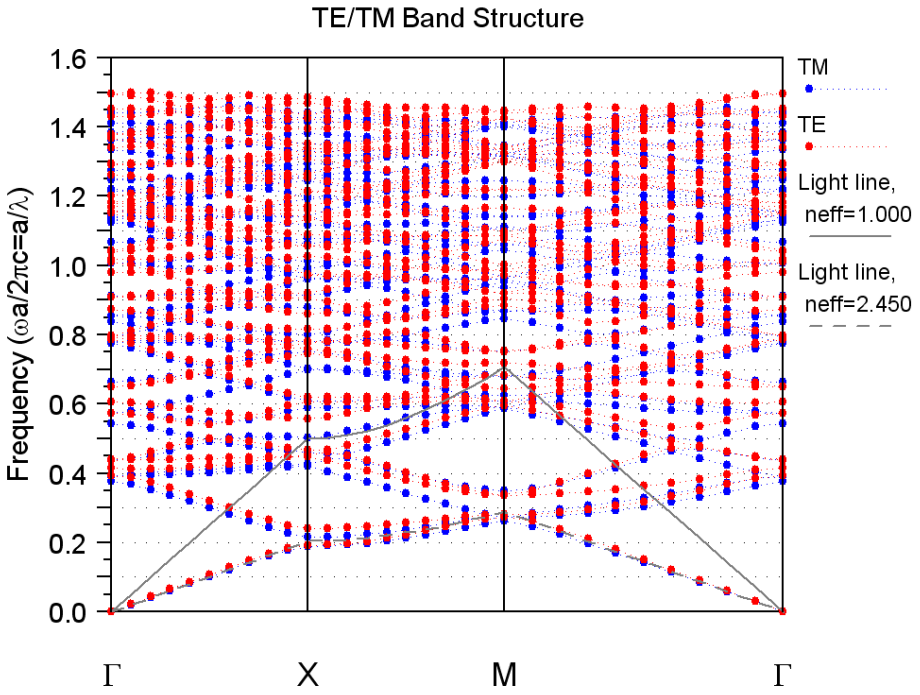

Figure 6.19 TE-TM band diagram of square hole PC structure with filling ratio of 0.2

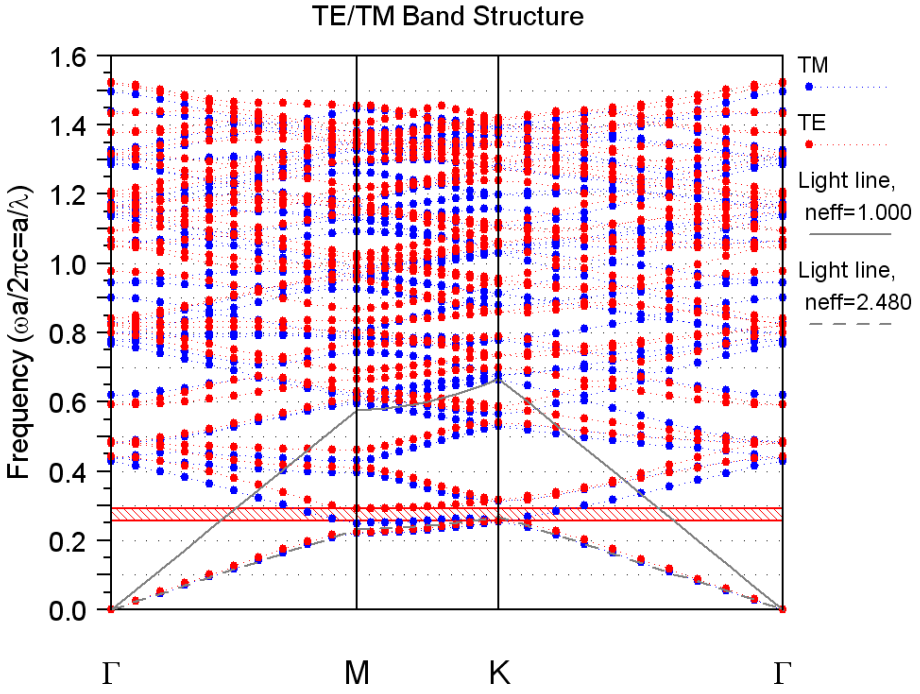

Figure 6.20 TE-TM band diagram of triangular hole PC structure with filling ratio of 0.23

6.2.2 2-D integral method simulations

Integral equation is one of the electromagnetic approach among rigorous methods. This method is one of the first methods that have been used to solve problems of periodic and non-periodic structures [126][127]. It attracts attention mainly because integral method is fast and powerful tool especially for researches on 2D diffraction problems [128][129].

The software package used as integral method tool in this thesis is PCGrate ®. It calculates the diffraction intensity and near-zone diffraction field for 2 dimensional problems with given polarization state. It was used for fast calculation of Maxwell Equations in a periodic media in order to make a rough design of diffraction photonic crystals. Main parameters considered of photonic crystal structure are PC etch depth, PC lattice constant, PC lattice type and filling ratio. Among these, effects of all parameters except lattice type can be observed by sweeping the parameters consequently, in two dimensions though. By using 2D space of integral method, rectangular PC lattice type can be approximated.

Multi-parameter sweep simulations were done in order to examine the effect of each PC parameter in extraction efficiency. Moreover, two different PC lattice borders were used in two sets of simulations. In one of the sets, regular rectangular PC lattice borders (Figure 6.21-a) with vertical side-wall shape were used. In the other set of simulations, a sinusoidal shaped PC lattice border (Figure 6.21-b) was used in order to inspect the effect of PC fabrication issues such as inclined PC sidewalls and diameter differences between top and bottom of PC cylinder holes. Parameters and their range swept in the simulations can be seen from the Table 6.1. Related matlab codes can be found in the appendix.

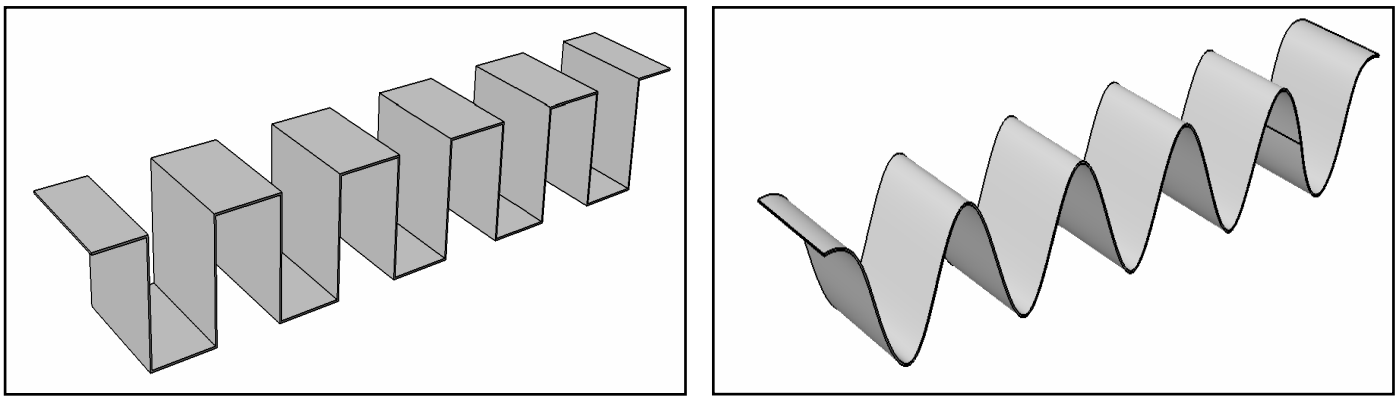

a. **b.**

Figure 6.21 PC lattice borders used in 2D integral method simulations

a. Rectangular PC lattice border b. Sinusoidal PC lattice border

PC Design Parameters	Sweep Range	Sweep Interval
PC lattice period (nm)	200 – 1000	10 nm
PC lattice depth (nm)	100 – 200	10 nm
PC d/a ratio (PC diameter/lattice pitch)	0.125 – 0.875	0.125

Table 6.1 2D integral method simulation sweeping PC design parameters

In all simulations, plane wave source for range of incident angles between 0° and 90° by 2° intervals were used. At each interval, transmission rates were recorded and plotted in incident angle vs. transmission ratio graph. In order to find total transmission, all transmission function was integrated over 90° interval. To include 3D effect into the 2D simulation, this integration was integrated over 360°. Below there is the formula used for calculating the transmission ratio. Extraction enhancement was calculated by dividing the resultant transmission ratio of the simulation with PC structure to that of simulation without PC structure.

$$T = \frac{1}{2}\int_0^{2\pi}\int_0^{\pi/2} T(\theta)\sin\theta d\theta d\phi \tag{6.1}$$

where $T(\theta)$ is transmission ratio, θ is incident angle. Because light going out from top surface is considered, total area transmission was divided by 2.

In order to confirm PCGrate results, 2D FDTD simulation with the same parameters and using plane waves as the source for PC lattice diameter of 520 nm with r/a ratio of 0.25. Results of both FDTD and integral method simulations overlapped well. Therefore, results of integral method were concluded to be acceptable to gain an insight about the physics of the system and to pre-design the PC structure to be embedded in InGaN/GaN LED device.

In the Figure 6.22, graphical result of the 2D integral method simulation is stated. In this simulation, refractive index of GaN dielectric was taken as 2.7, refractive index of air as 1. Sapphire layer, multi quantum well region and metal contacts were not introduced into the simulation. PC design parameters including PC lattice period and PC lattice depth were swept as stated in the Table 6.1. Ratio of the diameter of the PC lattice to the PC lattice pitch was

taken constant as 0.5. Rectangular PC lattice border was used for this simulation. PC extraction enhancement was calculated by dividing transmissions of single PC simulations individually to the non-PC simulation transmission result. In total, 880 individual simulations were completed and integrated to produce the graph.

Maximum extraction enhancement obtained was 3.2 times with respect to system without PC structure. Corresponding PC parameters were PC lattice diameter of 260 nm, PC lattice period of 520 nm and PC lattice depth of 180 nm.

However, this simulation did not guarantee whether the extraction enhancement of 3.2 was the highest achievable value in this lattice period and lattice depth range since d/a ratio was kept constant. Therefore, a group of simulations including sweeping of d/a ratio were performed in order to see the effect of filling ratio on the extraction efficiency. Because this time number of PC parameters is three, enhancement factor is drawn in a 2D graph below. No parameter regarding material and PC border was changed with respect to 2D simulation in Figure 6.22.

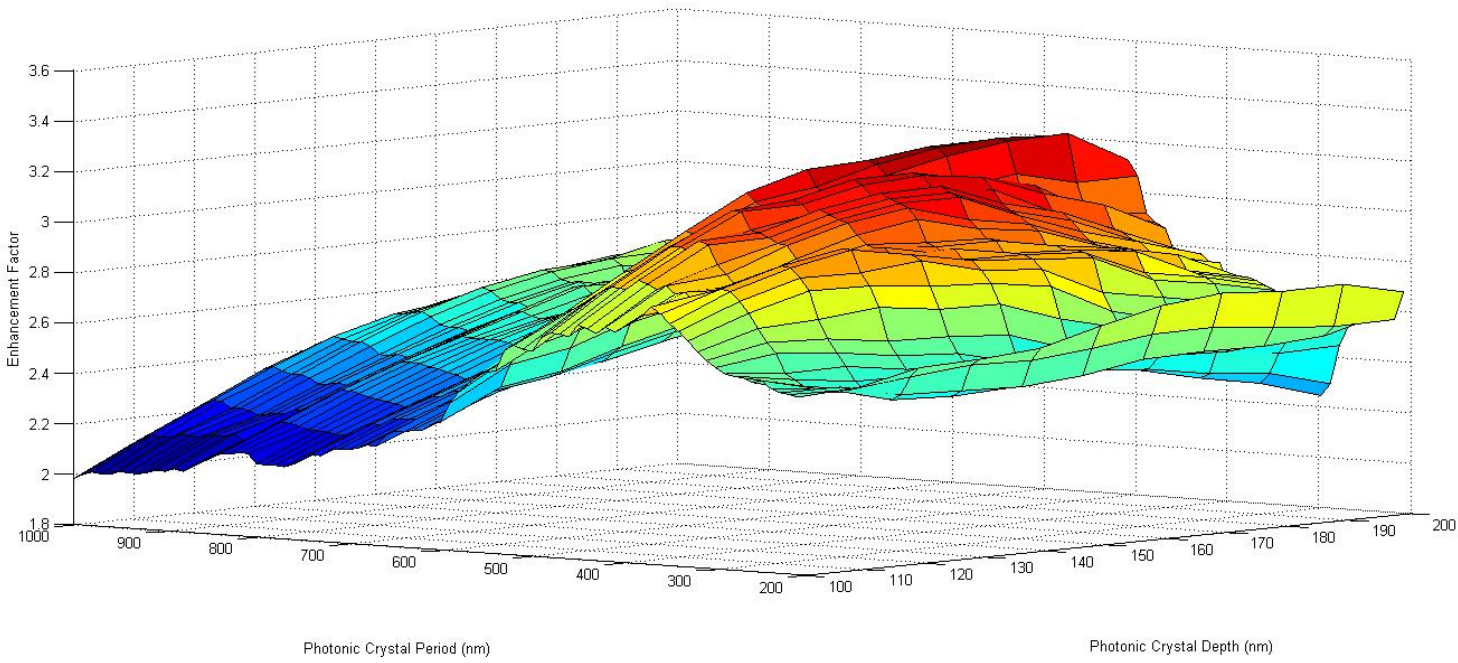

Figure 6.22 2D integral method simulation using rectangular PC border

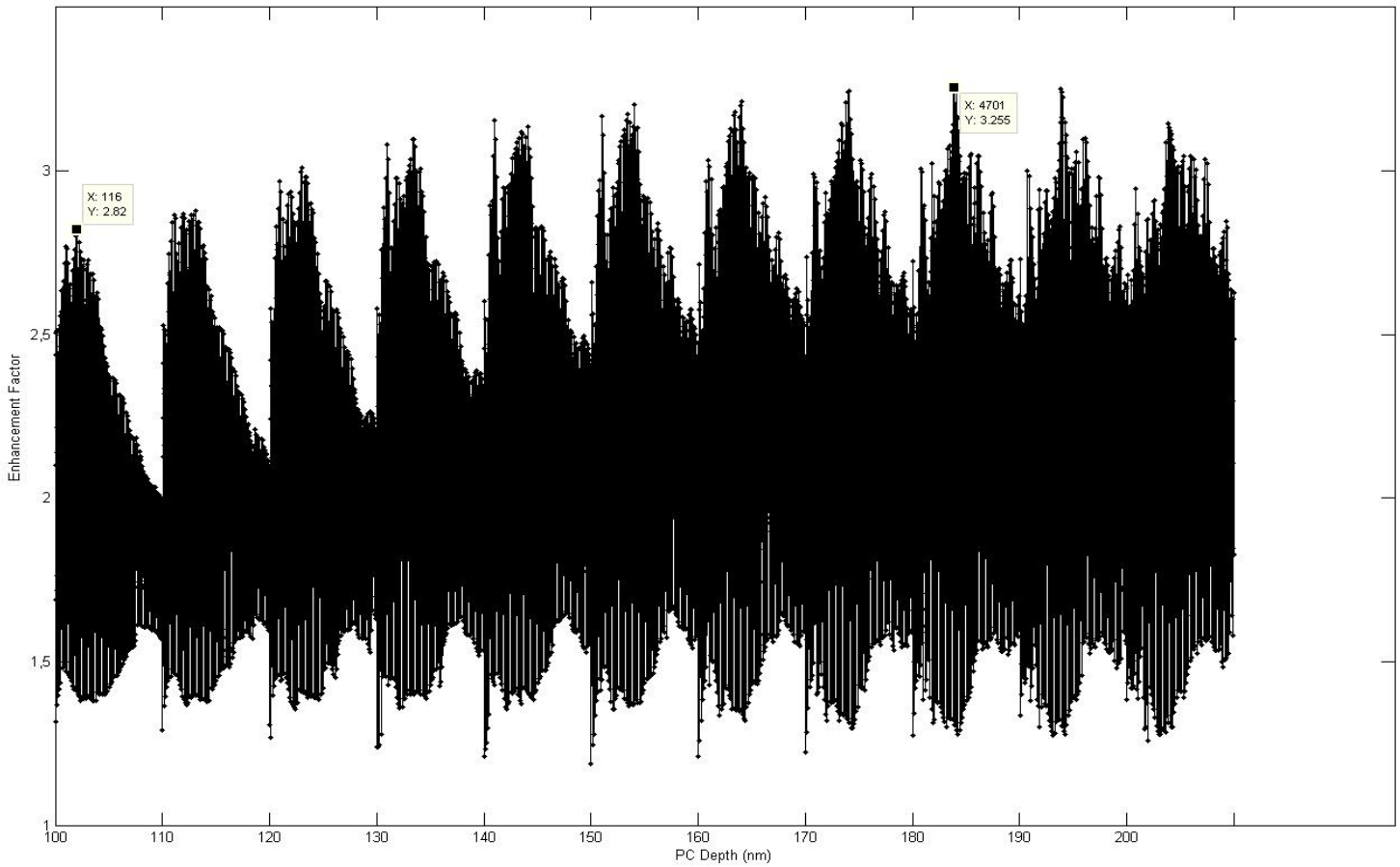

Figure 6.23 2D integral method simulation including PC design parameters of PC depth, filling ratio, PC period

All PC parameters given in Figure 6.23 were swept with the ranges stated in that Table 6.1. In total, 6160 single simulations were integrated.

In Figure 6.23, plot is drawn such that all parameters were added sequentially on the graph. PC depth is outlined on the x axis. At each PC depth value, total number of simulations is 560 which are formed by 7 different filling ratio with 80 varied lattice period. This full 2D simulation showed that maximum enhancement was obtained with d/a ratio of 0.5 for both PC depth values of 180 nm and 100 nm.

As the etch depth of PCs is increased, extraction efficiency increases up to λ/n where λ is free space wavelength, n is refractive index of the dielectric. After this value, efficiency comes to convergence [130]. In GaN material with refractive index of 2.7 and emission wavelength of 390 nm, this value is around 145 nm. In Figure 6.23 above, this was also one of the outcomes of the simulation. As it is seen from the figure, after PC depth of 140 nm, slope of extraction efficiency enhancement was reduced and it converged to value about 3.1-3.2 around t=180 nm PC depth.

Although simulations offer maximum enhancement at 180 nm PC depth, PCs were fabricated at d/a ratio of 0.5 with around 100 nm depth in favor of fabrication ease. At 100 nm PC depth, 2D integral method simulation (Figure 6.23) gave around 2.8 times enhancement. Below there is the graph of simulation result regarding d/a ratio versus extraction enhancement factor at PC depth of 90 nm with period of 520 nm in Figure 6.24. Maximum enhancement was obtained at d/a ratio of 0.5. This PC structure was diameter of 260 nm with period of 520 nm.

However, during fabrication, PC structures could not be etched vertically because of several effects such as RIE lag, positive resist slope, PMMA undercutting issues etc. In order to include the effect of fabrication issues, one more set of simulations was done by using sinusoidal PC border shape which was shown in Figure 6.21-b. Since fabricated PC shape was between a perfect rectangular border and a perfect sinusoidal border, measured extraction efficiency enhancement would be expected in between regarding simulations of both types of borders. Below in the Figure 6.25, ratio of extraction efficiency enhancements gathered by 2D integral method simulations of PC structures with rectangular border and sinusoidal border are plotted.

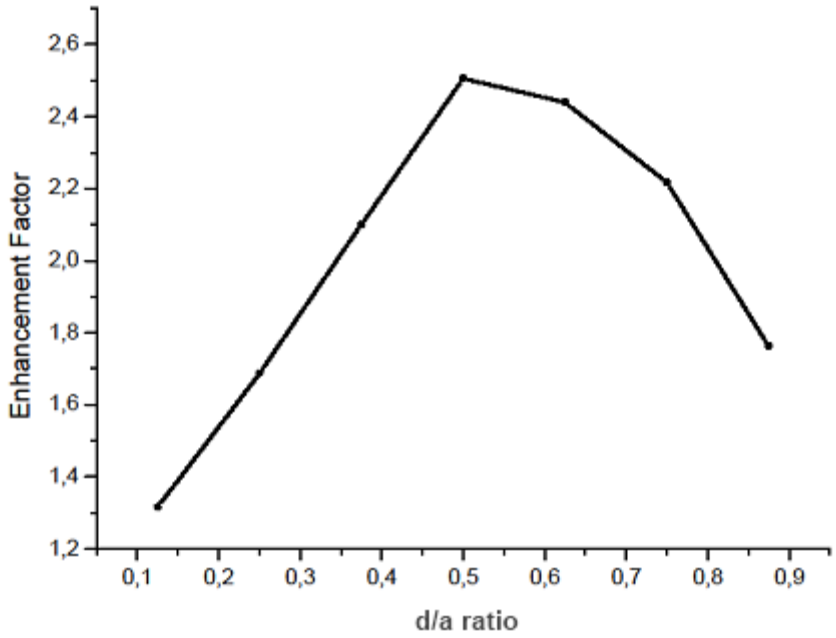

Figure 6.24 d/a ratio vs. enhancement factor for PC structure a=520 nm, t=90 nm

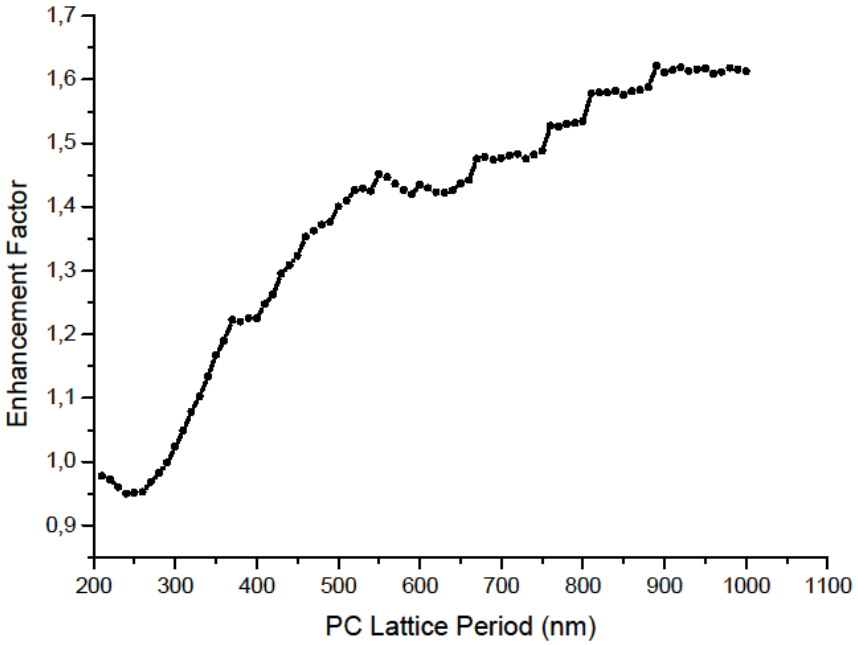

Figure 6.25 Extraction enhancement ratio of rectangular PC border to sinusoidal PC border

Using rectangular PC border rather than sinusoidal PC border increases enhancement by 35-40% for PC period of about 500 nm. Therefore, considering fabricated PC structures are in between of rectangular and sinusoidal shape, enhancement decrease of around 15-20% is expected between simulations and measurements.

One more simulation with design parameters of depth of 100 nm, and period of 520 nm with d/a ratio of 0.5 was done using rectangular and sinusoidal PC border shapes. Plane waves were used in the range between 0° and 90°. Resultant transmission values were integrated two times as described previously. Plot of simulation done for no PC structure was also figured below for comparison. (Figure 6.26, Figure 6.27, Figure 6.28).

From the Figure 6.28, critical angle of GaN-air interface can be seen clearly at around 22-24°. When there is no PC used in the LED chip, no light can be transmitted into air region for incident angles larger than critical angle. However, PC structures help this trapped light to couple out which result in enhanced extraction. One can see transmission over critical angle for PC LED structures.

For rectangular PC border structure, extraction enhancement with respect to no PC structure was calculated to be around 2.8. However, regarding sinusoidal PC border, enhancement

factor was about 2. Therefore, considering 2D integral method simulations, expected extraction efficiency enhancement of PC LEDs with respect to no PC chips is between 2 and 2.8.

6.2.3 FDTD Simulations

In time domain simulations, most commonly used technique is finite difference time domain (FDTD) method. In this method, space and time are divided into grids and derivative calculations of Maxwell equations are done by finite differences that are pre-determined by spatial grid size and time step.

FDTD method is a fully vectorial method which gives both frequency domain response and time domain response. This method is useful for any type of electromagnetic problem and device. Material of interest with its structure is defined in discrete cells. Electromagnetic fields are also described in those meshes, which are called Yee cells (Figure 6.29). Time is discretized with respect to spatial mesh cell considering the speed of light in that length of the cell. Maxwell equations are then solved discretely in these cells. E field of the mode at time of T=t is calculated from the information of E field and H field at times T=t-Δt and T=t-Δt/2 respectively. Same procedure applies for H field. In the limit of zero grid, FDTD simulation calculates exact Maxwell equations.

In FDTD program, total of six equations are solved recursively for every Yee mesh point which are denoted by i, j, k. These equations are stated below in (6.2).

In these equations, E is electric field, H is magnetic field, ε is electric permittivity, μ is magnetic permeability. FDTD program needs values of field components at time of one step before in order to calculate those of next step. This is because FDTD is based on converging time derivative of Maxwell equations by central finite difference method. Electric field and magnetic field components are calculated at grid points. E fields are computed at time of nΔt and H fields are computed at time of (n+1/2)Δt where Δt is the discrete time step and n is integer which represents the number of computation step.

FDTD simulation is continued typically until no electromagnetic field in the simulation domain is left. After the end of the simulation, frequency domain response is obtained by Fourier transform of time domain results. Furthermore, near field results can be transferred into far field in order to obtain far field scattering results.

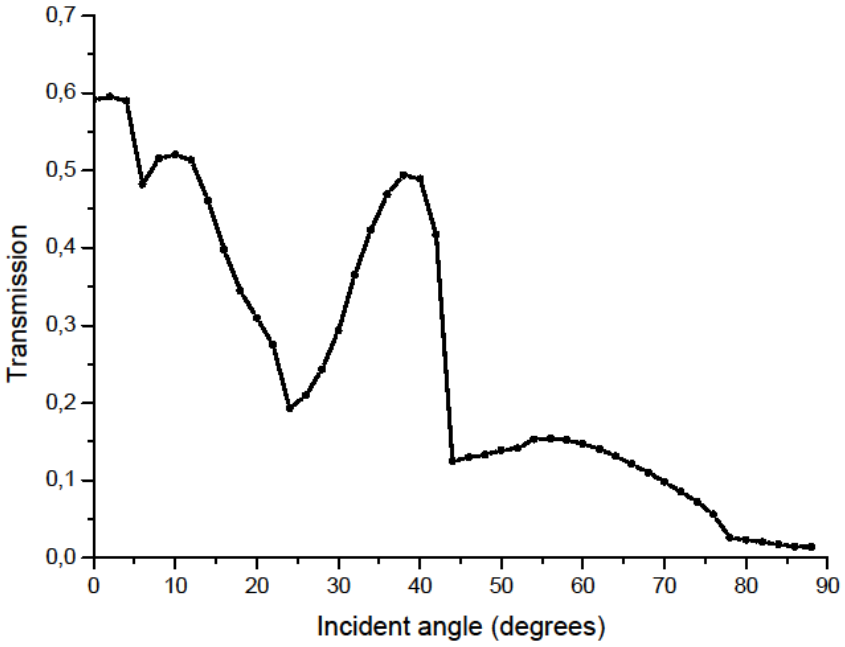

Figure 6.26 Transmission vs. incident angle plot for PC structure with rectangular border

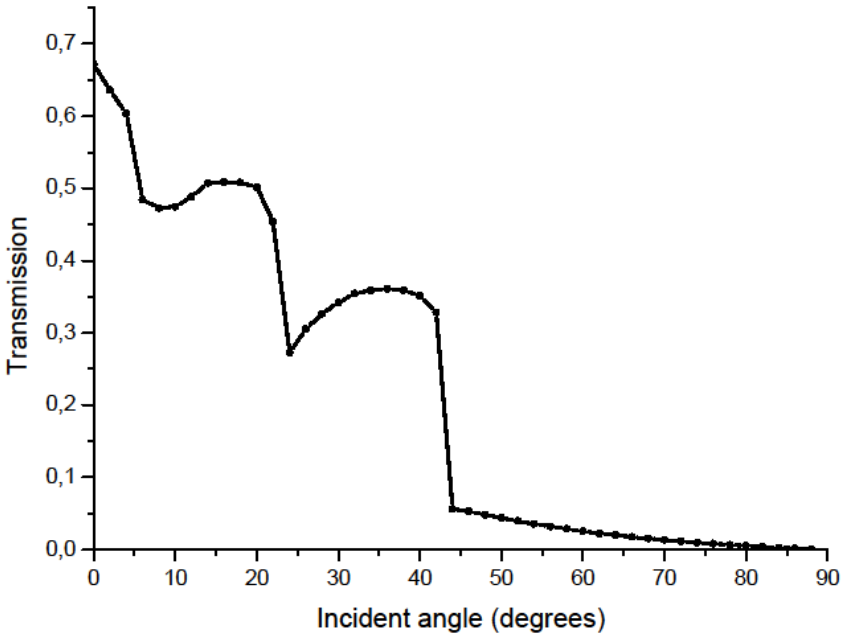

Figure 6.27 Transmission vs. incident angle plot for PC structure with sinusoidal border

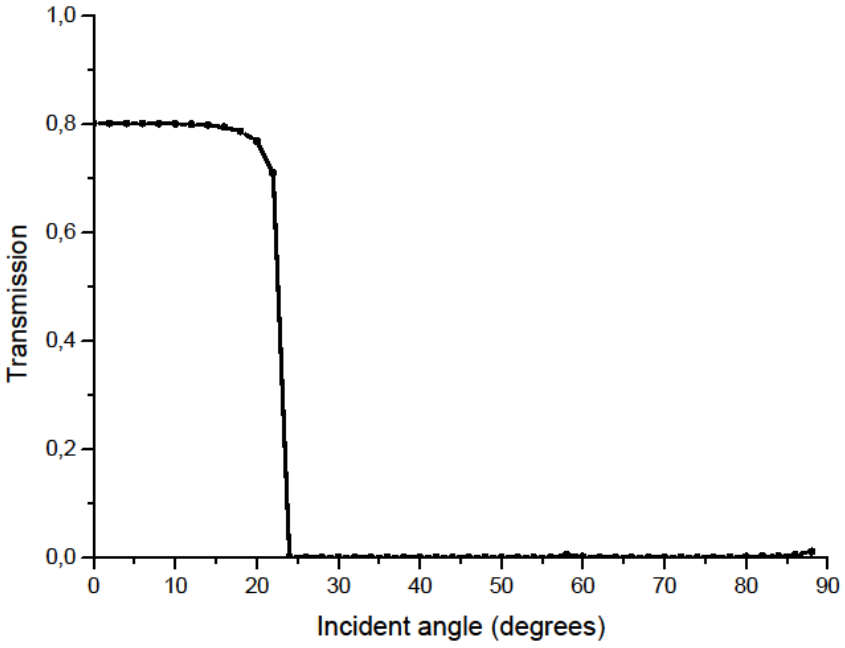

Figure 6.28 Transmission vs. incident angle plot for structure without PC

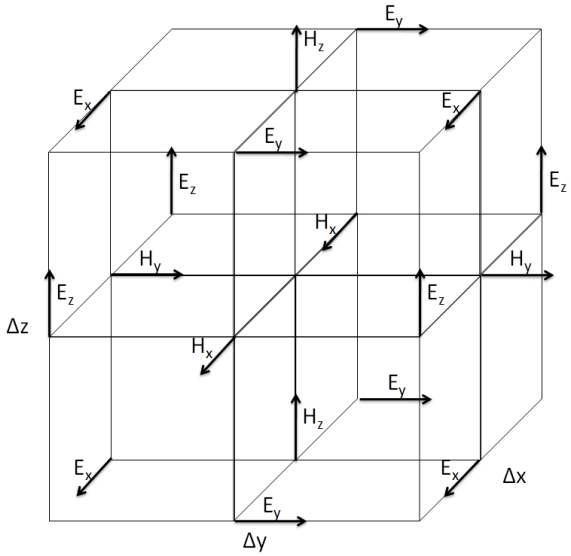

Figure 6.29 Yee's Cell for FDTD method

$$
\begin{aligned}
H_{x(i,j,k)}^{n+1/2} &= H_{x(i,j,k)}^{n-1/2} + \frac{\nabla t}{\mu \nabla z}\left(E_{y(i,j,k)}^{n} - E_{y(i,j,k-1)}^{n}\right) - \frac{\nabla t}{\mu \nabla y}\left(E_{z(i,j,k)}^{n} - E_{z(i,j-1,k)}^{n}\right) \\
E_{x(i,j,k)}^{n+1} &= E_{x(i,j,k)}^{n} + \frac{\nabla t}{\varepsilon \nabla y}\left(H_{z(i,j+1,k)}^{n+1/2} - H_{z(i,j,k)}^{n+1/2}\right) - \frac{\nabla t}{\varepsilon \nabla z}\left(H_{y(i,j,k+1)}^{n+1/2} - H_{y(i,j,k)}^{n+1/2}\right) \\
H_{y(i,j,k)}^{n+1/2} &= H_{y(i,j,k)}^{n-1/2} + \frac{\nabla t}{\mu \nabla x}\left(E_{z(i,j,k)}^{n} - E_{z(i-1,j,k)}^{n}\right) - \frac{\nabla t}{\mu \nabla z}\left(E_{x(i,j,k)}^{n} - E_{x(i,j,k-1)}^{n}\right) \\
E_{y(i,j,k)}^{n+1} &= E_{y(i,j,k)}^{n} + \frac{\nabla t}{\varepsilon \nabla z}\left(H_{x(i,j,k+1)}^{n+1/2} - H_{x(i,j,k)}^{n+1/2}\right) - \frac{\nabla t}{\varepsilon \nabla x}\left(H_{z(i+1,j,k)}^{n+1/2} - H_{z(i,j,k)}^{n+1/2}\right) \\
H_{z(i,j,k)}^{n+1/2} &= H_{z(i,j,k)}^{n-1/2} + \frac{\nabla t}{\mu \nabla y}\left(E_{x(i,j,k)}^{n} - E_{x(i,j-1,k)}^{n}\right) - \frac{\nabla t}{\mu \nabla x}\left(E_{y(i,j,k)}^{n} - E_{y(i-1,j,k)}^{n}\right) \\
E_{z(i,j,k)}^{n+1} &= E_{z(i,j,k)}^{n} + \frac{\nabla t}{\varepsilon \nabla x}\left(H_{y(i+1,j,k)}^{n+1/2} - H_{y(i,j,k)}^{n+1/2}\right) - \frac{\nabla t}{\varepsilon \nabla y}\left(H_{x(i,j+1,k)}^{n+1/2} - H_{y(i,j,k)}^{n+1/2}\right)
\end{aligned}
\tag{6.2}
$$

While calculating far field from near field data, one should be careful about electromagnetic fields in the simulation region. All fields must be zero at the end of the structures for accurate Fourier transformation.

In FDTD simulations, grid size is an important factor which determines the validity of the simulation and also total time that the simulation is completed. As the spatial resolution is increased, required time for simulation to end up is scaled not by third power as expected but by fourth power. Reason is temporal resolution. As grid size is decreased to get more valid simulations, time step should also be decreased in order simulation calculations to converge. This results with a fourth power dependence.

Especially for 3D FDTD simulations, system may become unstable mainly because of mesh aspect ratio. This was also one of the issues faced with in this thesis work. In order to stabilize the simulation system, time step size should be reduced. However, since as time step is reduced, simulation time will be increased, one should carefully optimize the required time step value.

Boundary conditions are required because simulation region must be in finite size regarding computational resources and simulation time. In the simulations for this thesis, two types of boundary conditions were used, perfectly matched layer (PML) and periodic boundary conditions.

PML boundary was used as numerically absorbing layer. This is not a physical boundary but it is introduced into simulation in order to suppress the reflection from the end of the simulation region which is a down-scaled version of the real device. PML prevents electromagnetic field to reflect back into the simulation region but rather approximates a radiation field which travels out of the simulation region. For practical simulation results, half of wavelength distance was left between the monitors and the PML region [131]. The most crucial part of using PML is to extend the structures to be simulated into the PML boundary. Otherwise, unexpected results might occur.

Periodic boundary condition is especially for structures placed with periodicity in the system. Periodic boundary was used to pretend simulated device as infinite. This kind of boundary neglects all the finite size effects though [132].

6.2.3.1 2D and 3D PC LED FDTD Simulations

FDTD method is the most commonly used method for PCs in order to determine the reflection and transmission properties of the structure. When the mode is started to propagate in the medium, calculations are done based on time stepping for up-coming grid repeatedly. However, although this technique is extremely powerful, larger dimensions of simulation area increases the calculation time and number of calculations become extremely high. Computational properties increase exponentially with the size of the simulation [120]. Therefore, grid size should be reasonable.

For LED case, minimum grid-size Δx should be smaller than λ/15n where λ is free space wavelength and n is refractive index of dielectric. In GaN material with 390 nm free space wavelength and 2.7 refractive index,Δx should be smaller than 10 nm. Time step is related to the spatial grid size by the inequality below.

$$c\Delta t = \frac{1}{\sqrt{\left(\frac{1}{\Delta x^2} + \frac{1}{\Delta y^2} + \frac{1}{\Delta z^2}\right)}} \tag{6.3}$$

where Δt is time step, c is speed of light, Δx, Δy, Δz are grid sizes along x, y, z directions respectively. Taking 10 nm for grid size gives 0.02 fs. Therefore, time step should be smaller than 0.02 fs for a stable computation.

In the simulations worked out in this thesis, large number of trials were done to find optimum grid size and time step. Optimized values were slightly lower than the minimum requirements. Even those slight changes in time step and grid size result in huge extra computation time and computation resources especially in 3D simulation environment.

In 2D simulations, simulation region length of 15 periods was used. However, for 3D simulations, simulation area was restricted with 5x5 lattice periods because of required excessive computational time and resources. Although this area is much smaller than the real device, because even three periods of holes are enough to simulate the structure for light extraction and band-gap purposes in 3D FDTD [119], it is acceptable. Using appropriate boundary conditions such as periodic boundary condition and perfect matched layer, it was tried to compensate the scale effect though. However, while concluding simulation results, scale effect should be considered.

Both in 2D and 3D simulations, metal contacts and absorption effects of materials and quantum well region were ignored. Quantum well layer was simulated as one layer of dipole sources.

As a course of its nature, PC design requires parameter sweeping. Therefore, series of simulations were done in order to obtain best design parameter. Furthermore, simulation parameters necessitate optimization regarding balance among the relevance of the results, computational time and resources, boundary conditions and simplification of the structure. These optimization based simulation runs involve large number of simulations as well. Scripting language of the software package of Lumerical FDTD Solutions® was used for creating simulation region and running simulations. Afterward the simulations end, post-processing was done by using scripts since scripting gives more flexibility and more choices on the outcomes of the simulation. All scripts that were used during simulation work can be found in the appendix.

Extraction efficiency enhancement was calculated using a power monitor in the simulation region. Near field transmission function was used in order to obtain measure of far-field power of the modes. This procedure was repeated both for the structures with PC and without PC patterning. By taking power measurement from far field function enabled to compute resultant energy rate for a specific solid angle. Below is the formulation used to obtain extraction efficiency enhancement.

Complex Poynting vector was used to calculate power flow with a specific direction and solid angle.

$$\vec{P} = \vec{E}(\omega) \times conj\, \vec{H}(\omega) \tag{6.4}$$

Poynting vector can be calculated by using far-field relationships between electric field E and magnetic field H.

$$P = n\sqrt{\frac{\varepsilon_0}{\mu_0}}\left|\vec{E}\right|^2 \tag{6.5}$$

Power is proportional to the real part of the Poynting vector. Imaginary part is related to the evanescent waves that can be seen in total internal reflection (TIR) or mode propagation in photonic band gap etc. In order to calculate the power, this real part of Poynting vector is integrated over a surface of interest on the power monitor.

$$Power(\omega) = \frac{1}{2}\int_S real(\vec{P}) d\vec{S} \tag{6.6}$$

$\frac{1}{2}$ in front of the integral comes from the time averaging of continous wave field. In order to evaluate transmission, power measured by monitor is divided by source power.

$$T(\omega) = \frac{\frac{1}{2}\int real\left(P_{monitor}(\omega)\right) dx}{\frac{1}{2}\int real\left(P_{source}(\omega)\right) dx} \tag{6.7}$$

Regarding calculation of extraction efficiency enhancement, ratio of transmission evaluated above for structure with PC and without PC patterning is taken.

$$\eta_{ext} = \frac{T_{PC}(\omega)}{T_{noPC}(\omega)} \tag{6.8}$$

6.2.3.2 2D FDTD Simulations

2D simulations were done to get an insight of FDTD method and the PC effect on propagation of light. Quantitively accurate results were not expected but 2D simulations could give some good qualitive insight to the problem.

Below in Figure 6.30, there is the simulation region for two dimensional PC structure embedded in GaN material. Simulation components were kept simple and few. Sapphire layer were not included which result in decrease in total extraction efficiency at the end of simulations. Refractive index of GaN was taken as 2.7 without imaginary components, which means no absorption was introduced. Power monitor was placed 200 nm above (half of wavelength) from top of PC structures, air-GaN interface where laterally guided modes were seperated from vertical radiated modes [117]. Simulation region was taken as the length of 15 PC periods. This length was optimized after several trials of simulations until transmitted energy came to a convergence.

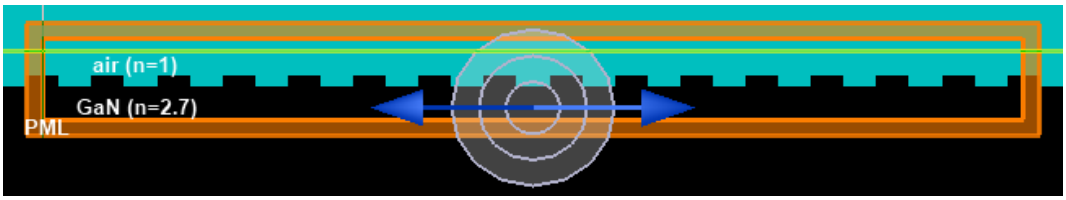

Figure 6.30 2D simulation region used in thesis work

Below in the Table 6.2, one can find simulation parameters that were used in 2D FDTD simulations.

Simulation region (x direction)	15 x PC lattice period
Simulation region (y direction)	700 nm
Grid size Δx	10 nm
Grid size Δy	10 nm
Mesh refinement	10
Boundary condition	PML

Table 6.2 2D PC FDTD Simulation parameters

InGaN/GaN LEDs emits light mainly in TE mode [104][106][107] [133]. Therefore, single dipole polarized in PC plane was used, which would also help to see the far-field pattern in 2D and 3D [77] [134]. To include effect of dipole place, one period was divided into 10 equal

grids and 10 simulations were done with a TE polarized dipole placed at the grid in turn (Figure 6.31).

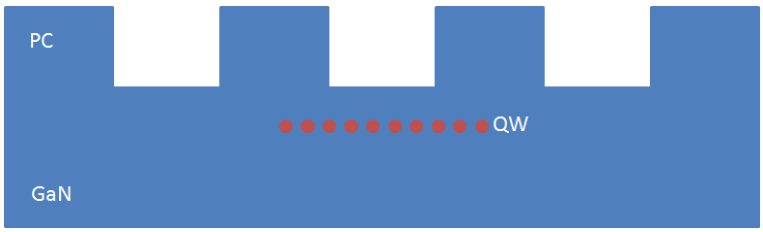

Figure 6.31 Different dipole positions along PC period

Afterwards, far-fields of every single simulation were calculated and summed up to obtain the final far-field pattern of the structure. Using this far-field function, extraction efficiency was calculated by taking the ratio of total transmitted power over total emitted power in the simulation region.

Far-field emission pattern is plotted in Figure 6.32 below. In this simulation, PC depth was 100 nm, d/a ratio was 0.5 and PC period was 520 nm.

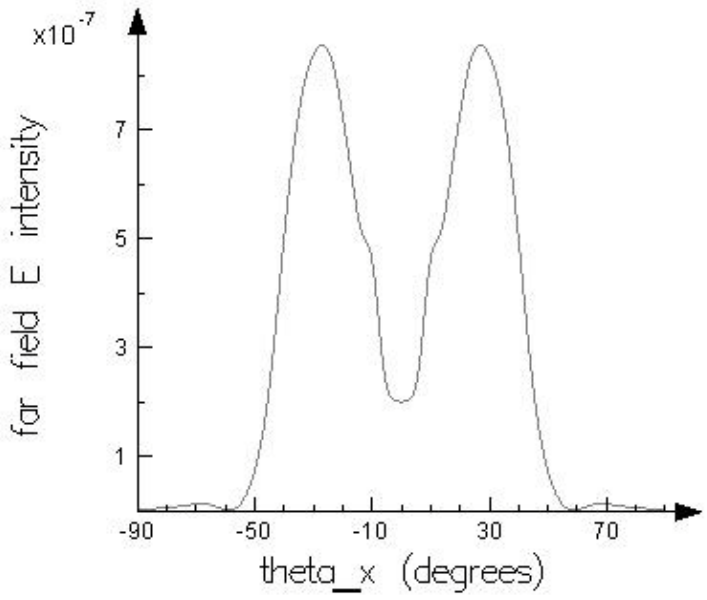

Figure 6.32 Far-field pattern of 2D PC simulation

Typical rabbit-ear far-field pattern is clear in the final plot. This simulation was done with TE polarized dipole placed just under the PC hole.

Photonic crystals fold the guided light in the high index dielectric into the lower index medium by means of Bragg scattering. While modes with incident angles higher than critical angle reflected back from the interface in the region without PC structures, PC induced Bloch modes can couple out from the device although they have incident angles greater than critical angle. Movie snapshots below were taken from 2D simulation air-PC, GaN, sapphire system with refractive indices of 1, 2.7, 1.7 respectively. When there is no PC in the system, 66% of all the modes are tapped in GaN region, 22% of light is guided in sapphire and the rest is out-coupled. This case can be seen from the Figure 6.33. However, when PC is used, light originally trapped in GaN couples out from the device which result in enhanced extraction, as given in Figure 6.34.

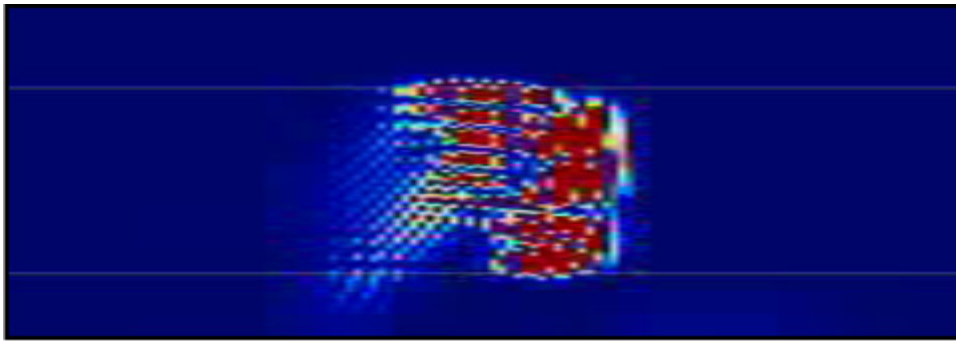

Figure 6.33 System with no PC structure

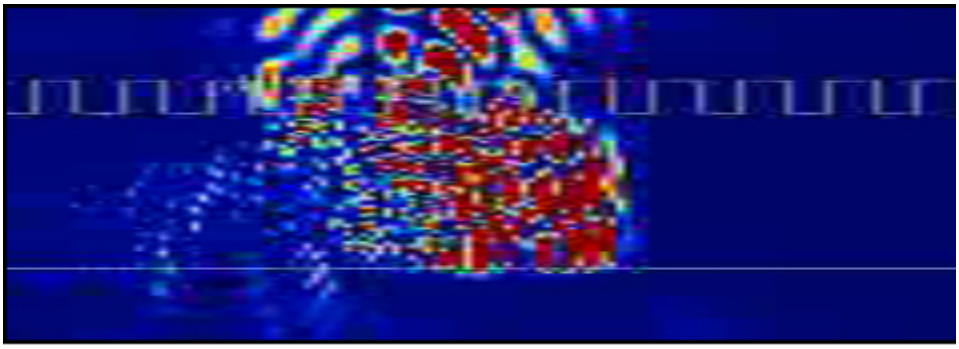

Figure 6.34 System with PC structure

It is clear from the figures that PC enhances the extraction from the device. It also reduces the group velocity so that light can interact with the PC structure for extended time. Snapshots above were taken at exactly the same simulation time. In this simulation, depth of PC was designed to be as 180 nm.

2D PC simulations were shown that they could be used at least to obtain qualitative conclusions. Therefore, series of simulations by varying PC design parameters of depth, period and filling ratio were completed to see the extraction tendency with respect to PC parameters. Results would be evaluated in comparison by means of quality. Although quantity of the extraction efficiency enhancement results would not be accurate since it was 2D simulation, tendency of enhancement or reduce of extraction with respect to design parameters could be achieved.

In this purpose, ranges of PC parameters that are stated in the Table 6.3 were used. Total of 8946 simulations were carried out. Simulation parameters were the same as in Table 6.2. Simulation scripts can be found in appendix.

	Range
PC period (nm)	210 - 1700
PC depth (nm)	30 - 210
PC d/a ratio	0.5-0.7

Table 6.3 2D FDTD PC parameter sweeping ranges

At the end of simulations, results were integrated and summed up into matrices to plot the corresponding graphs. Below in Figure 6.35, results regarding PC diameter/period ratio of 0.5 with depth of 120 nm were shown. Although quantities of final efficiency extractions were not relevant, tendency of the enhancement function gave an overview.

Around 500 nm PC period, extraction function was maximum for especially small solid angles. This result was expected since PC structure directs light into vertical radiation more than in higher solid angles. Tendency of high extraction for lower solid angles was also confirmed by 3D FDTD simulations.

In 2D simulations, highest extraction efficiency was obtained by d/a ratio of about 0.6. From integral method simulations, obtained result was 0.5 but sweep intervals of d/a ratio was kept rather high in those calculations. However in FDTD 2D simulations, d/a ratio was swept in fine intervals especially in the range of 0.5 and 0.7 where most enhancement was expected.

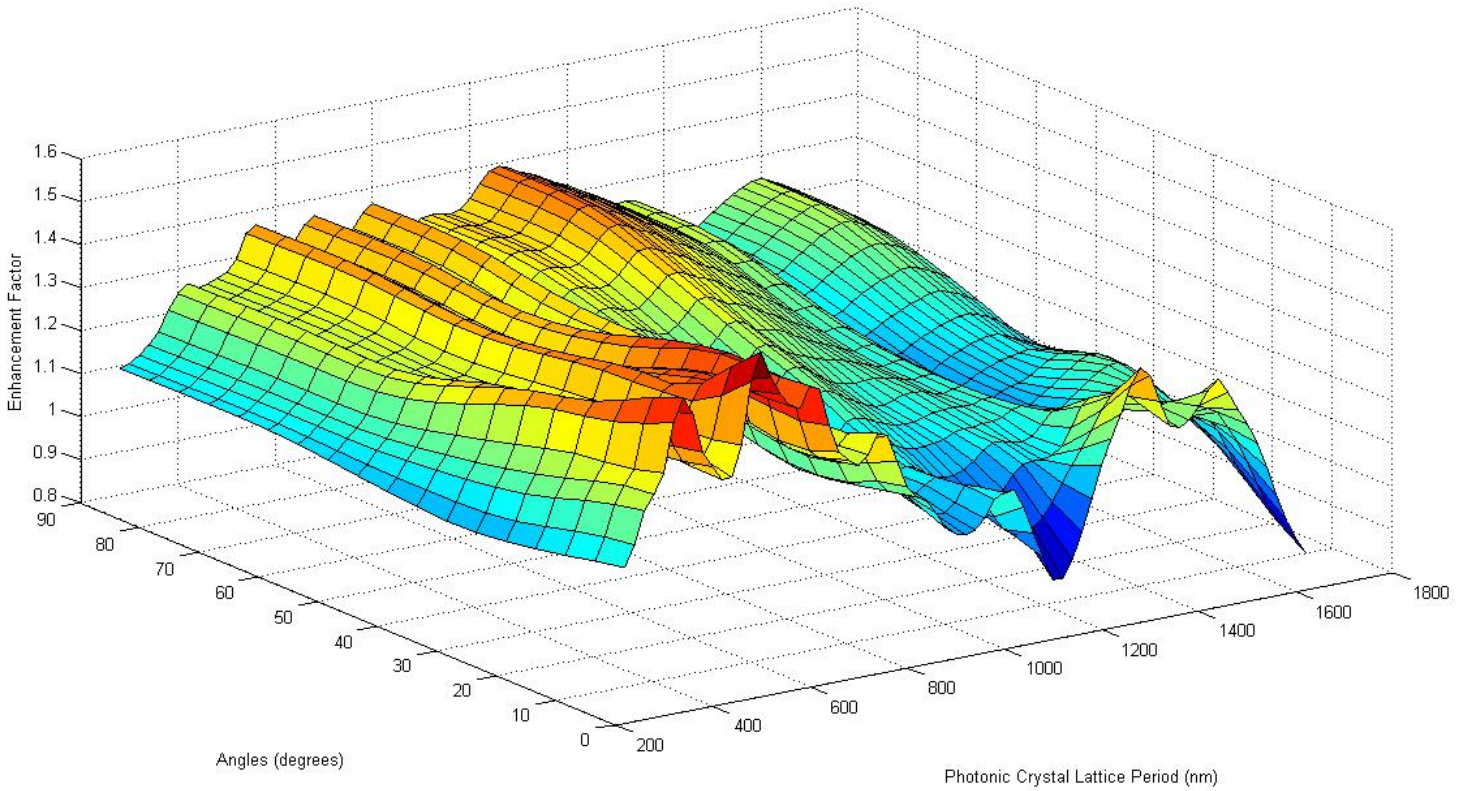

Figure 6.35 2D PC FDTD simulation with d/a ratio of 0.5

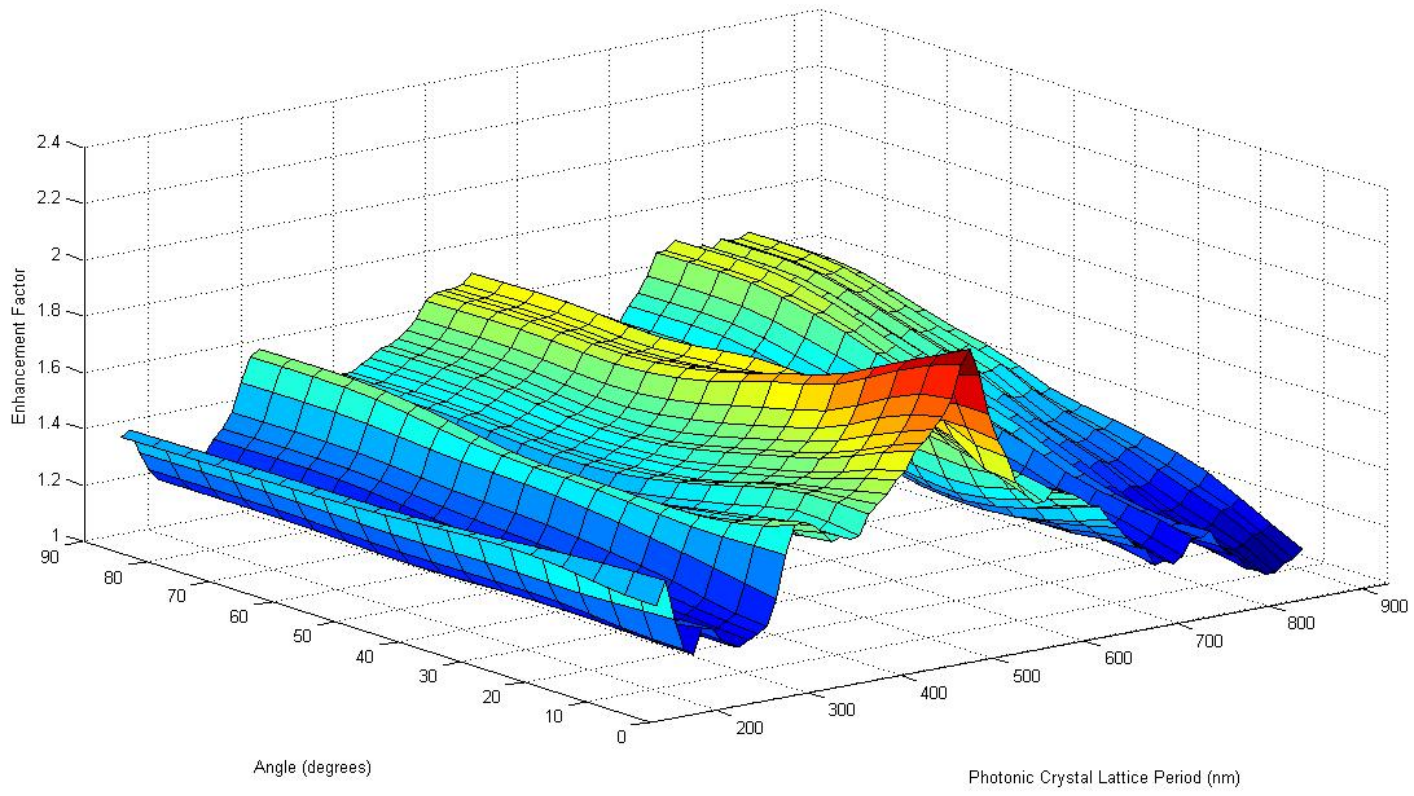

Figure 6.36 2D FDTD simulation with maximum enhancement at d/a ratio of about 0.6

Therefore, it is possible that 2D integral method simulations could not catch the higher extraction at d/a ratio of 0.6 since swept parameters around this range was 0.5 – 0.63 and 0.75 in integral method simulation.

In this simulation shown in Figure 6.36, around period of 500-520 nm PC structures, extraction made maximum point for low solid angles in the range of 10° to 30°. This result was also in agreement with other 2D and 3D simulations.

6.2.3.3 3D FDTD Simulations

Qualitative results were obtained by 2D simulations, however in order to get quantitative outcomes, 3D simulations are required since the three dimensional LED device with PC structure is represented best by 3D simulations.

Two different designs for PC LED structures were simulated in 3D FDTD method with two different software packages, RSoft Fullwave ® and Lumerical FDTD Solutions®.

6.2.3.3.1 Plane wave simulations

One of the designs was related to result of band gap calculations stated in this chapter previously. In these calculations, highest ratio of band gap was obtained by filling ratio of around 0.6 (Figure 6.17). Using filling ratio of 0.6 and PC depth of 100 nm, PC period design parameter was swept in 3D FDTD simulation series using RSoft Fullwave ® software package. Details about this series of simulations can be found in the Table 6.4 below.

In this series of simulations, grid size was kept rather high, at maximum allowable value that was discussed in this chapter previously, at 10 nm for x and y directions and at 5 nm for z direction. Reason for lower z grid size was to increase resolution where modes saw PC structure. Total of 558 simulations were done which took more than a month time to be completed. Since multi quantum well mainly emits light in TE polarization, plane waves with TE polarized emission were used. Propagation direction of plane waves was varied between 0° and 90° by 5° intervals. Transmission was calculated for every single plane wave direction and all 18 transmission results were integrated by introducing weighting of propagation angle θ. This method was also used for integral method simulation, in two dimensions though. Related scripts can be examined in the appendix. In this simulation sweeping, in order to decrease required computational time and resources, sapphire layer was not modeled.

Furthermore, metal contacts and absorption were not taken into consideration. Resultant enhancement function is plotted in Figure 6.37 below.

Grid size Δx (nm)	10
Grid size Δy (nm)	5
Grid size Δz (nm)	10
Boundary condition (x direction)	Periodic
Boundary condition (y direction)	Periodic
Boundary condition (z direction)	PML
Simulation region	7 x 7 PC lattice period
Source type	Plane wave
Source polarization	TE
PC lattice period range (nm)	200 - 500
PC filling ratio	0.6

Table 6.4 3D FDTD plane wave simulation parameters

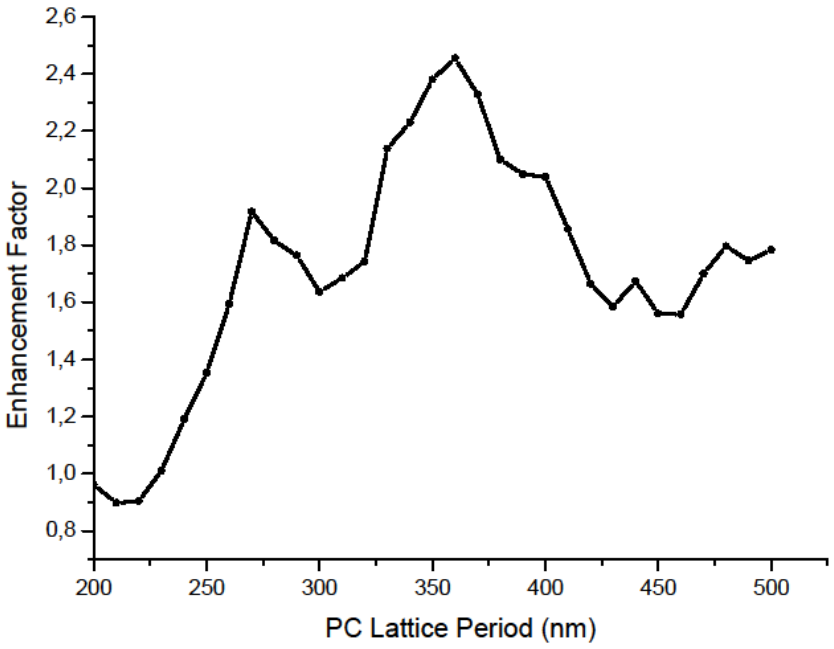

Figure 6.37 3D FDTD plane wave simulation for filling ratio of 0.6

This simulation was based on photonic band gap approach in contrast to 2D simulations, which were based on Bragg diffraction effect. According to simulation results, maximum enhancement was obtained at around 370 nm PC lattice period. For the lattice period range of 200-230 nm, extraction became even worse mainly because of destructive interference of Bragg modes. At period of 500 nm, extraction efficiency enhancement was around 2. When this graph is compared to 2D simulation plots, one can see that tolerance in PC lattice dimensions is very low in band gap approach. Even 30 nm difference results in 20 % decrease in extraction efficiency enhancement.

Therefore, this PC design was not fabricated because of fabrication and processing issues. First of all, filling ratio of 0.6 is approximately equal to d/a ratio of 0.8. It is very hard to pattern PC structures with this ratio on GaN precisely because of undercutting and scattering effects in e-beam lithography. Furthermore, since most of the p type material will be etched with this filling ratio, resistivity of the device will be increased which was not considered in the FDTD simulations. Heat transfer and thermal break-down of the device will be other issues related to working of the device.

6.2.3.3.2 Point Dipole Simulations

These simulations were done by using Lumerical FDTD Solutions® software package. Fabricated PC structures were simulated by using 3D FDTD method. Simulations were done using point dipoles as source since dipole source simulates best the light coming out from the quantum well region [132] [134] [135]. Since 400 nm InGaN/GaN MQW LEDs emits around 80% of light in TE polarization because of piezoelectric effects in quantum well region, FDTD simulations were done using TE dipoles which were polarized in the plane of PC structures [132] [134]. In order to simulate TE polarized light, TM polarized dipoles in z direction can also be used [117] [135]. Single dipole [134] [136] or number of dipoles spreaded along quantum well layer [132] can be used in simulations. As boundary condition, PML or periodic boundaries can be applied. However, periodic boundaries assume the structure is infinite, therefore finite size effects of LEDs cannot be considered in this boundary condition. All these simulation parameters were tried and decided to use PML boundary condition with a single dipole polarized in plane of PC structures. Periodic boundary conditions and large number of dipoles spreaded along a plane required excessive

amounts of computational resource and time in 3D which were not feasible to simulate on a single core. Furthermore, using a single dipole gave more accurate far-field patterns.

Details about simulation parameters are explained below. In order to visualize the structure in simulation region, model created in FDTD software is figured out in Figure 6.38.

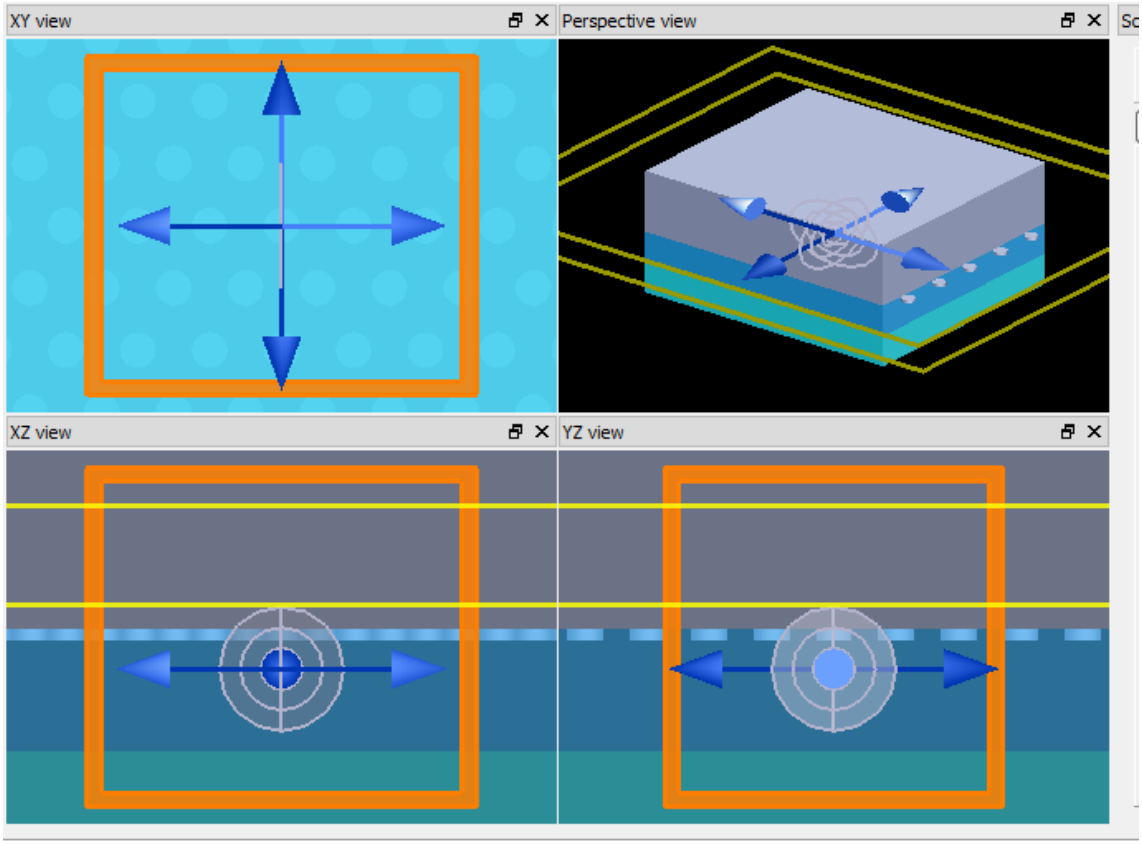

Figure 6.38 3D FDTD simulated PC LED model

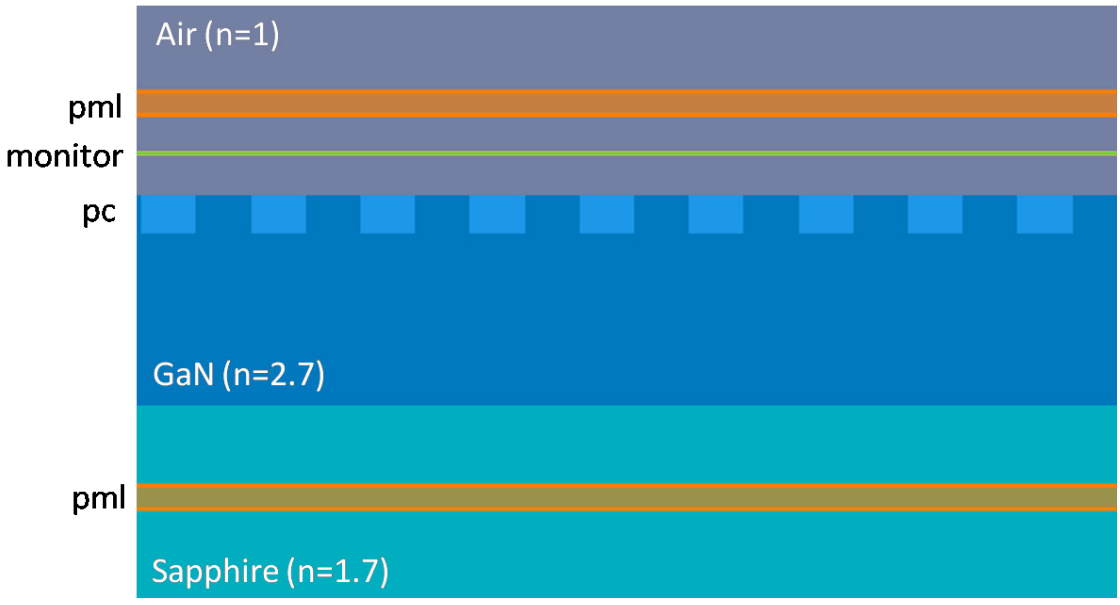

Figure 6.39 Cross-section of 3D FDTD PC LED simulation model

Dimensions of real LED devices are extremely large for simulating in the same scale. Therefore, sub-scaled model of the device should be modeled to simulate while trying not to alter physics of the device. Boundary conditions help to reduce sub-scaling effects.

Since refractive index of GaN is around 2.7, emission wavelength in GaN is smaller than 145 nm. Therefore, although thickness of GaN layer is larger in real device, GaN layer thickness of 1000 nm is enough to generate multiple modes in simulation. Moreover, real sapphire thickness is around 430 microns which is too much for a simulation. Since most of the light comes to the sapphire does not return to the GaN layer, thickness of sapphire is taken as 1000 nm as well. In order to reduce sub-scaling effect, PML boundary condition is applied to the end of the sapphire in the model [132].

Multi quantum well layer was simulated as a single TE polarized electric dipole along PC plane. Dipole was placed in the middle of MQW region. Cross-section of the PC LED model is given below in Figure 6.39.

Power monitor was placed at half of wavelength distance from top of air-GaN interface where laterally guided modes are separated from vertically radiated modes [136]. Transmitted power into air is measured by integrating the Poynting vectors at a definite distance from the air-PC region in the simulation as described in this chapter before [132].

Length of simulation region in x and y directions was restricted at 5 x PC lattice periods in order to reduce computational time and resources. Three periods of holes are stated to be enough to simulate the structure for light extraction and band-gap purposes in 3D FDTD [119].

Details about simulation parameters are given as a table in Table 6.5 below.

In order to get accurate result for PC LED simulations, mesh size was adjusted such that integer number of grids were included per each lattice period. Mesh refinement value of 5 was used to increase resolution near structure interfaces. However, enhancing grid size and mesh refinement increases simulation time and computational resources exponentially. Therefore, optimized values were used. Two different lattice types of PC structures were simulated. In both lattice types of structures, PC period and PC diameter were fixed at 520 nm and 260 nm respectively. However, because areas of unit cells for square and triangular lattices are different, their filling ratios became to be 0.2 and 0.23 correspondingly.

In the Figure 6.40 is the map of refractive index variation for triangular PC structure.

Grid size Δx (nm)	9.45
Grid size Δy (nm)	8.18
Grid size Δz (nm)	9.5
Mesh refinement	5
Time step Δt (fs)	0.016
Boundary condition (x direction)	PML
Boundary condition (y direction)	PML
Boundary condition (z direction)	PML
Simulation region	5 x 5 PC lattice period
Source type	Electric dipole
Source polarization	TE
Source wavelength (nm)	390
PC lattice type	Triangular, square
PC lattice period (nm)	520
PC diameter (nm)	260
PC filling ratio (triangular)	0.23
PC filling ratio (square)	0.2

Table 6.5 3D FDTD point dipole simulations overview

Blue circles represent PC air holes with refractive index of 1, red area represents GaN dielectric with refractive index of 2.7. Four simulations were run for each PC design. Single TE dipole was located at two different positions, one position was just under air hole, and one position was between the air holes which were shown as black dots in refractive index map. For each position, simulations were run with dipoles oriented along x direction and along y direction consequently. Same dipole locations and directions were used in four more simulations of non-PC structured LED devices. In total, eight simulations were run to calculate extraction efficiency of one PC design.

In order to calculate power flow along vertical direction, Poynting vectors were integrated along the surface on power monitor over a conic angle of 29°. Solid angle was chosen as 29° since numerical aperture of the lens that was used to take CCD images of the PC LEDs on probe station was 0.25. Moreover, distance of silicon photodiode from top of PC LED during optical power measurement was adjusted such that solid angle of light collected by photodiode was 29°.

Extraction efficiency calculations were done in this way: Transmitted powers were calculated for both devices with PC and without PC patterning. Since there were four simulations for each one regarding different dipole positions, weighting for dipole positions based on filling ratio were used while adding up the transmission values. Afterwards, extraction efficiency was found by taking ratio of the weighted transmitted power values of device simulation with PC patterning and device simulation without PC patterning.

Below are the far field patterns obtained from simulation of LED with and without triangular PC lattice patterning on p layer in Figure 6.41.

As seen from far field patterns, bare GaN has broad resonance while PC GaN shows six-fold symmetry caused by Bragg diffraction of triangular PC structures.

Transmitted far field power flow of TE dipole located just under air hole with directions along x and along y regarding triangular PC lattice LED were calculated to be 6.9 fW each that added up to 13.8 fW. Transmitted power flow of that of PC LEDs with dipole positioned in between air holes were 13.2 fW and 12.5 fW respectively, which added up to 25.7 fW. Since filling ratio was about 0.23 for this lattice type, weighted average of total transmitted power can be calculated as,

$$P_{PC} = 25.7 \text{ x } 0.77 + 13.8 \text{ x } 0.23$$

$$P_{PC} = 23 \text{ fW}$$

Transmitted far field power flow of TE dipole located at same positions with PC patterned LEDs regarding no PC simulation were calculated to be 3.7 fW and 3.6 fW respectively for each dipole positions. Therefore, total transmitted power flow for LED device without PC patterning considering 50% weighting factor was,

$$P_{NoPC} = 7.3 \text{ x } 0.5 + 7.3 \text{ x } 0.5$$

$$P_{NoPC} = 7.3 \text{ fW}$$

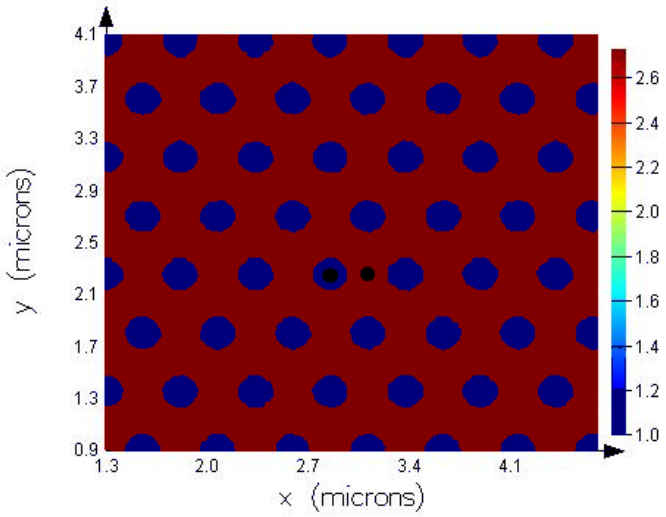

Figure 6.40 Refractive index map of triangular PC lattice

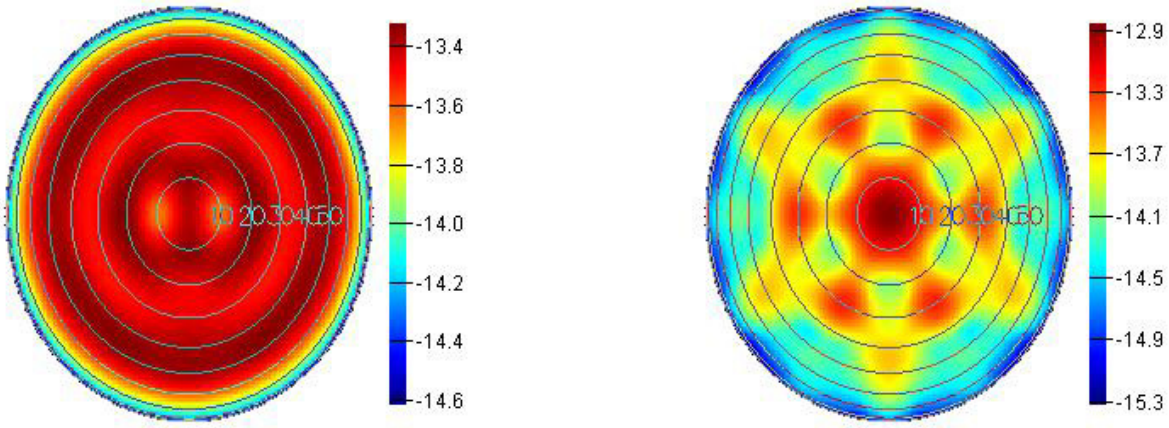

a. **b.**

Figure 6.41 Far field patterns of LEDs

a. without PC patterning b. with triangular PC patterning

Extraction efficiency enhancement was calculated by dividing net power flow PC structure over solid angle of 29° to that of device with no PC structure over 29° conic angle.

$$\eta_{ext} = 23 / 7.3$$

$$\eta_{ext} = 3.1$$

Extraction enhancement for triangular PC lattice structure was calculated as 3.1. Corresponding scripts that were used to calculate power flows and extraction efficiency can be found in appendix.

Below in the Figure 6.42, refractive index map of square PC lattice type is stated.

This time, simulations were modeled regarding square type PC lattice. Used simulation and design parameters were the same with that of triangular lattice simulation except lattice type. Two black dots shown in refractive index map are dipole positions used in simulations. Since square lattice has a filling ratio of 0.2, weighting constant used regarding power flow computation was 0.2.

Below are the far field patterns obtained from the square PC simulation in Figure 6.43. Related scripts used to plot these figures are given in appendix. In order to plot total far field pattern, far field patterns of each single simulation was integrated and normalized.

As seen from far field patterns shown, bare GaN has broad resonance while PC GaN shows four-fold symmetry caused by Bragg diffraction of square PC structures.

Power flow and enhancement in extraction efficiency were calculated in the same manner as that of triangular lattice. For TE dipoles positioned just under dipoles, transmitted power flow were calculated to be 9.26 fW and 9.13 fW. Power flow for the next position was found to be 10.49 fW and 10.51 fW. Because in square lattice symmetry was lower, not much difference among different positions of dipoles was encountered. Considering LED simulation with no PC structure, there is no difference and power transmission rates were used as the same with that of triangular lattice simulation. Calculations and the enhancement result were stated below. However, this time filling ratio is 0.2.

$$P_{PC} = 21 \text{ x } 0.8 + 18.39 \text{ x } 0.2$$

$$P_{PC} = 20.5 \text{ fW}$$

Transmitted far field power flow of TE dipole located at same positions with PC patterned LEDs regarding no PC simulation were calculated to be 3.7 fW and 3.6 fW respectively for

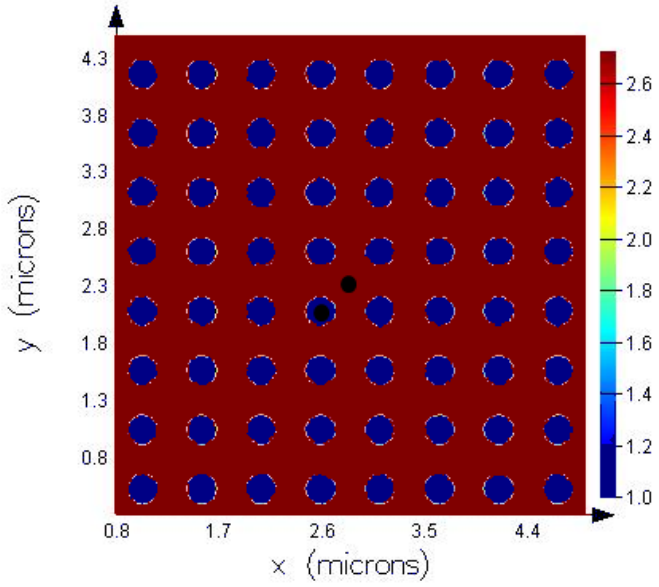

Figure 6.42 Refractive index map of square PC lattice

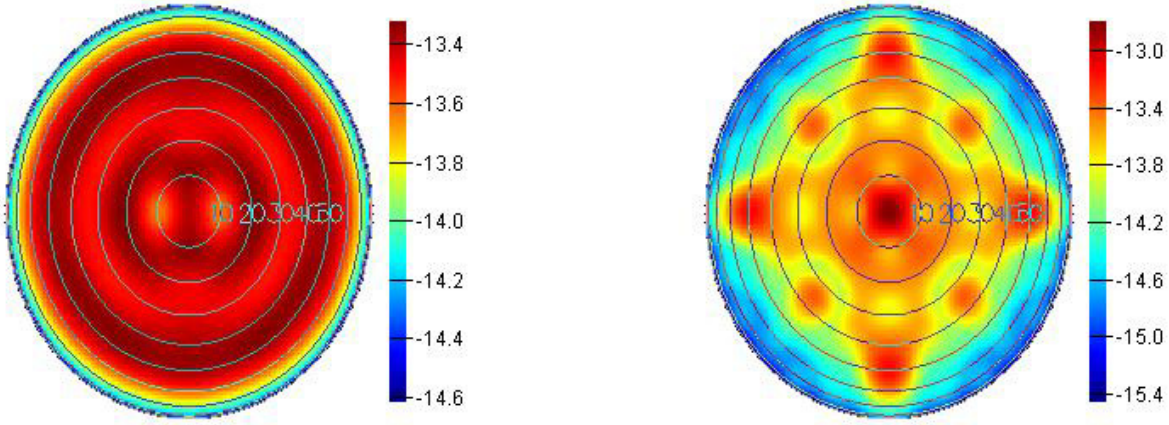

a. **b.**

Figure 6.43 Far field patterns of LEDs

a. without PC patterning b. with square PC patterning

each dipole positions. Therefore, total transmitted power flow for LED device without PC patterning considering 50% weighting factor was,

$$P_{NoPC} = 7.3 \text{ x } 0.5 + 7.3 \text{ x } 0.5$$

$$P_{NoPC} = 7.3 \text{ fW}$$

$$\eta_{ext} = 20.5/ 7.3$$

$$\eta_{ext} = 2.8$$

As a result, triangular lattice type had more enhancement which was an expected outcome. Because while square lattice has four fold symmetry, triangular lattice type has six-fold symmetry, this structure can diffract and fold the guided light in GaN semiconductor much more efficiently which results in higher extraction efficiency.

6.3 Comparison of simulations and measurements

In the optical power measurements and CCD image-intensity plots, extraction efficiency enhancement was found to be around 2.5-2.6 for triangular lattice and around 2.1-2.2 for square lattice, which were also consistent with the literature. Number of simulations were done in 2D and 3D using integral method and FDTD method. As stated in integral method simulations, perfect structure gave enhancement of 2.8 and worst case structure (sinusoidal PC border shape) gave enhancement of 2. It was concluded that enhancement that would be gained with real structure would be between these top and low values. In FDTD simulations, it was found that performance of triangular PC lattice was higher than that of square lattice, which was also the case in measurements.

In square PC lattice simulations, obtained enhancement was around 2.8. This enhancement values increased to 3.1 when lattice type used for PC was changed to triangular. In 2D simulations, it was expected a reduce in enhancement about 15% to 20% regarding simulations for real PC lattice because of fabrication issues. From the final results of 3D FDTD, these expectations were verified.

To list the possible effects which are responsible of this decrease in efficiency;

- RIE etch step causes damage in active layer. It can also initiate traps and defects for carriers and affect top layer of GaN p++ region [66] [137]. All these reduce the light coming out of the device.
- Electron beams during e-beam lithography gives irreversible harm to quantum well region which decreases the rate of radiative recombination.
- Simulations do not consider fabrication issues such as damages and defect trap centers.
- Since device is quite simplified in simulation considering computational resources and simulation time, some layers such as metal contacts, quantum wells and barriers, defects and dopants are not modeled which affect the final result.
- Material absorption is ignored in the simulations [134].
- Reduced simulation area also cannot represent the real device completely.
- Fabrication capabilities which affect the final shape of the PC structures are one of the most possible reasons in lower enhancement. Inclined side-walls of PC structures decrease amount of light extraction.

Some or most of the statements above affected the work in this thesis and these were the main reasons of lower enhancement obtained in measurements with respect to simulations.

Chapter 7

7. Conclusion

III nitrides and especially GaN have had tremendous effects for the development of opto-electronic devices. They have been using as back light in LCD televisions, in high pressure-high temperature photo-sensing applications, blue ray optical disks, solid state white light illumination sources. However, optical problems caused by their high refractive index limit their performances and application areas.

Although they can cover all the visible spectrum and UV region, because of total internal reflection, their extraction efficiency are very low, even though internal quantum efficiency is almost unity. Some geometrical approaches have been tried including surface texturing, micro-array patterning, facet shaping, plasmonics and photonic crystals. However, most of these approaches are based on random scattering of light.

In this thesis, because of its superior properties such as ability to control light propagation and shaping the profile extracted light, photonic crystals are studied for enhancing the extraction of light which has already been trapped in GaN material.

I-V characteristics, optical power measurements and CCD image intensities were completed at the same time with simulations using integral method, plane wave expansion method and finite difference time domain method. Results of both measurements and simulations were in agreement. For square PC lattice type, extraction efficiency enhancement measured was 2.1-2.2 while results of the simulations were about 2.8. For triangular lattice type, measurement gave enhancement of 2.5-2.6 where simulation results were around 3.1.

Main reason for this difference was fabrication issues. As also stated in 2D integral method simulations, imperfect PC structures may cause up to 40% reduction in extraction enhancement. In the case of this thesis work, this decrease was around 15%-20% which was expected and stated previously in 2D simulations section.

8. Appendix

8.1 2D FDTD Simulation Lumerical Scripts

8.1.1 Pre-processing

The script below was written for pre-processing. Simulation parameters and material properties were defined in this script.

```
pc=1;
increment=10e-9;
pcheight=30e-9;
airheight=700e-9;
air=1;
gan=2.5;
lambda=400e-9;
lambda_gan=lambda/gan;
nx=20;
mesh_constant=15;
sourceplace=270e-9;
monitorplace=200e-9;
freespace=100e-9;
for (per=1.5:0.1:2)
{
for (n=30:30:210)
{
pcdia=140e-9;
period=per*pcdia;
pcheight=n*10^-9;
for (j=0:70) #dffrnt pc periods
{
for (k=1:3)
{
if (pc==1)
{
addrect;
set("x",0);
set("y",0);
set("x span",pcdia);
set("y span",pcheight);
set("index",air);
for (i=1:nx)
{
copy(period,0,0);
}
}
addrect;
set("x",nx*period/2);
set("y",(pcheight+airheight)/2);
set("x span",nx*period+pcdia);
set("y span",airheight);
set("index",1);
simulation;
```

```
addfdtd;
set("background index",gan);
set("x",nx*period/2);
set("y min",(pcheight/2-sourceplace-freespace));
set("y max",(pcheight/2+monitorplace+freespace));
set("x span",15*period);
set("mesh type","uniform");
if
(round(period/lambda_gan*mesh_constant)<(period/lambda_gan*mesh_constant))
{
set("dx",period/(round(period/lambda_gan*mesh_constant)+1));
}
else
{
set("dx",period/round(period/lambda_gan*mesh_constant));
}
set("dy",get("dx"));
set("use mesh refinement",1);
set("meshing refinement",10);
sources;
adddipole;
if (k==1)
{
set("dipole type", "electric dipole");
set("polarization","TE");
set("phi",90);
filename="TE90";
}
if (k==2)
{
set("dipole type", "electric dipole");
set("polarization","TE");
set("phi",0);
filename="TE0";
}
if (k==3)
{
set("dipole type", "electric dipole");
set("polarization","TM");
filename="TM";
}
if (pc==1)
{
for (m=0:65:260)
{
if (m==0)
{
set("x",nx*period/2);
}
if (m==65)
{
set("x",pcdia/4+nx*period/2);
}
if (m==130)
{
set("x",pcdia/2+nx*period/2);
}
if (m==195)
{
set("x",(pcdia+period)/4+nx*period/2);
}
```

```
if (m==260)
{
set("x",period/2+nx*period/2);
}
set("y",(pcheight/2-sourceplace));
set("wavelength start",lambda);
set("wavelength stop",lambda);
monitors;
addpower;
set("x",nx*period/2);
set("x span",nx*period);
set("x span",nx*period*2);
set("y",pcheight/2+monitorplace);
set("output power",1);
save(num2str(j)+filename+"_m"+num2str(m)+"_t"+num2str(n)+"_per"+num2str(per
)+"_tez.fsp");
run(2);
switchtolayout;
monitors;
deleteall;
sources;
select("source1");
}
}
if (pc==0)
{
set("x",nx*period/2);
set("y",(pcheight/2-sourceplace));
set("wavelength start",lambda);
set("wavelength stop",lambda);
monitors;
addpower;
set("x",nx*period/2);
set("x span",nx*period);
set("x span",nx*period*2);
set("y",pcheight/2+monitorplace);
set("output power",1);
save(num2str(j)+filename+"_tez.fsp");
run(2);
switchtolayout;
}
structures;
deleteall;
simulation;
deleteall;
sources;
deleteall;
monitors;
deleteall;
}
pcdia=pcdia+increment;
period=per*pcdia;
}
}
}
```

8.1.2 Post-processing

This script was written in order to calculate near field transmission and power flow, far field power flow and power ratios in ascending solid angles. Results were saved in matrices in matlab format.

```
pc=1;
farfieldfilter(1);
per_sayisi=0;
for (per=1.5:0.1:2)
{
per_sayisi=per_sayisi+1;
n_sayisi=0;
for (n=30:30:60)
{
n_sayisi=n_sayisi+1;
for (j=0:1)
{
for (k=1:3)
{
if (pc==1)
{
for (m=0:65:260)
{
if (k==1)
{
filename="TE90";
load(num2str(j)+filename+"_m"+num2str(m)+"_t"+num2str(n)+"_per"+num2str(per
)+"_tez.fsp");
}
if (k==2)
{
filename="TE0";
load(num2str(j)+filename+"_m"+num2str(m)+"_t"+num2str(n)+"_per"+num2str(per
)+"_tez.fsp");
}
if (k==3)
{
filename="TM";
load(num2str(j)+filename+"_m"+num2str(m)+"_t"+num2str(n)+"_per"+num2str(per
)+"_tez.fsp");
}
f=getdata("monitor1","f");
T=transmission("monitor1");
p=getdata("monitor1","power");
d=dipolepower(f);
s=sourcepower(f);
E2_near = getelectric("monitor1");
E2_far=farfield2d("monitor1",1,2001);
theta=farfieldangle("monitor1",1,2001);
theta_new=linspace(-90,90,2001);
E2_far_new=interp(E2_far,theta,theta_new);
write(num2str(j)+filename+"_m"+num2str(m)+"_t"+num2str(n)+"_per"+num2str(pe
r)+"_tez.txt","Transmission by command");
write(num2str(j)+filename+"_m"+num2str(m)+"_t"+num2str(n)+"_per"+num2str(pe
r)+"_tez.txt",num2str(T));
write(num2str(j)+filename+"_m"+num2str(m)+"_t"+num2str(n)+"_per"+num2str(pe
r)+"_tez.txt","Transmission by integration");
```

```
write(num2str(j)+filename+"_m"+num2str(m)+"_t"+num2str(n)+"_per"+num2str(pe
r)+"_tez_new.txt","Transmission by command");
write(num2str(j)+filename+"_m"+num2str(m)+"_t"+num2str(n)+"_per"+num2str(pe
r)+"_tez_new.txt",num2str(T));
write(num2str(j)+filename+"_m"+num2str(m)+"_t"+num2str(n)+"_per"+num2str(pe
r)+"_tez_new.txt","Transmission by integration");
int=1:18;
intp=1:18;
tr_d=1:18;
tr_s=1:18;
int_new=1:18;
intp_new=1:18;
tr_new_d=1:18;
tr_new_s=1:18;
for (i=1:18)
{
aci=5*i;
int(i)=farfield2dintegrate(E2_far,theta,aci);
intp(i)=0.5*sqrt(eps0/mu0)*int(i);
tr_d(i)=intp(i)/d;#dipole power transmission
tr_s(i)=intp(i)/s;#source power transmission
int_new(i)=farfield2dintegrate(E2_far_new,theta_new,aci);
intp_new(i)=0.5*sqrt(eps0/mu0)*int_new(i);
tr_new_d(i)=intp_new(i)/d;
tr_new_s(i)=intp_new(i)/s;
write(num2str(j)+filename+"_m"+num2str(m)+"_t"+num2str(n)+"_per"+num2str(pe
r)+"_tez.txt",num2str(tr_d(i)));
write(num2str(j)+filename+"_m"+num2str(m)+"_t"+num2str(n)+"_per"+num2str(pe
r)+"_tez_new.txt",num2str(tr_new_d(i)));
}
savedata(num2str(j)+filename+"_m"+num2str(m)+"_t"+num2str(n)+"_per"+num2str
(per)+"_data.ldf",E2_near,E2_far,E2_far_new,theta,theta_new,T,p,d,s,int,int
p,tr_d,tr_s,int_new,intp_new,tr_new_d,tr_new_s);
}
}
if (pc==0)
{
if (k==1)
{
filename="TE90";
load(num2str(j)+filename+"_tez.fsp");
}
if (k==2)
{
filename="TE0";
load(num2str(j)+filename+"_tez.fsp");
}
if (k==3)
{
filename="TM";
load(num2str(j)+filename+"_tez.fsp");
}
f=getdata("monitor1","f");
T=transmission("monitor1");
p=getdata("monitor1","power");
d=dipolepower(f);
s=sourcepower(f);
E2_near = getelectric("monitor1");
E2_far=farfield2d("monitor1",1,2001);
theta=farfieldangle("monitor1",1,2001);
theta_new=linspace(-90,90,2001);
```

```
E2_far_new=interp(E2_far,theta,theta_new);
write(num2str(j)+filename+"_tez.txt","Transmission by command");
write(num2str(j)+filename+"_tez.txt",num2str(T));
write(num2str(j)+filename+"_tez.txt","Transmission by integration");
write(num2str(j)+filename+"_tez_new.txt","Transmission by command");
write(num2str(j)+filename+"_tez_new.txt",num2str(T));
write(num2str(j)+filename+"_tez_new.txt","Transmission by integration");
int=1:18;
intp=1:18;
tr_d=1:18;
tr_s=1:18;
int_new=1:18;
intp_new=1:18;
tr_new_d=1:18;
tr_new_s=1:18;
for (i=1:18)
{
aci=5*i;
int(i)=farfield2dintegrate(E2_far,theta,aci);
intp(i)=0.5*sqrt(eps0/mu0)*int(i);
tr_d(i)=intp(i)/d;
tr_s(i)=intp(i)/s;
int_new(i)=farfield2dintegrate(E2_far_new,theta_new,aci);
intp_new(i)=0.5*sqrt(eps0/mu0)*int_new(i);
tr_new_d(i)=intp_new(i)/d;
tr_new_s(i)=intp_new(i)/s;
write(num2str(j)+filename+"_tez.txt",num2str(tr_d(i)));
write(num2str(j)+filename+"_tez_new.txt",num2str(tr_new_d(i)));
}
savedata(num2str(j)+filename+"_data.ldf",E2_near,E2_far,E2_far_new,theta,th
eta_new,T,p,d,s,int,intp,tr_d,tr_s,int_new,intp_new,tr_new_d,tr_new_s);
}
}
}
}
}
toplam=(j+1)*n_sayisi*per_sayisi*3*5;#top sim sayisi
tr_pc_all_d=matrix(18,toplam);
tr_pc_all_s=matrix(18,toplam);
tr_nopc_all=matrix(18,3);
savedata("toplam_tr_data.ldf",tr_pc_all_d,tr_pc_all_s,tr_nopc_all);
```

8.1.3 Finalizing

This script was written in order to evaluate the calculations made in post-processing. Results were put in order and 4x4 matrices were formed regarding plotting issues.

```
a1=1/3;
a2=1/3;
a3=1/3;
pc=1;
p_polarization=0;
per_sayisi=0;
z=1;
loaddata("toplam_tr_data.ldf");
if (pc==1)
{
for (per=1.5:0.1:2)
{
per_sayisi=per_sayisi+1;
n_sayisi=0;
for (n=30:30:210)
{
n_sayisi=n_sayisi+1;
for (j=0:70)
{
for (k=1:3)
{
for (m=0:65:260)
{
if (k==1)
{
filename="TE90";
loaddata(num2str(j)+filename+"_m"+num2str(m)+"_t"+num2str(n)+"_per"+num2str
(per)+"_data.ldf");
}
if (k==2)
{
filename="TE0";
loaddata(num2str(j)+filename+"_m"+num2str(m)+"_t"+num2str(n)+"_per"+num2str
(per)+"_data.ldf");
}
if (k==3)
{
if (p_polarization==0)
{
filename="TM";
loaddata(num2str(j)+filename+"_m"+num2str(m)+"_t"+num2str(n)+"_per"+num2str
(per)+"_data.ldf");
}
}
for (i=1:18)
{
tr_pc_all_d(i,z)=tr_d(i);
tr_pc_all_s(i,z)=tr_s(i);
}
z=z+1;
}#for
}#k
}#j
}#n
```

```
}#per
d_matrix=(j+1)*15*n_sayisi*per_sayisi;
if (p_polarization==1)
{
d_matrix=(j+1)*10*n_sayisi*per_sayisi;
}
kacli=d_matrix/5;
transverse_m0_d=matrix(18,kacli);
transverse_m65_d=matrix(18,kacli);
transverse_m130_d=matrix(18,kacli);
transverse_m195_d=matrix(18,kacli);
transverse_m260_d=matrix(18,kacli);
total_d=matrix(18,kacli);

transverse_m0_s=matrix(18,kacli);
transverse_m65_s=matrix(18,kacli);
transverse_m130_s=matrix(18,kacli);
transverse_m195_s=matrix(18,kacli);
transverse_m260_s=matrix(18,kacli);
total_s=matrix(18,kacli);

secondterm=1;
for (w=1:5:d_matrix)
{
for (tmp=1:18)
{
transverse_m0_d(tmp,secondterm)=tr_pc_all_d(tmp,w);
transverse_m65_d(tmp,secondterm)=tr_pc_all_d(tmp,w+1);
transverse_m130_d(tmp,secondterm)=tr_pc_all_d(tmp,w+2);
transverse_m195_d(tmp,secondterm)=tr_pc_all_d(tmp,w+3);
transverse_m260_d(tmp,secondterm)=tr_pc_all_d(tmp,w+4);
total_d(tmp,secondterm)=(transverse_m0_d(tmp,secondterm)+transverse_m65_d(t
mp,secondterm)+transverse_m130_d(tmp,secondterm)+transverse_m195_d(tmp,seco
ndterm)+transverse_m260_d(tmp,secondterm))/5;

transverse_m0_s(tmp,secondterm)=tr_pc_all_s(tmp,w);
transverse_m65_s(tmp,secondterm)=tr_pc_all_s(tmp,w+1);
transverse_m130_s(tmp,secondterm)=tr_pc_all_s(tmp,w+2);
transverse_m195_s(tmp,secondterm)=tr_pc_all_s(tmp,w+3);
transverse_m260_s(tmp,secondterm)=tr_pc_all_s(tmp,w+4);
total_s(tmp,secondterm)=(transverse_m0_s(tmp,secondterm)+transverse_m65_s(t
mp,secondterm)+transverse_m130_s(tmp,secondterm)+transverse_m195_s(tmp,seco
ndterm)+transverse_m260_s(tmp,secondterm))/5;
}
secondterm=secondterm+1;
}
matlabsave("matrisler1_pc_d",total_d,tr_pc_all_d,transverse_m0_d,transverse
_m65_d,transverse_m130_d,transverse_m195_d,transverse_m260_d);
matlabsave("matrisler1_pc_s",total_s,tr_pc_all_s,transverse_m0_s,transverse
_m65_s,transverse_m130_s,transverse_m195_s,transverse_m260_s);
if (p_polarization==0)
{
kacli2=d_matrix/15;
TE90_d=matrix(18,kacli2);
TE0_d=matrix(18,kacli2);
TM_d=matrix(18,kacli2);

TE90_s=matrix(18,kacli2);
TE0_s=matrix(18,kacli2);
TM_s=matrix(18,kacli2);
```

```
secondterm=1;
for (w=1:15:d_matrix)
{
for (tmp=1:18)
{
TE90_d(tmp,secondterm)=(tr_pc_all_d(tmp,w)+tr_pc_all_d(tmp,w+1)+tr_pc_all_d
(tmp,w+2)+tr_pc_all_d(tmp,w+3)+tr_pc_all_d(tmp,w+4))/5;
TE0_d(tmp,secondterm)=(tr_pc_all_d(tmp,w+5)+tr_pc_all_d(tmp,w+6)+tr_pc_all_
d(tmp,w+7)+tr_pc_all_d(tmp,w+8)+tr_pc_all_d(tmp,w+9))/5;
TM_d(tmp,secondterm)=(tr_pc_all_d(tmp,w+10)+tr_pc_all_d(tmp,w+11)+tr_pc_all
_d(tmp,w+12)+tr_pc_all_d(tmp,w+13)+tr_pc_all_d(tmp,w+14))/5;

TE90_s(tmp,secondterm)=(tr_pc_all_s(tmp,w)+tr_pc_all_s(tmp,w+1)+tr_pc_all_s
(tmp,w+2)+tr_pc_all_s(tmp,w+3)+tr_pc_all_s(tmp,w+4))/5;
TE0_s(tmp,secondterm)=(tr_pc_all_s(tmp,w+5)+tr_pc_all_s(tmp,w+6)+tr_pc_all_
s(tmp,w+7)+tr_pc_all_s(tmp,w+8)+tr_pc_all_s(tmp,w+9))/5;
TM_s(tmp,secondterm)=(tr_pc_all_s(tmp,w+10)+tr_pc_all_s(tmp,w+11)+tr_pc_all
_s(tmp,w+12)+tr_pc_all_s(tmp,w+13)+tr_pc_all_s(tmp,w+14))/5;
}
secondterm=secondterm+1;
}
}#p_pol
if (p_polarization==1)
{
kacli2=d_matrix/10;
TE90_d=matrix(18,kacli2);
TE0_d=matrix(18,kacli2);
#TM_d=matrix(18,kacli2);

TE90_s=matrix(18,kacli2);
TE0_s=matrix(18,kacli2);
#TM_s=matrix(18,kacli2);
secondterm=1;
for (w=1:10:d_matrix)
{
for (tmp=1:18)
{
TE90_d(tmp,secondterm)=(tr_pc_all_d(tmp,w)+tr_pc_all_d(tmp,w+1)+tr_pc_all_d
(tmp,w+2)+tr_pc_all_d(tmp,w+3)+tr_pc_all_d(tmp,w+4))/5;
TE0_d(tmp,secondterm)=(tr_pc_all_d(tmp,w+5)+tr_pc_all_d(tmp,w+6)+tr_pc_all_
d(tmp,w+7)+tr_pc_all_d(tmp,w+8)+tr_pc_all_d(tmp,w+9))/5;
#TM_d(tmp,secondterm)=(tr_pc_all_d(tmp,w+10)+tr_pc_all_d(tmp,w+11)+tr_pc_al
l_d(tmp,w+12)+tr_pc_all_d(tmp,w+13)+tr_pc_all_d(tmp,w+14))/5;

TE90_s(tmp,secondterm)=(tr_pc_all_s(tmp,w)+tr_pc_all_s(tmp,w+1)+tr_pc_all_s
(tmp,w+2)+tr_pc_all_s(tmp,w+3)+tr_pc_all_s(tmp,w+4))/5;
TE0_s(tmp,secondterm)=(tr_pc_all_s(tmp,w+5)+tr_pc_all_s(tmp,w+6)+tr_pc_all_
s(tmp,w+7)+tr_pc_all_s(tmp,w+8)+tr_pc_all_s(tmp,w+9))/5;
#TM_s(tmp,secondterm)=(tr_pc_all_s(tmp,w+10)+tr_pc_all_s(tmp,w+11)+tr_pc_al
l_s(tmp,w+12)+tr_pc_all_s(tmp,w+13)+tr_pc_all_s(tmp,w+14))/5;
}
secondterm=secondterm+1;
}
}#p_pol
temp=1;
TE90_t_d=matrix(18,j+1,n_sayisi,per_sayisi);
TE0_t_d=matrix(18,j+1,n_sayisi,per_sayisi);
TM_t_d=matrix(18,j+1,n_sayisi,per_sayisi);
total_t_d=matrix(18,j+1,n_sayisi,per_sayisi);

TE90_t_s=matrix(18,j+1,n_sayisi,per_sayisi);
```

```
TE0_t_s=matrix(18,j+1,n_sayisi,per_sayisi);
TM_t_s=matrix(18,j+1,n_sayisi,per_sayisi);
total_t_s=matrix(18,j+1,n_sayisi,per_sayisi);

for (q=1:per_sayisi)
{
for (v=1:n_sayisi)
{
for (u=1:j+1)
{
for (b=1:18)
{
TE90_t_d(b,u,v,q)=TE90_d(b,temp);
TE0_t_d(b,u,v,q)=TE0_d(b,temp);

TE90_t_s(b,u,v,q)=TE90_s(b,temp);
TE0_t_s(b,u,v,q)=TE0_s(b,temp);
if (p_polarization==0)
{
TM_t_d(b,u,v,q)=TM_d(b,temp);
total_t_d(b,u,v,q)=a1*TE90_t_d(b,u,v,q)+a2*TE0_t_d(b,u,v,q)+a3*TM_t_d(b,u,v
,q);

TM_t_s(b,u,v,q)=TM_s(b,temp);
total_t_s(b,u,v,q)=a1*TE90_t_s(b,u,v,q)+a2*TE0_t_s(b,u,v,q)+a3*TM_t_s(b,u,v
,q);
}
if (p_polarization==1)
{
total_t_d(b,u,v,q)=a*TE90_t_d(b,u,v,q)+b*TE0_t_d(b,u,v,q);
total_t_s(b,u,v,q)=a*TE90_t_s(b,u,v,q)+b*TE0_t_s(b,u,v,q);
}
}#for
temp=temp+1;
}#u
}#v
}#q
matlabsave("matrisler2_pc_d",TE90_d,TE0_d,TM_d,TE90_t_d,TE0_t_d,TM_t_d,tota
l_t_d);
matlabsave("matrisler2_pc_s",TE90_s,TE0_s,TM_s,TE90_t_s,TE0_t_s,TM_t_s,tota
l_t_s);
}#pc
if (pc==0)
{
total_nopc=matrix(18,1);
for (j=0)
{
for (k=1:3)
{
if (k==1)
{
filename="TE90";
loaddata(num2str(j)+filename+"_data.ldf");
}
if (k==2)
{
filename="TE0";
loaddata(num2str(j)+filename+"_data.ldf");
}
if (k==3)
{
```

```
if (p_polarization==0)
{
filename="TM";
loaddata(num2str(j)+filename+"_data.ldf");
}
}
for (i=1:18)
{
tr_nopc_all(i,z)=tr(i);
}
z=z+1;
}
}
for (i=1:18)
{
total_nopc(i)=(a1*tr_nopc_all(i,1)+a2*tr_nopc_all(i,2)+a3*tr_nopc_all(i,3))
;
}
matlabsave("matrisler_nopc",tr_nopc_all,total_nopc);
}
```

8.2 2D Integral Method Simulation Matlab Codes

8.2.1 Pre-processing

Matlab code below was written for preparing the xml files to be used in the software and running the simulation.

```
clear all
close all
clc

for t=[100:10:200]
for i=[210:10:1000]
for m=[1:1:7]

fid=fopen('kare.xml');
fid2 = fopen(['kare_t', num2str(t), '_', num2str(i), '_', num2str(m/8),
'.xml'],'w');

for ii=1:10
    tline = fgetl(fid);
    fprintf(fid2,tline);
    fprintf(fid2,'\n');
end;

    tline = fgetl(fid);
    fprintf(fid2,['<Period unit="nm">', num2str(4*i), '.', num2str(0),
'</Period>']);
    fprintf(fid2,'\n');
for ii=12:22
tline = fgetl(fid);
fprintf(fid2,tline);
fprintf(fid2,'\n');
end
tline=fgetl(fid);
fprintf(fid2, ['<Polygonal Is_from_file="false" Scaling_coefficient="',
num2str(t/i),  num2str(0), num2str(0), num2str(0), num2str(0), num2str(0),
num2str(0), num2str(0), num2str(0), num2str(0), num2str(0), num2str(0),
num2str(0), num2str(0), num2str(0), num2str(0), num2str(0), num2str(0), '"
Absolute_plain_border="false">']);
fprintf(fid2,'\n');

tline=fgetl(fid);
fprintf(fid2, tline);
fprintf(fid2,'\n');

tline=fgetl(fid);
fprintf(fid2, ['<point x_coordinate="',
num2str(m/8*0.00000000000000000000), '"
y_coordinate="0.00000000000000000000">']);
fprintf(fid2, '\n');

tline=fgetl(fid);
fprintf(fid2, tline);
fprintf(fid2,'\n');
```

```
tline=fgetl(fid);
fprintf(fid2, ['<point x_coordinate="', num2str(m/8*0.25-0.0001), '"
y_coordinate="0.00000000000000000000">']);
fprintf(fid2, '\n');

tline=fgetl(fid);
fprintf(fid2, tline);
fprintf(fid2,'\n');

tline=fgetl(fid);
fprintf(fid2, ['<point x_coordinate="', num2str(m/8*0.25), '"
y_coordinate="0.25000000000000000000">']);
fprintf(fid2, '\n');

tline=fgetl(fid);
fprintf(fid2, tline);
fprintf(fid2,'\n');

tline=fgetl(fid);
fprintf(fid2, ['<point x_coordinate="', num2str(0.25-0.0001), '"
y_coordinate="0.25000000000000000000">']);
fprintf(fid2, '\n');

tline=fgetl(fid);
fprintf(fid2, tline);
fprintf(fid2,'\n');

tline=fgetl(fid);
fprintf(fid2, ['<point x_coordinate="', num2str(0.25), '"
y_coordinate="0.00000000000000000000">']);
fprintf(fid2, '\n');

tline=fgetl(fid);
fprintf(fid2, tline);
fprintf(fid2,'\n');

tline=fgetl(fid);
fprintf(fid2, ['<point x_coordinate="', num2str(m/8*0.25+0.25-0.0001), '"
y_coordinate="0.00000000000000000000">']);
fprintf(fid2, '\n');

tline=fgetl(fid);
fprintf(fid2, tline);
fprintf(fid2,'\n');

tline=fgetl(fid);
fprintf(fid2, ['<point x_coordinate="', num2str(m/8*0.25+0.25), '"
y_coordinate="0.25000000000000000000">']);
fprintf(fid2, '\n');

tline=fgetl(fid);
fprintf(fid2, tline);
fprintf(fid2,'\n');

tline=fgetl(fid);
fprintf(fid2, ['<point x_coordinate="', num2str(0.5-0.0001), '"
y_coordinate="0.25000000000000000000">']);
fprintf(fid2, '\n');

tline=fgetl(fid);
fprintf(fid2, tline);
```

```
fprintf(fid2,'\n');

tline=fgetl(fid);
fprintf(fid2, ['<point x_coordinate="', num2str(0.5), '"
y_coordinate="0.00000000000000000000">']);
fprintf(fid2, '\n');

tline=fgetl(fid);
fprintf(fid2, tline);
fprintf(fid2,'\n');

tline=fgetl(fid);
fprintf(fid2, ['<point x_coordinate="', num2str(m/8*0.25+0.5-0.0001), '"
y_coordinate="0.00000000000000000000">']);
fprintf(fid2, '\n');

tline=fgetl(fid);
fprintf(fid2, tline);
fprintf(fid2,'\n');

tline=fgetl(fid);
fprintf(fid2, ['<point x_coordinate="', num2str(m/8*0.25+0.5), '"
y_coordinate="0.25000000000000000000">']);
fprintf(fid2, '\n');

tline=fgetl(fid);
fprintf(fid2, tline);
fprintf(fid2,'\n');

tline=fgetl(fid);
fprintf(fid2, ['<point x_coordinate="', num2str(0.75-0.0001), '"
y_coordinate="0.25000000000000000000">']);
fprintf(fid2, '\n');

tline=fgetl(fid);
fprintf(fid2, tline);
fprintf(fid2,'\n');

tline=fgetl(fid);
fprintf(fid2, ['<point x_coordinate="', num2str(0.75), '"
y_coordinate="0.00000000000000000000">']);
fprintf(fid2, '\n');

tline=fgetl(fid);
fprintf(fid2, tline);
fprintf(fid2,'\n');

tline=fgetl(fid);
fprintf(fid2, ['<point x_coordinate="', num2str(m/8*0.25+0.75-0.0001), '"
y_coordinate="0.00000000000000000000">']);
fprintf(fid2, '\n');

tline=fgetl(fid);
fprintf(fid2, tline);
fprintf(fid2,'\n');

tline=fgetl(fid);
fprintf(fid2, ['<point x_coordinate="', num2str(m/8*0.25+0.75), '"
y_coordinate="0.25000000000000000000">']);
fprintf(fid2, '\n');
```

```
tline=fgetl(fid);
fprintf(fid2, tline);
fprintf(fid2,'\n');

tline=fgetl(fid);
fprintf(fid2, ['<point x_coordinate="', num2str(1-0.0001), '"
y_coordinate="0.250000000000000000000">']);
fprintf(fid2, '\n');

tline=fgetl(fid);
fprintf(fid2, tline);
fprintf(fid2,'\n');

tline=fgetl(fid);
fprintf(fid2, ['<point x_coordinate="', num2str(1), '"
y_coordinate="0.000000000000000000000">']);
fprintf(fid2, '\n');

%  tline = fgetl(fid);
% %   fprintf(fid2,'asd');
% fprintf(fid2,['<Type_of_interpolation>cubic</Type_of_interpolation>']);
while (1)
        tline = fgetl(fid);
         if ~ischar(tline), break, end
         fprintf(fid2,tline);
         fprintf(fid2,'\n');
    end


 fclose(fid);
 fclose(fid2);
end
end
end

fid = fopen('mybat.bat','wt');     % 'wt' means "write text"

for t=[100:10:200]
for i=[210:10:1000]
for m=[1:1:7]

    y=['consolesolver.exe -s kare_t' num2str(t) '_' num2str(i) '_'
num2str(m/8) '.xml'];

    fprintf(fid,y);
    fprintf(fid,'\n');

end
end
end
fclose(fid);
```

8.2.2 Post-processing

This matlab code was written for evaluating and arranging results in a matrix form.

```
clear all
close all
clc

final=zeros(45,2,6160);

d=1;

for t=[100:10:200]
for i=[210:10:1000]
for m=[1:1:7]

fid=fopen(['kare_t', num2str(t), '_', num2str(i), '_', num2str(m/8),
'_results.xml']);


k=1;
tline='a';
while (6)
%     ~isequal(tline,'</Solved_task>')
    tline = fgetl(fid);
    if ~ischar(tline), break, end
%     fprintf(tline);
%     fprintf('\n');
    a=regexp(tline, 'Transmitted_energy="\w*.\w*"', 'match');
%     k=k+1;
    if ~isequal(a,{});
        result(k)=a;
    k=k+1;
    end
end
fin=cell2mat(result);
z=char(zeros(45,22));
for j=1:45

    for x=1:22
        z(j,x)=fin((j-1)*43+x+20);
    end

end

sonz=str2num(z);

    for y=1:44
        final(y+1,1,d)=2*y;
    end

    for y=1:45
        final(y,2,d)=sonz(y);
    end

d=d+1;
fclose(fid);
```

```
end
end
end
```

8.2.3 Finalizing and Plotting

This matlab code was written to calculate transmitted power for each simulation and to plot the incident angle versus transmission.

```
%escape from a uniform refractive index slab, no grating

dtheta=1e-4;
theta=0:dtheta:pi/2*0.89;
TT=zeros(size(theta));
% thetac=90/180*pi;
nsubs=2.7;
thetac=asin(1/nsubs);
TT(find(theta<thetac))=1;
% subplot(62,1,1);
% plot(theta/pi*180,TT);
dI=dtheta*sin(theta).*TT;
myintegral=sum(dI)/2 %bottom half is always lost
% title(['Bare surface, escaped percentage is:
',num2str(myintegral*100),'%']);
fprintf(['Bare surface, escaped percentage is:
',num2str(myintegral*100),'%']);

matrix=zeros(6160,2);
for p= 1:6160

TT2=interp1(final(:,1,p)/180*pi,final(:,2,p),theta);
% subplot(62,1,p+1);
% plot(theta/pi*180,TT2);
dI=dtheta*sin(theta).*TT2;
myintegral=sum(dI)/2; %bottom half is always lost
% title(['grating ',p, 'escaped percentage is: ',
num2str(myintegral*100),'%']);
fprintf('\ngrating, escaped percentage is: %g with %g.
line',myintegral*100, p);
matrix(p,2)=myintegral*100;
end

%save('matrixt200')
plot(matrix)
```

8.3 3D FDTD Simulation Lumerical Scripts

8.3.1 Square PC lattice

This script was written for arranging simulation area, adjusting parameters and identifying material properties in three dimensions for square lattice PC structure.

```
pc=1;
increment=10e-9;
pcheight=120e-9;
airheight=2000e-9;
ganheight=1e-6;
sappheight=1000e-9;
air=1;
gan=2.729;
lambda=390e-9;
lambda_gan=lambda/gan;
nx=10;
ny=nx;
mesh_constant=15;
sourceplace=325e-9;
monitorplace=1e-6;
freespace=100e-9;
fdtd_xspan=5;
sourceno=1;
for (per=2)
{
for (n=120)
{
pcdia=260e-9;
period=per*pcdia;
pcheight=n*10^-9;
for (j=0) #dffrnt pc periods
{
for (k=2)
{
if (pc==1)
{
h=1001;
addcircle;
set("name",h);
set("x",0);
set("y",0);
set("z",0);
set("radius",pcdia/2);
set("z span",pcheight);
set("material","etch");
set("override mesh order from material database",1);
set("mesh order",1);
for(i=1:nx)
{
copy(period,0,0);
}
selectall;
for(q=1:ny)
{
copy(0,period,0);
}
```

```
}
addrect;
set("x",nx*period/2);
set("y",sqrt(3)/2*period*ny/2);
set("z",(pcheight+airheight)/2);
set("x span",nx*period+pcdia);
set("y span",sqrt(3)/2*period*ny+pcdia);
set("z span",airheight);
set("material","etch");
set("override mesh order from material database",1);
set("mesh order",1);
addrect;
set("x",nx*period/2);
set("y",sqrt(3)/2*period*ny/2);
set("z min",pcheight/2-ganheight);
set("x span",nx*period+pcdia);
set("y span",sqrt(3)/2*period*ny+pcdia);
set("z max",pcheight/2);
set("index",gan);
set("override mesh order from material database",1);
set("mesh order",2);
addrect;
set("x",nx*period/2);
set("y",sqrt(3)/2*period*ny/2);
set("z min",pcheight/2-ganheight-sappheight);
set("z max",pcheight/2-ganheight);
set("x span",nx*period+pcdia);
set("y span",sqrt(3)/2*period*ny+pcdia);
set("index",1.7);
set("override mesh order from material database",1);
set("mesh order",3);
simulation;
addfdtd;
set("background index",gan);
set("x",nx*period/2);
set("y",period*ny/2);
set("z min",pcheight/2-ganheight-333e-9);
set("z max",pcheight/2+1.2e-6);
set("x span",fdtd_xspan*period);
set("y span",period*fdtd_xspan);
set("mesh type","uniform");
if
(round(period/lambda_gan*mesh_constant)<(period/lambda_gan*mesh_constant))
{
set("dx",period/(round(period/lambda_gan*mesh_constant)+1));
}
else
{
set("dx",period/round(period/lambda_gan*mesh_constant));
}
set("dy",get("dx")*sqrt(3)/2);
set("use mesh refinement",1);
set("meshing refinement",5);
#set("x min bc","Periodic");
sources;
#turn=-59*0.25;
adddipole;
if (k==2)
{
set("dipole type", "electric dipole");
```

```
set("theta",90);
set("phi",rand*360);
set("phase",rand*360);
filename="TE";
}
set("x",(nx-fdtd_xspan)*period/2+fdtd_xspan*period/(sourceno+1));
set("y",period*ny/2);
set("z",(pcheight/2-sourceplace));

set("wavelength start",lambda);
set("wavelength stop",lambda);

}
}
monitors;
addpower;
set("x",nx*period/2);
set("y",sqrt(3)/2*period*ny/2);
set("y span",sqrt(3)/2*period*ny*2);
set("x span",nx*period);
set("x span",nx*period*2);
set("z",pcheight/2+monitorplace);
set("output power",1);
addmovie;
set("monitor type","2D Y-normal");
set("x",nx*period/2);
set("y",sqrt(3)/2*period*ny/2);
set("z",-300e-9);
set("x span",nx*period*2);
set("z span",5e-6);
save(num2str(pc)+num2str(j)+filename+"_t"+num2str(n)+"_per"+num2str(per)+"_
tez.fsp");
#run(2);
switchtolayout;
structures;
deleteall;
simulation;
deleteall;
sources;
deleteall;
monitors;
deleteall;
}
pcdia=pcdia+increment;
period=per*pcdia;
}
```

8.3.2 Triangular PC Lattice

This script was written for pre-processing of triangular PC lattice.

```
#loaddata("msayisi.ldf");
pc=0;
increment=10e-9;
pcheight=90e-9;
airheight=2000e-9;
ganheight=1e-6;
sappheight=1000e-9;
air=1;
gan=2.729;
lambda=390e-9;
lambda_gan=lambda/gan;
nx=10;
ny=nx;
mesh_constant=15;
sourceplace=325e-9;
monitorplace=1e-6;
freespace=100e-9;
fdtd_xspan=5;
sourcesayisi=1;
msayisi=1;
mysayisi=1;
kontrol=0;
for (per=2)
{
for (n=90)
{
pcdia=260e-9;
period=per*pcdia;
pcheight=n*10^-9;
for (j=0) #dffrnt pc periods
{
#load(num2str(pc)+num2str(j)+"TE"+"_t"+num2str(n)+"_per"+num2str(per)+"_tez
3d.fsp");
for (k=2)
{
sources;
#turn=-59*0.25;
for (my=mysayisi:1:sourcesayisi)
{

for (m=msayisi:1:sourcesayisi)
{
msayisi=msayisi+1;
kontrol=0;#mysayisi artmasin
if (m==sourcesayisi)
{
msayisi=1;
kontrol=1;
}
adddipole;
if (k==2)
{
set("dipole type", "electric dipole");
set("theta",90);
set("phi",rand*360);
set("phase",rand*360);
```

```
filename="TE";
}
set("x",(nx-fdtd_xspan)*period/2+fdtd_xspan*period/(sourcesayisi+1)*m);
set("y",sqrt(3)/2*period*ny/2-
sqrt(3)/2*period*fdtd_xspan/2+sqrt(3)/2*period*fdtd_xspan/(sourcesayisi+1)*
my);
#set("x",pcdia*turn+nx*period/2);
#turn=turn+0.25;
set("z",(pcheight/2-sourceplace));
set("wavelength start",lambda);
set("wavelength stop",lambda);
if (kontrol==1)
{
mysayisi=mysayisi+1;
}
#if (round(m/10)==(m/10))
#{
#if (my!=sourcesayisi)
#{
#savedata("msayisi.ldf",msayisi,mysayisi,kontrol);
#save;
#exit(2);
#}
#}
}
}
if (pc==1)
{
h=1001;
addcircle;
set("name",h);
set("x",0);
set("y",0);
set("z",0);
set("radius",pcdia/2);
set("z span",pcheight);
set("material","etch");
set("override mesh order from material database",1);
set("mesh order",1);
for(q=0:ny)
{
for(i=1:nx)
{
copy(period,0,0);
set("name",i+q*nx);
}
select(num2str(h));
if (round(q/2)*2==q)
{
copy(period/2,sqrt(3)/2*period,0);
h=h+1;
set("name",h);
}
else
{
copy(-period/2,sqrt(3)/2*period,0);
h=h+1;
set("name",h);
}
}
delete;#delete last circle
```

```
}
addrect;
set("x",nx*period/2);
set("y",sqrt(3)/2*period*ny/2);
set("z",(pcheight+airheight)/2);
set("x span",nx*period+pcdia);
set("y span",sqrt(3)/2*period*ny+pcdia);
set("z span",airheight);
set("material","etch");
set("override mesh order from material database",1);
set("mesh order",1);
addrect;
set("x",nx*period/2);
set("y",sqrt(3)/2*period*ny/2);
set("z min",pcheight/2-ganheight);
set("x span",nx*period+pcdia);
set("y span",sqrt(3)/2*period*ny+pcdia);
set("z max",pcheight/2);
set("index",gan);
set("override mesh order from material database",1);
set("mesh order",2);
addrect;
set("x",nx*period/2);
set("y",sqrt(3)/2*period*ny/2);
set("z min",pcheight/2-ganheight-sappheight);
set("z max",pcheight/2-ganheight);
set("x span",nx*period+pcdia);
set("y span",sqrt(3)/2*period*ny+pcdia);
set("index",1.7);
set("override mesh order from material database",1);
set("mesh order",3);
simulation;
addfdtd;
set("background index",gan);
set("x",nx*period/2);
set("y",sqrt(3)/2*period*ny/2);
set("z min",pcheight/2-ganheight-333e-9);
set("z max",pcheight/2+1.2e-6);
set("x span",fdtd_xspan*period);
set("y span",sqrt(3)/2*period*fdtd_xspan);
set("mesh type","uniform");
if
(round(period/lambda_gan*mesh_constant)<(period/lambda_gan*mesh_constant))
{
set("dx",period/(round(period/lambda_gan*mesh_constant)+1));
}
else
{
set("dx",period/round(period/lambda_gan*mesh_constant));
}
set("dy",get("dx")*sqrt(3)/2);
set("use mesh refinement",1);
set("meshing refinement",5);
#set("x min bc","Periodic");

monitors;
addpower;
set("x",nx*period/2);
set("y",sqrt(3)/2*period*ny/2);
set("y span",sqrt(3)/2*period*ny*2);
set("x span",nx*period);
```

```
set("x span",nx*period*2);
set("z",pcheight/2+monitorplace);
set("output power",1);
addmovie;
set("monitor type","2D Y-normal");
set("x",nx*period/2);
set("y",sqrt(3)/2*period*ny/2);
set("z",-300e-9);
set("x span",nx*period*2);
set("z span",5e-6);
save(num2str(pc)+num2str(j)+filename+"_t"+num2str(n)+"_per"+num2str(per)+"_
tez3d.fsp");
#run(2);
switchtolayout;
structures;
deleteall;
simulation;
deleteall;
sources;
deleteall;
monitors;
deleteall;
}
pcdia=pcdia+increment;
period=per*pcdia;
}
}
}
msayisi=1;
mysayisi=1;
kontrol=0;
savedata("msayisi.ldf",msayisi,mysayisi,kontrol);
exit(2);
new3d;
save("00TE_t90_per2_tez3d.fsp");
```

8.4 Far Field Pattern Calculations Lumerical Scripts

This script was written to integrate and plot far field patterns of simulations.

```
farfieldfilter(0.12);
load("00TE_t90_per2_tez3d_9.5nmzmesh.fsp");
E2_far_nopc=farfield3d("monitor6");
load("00TE_t90_theta90.fsp");
E2_far_nopc2=farfield3d("monitor6");
E2_far_nopc=E2_far_nopc+E2_far_nopc2;
ux = farfieldux("monitor2");
uy = farfielduy("monitor2");
image(ux,uy,E2_far_nopc,"","","","polar");

load("10TE_t90_per2_tez3d_z9.5nmmesh.fsp");
E2_far_pc=farfield3d("monitor2");
load("10TE_t90_theta90.fsp");
E2_far_pc2=farfield3d("monitor2");
ux = farfieldux("monitor2");
uy = farfielduy("monitor2");
E2_far_pc=E2_far_pc+E2_far_pc2;

image(ux,uy,E2_far_pc,"","","","polar");


load("10TE_t90_per2_PCplace2.fsp");
E2_far_pc=farfield3d("monitor2");
load("10TE_t90_theta90_PCplace_2.fsp");
E2_far_pc2=farfield3d("monitor2");
ux = farfieldux("monitor2");
uy = farfielduy("monitor2");
E2_far_pc=E2_far_pc+E2_far_pc2;

image(ux,uy,E2_far_pc,"","","","polar");
image(ux,uy,E2_far_pc,"","","","logplot,polar");
```

8.5 Power Calculations

Power flow measurements were done using power monitor and the scripts below. Calculating power can be done in more than one method. Therefore, all of them was tried and checked whether the results were in agreement.

```
f=getdata("monitor1","f");
T=transmission("monitor1");
p=getdata("monitor1","power");
d=dipolepower(f);
s=sourcepower(f);
E2_near = getelectric("monitor1");
E2_far=farfield2d("monitor1",1,2001);
theta=farfieldangle("monitor1",1,2001);
x=getdata("monitor1","x");
y=getdata("monitor1","y");
Ex=getdata("monitor1","Ex");
Ey=getdata("monitor1","Ey");
Hz=getdata("monitor1","Hz");
?power1=integrate(Ex*conj(Hz),1,x)/2;
Py=getdata("monitor1","Py");
?power2=0.5*integrate(Py,1,x);
```

8.6 3D FDTD Simulation Fullwave Matlab Codes

Below in the matlab codes, 3D FDTD simulation results were plotted as stated in chapter 6.

```
%escape from a uniform refractive index slab, no grating

dtheta=1e-4;
% dtheta=1;
theta=0:dtheta:pi/2*85/90;
% theta=0:dtheta:87;
TT=zeros(size(theta));
% thetac=90/180*pi;
nsubs=2.7;
thetac=asin(1/nsubs);

TT(find(theta<thetac))=1;
subplot(12,2,1);
plot(theta/pi*180,TT);
% plot(theta,TT);
dI=dtheta*sin(theta).*TT;
% dI=dtheta*pi/180*sin(theta*pi/180).*TT;
myintegral=sum(dI)/2; %bottom half is always lost
title(['Bare surface, escaped percentage is:
',num2str(myintegral*100),'%']);

pc=[7.71796512e-001; 7.21855504e-001; 6.89066674e-001; 6.85427186e-001;
1.53521188e-001; 4.40781207e-002; 2.27180923e-003; 2.58478289e-002;
2.56512063e-003; 1.31776854e-002; 7.74174736e-003;6.1166382959e-
003;4.8383710106e-003;1.5917099661e-003;8.2322468288e-003;1.9137955600e-
002;2.3516038480e-002;2.3046701170e-002
7.40744070e-001; 7.01030095e-001; 6.58110500e-001; 6.55685669e-001;
4.00677859e-001; 2.47747298e-001; 6.31624225e-003; 1.89988456e-002;
5.54081040e-003; 4.74025645e-004; 7.67535442e-004;4.1154893683e-
003;5.3566663156e-003;8.7845874448e-003;1.0573309668e-002;2.2724308068e-
003;4.2688270610e-004;3.4151307464e-003
7.16701929e-001; 6.79134547e-001; 6.28863591e-001; 6.17806690e-001;
4.24224646e-001; 1.39061346e-001; 3.72005728e-002; 5.56784592e-003;
2.95577930e-002; 2.55181136e-002; 2.01313816e-002;5.4638973345e-
003;1.0227782556e-002;6.0987025118e-003;2.2103928541e-004;7.7715825973e-
003;1.8495537603e-002;2.5873558927e-002
6.93141501e-001; 6.59943555e-001; 6.02368929e-001; 5.51597794e-001;
3.06439745e-001; 3.75483631e-002; 5.42895592e-002; 3.71147931e-002;
8.67761981e-002; 8.45028854e-002; 2.66414539e-002;3.3019650712e-
002;1.4472547144e-002;6.6399926418e-003;2.0263266271e-002;2.1295623272e-
002;1.1652943421e-002;5.3872986992e-003
6.69111403e-001; 6.46937258e-001; 5.80840155e-001; 4.21656981e-001;
1.04722461e-001; 6.22869313e-003; 1.02563457e-001; 1.21717673e-001;
1.41887069e-001; 8.86161806e-002;6.9640148794e-002;3.4502765301e-
002;9.6316264387e-003;2.9830574854e-002;2.5037650642e-002;1.7526661977e-
002;1.9167682567e-002;2.3927170793e-002
6.54122824e-001; 6.42044670e-001; 5.40400679e-001; 2.75665216e-001;
6.71624025e-002; 1.38961659e-002; 2.08245192e-001; 1.56073668e-001;
1.46589743e-001; 7.75994621e-002;6.2458606856e-002;3.7446322036e-
003;2.7668962332e-002;3.4492326985e-002;3.4229144125e-002;4.7023575541e-
002;5.6798996285e-002;5.5513815628e-002
6.41699847e-001; 6.47798171e-001; 5.06190984e-001; 1.85989586e-001;
1.14263943e-001; 1.41622011e-001; 4.80142007e-001; 1.54386126e-001;
1.12835192e-001; 5.62183542e-002;5.1749470722e-004;5.2671509460e-
```

```
003;4.0989606189e-002;3.9535158390e-002;3.5771064730e-002;2.0322840387e-
002;8.8850795645e-003;5.1225397325e-003
6.35993969e-001; 6.61189992e-001; 3.61897534e-001; 1.20383670e-001;
3.11334538e-001; 4.75395909e-001; 6.34786023e-001; 1.31453234e-001;
5.80919419e-002; 6.48751974e-002;4.0119689401e-002;5.8378146486e-
002;4.6422322131e-002;4.7441152538e-002;2.6725612312e-002;1.5352325120e-
002;2.3492214021e-002;4.8329229889e-002
6.38368241e-001; 6.80849088e-001; 1.42275012e-001; 5.95858352e-002;
5.07191949e-001; 6.21090104e-001; 4.56857572e-001; 1.62603788e-001;
3.74485971e-002; 8.38567501e-002;8.4113456538e-002;6.3734940781e-
002;6.8051122129e-002;4.3206112177e-002;3.9725113895e-002;4.1412779102e-
002;3.1537994992e-002;2.1565157461e-002
6.42042908e-001; 6.76145385e-001; 8.57049631e-002; 2.63078992e-002;
6.05413466e-001; 6.49153296e-001; 2.71892165e-001; 1.48575865e-001;
7.00190342e-002; 1.06333775e-001;8.7843001242e-002;7.9703566051e-
002;6.2314138384e-002;5.3267209050e-002;4.4667089447e-002;2.1328557849e-
002;5.6627656768e-003;7.6681336077e-003
];

acilar=[0   5     10    15    20    25    30    35    40    45    50    55
      60    65    70    75    80    85];
grt1=zeros(10,18);
k=1;
for i=1:180
    grt1(ceil(i/18),k)= pc(i);
    if k==18;
        k=0;
    end
    k=k+1;
end

j=2;
m=0;
a=1;
for i=1:18:179
    TT2=interp1(acilar/180*pi,grt1(ceil(i/18),:),theta);
subplot(12,1,j);
plot(theta/pi*180,TT2);
dI=dtheta*sin(theta).*TT2;
myintegral1(a)=sum(dI)/2; %bottom half is always lost
title(['pc',  num2str(200+m), ':', num2str(myintegral1(a)*100),'%']);
j=j+1;
m=m+10;
a=a+1;
end

nopc=[7.93428437e-001; 7.36421079e-001; 7.01481292e-001; 6.99433651e-001;
1.59356967e-001; 4.78156068e-002; 1.08761329e-004; 2.66408010e-002;
4.14231176e-004; 1.79157154e-002; 1.46496891e-004; 1.24061504e-002;
7.55847318e-003; 4.31006249e-004; 1.08008005e-002; 2.18960383e-002;
2.60313055e-002; 2.52138195e-002;
7.98221453e-001; 7.50500466e-001; 7.04763440e-001; 7.01035119e-001;
4.21647630e-001; 2.61429428e-001; 7.45056234e-003; 2.75814371e-002;
1.53083953e-002; 8.51040014e-003; 1.01457271e-002; 1.09151928e-002;
9.72390091e-004; 1.47506126e-002; 1.34084357e-002; 2.67520459e-003;
5.65902723e-004; 4.10403978e-003;
7.94532098e-001; 7.59935509e-001; 7.00709456e-001; 6.85984976e-001;
5.18198420e-001; 1.71650953e-001; 5.16743824e-002; 1.90567695e-003;
2.68972464e-002; 8.17740939e-004; 1.68527391e-002; 6.95358356e-005;
1.36914103e-002; 6.90263866e-003; 3.11573334e-004; 8.62427597e-003;
2.03000660e-002; 2.82800726e-002;
```

```
7.94634252e-001; 7.65547477e-001; 7.00978520e-001; 6.62922291e-001;
5.64989448e-001; 8.14561282e-002; 6.93899383e-002; 4.70411758e-003;
1.15716922e-002; 1.46422826e-002; 2.90572531e-003; 1.07759140e-002;
6.79162072e-003; 1.39058736e-003; 1.38686659e-002; 1.65679631e-002;
8.97781264e-003; 3.64907935e-003;
7.99228848e-001; 7.70310246e-001; 7.04908849e-001; 6.36504945e-001;
5.59569377e-001; 4.01174461e-002; 3.75364275e-002; 2.39311618e-002;
4.27552389e-004; 1.55026654e-002; 3.19993410e-003; 1.03719763e-002;
7.56699417e-004; 1.17197080e-002; 6.38068500e-003; 4.89369168e-004;
2.79579629e-003; 7.84648195e-003;
7.93350587e-001; 7.74283844e-001; 7.12375837e-001; 6.14760747e-001;
4.81403816e-001; 1.06634537e-002; 1.60288690e-003; 2.27899783e-002;
1.02471282e-002; 1.90209028e-003; 1.27498424e-002; 1.78775618e-004;
1.05004493e-002; 3.94494285e-003; 1.70480051e-003; 1.59408553e-002;
3.15349760e-002; 3.75367375e-002;
7.94838401e-001; 7.78763361e-001; 7.21555279e-001; 6.05451904e-001;
2.97977660e-001; 9.17899120e-002; 4.47444755e-004; 5.59157281e-003;
1.46282010e-002; 2.85070994e-003; 5.35291968e-003; 5.86946750e-003;
4.87856290e-003; 1.89936022e-003; 1.03990842e-002; 7.94930232e-003;
3.06462663e-003; 1.34327967e-003;
7.94972137e-001; 7.83011199e-001; 7.39850109e-001; 6.35622232e-001;
3.15944831e-001; 1.44453661e-001; 2.94598433e-002; 7.27454800e-004;
8.98798234e-003; 1.42734871e-002; 2.52144864e-004; 1.04466184e-002;
6.54110804e-004; 1.10227741e-002; 5.71010550e-003; 1.28195578e-003;
9.10793084e-003; 2.92411026e-002;
7.93739159e-001; 7.86006897e-001; 7.50652252e-001; 6.66707033e-001;
4.29466059e-001; 1.59663457e-001; 5.88634454e-002; 1.38275727e-002;
4.37396651e-004; 1.00223124e-002; 1.08447230e-002; 7.21449930e-004;
1.12766984e-002; 2.39672323e-003; 5.12979970e-003; 1.64788056e-002;
1.69879682e-002; 1.32135715e-002;
7.98547590e-001; 7.88023895e-001; 7.57736997e-001; 6.86711703e-001;
4.97522714e-001; 8.54595768e-002; 4.03291945e-002; 2.71444407e-002;
1.09464953e-002; 6.77450809e-005; 1.06973512e-002; 5.60539112e-003;
5.72362909e-003; 4.25333665e-003; 1.53544068e-002; 1.03376023e-002;
3.54382804e-003; 6.54764990e-003;
];

grt2=zeros(10,18);
k=1;
for i=1:180
    grt2(ceil(i/18),k)= nopc(i);
    if k==18;
        k=0;
    end
    k=k+1;
end

j=1;
m=0;
a=1;
figure;
for i=1:18:179
    TT2=interp1(acilar/180*pi,grt2(ceil(i/18),:),theta);
subplot(11,1,j);
plot(theta/pi*180,TT2);
dI=dtheta*sin(theta).*TT2;
myintegral2(a)=sum(dI)/2; %bottom half is always lost
title(['nopc',  num2str(200+m), ':', num2str(myintegral2(a)*100),'%']);
j=j+1;
m=m+10;
a=a+1;
```

```
end

figure;
x=[200 210 220 230 240 250 260 270 280 290];
plot(x , myintegral1./myintegral2);
title('pc/nopc');
```

```
%escape from a uniform refractive index slab, no grating

dtheta=1e-4;
% dtheta=1;
theta=0:dtheta:pi/2*85/90;
% theta=0:dtheta:87;
TT=zeros(size(theta));
% thetac=90/180*pi;
nsubs=2.7;
thetac=asin(1/nsubs);

TT(find(theta<thetac))=1;
subplot(12,2,1);
plot(theta/pi*180,TT);
% plot(theta,TT);
dI=dtheta*sin(theta).*TT;
% dI=dtheta*pi/180*sin(theta*pi/180).*TT;
myintegral=sum(dI)/2; %bottom half is always lost
title(['Bare surface, escaped percentage is:
',num2str(myintegral*100),'%']);

pc=[6.56215025e-001 ; 5.50546489e-001 ; 9.52995179e-002 ; 4.22024299e-002 ;
5.91753101e-001 ; 5.47892635e-001 ; 1.56682656e-001 ; 9.73504273e-002 ;
1.14375114e-001 ; 1.28787677e-001 ; 9.01977485e-002 ; 8.16099200e-002 ;
6.42520597e-002 ; 4.45600436e-002 ; 9.99607838e-003 ; 1.70545316e-002 ;
2.93420798e-002 ; 3.27646201e-002 ;

6.47370217e-001 ; 2.93303481e-001 ; 1.14841688e-001 ; 3.02167671e-001 ;
5.23986908e-001 ; 3.85761483e-001 ; 1.26919050e-001 ; 7.52148726e-002 ;
1.64350376e-001 ; 1.32750485e-001 ; 1.16020349e-001 ; 7.35097417e-002 ;
6.98512127e-002 ; 3.21455495e-002 ; 3.45621935e-002 ; 3.68537095e-002 ;
2.42155925e-002 ; 1.05797270e-002 ;

6.82514570e-001 ; 2.03677196e-001 ; 1.35258966e-001 ; 3.97068858e-001 ;
4.24257213e-001 ; 2.37985426e-001 ; 1.90460060e-001 ; 9.03686568e-002 ;
2.25299647e-001 ; 1.47099480e-001 ; 1.10023563e-001 ; 8.57314886e-002 ;
5.72144872e-002 ; 4.83939282e-002 ; 1.96753363e-002 ; 4.26478090e-003 ;
1.36870111e-002 ; 2.37284756e-002 ;

8.10176230e-001 ; 2.25388227e-001 ; 1.59164214e-001 ; 3.84912042e-001 ;
3.05450319e-001 ; 2.01555205e-001 ; 2.73572097e-001 ; 2.67540218e-001 ;
2.78089479e-001 ; 1.85156799e-001 ; 9.83950169e-002 ; 9.45005392e-002 ;
7.01581829e-002 ; 3.07113708e-002 ; 3.80899796e-003 ; 2.44105001e-002 ;
3.91062095e-002 ; 3.68754057e-002 ;

8.14314209e-001 ; 2.58864924e-001 ; 1.61142512e-001 ; 3.32724543e-001 ;
2.30727476e-001 ; 2.80937313e-001 ; 4.59798996e-001 ; 4.14487968e-001 ;
2.98859132e-001 ; 2.09103078e-001 ; 1.21224020e-001 ; 8.80440640e-002 ;
6.50571340e-002 ; 2.05442543e-003 ; 2.11461330e-002 ; 1.02022726e-002 ;
1.26985608e-003 ; 5.47917802e-003 ;
```

```
6.31688601e-001 ; 3.02129853e-001 ; 2.04519480e-001 ; 2.70906301e-001 ;
2.24317515e-001 ; 3.28319603e-001 ; 5.35817266e-001 ; 4.56259721e-001 ;
2.82136257e-001 ; 1.77090314e-001 ; 1.41312463e-001 ; 9.62193871e-002 ;
1.95771027e-002 ; 1.97894275e-002 ; 8.72529733e-003 ; 3.55441681e-003 ;
2.30754328e-002 ; 4.42514979e-002 ;

4.10767679e-001 ; 3.51909731e-001 ; 2.94929804e-001 ; 2.56230240e-001 ;
2.48406049e-001 ; 3.39878273e-001 ; 5.27034183e-001 ; 4.58675283e-001 ;
2.77281652e-001 ; 1.79658741e-001 ; 1.21685299e-001 ; 8.58559735e-002 ;
1.64463440e-002 ; 1.89552317e-002 ; 7.13751415e-003 ; 2.45749517e-002 ;
1.61372306e-002 ; 7.28053822e-003 ;

2.75731795e-001 ; 3.71634472e-001 ; 3.29596781e-001 ; 2.65220159e-001 ;
2.67660128e-001 ; 3.25656602e-001 ; 4.70449207e-001 ; 4.03597958e-001 ;
2.83474890e-001 ; 2.17522244e-001 ; 1.10332923e-001 ; 3.63799928e-002 ;
3.87779196e-002 ; 1.20390051e-002 ; 2.64804020e-002 ; 1.54448473e-002 ;
1.08229275e-002 ; 1.95487376e-002 ;

2.07029823e-001 ; 3.14427778e-001 ; 3.40223724e-001 ; 2.81973744e-001 ;
2.83296982e-001 ; 2.94903194e-001 ; 3.93514950e-001 ; 3.51145131e-001 ;
2.93184238e-001 ; 1.95698206e-001 ; 9.55113462e-002 ; 3.14986180e-002 ;
3.57574107e-002 ; 3.37343383e-002 ; 2.41068165e-002 ; 2.82358284e-002 ;
3.40499185e-002 ; 2.84270053e-002 ;

1.72450336e-001 ; 2.15573469e-001 ; 3.26204212e-001 ; 2.96779038e-001 ;
2.89099352e-001 ; 2.68579331e-001 ; 3.40111859e-001 ; 3.93201735e-001 ;
3.16000817e-001 ; 8.88531172e-002 ; 6.72266888e-002 ; 5.94395127e-002 ;
3.89652203e-002 ; 4.29383049e-002 ; 3.80824297e-002 ; 3.29585507e-002 ;
1.76903300e-002 ; 9.82730411e-003 ;

1.54696611e-001 ; 1.77375914e-001 ; 3.27998004e-001 ; 3.29816355e-001 ;
2.96894868e-001 ; 2.84730668e-001 ; 3.13833227e-001 ; 3.89422801e-001 ;
3.01451400e-001 ; 4.08470778e-002 ; 4.59963943e-002 ; 6.37641787e-002 ;
5.66557102e-002 ; 4.45107882e-002 ; 2.90544298e-002 ; 1.00453313e-002 ;
2.51358194e-002 ; 3.70276500e-002 ;

];

acilar=[0   5     10    15    20    25    30    35    40    45    50    55
      60    65    70    75    80    85];
grt1=zeros(11,18);
k=1;
for i=1:198
    grt1(ceil(i/18),k)= pc(i);
    if k==18;
        k=0;
    end
    k=k+1;
end

j=2;
m=0;
a=1;
for i=1:18:197
    TT2=interp1(acilar/180*pi,grt1(ceil(i/18),:),theta);
subplot(12,1,j);
plot(theta/pi*180,TT2);
dI=dtheta*sin(theta).*TT2;
myintegral1(a)=sum(dI)/2; %bottom half is always lost
title(['pc',  num2str(300+m), ':', num2str(myintegral1(a)*100),'%']);
j=j+1;
```

```
m=m+10;
a=a+1;
end

nopc=[7.95199514e-001 ; 7.89267708e-001 ; 7.62262226e-001 ; 7.00358427e-001
; 5.48068520e-001 ; 4.24266069e-002 ; 5.39755584e-003 ; 1.60788994e-002 ;
1.82817982e-002 ; 7.86823640e-003 ; 2.61526792e-004 ; 1.04488466e-002 ;
1.25527711e-003 ; 1.02418246e-002 ; 2.82885152e-004 ; 7.28375708e-003 ;
1.84280625e-002 ; 2.29524621e-002 ;

7.98101738e-001 ; 7.89274105e-001 ; 7.59603586e-001 ; 6.97849720e-001 ;
5.60293718e-001 ; 1.03932520e-002 ; 2.18648357e-003 ; 5.20447113e-004 ;
7.51489256e-003 ; 1.28701311e-002 ; 5.45343258e-003 ; 1.25225534e-003 ;
9.55656400e-003 ; 6.06092699e-004 ; 8.28731660e-003 ; 1.83190540e-002 ;
1.53627844e-002 ; 8.15423267e-003 ;

7.98468953e-001 ; 7.86199117e-001 ; 7.52055612e-001 ; 6.81831684e-001 ;
5.03275459e-001 ; 5.38753306e-002 ; 1.37917543e-002 ; 2.47179202e-003 ;
4.30694065e-004 ; 3.17845295e-003 ; 9.02795474e-003 ; 3.02086871e-003 ;
2.99499856e-003 ; 4.74444476e-003 ; 5.71096093e-003 ; 1.28806610e-004 ;
5.46862173e-003 ; 1.24365766e-002 ;

7.92401917e-001 ; 7.83189777e-001 ; 7.43777053e-001 ; 6.56135964e-001 ;
3.90240345e-001 ; 7.68487345e-003 ; 2.90105716e-002 ; 1.32498286e-002 ;
7.31039022e-003 ; 8.57725440e-004 ; 1.86380259e-003 ; 7.75518532e-003 ;
1.02210392e-003 ; 6.15403536e-003 ; 2.88151644e-004 ; 9.34172315e-003 ;
1.89349984e-002 ; 2.07522464e-002 ;

7.93179582e-001 ; 7.80773524e-001 ; 7.36815538e-001 ; 6.47217515e-001 ;
4.01121962e-001 ; 1.25870480e-001 ; 3.38763535e-002 ; 1.91675164e-002 ;
1.52373842e-002 ; 9.79895675e-003 ; 1.79535418e-003 ; 1.97109272e-003 ;
7.75478375e-003 ; 9.97954647e-005 ; 7.57470479e-003 ; 4.64655993e-003 ;
3.08334635e-004 ; 1.73804443e-003 ;

7.93327073e-001 ; 7.77958222e-001 ; 7.29237776e-001 ; 6.43690585e-001 ;
4.41229790e-001 ; 8.54495793e-002 ; 7.61459382e-003 ; 5.87720330e-003 ;
7.07519359e-003 ; 9.62496383e-003 ; 9.33124315e-003 ; 1.87699150e-003 ;
3.01070263e-003 ; 5.47441208e-003 ; 3.56181937e-003 ; 8.26789066e-004 ;
9.42540985e-003 ; 2.06290311e-002 ;

7.92876270e-001 ; 7.74602589e-001 ; 7.22775766e-001 ; 6.45385522e-001 ;
4.84399296e-001 ; 4.42979997e-002 ; 3.55116594e-003 ; 3.72803884e-004 ;
4.35680877e-004 ; 7.82666647e-004 ; 5.11259178e-003 ; 8.32155910e-003 ;
1.15719371e-003 ; 5.57490852e-003 ; 1.37300336e-003 ; 9.66212917e-003 ;
7.05244389e-003 ; 3.10068001e-003 ;

7.99609199e-001 ; 7.72573670e-001 ; 7.21435003e-001 ; 6.58859163e-001 ;
5.29820067e-001 ; 2.10680290e-002 ; 1.30502521e-002 ; 9.53328254e-003 ;
7.85524499e-003 ; 3.41032757e-003 ; 7.95913780e-005 ; 2.98677334e-003 ;
7.21199576e-003 ; 1.05129751e-004 ; 7.73540830e-003 ; 3.41340701e-003 ;
7.51877239e-004 ; 4.93092283e-003 ;

7.98203049e-001 ; 7.68817346e-001 ; 7.20721875e-001 ; 6.74425940e-001 ;
5.55022616e-001 ; 1.52394087e-002 ; 2.75112314e-002 ; 1.60659428e-002 ;
1.24932482e-002 ; 9.75703402e-003 ; 6.26721597e-003 ; 9.47186181e-004 ;
2.46462404e-003 ; 6.31578766e-003 ; 1.42799643e-003 ; 4.55595165e-003 ;
1.26993967e-002 ; 1.30497495e-002 ;

7.94866930e-001 ; 7.63271137e-001 ; 7.21361449e-001 ; 6.89872771e-001 ;
5.28420537e-001 ; 3.10583170e-002 ; 1.98126738e-002 ; 8.49290528e-003 ;
5.07024174e-003 ; 4.59964192e-003 ; 6.28930206e-003 ; 6.47849844e-003 ;
```

```
1.10251691e-003 ; 3.86954538e-003 ; 3.04631913e-003 ; 9.52929540e-003 ;
5.72883986e-003 ; 2.20201475e-003 ;

7.92523163e-001 ; 7.61114912e-001 ; 7.30908896e-001 ; 6.99279275e-001 ;
4.67577927e-001 ; 6.88595329e-002 ; 6.10429534e-003 ; 6.27155184e-005 ;
4.34872216e-004 ; 5.58394967e-005 ; 2.91214566e-004 ; 3.30090811e-003 ;
6.59808383e-003 ; 6.99303647e-004 ; 6.57618331e-003 ; 9.92311236e-005 ;
7.62346393e-003 ; 1.55978118e-002 ;

]

grt2=zeros(11,18);
k=1;
for i=1:198
    grt2(ceil(i/18),k)= nopc(i);
    if k==18;
        k=0;
    end
    k=k+1;
end

j=1;
m=0;
a=1;
figure;
for i=1:18:197
    TT2=interp1(acilar/180*pi,grt2(ceil(i/18),:),theta);
subplot(11,1,j);
plot(theta/pi*180,TT2);
dI=dtheta*sin(theta).*TT2;
myintegral2(a)=sum(dI)/2; %bottom half is always lost
title(['nopc',  num2str(300+m), ':', num2str(myintegral2(a)*100),'%']);
j=j+1;
m=m+10;
a=a+1;
end

figure;
x=[300 310 320 330 340 350 360 370 380 390 400];
plot(x , myintegral1./myintegral2);
title('pc/nopc');
```

```
%escape from a uniform refractive index slab, no grating

dtheta=1e-4;
% dtheta=1;
theta=0:dtheta:pi/2*85/90;
% theta=0:dtheta:87;
TT=zeros(size(theta));
% thetac=90/180*pi;
nsubs=2.7;
thetac=asin(1/nsubs);

TT(find(theta<thetac))=1;
subplot(12,2,1);
plot(theta/pi*180,TT);
% plot(theta,TT);
dI=dtheta*sin(theta).*TT;
% dI=dtheta*pi/180*sin(theta*pi/180).*TT;
```

```
myintegral=sum(dI)/2; %bottom half is always lost
title(['Bare surface, escaped percentage is:
',num2str(myintegral*100),'%']);

pc=[1.54696611e-001 ; 1.77375914e-001 ; 3.27998004e-001 ; 3.29816355e-001 ;
2.96894868e-001 ; 2.84730668e-001 ; 3.13833227e-001 ; 3.89422801e-001 ;
3.01451400e-001 ; 4.08470778e-002 ; 4.59963943e-002 ; 6.37641787e-002 ;
5.66557102e-002 ; 4.45107882e-002 ; 2.90544298e-002 ; 1.00453313e-002 ;
2.51358194e-002 ; 3.70276500e-002 ;

1.42613103e-001 ; 2.81934238e-001 ; 3.54265897e-001 ; 3.42009286e-001 ;
2.86556582e-001 ; 2.76998111e-001 ; 2.96689157e-001 ; 3.09772614e-001 ;
2.01456897e-001 ; 7.73220907e-002 ; 6.23564825e-002 ; 7.74423743e-002 ;
4.64202107e-002 ; 3.81331848e-002 ; 1.06336725e-002 ; 2.79170296e-002 ;
3.38405458e-002 ; 2.54307128e-002 ;

1.33128511e-001 ; 3.44788925e-001 ; 3.79128236e-001 ; 3.31859640e-001 ;
2.53872078e-001 ; 2.45672987e-001 ; 2.69856042e-001 ; 2.24844302e-001 ;
1.31207023e-001 ; 8.59030377e-002 ; 8.70396326e-002 ; 7.68396737e-002 ;
3.36896480e-002 ; 1.82192225e-002 ; 2.54071486e-002 ; 1.85937223e-002 ;
1.35618835e-002 ; 2.24268895e-002 ;

1.17065664e-001 ; 3.12628370e-001 ; 3.93316370e-001 ; 3.07770086e-001 ;
2.20248779e-001 ; 1.98634228e-001 ; 2.23201727e-001 ; 1.59721242e-001 ;
1.59421723e-001 ; 7.92397728e-002 ; 1.00224036e-001 ; 6.16916309e-002 ;
4.52053083e-002 ; 3.19800258e-002 ; 2.48542792e-002 ; 2.01824642e-002 ;
3.23118600e-002 ; 3.64917350e-002 ;

6.19746088e-002 ; 2.54139193e-001 ; 3.91216474e-001 ; 2.64818924e-001 ;
2.13743389e-001 ; 1.61069220e-001 ; 1.59409107e-001 ; 1.32121345e-001 ;
1.96973618e-001 ; 1.12300455e-001 ; 1.11746996e-001 ; 8.37701301e-002 ;
6.18569128e-002 ; 4.80237859e-002 ; 2.88547297e-002 ; 3.04302556e-002 ;
1.30950030e-002 ; 9.13813827e-003 ;

2.61123623e-002 ; 2.48300697e-001 ; 3.54715298e-001 ; 2.15856691e-001 ;
2.33950018e-001 ; 1.36524855e-001 ; 1.05108104e-001 ; 1.16026889e-001 ;
1.36441289e-001 ; 1.09589468e-001 ; 1.24892125e-001 ; 1.05993937e-001 ;
8.90722831e-002 ; 4.45263596e-002 ; 3.95606531e-002 ; 1.37994593e-002 ;
1.93724086e-002 ; 3.25984831e-002 ;

1.30125989e-001 ; 2.72005849e-001 ; 3.10948763e-001 ; 2.01017364e-001 ;
2.50142820e-001 ; 1.25942512e-001 ; 9.49449597e-002 ; 1.06441673e-001 ;
1.09724840e-001 ; 1.42757096e-001 ; 1.27595269e-001 ; 1.16127669e-001 ;
9.04530287e-002 ; 6.82549588e-002 ; 2.23033018e-002 ; 2.73713532e-002 ;
2.76844674e-002 ; 1.43148782e-002 ;

2.66668960e-001 ; 2.97731194e-001 ; 2.90734375e-001 ; 2.36612880e-001 ;
2.51411988e-001 ; 1.15481914e-001 ; 9.87573363e-002 ; 1.18789826e-001 ;
1.64320297e-001 ; 1.71685094e-001 ; 1.43617276e-001 ; 1.22197157e-001 ;
9.21572342e-002 ; 5.63197857e-002 ; 3.66503457e-002 ; 2.82747588e-002 ;
1.20258639e-002 ; 1.34985360e-002 ;

3.50302876e-001 ; 3.22444991e-001 ; 2.95383880e-001 ; 2.64994330e-001 ;
2.39933625e-001 ; 1.30880427e-001 ; 1.10440504e-001 ; 1.50971491e-001 ;
1.65405947e-001 ; 1.81610130e-001 ; 1.53752134e-001 ; 1.20891257e-001 ;
8.58163043e-002 ; 4.50259541e-002 ; 4.10303105e-002 ; 1.91006497e-002 ;
3.67266945e-002 ; 4.31958860e-002 ;

4.13343298e-001 ; 3.43698443e-001 ; 3.17693093e-001 ; 2.85463988e-001 ;
2.29943267e-001 ; 1.65086841e-001 ; 1.51667875e-001 ; 1.53864220e-001 ;
1.63521729e-001 ; 1.67398404e-001 ; 1.37586543e-001 ; 9.12995778e-002 ;
```

```
6.54078068e-002 ; 5.02093816e-002 ; 2.61141722e-002 ; 3.46195516e-002 ;
2.64452644e-002 ; 1.45528515e-002 ;

4.57060098e-001 ; 3.68008086e-001 ; 3.42676418e-001 ; 3.04557406e-001 ;
2.31769742e-001 ; 1.89324280e-001 ; 1.90777293e-001 ; 1.48653044e-001 ;
1.50147415e-001 ; 1.66381513e-001 ; 1.23203176e-001 ; 6.44247447e-002 ;
4.49814046e-002 ; 4.01684169e-002 ; 3.58906584e-002 ; 2.23589817e-002 ;
2.17386716e-002 ; 6.46602001e-002 ;

];

acilar=[0   5     10    15    20    25    30    35    40    45    50    55
      60    65    70    75    80    85];
grt1=zeros(11,18);
k=1;
for i=1:198
    grt1(ceil(i/18),k)= pc(i);
    if k==18;
        k=0;
    end
    k=k+1;
end

j=2;
m=0;
a=1;
for i=1:18:197
    TT2=interp1(acilar/180*pi,grt1(ceil(i/18),:),theta);
subplot(12,1,j);
plot(theta/pi*180,TT2);
dI=dtheta*sin(theta).*TT2;
myintegral1(a)=sum(dI)/2; %bottom half is always lost
title(['pc',  num2str(400+m), ':', num2str(myintegral1(a)*100),'%']);
j=j+1;
m=m+10;
a=a+1;
end

nopc=[7.92523163e-001 ; 7.61114912e-001 ; 7.30908896e-001 ; 6.99279275e-001
; 4.67577927e-001 ; 6.88595329e-002 ; 6.10429534e-003 ; 6.27155184e-005 ;
4.34872216e-004 ; 5.58394967e-005 ; 2.91214566e-004 ; 3.30090811e-003 ;
6.59808383e-003 ; 6.99303647e-004 ; 6.57618331e-003 ; 9.92311236e-005 ;
7.62346393e-003 ; 1.55978118e-002 ;

7.97885022e-001 ; 7.61116133e-001 ; 7.41422601e-001 ; 6.95750836e-001 ;
4.54257128e-001 ; 8.07679916e-002 ; 4.11433471e-003 ; 3.41708640e-003 ;
7.51526186e-003 ; 6.37776814e-003 ; 3.67475651e-003 ; 4.18222541e-004 ;
2.08143441e-003 ; 7.06870652e-003 ; 1.27542465e-004 ; 8.85418142e-003 ;
1.51059340e-002 ; 1.27192607e-002 ;

7.94848564e-001 ; 7.60109694e-001 ; 7.48739937e-001 ; 6.87036418e-001 ;
4.55858985e-001 ; 4.57418740e-002 ; 9.31487112e-003 ; 1.47168440e-002 ;
1.25651993e-002 ; 9.11264597e-003 ; 7.84853715e-003 ; 6.30386455e-003 ;
1.51007240e-003 ; 1.99339122e-003 ; 5.50700240e-003 ; 3.67892106e-003 ;
6.25197016e-004 ; 6.81402867e-003 ;

7.99563059e-001 ; 7.59977179e-001 ; 7.54585832e-001 ; 6.72880442e-001 ;
4.77588940e-001 ; 2.69665005e-002 ; 2.75276545e-002 ; 1.43343151e-002 ;
5.32013857e-003 ; 1.91511790e-003 ; 1.91143315e-003 ; 4.03035665e-003 ;
6.24719198e-003 ; 1.48066345e-003 ; 4.09016144e-003 ; 1.46902102e-003 ;
```

```
1.18622158e-002 ; 1.85948405e-002 ;

7.95906642e-001 ; 7.59315304e-001 ; 7.59996707e-001 ; 6.57690182e-001 ;
5.11707453e-001 ; 6.03191591e-003 ; 2.43446744e-002 ; 3.34492077e-003 ;
4.34747103e-004 ; 1.21056677e-003 ; 1.04504463e-003 ; 6.90288293e-005 ;
1.46356132e-003 ; 5.51116186e-003 ; 3.30681496e-004 ; 6.90757795e-003 ;
2.52353614e-003 ; 1.76446059e-004 ;

8.00015758e-001 ; 7.59243329e-001 ; 7.62034370e-001 ; 6.48950275e-001 ;
5.47728620e-001 ; 1.82788778e-002 ; 5.74888925e-003 ; 2.92606683e-004 ;
5.84639463e-003 ; 6.88248438e-003 ; 6.00071468e-003 ; 4.42645646e-003 ;
1.24158204e-003 ; 9.39005093e-004 ; 4.97878981e-003 ; 9.36587678e-004 ;
2.07270227e-003 ; 8.84095826e-003 ;

7.94632647e-001 ; 7.58513317e-001 ; 7.57917198e-001 ; 6.50990786e-001 ;
5.45040821e-001 ; 2.72289271e-002 ; 4.16214135e-003 ; 6.64654901e-003 ;
9.48986342e-003 ; 5.38311728e-003 ; 3.56498078e-003 ; 4.03277326e-003 ;
5.02510713e-003 ; 1.86098022e-003 ; 1.94022278e-003 ; 3.04566678e-003 ;
8.30784853e-003 ; 5.63112317e-003 ;

7.98425526e-001 ; 7.60941659e-001 ; 7.52859038e-001 ; 6.65551014e-001 ;
5.16078589e-001 ; 6.79845654e-002 ; 4.40068248e-003 ; 1.36503004e-002 ;
4.60257496e-003 ; 2.19914663e-004 ; 3.12639686e-006 ; 2.08522647e-005 ;
1.35324953e-003 ; 4.94161478e-003 ; 1.05982477e-003 ; 5.56380385e-003 ;
1.05445611e-003 ; 6.42316308e-004 ;

7.93677152e-001 ; 7.63784058e-001 ; 7.46991673e-001 ; 6.79832241e-001 ;
4.88814078e-001 ; 4.66827446e-002 ; 2.31168002e-002 ; 8.19475752e-003 ;
4.36707596e-004 ; 3.41343389e-003 ; 4.77447556e-003 ; 3.97196029e-003 ;
1.49496908e-003 ; 4.13765638e-004 ; 5.81138643e-003 ; 7.63172068e-005 ;
8.27706017e-003 ; 1.60198890e-002 ;

7.97134695e-001 ; 7.66613019e-001 ; 7.42078357e-001 ; 6.93577826e-001 ;
4.71789847e-001 ; 3.01676950e-002 ; 2.58513660e-002 ; 1.24755496e-004 ;
6.23275039e-003 ; 7.93846430e-003 ; 5.69718058e-003 ; 4.96219793e-003 ;
5.41879574e-003 ; 2.93228207e-003 ; 8.96455098e-004 ; 5.82491031e-003 ;
7.79899698e-003 ; 4.02333192e-003 ;

8.00362300e-001 ; 7.69475980e-001 ; 7.37267286e-001 ; 6.99771901e-001 ;
4.74908151e-001 ; 1.75401682e-002 ; 9.05925524e-003 ; 2.92348812e-003 ;
9.93226908e-003 ; 3.15971699e-003 ; 3.67608914e-004 ; 1.51174402e-004 ;
1.05402752e-003 ; 4.47831049e-003 ; 3.12545176e-003 ; 3.58463244e-003 ;
1.54885853e-003 ; 1.97118792e-002 ;

]

grt2=zeros(11,18);
k=1;
for i=1:198
    grt2(ceil(i/18),k)= nopc(i);
    if k==18;
        k=0;
    end
    k=k+1;
end

j=1;
m=0;
a=1;
figure;
for i=1:18:197
```

```
    TT2=interp1(acilar/180*pi,grt2(ceil(i/18),:),theta);
subplot(11,1,j);
plot(theta/pi*180,TT2);
dI=dtheta*sin(theta).*TT2;
myintegral2(a)=sum(dI)/2; %bottom half is always lost
title(['nopc',  num2str(400+m), ':', num2str(myintegral2(a)*100),'%']);
j=j+1;
m=m+10;
a=a+1;
end

figure;
x=[400 410 420 430 440 450 460 470 480 490 500];
plot(x , myintegral1./myintegral2);
title('pc/nopc');
```

9. Bibliography

[1] I. Schnitzer, E. Yablonovitch, C. Caneau, T.J. Gmitter, and A. Scherer, *Appl. Phys. Lett.*, vol. 63, p. 2174, 1993.

[2] E.F. Schubert, Y.H. Wang, A.Y. Cho, L.W. Tu, and G.J. Zydzik, *Appl. Phys. Lett.*, vol. 60, p. 992, 1992.

[3] A. Scherer et al. K. Okamato, *Nature Mater.*, vol. 3, p. 601, 2004.

[4] N. Oder and J. Shakya et al., "III-Nitride photonic crystals," *Appl. Phys. Lett.*, vol. 83, p. 1231, 2003.

[5] Alexei A. Erchak et al., "Enhanced coupling to vertical radiation using a two-dimensional photonic crystal in a semiconductor light-emitting diode," *Appl. Phys. Lett.*, vol. 78, no. 5, pp. 563-565, 2001.

[6] A. David, S. Nakamura, and C. Wiesbuch et al., "Photonic bands in two – dimensionally patterned multimode GaN waveguides for ligth extraction," *Appl. Phys. Lett.*, vol. 87, 2005.

[7] J.J. Wierer and M.R. Krames et al., "InGaN/GaN quantum well heterostructure light emitting diodes employing photonic crystal structures," *Appl. Phys. Lett.*, vol. 84, p. 3885, 2004.

[8] N. Oder, K.H. Kim, J.Y. Lin, and H.X. Jiang, "III-nitride blue and ultraviolet photonic crystal light emitting diodes," *Appl. Phys. Lett.*, vol. 84, no. 4, pp. 466-468, 2004.

[9] J. Shakya et al., "Enhanced light extraction in III-Nitride ultraviolet photonic crystal light – emitting diodes," *Appl. Phys. Lett.*, vol. 85, p. 142, 2004.

[10] Teasung Kim, Paul O. Leisher, Talph Wirth, and Kent D. Choquette, "Photonic crystal structure effect on the enhancement in the external quantum efficiency of a red LED," *IEEE Photonics Technology Letters*, vol. 18, no. 17, 2006.

[11] F. Fichter, "Über Aluminiumnitrid," *Z. Anorg. Chem.*, vol. 54, pp. 322-327, 1907.

[12] F. Fitcher and F. Schröter, *Berichte der Deutschen Gesellschaft*, vol. 43, p. 1465, 1910.

[13] E. Tiede, M. Thiman, and K. Sensse, *Chem. Berichte*, vol. 61, p. 1568, 1928.

[14] W.C Johnson, J.P. Parsons, and M.C. Crew, *J. Phys. Chem.*, vol. 36, p. 2651, 1932.

[15] R. Juza and H. Hahn, *Zeitschr. Anorhan. Allgem. Chem.*, vol. 239, p. 282, 1938.

[16] H.P. Maruska and J.J. Tietjen, "The preparation and properties of vapor-deposited single-crystalline GaN," *Appl. Phys. lett.*, vol. 15, p. 367, 1969.

[17] J.I. Pankove and J.A. Hutchby, *J. Appl. Phys.*, vol. 47, p. 5387, 1976.

[18] R. Dingle, K.L. Shaklee, R.F. Leheny, and R.B. Zetterstrom, *Appl. Phys. Lett.*, vol. 19, p. 5, 1971.

[19] H.M. Manasevit, F.M. Erdmann, and W.I. Simpson, "The use of metalorganics in the preparation of semiconductor materials IV- The nitrides of aluminum and gallium," *Journal of the Electrochemical Society*, vol. 118, p. 1864, 1971.

[20] I. Akasaki and I. Hayashi, "The use of MBE in the preparation of semiconductor materials," *Industrial Science and Technology*, vol. 17, p. 48, 1976.

[21] S. Yoshida, S. Misawa, and S. Gonda, "Epitaxical growth of GaN/AlN heterostructures," *J. Vac. Sci. Technol. B (USA)*, vol. 1, no. 2, pp. 250-3, 1983.

[22] H. Amano, N. Sawaki, I. Akasaki, and Y. Toyoda, "Metalorganic vapor phase epitaxical growth of high quality GaN film using an AIN buffer layer," *Appl. Phys. Lett. (USA)*, vol. 48, no. 5, pp. 353-5, 1986.

[23] I. Akasaki, H. Amano, M. Kito, and K. Hiramatsu, "Photoluminescence of Mg-doped p-typr GaN and electroluminescence of GaN p-n junction LED," *J. Lumin*, vol. 48&49, p. 666, 1991.

[24] S. Nakamura, T. Mukal, M. Senoh, and N. Iwasa, "Thermal annealing effects on P-type Mg-doped GaN films," *Jpn. J. Appl. Phys., Part 2: Letters*, vol. 31, pp. 139-142, 1992.

[25] R. Niebuhr, K.H. Bachem, U. Kaufmann, M. Maier, and C. Merz, "Electrical and optical properties of oxygen doped GaN grown by MOCVD using N2O," *Journal of Electronic Materials*, vol. 26, no. 10, pp. 1127-1130, 1997.

[26] S. Nakamura, *Jpn. Appl. Phys.*, vol. 30, 1991.

[27] Akasaki et al., *J. Cryst. Growth*, vol. 98, p. 209, 1989.

[28] J. Jayapalan, B. Scromme, R. Vaudo, and V. Phanse, *Appl. Phys. Lett.*, vol. 73, p. 1188, 1998.

[29] B. Monemar, "Fundamental enrgy gap of GaN from photoluminescence excitation spectra," *Phys. Rev. B.*, vol. 10, p. 676, 1974.

[30] J.I. Pankove, E.A. Miller, and J.E. Berkeyheiser, *RCA Rev.*, vol. 32, p. 383, 1971.

[31] A.S. Barker and M. Ilegems, "Infrared lattice vibration and free-alectron dispersion in GaN," *Phys. Rev. B.*, vol. 7, p. 743, 1973.

[32] Takashi Matsuoka, Hiroshi Okamoto, Masashi Nakao, Hiroshi Harima, and Eiji Kurimoto, "Optical bandgap energy of wurtzite InN," *Appl. Phys. Lett.*, vol. 81, no. 7, p. 1246, 2002.

[33] V. Yu. Davydov, A.A. Klochikhin, R.P. Seisyan, V.V. Emtsev, and S.V. Ivanov, *Phys. Status Solidi B*, vol. 229, 2002.

[34] W.A. Harrison, *Electronic structure and the properties of solids*. New York: Dover Publications, 1989.

[35] D.R. Lide, *Handbook of Chemistry and Physics*.: CRC Press, 1992-1993.

[36] E.K. Sichel and J.I. Pankove, "Thermal conductivity of GaN, 25-360 K," *J. Phys. Chem. Solids*, vol. 38, p. 330, 1977.

[37] H. Morkoc, *Nitride Semiconductors and Devices*. New York: Springer, 1999.

[38] M. Leszczynski, H. Teisseyre, T. Suski, I. Grzegory, and M. Bockowski, "Lattice parameters of gallium nitride," *Appl. Phys. Lett.*, vol. 69, p. 73, 1994.

[39] S. Strite and H. Morkoc, "GaN, AIN and InN: A review," *J. Vac. Sci. Technol. B*, vol. 10, p. 1237, 1992.

[40] M. Leszczynski, T. Suski, H. Teisseyre, P. Perlin, and I. Grzegory, "Thermal expansion of gallium nitride," *J. Appl. Phys.*, vol. 76, p. 4909, 1994.

[41] B.C. Chung and M. Gershenzon, *Journal of Applied Physics Letters*, vol. 72, p. 651, 1992.

[42] J.D. Guo et al., "A bilayeer Ti/Ag ohmic contact for highly doped n-type GaN films,"

Appl. Phys. Lett., vol. 68, p. 235, 1996.

[43] H. Morkoc et. al., *Appl. Phys. Lett.*, 1994.

[44] J.I. Pankove and T.D. Moustakas, *Gallium Nitride (GaN) I, in Semiconductors and semimetals*, 50th ed.: Academic Press, 1999.

[45] X.H. Wu et al., "Defect structure of metal-organic chemical vapor deposition-grown epitaxial (0001) GaN/Al2O3," *Journal of Applied Physics*, vol. 80, no. 6, p. 3228, 1996.

[46] Y. Xin et al., "Direct observation of the core structures of threading dislocations in GaN," *Applied Physics Letters*, vol. 72, p. 2680, 1998.

[47] A. David and C. Weisbuch, "Optimization of light diffracting photonic crystals for high extraction efficiency LEDs," *J. Disp. Tech.*, vol. 3, p. 133, 2007.

[48] J.S. Speck and S.J. Rosner, "The role of threading dislocations in the physical properties of GaN and its alloys," *20th International Conference on Defects in Semiconductors (ICDS-20)*, 1999.

[49] P. Kozodoy et al., "Electrical characterization of GaN p-n junctions with and without threading dislocations," *Appl. Phys. Lett. (USA)*, vol. 73, no. 7, pp. 975-7, 1998.

[50] A. Usui, H. Sunakawa, A. Sakai, and A.A. Yamaguchi, "Thick GaN epitaxical growth with low dislocation density by hydride vapor phase epitaxy," *Jpn. J. Appl. Phys. (Japan)*, vol. 36, pp. L899-902, 1997.

[51] K. Hiramitsu, K. Nishiyama, M. Onishi, H. Mizutani, and M. Narukawa, "Fabrication and characterization of low defct density GaN using facet-controlled epitaxical lateral overgrowth (FACELO)," *J. of Cryst. Growth (Netherlands)*, vol. 221, pp. 316-26, 2000.

[52] U. Kaufmann, M. Kunzer, H. Obloh, and Ch. Manz, "Origin of defect-related photoluminescence bands in doped and nominally undoped GaN," *Physical Review B*, vol. 59, p. 5561, 1999.

[53] T. Ogino and M. Aoki, *Jpn. J. Appl. Phys.*, vol. 19, p. 2395, 1980.

[54] F.A. Ponce, D.P. Bour, W. Gotz, and P.J. Wright, *Appl. Phys. Lett.*, vol. 68, p. 57, 1996.

[55] Jörg Neugebauer and Chris G. Van de Walle, "Gallium vacancies and the yellow

luminescence in GaN," *Appl. Phys. Lett.*, vol. 69, no. 4, 1996.

[56] T. Suski, P. Perlin, H. Teisseyre, M. Leszczynski, and I. Grzegory, "Mechanism of yellow luminescence in GaN," *Appl. Phys. Lett.*, vol. 67, no. 15, 1995.

[57] P. Bhattacharya, *Semiconductor Optoelectronic Devices*.: Prentice Hall, 1997.

[58] B. Rau et al., "In – plane polarization anisotropy of the spontaneous emission of M – plane GaN/(Al, Ga)N quantum wells," *Appl. Phys. Lett.*, vol. 77, p. 3343, 2000.

[59] M.I. Nathan, W.P. Dumke, G. Burns, F.J. Dill, and G.J. Lasher, "Simulated emission radiation from GaAs p-n junctions," *Appl. Phys. Lett.*, vol. 1, p. 62, 1962.

[60] J.I. Panvoke, *Optical Process in semiconductors*. New Jersey: Pretice-Hall, 1971.

[61] S. Nakamura, M. Senoh, N. Iwasa, and S. Nagamaha, "High-power InGaN single-quantum-well-structure blue and violet light-emitting diodes," *Appl. Phys. Lett.*, vol. 67, no. 13, pp. 1868-1870, 1995.

[62] S. Nakamura, M. Senoh, N. Iwasa, and S. Nagahama, "High-brightness in InGaN blue, green and yellow light-emitting diodes with quantum well structures," *Jpn. J. Appl. Phys.*, vol. 34, pp. L797-L799, 1995.

[63] S. Nakamura, *The Blue Laser Diode*. Hong Kong: Springer, 1997.

[64] S. Kamiyama et al., "UV laser diode with 350.9-nm-lasing wavelength grown by hetero-epitaxical-lateral overgrowth technology," *IEEE Journal on Selected Topics in Quantum Electronics*, vol. 11, no. 5, pp. 1069-1073, 2005.

[65] K. Mayes et al., "High-power 280 nm AlGaN Light-emitting diodes based on an asymmetric single-quantum well," *Appl. Phys. Lett.*, vol. 84, no. 7, pp. 1046-1048, 2004.

[66] C. Weisbuch and P.M. Petroff et al., "Light extraction from GaN-based light emitting diode structures with a noninvasive two-dimensional photonic crystal," *Appl. Phys. Lett.*, vol. 94, pp. 23-101, 2009.

[67] C. Wiesmann et al., "Photonic crystal LEDs – designing light extraction," *Laser&Photon Rev.*, p. 1, 2008.

[68] S. Nakamura, M. Senoh, S. Nagahama, N. Iwasa, and T. Yamada, "InGaN-based multi-quantum-well-structure laser diodes," *Jpn. J. Appl. Phys.*, vol. 35, pp. L74-L76, 1996.

[69] M. Ferhat, J. Furthmuller, and F. Bechstedt, *Appl. Phys. Lett*, vol. 80, no. 8, 2002.

[70] R. Micheletto et al., "Near – field evidence of local polarized emission centers in InGaN/GaN materials," *Appl. Phys. Lett.*, vol. 95, 2009.

[71] J. Ruan et al., "Indium –Indium-induced effect on polarized electroluminescence from InGaN/GaN MQWs light emitting diodes," *Chin. Phys. Lett.*, vol. 26, no. 8, 2009.

[72] Lu Chen and Arto V. Nurmikko, "Fabrication and performance of efficient blue light emitting III-Nitride photonic crystals," *Appl. Phys. Lett.*, vol. 85, p. 3663, 2004.

[73] H. Ryou et al., "Control of quantum – confined Stark effect in InGaN – based quantum wells," *IEEE journal of selected topics in quantum electronics*, vol. 15, p. 1080, 2009.

[74] Yuoqun Li and Fengyi Jiang et al., "Study of polarization field in GaN – based blue LEDs on Si and sapphire substrate by electroluminescence," *Journal of Luminescence*, vol. 122-123, p. 567, 2007.

[75] Jonathan J. Wierer and Mischa M. Megens, "III-Nitride photonic crystal light emitting diodes with high extraction efficiency," *Nature Photonics*, vol. 3, p. 163, 2009.

[76] S. Nakamura and C. Weisbuch et al., "Directional emission control and increased light extraction in GaN photonic crystal light emitting diodes," *Appl. Phys. Lett.*, vol. 93, 2008.

[77] Han Youl Ryu, "Large enhancement of extraction efficiency in thin film photoniccrystal ingan light emitting diode structures," *Journal of Korean Physical Society*, vol. 55, no. 6, p. 2642, 2009.

[78] M. Boroditsky and E. Yablonovitch et al., "Light-emitting diode extraction efficiency," *SPIE-Int. Soc. Opt. Eng.*, vol. 3002, p. 119, 1997.

[79] T. Fujii et al., "Increase in the extraction efficiency of GaN-based light-emitting diodes via surface roughening," *Appl. Phys. Lett.*, vol. 84, no. 6, pp. 855-857, 2004.

[80] J.J. Wierer et al., "High-power algainn flip-chip light-emitting diodes," *Appl. Phys. Lett.*, vol. 78, no. 22, pp. 3379-3381, 2001.

[81] L. Brillouin, *Wave propagation in Periodic Structures: Electric Filters and Crystal Lattices*.: McGraw Hill, 1946.

[82] K. Othaka, "Energy band of photon and low energy photon diffraction," *Physical Review B*, vol. 19, no. 10, 1979.

[83] E. Yablonovitch, *Phys. Rev. Lett.* , vol. 58, p. 2059, 1987.

[84] S. John, *Phys. Rev. Lett.*, vol. 58, p. 2486, 1987.

[85] J.D. Joannopoulos et al., "Photonic crystals: putting a new twist on light," *Nature*, vol. 386, p. 143, 1997.

[86] E. Yablonovitch, T.J. Gmitter, and K.M. Leung, "Photonic band structure: The face-centered cubic case employing nonspherical atoms," *Phys. Rev. Lett.*, vol. 67, pp. 2295-2298, 1991.

[87] U. Gruning, V. Lehmann, and C.M. Engelhardt, "Two dimensional photonic band structures based on porous silicon," *Apl. Phys. Lett.*, vol. 66, pp. 3254-3256, 1995.

[88] T.F. Krauss, R.M. De La Rue, and S. Brand, "Two dimensional photonic band gap structures operating at near infrared wavelengths," *Nature*, vol. 383, pp. 699-702, 1996.

[89] A. Mekis et al., *Phys. Rev. Lett.*, vol. 77, p. 3787, 1996.

[90] L. Zhang and E.A. Fitzgerald et al., "Linearly polarized light emission from InGaN light emitting diode with subwavelength metallic nanograting," *Appl. Phys. Lett.*, vol. 95, 2009.

[91] M. Qi et al., "A three-dimensional optical photonic crystal with designed point defects," *Nature*, vol. 429, pp. 538-542, 2004.

[92] K. Ren, X. Ren, R. Li, J. Zhou, and D. Liu, "Creating “defects” in photonic crystals by controlling polarizations," *Phys. Lett. A*, vol. 325, pp. 415-419, 2004.

[93] P.V. Braun, S.A. Rinne, and F. Garcia-Santamaria, "Introducing Defects in 3D Photonic Crystals: State of the Art," *Advanced Materials*, vol. 18, pp. 2665-2678, 2006.

[94] O. Painter, J. Vuckovic, and A. Scherer, "Defect modes of a two-dimensional photonic crystal in an optically thin dielectric slab," *J. Opt. Soc. Am. B*, vol. 16, pp. 275-285,

1999.

[95] M.S. Thijssen et al., "Inhibited ight Propagation and Broadband Reflection in Photonic Air-Sphere Crystals," *Phys. Rev. Lett.*, vol. 83, pp. 2730-2733, 1999.

[96] P. Vukusic, J.R. Sambles, C.R. Lawrence, and R.J. Wootton, "Quantified interference and diffraction in single Morpho butterfly scales," *Proc. Roy. Soc: Bio. Sci.*, vol. 266, pp. 1403-1414, 1999.

[97] J. Zi et al., "Coloration strategies in peacock feathers," *Proc. Nat. Acad. Sci. USA*, vol. 100, pp. 12576-12578, 2003.

[98] Dae-Sung Song, Yong-Jea Lee, Han-woo Choi, and Yong-Hee Lee, *Appl. Phys. Lett.*, vol. 82, p. 3182, 2003.

[99] John D. Joannopoulos, Steven G. Johnson, Joshua N. Winn, *Molding the flow of light*, 2nd ed. USA: Princeton University Press, 2008.

[100] Neil W. Ashcroft, N. David Mermin, *Solid State Physics*, 1st ed. USA: Saunders College Publishing, 1976.

[101] A. David et al., "Photonic-crystal GaN light-emitting diodes with tailored guided modes distribution," *Appl. Phys. Lett.*, vol. 88, no. 6, 2006.

[102] D. Joannopoulos et al., "Enhanced coupling to vertical radiation using a two – dimensional photonic crystal in a semiconductor light – emitting diode," *Appl. Phys. Lett.*, vol. 78, p. 563, 2001.

[103] Min-Ki Kwon and Yong Chun Kim et al., "Enhanced emission efficiency of GaN/InGaN multiple quantum well light – emitting diode with an embedded photonic crystal," *Appl. Phys. Lett.*, vol. 92, 2008.

[104] Chun-Feng Lai and Wen-Yung Yeh et al., *Appl. Phys. Lett.*, vol. 92, 2008.

[105] E.Y. Lin et al., "Optical polarization and internal quantum efficiency for InGaN quantum wells on a – plane GaN," *Physica B: Condensed Matter*, vol. 405, no. 7, pp. 1857-1860, 2010.

[106] M.F. Schubert and E.F. Schubert et al., "Polarization of light emission by 460 nm GaInN/GaN light-emitting diodes grown on (0001) oriented sapphire substrates," *Appl.*

Phys. Lett., vol. 91, 2007.

[107] J. Shakya et al., "Polarization of III – Nitride blue and ultraviolet light – emitting diodes," *Apl. Phys. Lett.*, vol. 86, 2005.

[108] S. Fan, P.R. Villeneuve, J.D. Joannopoulos, and E.F. Schubert, "High extraction efficiency of spontaneous emission from slabs photonic crystals," *Phys. Rev. Lett.*, no. 78, pp. 3294-3297, 1997.

[109] M. Fujita, S. Takahashi, Y. Tanaka, T. Asano, and S Noda, "Simultaneous inhibition and redistribution of spontaneous light emission in photonic crystals," *Science*, vol. 308, pp. 1296-1298, 2005.

[110] E.M. Purcell, "Spontaneous emission probabilities at radio frequencies," *Phys. Rev.*, vol. 69, p. 681, 1946.

[111] M. Rattier, H. Benisty, R.P. Stanley, J.F. Carlin, and R. Houdré, *IEEE J. Sel. Top. Quantum Electron*, vol. 8, p. 238, 2002.

[112] H. Rigneault, F. Lemarchand, and A. Sentenac, *J. Opt. Soc. Am. A*, vol. 17, p. 1048, 2000.

[113] M. Boroditsky et al., *J. Lightwave Technol*, vol. 17, p. 2096, 1999.

[114] M. Boroditsky and E. Yablonovitch, "Spontaneous Emission extraction and Purcell enhancement from thin film 2-D photonic crytals.," *J. Lightwave Tech.*, vol. 17, p. 2096, 1999.

[115] T. Baba et al., *J. Lightwave Technol*, vol. 17, p. 2113, 1999.

[116] M. Rattier et al., "Omnidirectional and compact guided lightextraction from Archimedean photonic lattices," *Appl. Phys. Lett.*, vol. 83, p. 1238, 2003.

[117] Han-Youl Ryu et al., "Enhancement of light extraction from two – dimensional photonic crystal slab structures," *IEEE Journal on selected topics in quantum electronics*, vol. 8, p. 231, 2002.

[118] F. Scholz et al., *Jpn. J. Appl. Phys.*, vol. 37, p. 745, 1998.

[119] E.F. Schubert, "High extraction efficiency of spontaneous emission from slabs of

photonic crystals," *Phys. Rev. Lett.*, vol. 78, p. 3294, 1997.

[120] D.W. Prather et al., "Photonic crystal structures and applications: Perspective, overview, and development," *IEEE J. Sel. Top. Quantum Electronics*, vol. 12, p. 1416, 2006.

[121] D.H. Kim et al., "Enhanced light extraction from GaN-based light-emitting diodes with holographically generated two-dimensional photonic crystal patterns," *Appl. Phys. Lett.*, vol. 87, no. 20, 2005.

[122] E. Yablonovitch M. Boroditsky, *Lightwave Technology*, vol. 17, p. 2096, 1999.

[123] H. Ryu et. al, *Appl. Phys. Lett.*, vol. 78, p. 1174, 2001.

[124] M.E. Ryan, A.C. Camacho, and J.K. Bhardwaj, *Phys. Stat. Sol.-A*, vol. 176, p. 743, 1999.

[125] S. Randolph, "Focused, Nanoscale Electron-Beam-Induced Deposition and Etching," *Critical Reviews of Solid State and Materials Sciences*, vol. 31, p. 55, 2006.

[126] L.I. Goray, J.F. Seely, and S. Yu Sadov, "Spectral separation of the efficiencies of the inside and outside orders of soft-x-ray-extreme-ultraviolet gratings at near normal incidence," *J. Appl. Phys.*, vol. 100, no. 9, pp. 949-1113, 2006.

[127] L.I. Goray and J.F. Seely, "Efficiencies of master, replica and multilayer gratings for the soft x-ray-EUV range: modeling based on the modified integral method and comparisons to measurements," *Appl. Opt.*, vol. 41, no. 7, pp. 1434-1445, 2002.

[128] L.I. Goray, I.G. Kuznetsov, S. Yu Sadov, and D.A. Content, "Multilayer resonant subwavelength gratings: effects of waveguide modes and real groove profiles," *J. Opt. Soc. Am A*, vol. 23, no. 1, pp. 155-165, 2006.

[129] L.I. Goray, "Numerical analysis of the efficiency of multilayer-coated gratings using integral method," *Nuclear Inst. and Methods in Physics Research A*, vol. 536, no. 1-2, pp. 211-221, 2005.

[130] Hyun Kyong Cho et al., "Light extraction enhancement from nano-imprinted photonic crystal GaN – based blue light – emitting diodes," *Optics express*, vol. 14, p. 8654, 2006.

[131] J. P. Berenger, *J. Comput. Phys.*, vol. 114, p. 185, 1994.

[132] W.J. Choi and Q-Han Park, "FDTD simulation for light extraction in a GaN – based LED," *Journal of Korean Physical Society*, vol. 49, p. 877, 2006.

[133] M.E. Lin, Z. Ma, F.Y. Huang, Z.F. Fan, and L.H. Allen, "Low resistance ohmic contacts on wide band-gap GaN," *Appl. Phys. Lett.*, vol. 64, p. 1003, 1994.

[134] Han Youl Ryu, "Modification of the light extraction efficiency in micro-cavity vertical ingan light emitting diode structures," *Journal of Korean Physical Society*, vol. 55, no. 3, p. 1267, 2009.

[135] Chia-Hsin Chao and S.L. Chuang, "Theoretical demonstration of enhancement of light extraction of flip-chip GaN light-emitting diodes with photonic crystals," *Appl. Phys. Lett.*, vol. 89, pp. 91-116, 2006.

[136] Han Youl Ryu and Jeonh Ki Hwnag, "Enhancement of light extraction from two-dimensional photonic crystal slab structures," *IEEE Journal of Selected Topics in Quantum Electronics*, vol. 8, no. 2, 2002.

[137] S. Keller et al., "Optical and structural properties of GaN nanopillar and nanostripe arrays with embedded InGaN/GaN multi-quantum wells," *Journal of Applied Physics*, vol. 100, no. 5, p. 7, 2006.